Cosmic Shear Analysis of the Garching-Bonn Deep Survey

Dissertation

zur

Erlangung des Doktorgrades (Dr. rer. nat.)

der

Mathematisch-Naturwissenschaftlichen Fakultät

der

Rheinischen Friedrich-Wilhelms-Universität Bonn

vorgelegt von

Marco Hetterscheidt

aus

Emmerich

Bonn 2006

Angefertigt mit Genehmigung der Mathematisch-Naturwissenschaftlichen Fakultät der Rheinischen Friedrich-Wilhelems-Universität Bonn.

1. Referent: Prof. Dr. P. Schneider
2. Referent: Prof. Dr. K. S. de Boer

Tag der Promotion: 07.02.2007

Contents

List of Figures

Chapter 1

Introduction

A few decades ago, cosmology was a very data-starved science dominated by a number of speculative theories. However, as we have entered a new era of powerful instruments, cosmologists are confronted with a huge amount of high-quality data. With high-precision cosmological observations at hand we are now able to actually test and complete the cosmological paradigm. Measurements of the cosmic microwave background using the Cosmic Background Explorer (COBE, launched in 1989) and the Wilkinson Microwave Anisotropy Probe (WMAP, launched in 2001) represent a major progress in our understanding of the Universe. Measurements of supernovae Type Ia, galaxy distributions, the Lyman α-forest and gravitational lensing with data from the Hubble space telescope (HST, fully functional since 1993) and large optical telescopes like the Very Large Telescope (VLT, first light in 1999) further deepened our understanding of the Universe. With complementary measurements of, e.g., the galaxy cluster abundance using X-ray satellites like ROSAT and ASCA (launched in 1990 and 1993, respectively) the formulated cosmological models can be confirmed independently. Using these high-precision measurements we actually know for the first time the composition and geometry of our Universe in great detail, and a standard model of cosmology, the so-called concordance model, has emerged and seems to be consistent with most of the observations.

The global dynamics of the Universe, such as its curvature and expansion rate, and the statistical properties, characterised by the matter power spectrum, can be described by simple parameterisations, the so-called cosmological parameters. Cosmological models of the Universe predict these parameters, hence measuring them allows us to test different models.

The coherent gravitational light deflection of distant galaxies by the tidal gravitational field of the large-scale structure (LSS) of the Universe induces weak shape and size distortions of galaxy images. This weak gravitational lensing effect by the LSS is called *cosmic shear* and can be measured in a statistical way. Cosmic shear analyses represent a powerful method to explore the statistical properties of the (projected) LSS. It is nowadays one of the pillars to reveal valuable information about cosmology and to determine constraints on cosmological parameters. In particular, the cosmic shear signal is sensitive to the amplitude of density fluctuations of the LSS, characterised by the total matter density $\Omega_{\rm m}$

and the mass power spectrum normalisation σ_8. Especially for the determination of the normalisation parameter, σ_8, cosmic shear is superior to other methods because:

(A) it is independent of any assumptions regarding the relation between dark and luminous matter; one therefore does not have to model, for example, the relation between galaxy cluster mass and its luminosity or the bias between galaxies and dark matter as it is required in galaxy surveys;

(B) it is sensitive to the non-linear part of the matter power spectrum. It therefore is suited to test the complex theories of structure growth on small physical scales since the amplitude of the cosmic shear signal increases as angular (physical) scales decreases. In contrast to that, cosmic microwave background (CMB) experiments are only sensitive to much larger, linear scales, and only measure the temperature power spectrum normalisation of the early Universe.

With cosmic shear analyses one measures the statistical properties of the *projected* LSS out to a redshift of about unity. The non-linear structure growth and projection effects dilute most of the primordial features like the imprints of the baryon acoustic oscillations on the matter power spectrum. Hence, cosmic shear alone cannot determine cosmological parameters uniquely. In fact, there exist strong degeneracies between, e.g., the power spectrum normalisation and the total matter density. However, the combination with other independent and complementary experiments that probe the power spectrum on larger, linear scales breaks the parameter degeneracies. Measurements of the CMB, for instance, yield degeneracies in the Ω_m-σ_8 plane that are almost perpendicular to those of the cosmic shear measurements. Combining different types of observations with cosmic shear results not only substantially improves the estimate of cosmological parameters but also provides consistency checks.

The shape distortion of distant galaxy images induced by the LSS is mostly weak and its measurement for single source galaxies is extremely noisy. Hence, we need wide and deep fields to obtain a sufficient number of distant galaxies to reach a significant cosmic shear signal for precise estimates of cosmological parameters and, in particular, to shed light on the nature of dark matter and dark energy. Ongoing and future deep wide-field surveys using state-of-the-art telescopes and multi-chip cameras with field-of-views of one square degree or more will provide us with the required large, high-quality data sets.

These future surveys will produce several dozen terabytes of data per year. The data will be extremely difficult to reduce and calibrate due to the multi-chip layout and size of the cameras. To handle this huge amount of data and to produce co-added mosaics from individual exposures having a common high-quality standard the cosmology group in Bonn developed a stand-alone, nearly fully automatic pipeline. The data reduction process provides a precise alignment of galaxy images of different exposures that are finally co-added on a sub-pixel basis to obtain unbiased galaxy shape measurements. Additionally, our pipeline removes all instrumental signatures, accurately maps the noise properties of the co-added image and delivers quality control plots during the whole data reduction process.

Correlations of the weak gravitational shape distortions of distant galaxies are directly related to the matter power spectrum and its underlying cosmology. However, the measured correlations can be an order of magnitude lower than correlations induced by systematic effects, like the anisotropic point spread function (PSF). The correction of these unwanted, but unavoidable, systematic effects is a challenging issue that has to be carried out and tested carefully. The current statistical errors of cosmic shear measurements are of the order of five percent and will drop to less than one percent during the next few years. We, therefore, are entering a phase where systematic errors may begin to dominate over statistical errors. To respond to this progression, the Shear TEsting Programme (STEP), a world-wide collaborative project of 16 different groups, was initiated in June 2004. Its aim is to improve the accuracy and reliability of cosmic shear measurements, and to allow for precise tests of the predictions of the concordance model. Here we present the current status of this unique project.

Due to the need for high-quality data, only just six years ago a significant cosmic shear signal on angular scales between one and 10 arcminutes has been measured independently by four different groups (Bacon et al. 2000; Van Waerbeke et al. 2000; Kaiser et al. 2000; Wittman et al. 2000). Within the error bars their results agreed very well with the currently favoured cosmological model. More recently, several other cosmic shear measurements have been carried out from wide-field ground-based and very deep space-based observations. The statistical errors of these measurements are already small enough not only to distinguish between different cosmological models but to estimate cosmological parameters with high accuracy.

In this work we perform a cosmic shear analysis of the *Garching-Bonn Deep Survey* (GaBoDS), a large (mainly archival) data set of deep ground-based observations, obtained with the Wide Field Imager of the MPG/ESO 2.2m telescope. The deep images were taken under superb seeing conditions (between $0\farcs7$ and $1\farcs2$) allowing us to achieve a high number density of background galaxies and to perform a good PSF correction. With this survey we determined constraints for the mass power spectrum normalisation, σ_8, the total matter density, Ω_m, and the dark energy density, Ω_Λ.

One advantage of this survey is that the single fields of our data set are widely separated in the sky, hence they are statistically independent. The noise of cosmic shear measurements is not only due to the shape measurements of the source galaxies but also due to the fluctuations of cosmic shear signals for different lines-of-sight. This sample variance is also called cosmic variance. On small angular scales the statistical noise due to galaxy shapes is the dominant noise contribution and on large angular scales the cosmic variance. The cosmic variance and hence the total cosmic shear measurement error therefore can be estimated in an unbiased way directly from the data, since the observed fields are uncorrelated. For cosmic shear analyses not only the shape of source galaxies but also their redshift has to be known. Another advantage of the GaBoDS is that, in contrast to other cosmic shear surveys, we measure the redshift distribution directly from a sub-sample of *lensing* galaxies. Here we do not have to use an external redshift distribution, since the GaBoDS comprises the *Deep Public Survey* (DPS), a multi-colour survey suitable for redshift estimates.

Thesis content

The aim of this thesis is to obtain an unbiased cosmic shear signal from archival wide-field data reduced with our nearly fully automatic data reduction pipeline and to address the problems of potential systematic errors. Combining the cosmic shear signal with a measured redshift distribution obtained from a data sub-sample we aim for determining constraints on cosmological parameters. The thesis is organised as follows:

- In Chapter 2 we give the foundations of the standard model of cosmology needed for an understanding of our cosmological parameter estimate using cosmic shear. We introduce the homogeneous, isotropic Universe together with the theory of structure formation and its statistical description.

- In Chapter 3 we describe the basic principle of gravitational lensing and present the theoretical groundwork of cosmic shear used in later Chapters.

- In Chapter 4 we first introduce the GaBoDS and the DPS archival data set. We describe the data reduction with our developed GaBoDS image reduction pipeline which we describe in detail in the second part of this Chapter. The data characteristics are published in Schirmer et al. (2006) and Hildebrandt et al. (2006), and the full description of the pipeline is given in Erben et al. (2005).

- In Chapter 5 we describe the theoretical PSF correction formalism and our practical implementation. Furthermore, we describe the shear catalogue creation and give a summary of our findings of the STEP project. The practical implementation of the PSF correction formalism we used in our analysis are published in Hetterscheidt et al. (2005, 2006). The results of the STEP project are published in Heymans et al. (2006a) and Massey et al. (2006).

- In Chapter 6 we present the cosmic shear analysis and data validation of the GaBoDS data set. Combining the cosmic shear signal with a photometric redshift distribution of a galaxy sub-sample obtained from the *UBVRI* observations of the DPS we determine constraints for the matter density $\Omega_{\rm m}$, the mass density power spectrum normalisation σ_8, and the dark energy density Ω_Λ. Additionally we discuss in detail the influence of systematic errors on the cosmic shear signal and the subsequent parameter estimates. This part of the thesis is published in Hetterscheidt et al. (2006).

- In Chapter 7 we conclude with a summary of the major results and give an outlook of future cosmic shear analyses.

It is obvious that the introduction part (Chapter 2 and 3) cannot be complete, however, we give a self-contained depiction of cosmology and weak gravitational lensing in the framework of the aim of the thesis. Chapters 4 and 5 are rather technical and are discussed in detail since obtaining unbiased shear estimates is the most essential part of all cosmic shear analyses. Chapter 6 concentrates on the scientific questions and comprises the main results of the thesis.

Chapter 2

The standard model of cosmology

The standard model of cosmology describes the origin of matter, the dynamics of the Universe as a whole, as well as the statistical properties of the large-scale structure (LSS) of the Universe and their evolution in time. Two pillars of the standard model we discuss separately in this Chapter: the theory of the isotropic and homogeneous Universe and the theory of structure formation. The first theory is based on General Relativity and the cosmological principle which says that the Universe is isotropic around each point independent of its age. We describe the basics of the theory and some observational evidences in Sect. 2.1. Based on that we discuss the evolution of structure in the Universe and its statistical description (Sect. 2.2).

This Chapter is organised as follows. We start with an outline of the derivation of the Friedmann equations describing the evolution of an isotropic and homogeneous Universe and give some consequences for distance measures (Sects. 2.1.1–2.1.4). We then describe the striking observational evidences for an isotropic Universe, and finally give an overview of its composition (Sects. 2.1.5–2.1.6). In Sect. 2.2 we discuss the LSS, its formation and evolution in time, starting with linear perturbation theory (Sect. 2.2.1). In Sects. 2.2.2–2.2.4 we introduce the mass density power spectrum as a measure of the statistical properties of the Universe. We end Sect. 2.2 by giving an overview of the cosmological parameter estimates obtained from measurements of the cosmic microwave background with the WMAP satellite.

This Chapter is based on Fließbach (1998); Peacock (1999); Bartelmann & Schneider (2001); Meylan et al. (2006); and Schneider (2006).

2.1 The isotropic Universe

2.1.1 Field equations

The electromagnetic and gravitational forces are the only forces with infinite range. Since the Universe is on average electrically neutral the gravitational force is dominant on cosmological scales. Not only the motion of the planets in our Solar System and of our Sun

in the potential of the Galaxy can be described by gravity but also the formation of structure in the Universe, its dynamics and evolution as a whole. In 1915 Einstein formulated a theory of gravity, the General Theory of Relativity. It describes gravity as a property of the four-dimensional space-time which is deformed in the presence of masses. In this framework, the four-dimensional space-time is characterised by the metric tensor $g_{\alpha\beta}$. The dynamics of the metric tensor are governed by Einstein's field equations (Einstein 1916):

$$G_{\alpha\beta} = \frac{8\pi G}{c^2} T_{\alpha\beta} + \Lambda g_{\alpha\beta}, \tag{2.1}$$

where $c = 3 \times 10^8\,\mathrm{m\,s^{-1}}$ is the vacuum speed of light, $G = 6.673 \times 10^{-11}\,\mathrm{kg\,m^{-1}\,s^{-2}}$ is the gravitational constant and Λ is the cosmological constant. The Einstein tensor, $G_{\alpha\beta}$, is constructed from the first and second derivatives of $g_{\alpha\beta}$. The total matter and total energy content of the Universe is described by the energy-momentum tensor, $T_{\alpha\beta}$. The addition of the cosmological constant is a generalisation of the field equations and was introduced by Einstein to allow for a static Universe.

In the 1920s Hubble measured distances to Cepheids in spiral nebulae and discovered that they were well located outside our Galaxy. After these measurements it was accepted that the nebulae were galaxies comperable to our Milky Way. Hubble (1929) combined his and Shapley's (1924a,b) measurements of galaxy distances with measurements of the redshifts associated with the galaxies (e.g. Slipher 1917) and found a roughly linear increase of the object distances with their redshifts. After observing the so-called Hubble flow, indicating the expansion of the Universe, Einstein rejected Λ as it seemed to be a superfluous admixture. However, recent observations suggest that the Universe experiences an expansion that is accelerated. The cosmological constant Λ was therefore reintroduced in order to describe the acceleration, see Sect. 2.1.6.

2.1.2 Cosmological principle and Friedmann equations

The largest coherent structures observed in the Universe are super-clusters with sizes of $\sim 150\,\mathrm{Mpc}$. Compared to the size of the visible Universe ($\sim 4000\,\mathrm{Mpc}$) these structures are small. On average the density of the Universe is therefore homogeneous, where the largest observed structures can be seen as density perturbations. In first-order approximation these density perturbations can be neglected. In addition, the Universe is isotropic around us. Observationally this is verified by the nearly isotropic distribution of distant galaxies and radio sources, and especially by the near-isotropy of the cosmic microwave background (Sect. 2.1.5). Assuming that the Earth is not a special place in the Universe the *cosmological principle* follows: *the Universe is isotropic around any point, and all fundamental observers experience the same history of the Universe.*

Robertson (1935) and Walker (1936) found independently a metric which obeys the cosmological principle, the so-called Robertson-Walker metric (RWM):

$$\mathrm{d}s^2 = g_{\alpha\beta}\,\mathrm{d}x^\alpha\,\mathrm{d}x^\beta = c^2\,\mathrm{d}t^2 - a^2(t)\,\mathrm{d}l^2, \tag{2.2}$$

with the line element $\mathrm{d}l$ describing the homogeneous and isotropic space-like hypersurface,

$$\mathrm{d}l^2 = \mathrm{d}w^2 + f_\mathrm{K}^2(w)(\,\mathrm{d}\phi^2 + \sin^2\phi\,\mathrm{d}\theta^2), \tag{2.3}$$

where θ and ϕ are angular coordinates. The variable t is the cosmic time and $a(t)$ is the scale factor which describes the overall expansion or contraction of the Universe. The present-day value of the scale factor is defined to be $a(t_0) \equiv 1$. The function $f_\mathrm{K}(w)$ is the comoving angular diameter distance and is determined by the geometry of space-time:

$$f_\mathrm{K}(w) = \begin{cases} 1/\sqrt{K}\sin(\sqrt{K}w), & K > 0 \\ w, & K = 0 \\ 1/\sqrt{-K}\sinh(\sqrt{-K}w), & K < 0, \end{cases} \tag{2.4}$$

where K is the curvature. The curvature determines whether the geometry of the three-dimensional space-like hypersurface defined by $t = \text{const}$ is Euclidean ($K = 0$), spherical ($K > 0$) or hyperbolic ($K < 0$).

Einstein's field equations (2.1) simplify considerably if the metric tensor $g_{\alpha\beta}$ is given by the RWM (2.2). In this case $T_{\alpha\beta}$ is given by a energy-momentum tensor of a homogeneous perfect fluid, which is characterised by its pressure $p(t)$ and density $\rho(t)$. Einstein's field equations simplify to the two Friedmann equations (Friedmann 1922, 1924):

$$\left(\frac{\dot{a}}{a}\right)^2 = \frac{8\pi G}{3}\rho - \frac{Kc^2}{a^2} + \frac{\Lambda}{3} \tag{2.5}$$

and

$$\frac{\ddot{a}}{a} = -\frac{4}{3}\pi G\left(\rho + \frac{3p}{c^2}\right) + \frac{\Lambda}{3}. \tag{2.6}$$

Differentiating Eq. (2.5) with respect to the cosmic time and inserting the result into Eq. (2.6) yields the conservation law for the energy density

$$\frac{\mathrm{d}}{\mathrm{d}t}\left(c^2\rho(t)\,a^3(t)\right) = -p(t)\,\frac{\mathrm{d}}{\mathrm{d}t}a^3(t). \tag{2.7}$$

The dynamics of the Universe, the evolution of the scale factor, is completely determined by Eqs. (2.5) and (2.7).

2.1.3 The Hubble function and density parameters

The Hubble function

A useful definition is the Hubble function $H(t)$ which is defined as $H(t) \equiv \dot{a}/a$; it expresses the expansion rate of the Universe. The expansion rate today, the present value of the Hubble function, is given by the Hubble constant $H(t_0) \equiv H_0$. It is usually parameterised as $H_0 = 100\,h\,\mathrm{km\,s^{-1}\,Mpc^{-1}}$, where h accounts for the measurement uncertainties.

Via the Hubble constant we can easily estimate the age of the Universe assuming a constant expansion velocity: $t_0 = 1/H_0 \approx 10\,h^{-1}\,\mathrm{Gyr}$ and the size of the visible Universe: $R_{\mathrm{H}_0} = c/H_0 \approx 3000\,h^{-1}\,\mathrm{Mpc}$ (Hubble radius). These simple estimates already indicate that the Hubble constant is one of the most important constants in cosmology. Measuring it accurately was a motivation for building the Hubble Space Telescope (HST) and initiating the HST Key Project (Freedman et al. 2001). With the HST it was possible to accurately determine distances to a sample of nearby galaxies using the period-luminosity relation of Cepheids. The Hubble constant was then determined by applying the Cepheid calibration to secondary distance indicators further out in the Hubble flow, see Freedman et al. (2001). The HST Key Project yielded a value of $H_0 = (72 \pm 3 \pm 7)\,\mathrm{km\,s^{-1}\,Mpc^{-1}}$ (statistical and systematic errors). Although some other measurements (e.g. Tammann et al. 2003; Kochanek & Schechter 2004) yield significantly lower values of the Hubble constant most measurements using different techniques converge to a value similar to that of the HST Key Project (e.g. Saha et al. 2006; Riess et al. 2005, using gravitational lens time delays and supernovae Type Ia, respectively).

Density parameters

The Universe-filling cosmic fluid is described by the equation-of-state, which relates its density ρ and pressure p via

$$p = w_{\mathrm{eos}} c^2 \rho, \tag{2.8}$$

with w_{eos} being a constant called equation-of-state parameter. Eqs. (2.7) and (2.8) yield

$$\rho(a) = a^{-3(w_{\mathrm{eos}}+1)} \tag{2.9}$$

The total cosmic fluid is a mixture of three components having different equation-of-state parameters. One component consists of non-relativistic, pressureless particles, called *dust*, with density ρ_{m} and an equation-of-state parameter of $w_{\mathrm{eos}} = 0$. Another component consists of relativistic particles with density ρ_{R} and $w_{\mathrm{eos}} = 1/3$; the essential parts are CMB photons and primordial relativistic neutrinos. The cosmological constant can formally be interpreted as a fluid with negative pressure, $w_{\mathrm{eos}} = -1$, hence with a constant energy density ρ_Λ. The energy density ρ_Λ is the third component of the cosmic fluid. The density and pressure of the Universe is then given by:

$$\rho = \rho_{\mathrm{m}} + \rho_{\mathrm{R}} + \rho_\Lambda = \frac{\rho_{\mathrm{m},0}}{a^3} + \frac{\rho_{\mathrm{R},0}}{a^4} + \rho_\Lambda, \tag{2.10}$$

$$p = \frac{1}{3}\rho_{\mathrm{R}} c^2 - \rho_\Lambda c^2 = \frac{1}{3}\frac{\rho_{\mathrm{R},0}}{a^4} c^2 - \rho_\Lambda c^2, \tag{2.11}$$

where the index '0' denotes the present-day value.

The different densities are usually expressed by the present-day density parameters: the total matter density, Ω_{m}, the dark energy density, Ω_Λ, and the relativistic matter density, Ω_{R}, where Ω_{m} and Ω_{R} are defined in terms of the so-called critical density, ρ_{cr}:

$$\Omega_{\mathrm{m}} \equiv \frac{\rho_{\mathrm{m}}}{\rho_{\mathrm{cr}}}, \qquad \Omega_{\mathrm{R}} \equiv \frac{\rho_{\mathrm{CMB}} + \rho_\nu}{\rho_{\mathrm{cr}}}, \tag{2.12}$$

where

$$\rho_{\rm cr} \equiv \frac{3H_0^2}{8\pi G} = 1.879 \times 10^{-29} h^2 \,\mathrm{g\,cm^{-3}}, \tag{2.13}$$

and $\rho_{\rm CMB} = 4.5 \times 10^{-34}\,\mathrm{g\,cm^{-3}}$ is the energy density of the photon background. The energy density of the neutrino background per species is given by $\rho_\nu = 5.2 \times 10^{-35}\mathrm{g\,cm^{-3}}$. Furthermore, the dark energy density is defined as

$$\Omega_\Lambda \equiv \frac{\Lambda}{3H_0^2}. \tag{2.14}$$

With the definitions of the Hubble function and density parameters we can rewrite the first Friedmann equation (2.5) to

$$H^2(t) = H_0^2 \left[a^{-4}(t)\,\Omega_{\rm R} + a^{-3}(t)\,\Omega_{\rm m} - a^{-2}(t)\,\frac{Kc^2}{H_0^2} + \Omega_\Lambda \right]. \tag{2.15}$$

Since $a(t_0) = 1$ and $H(t_0) = H_0$ we can express the curvature parameter by

$$K = \left(\frac{H_0}{c}\right)^2 (\Omega_{\rm R} + \Omega_{\rm m} + \Omega_\Lambda - 1). \tag{2.16}$$

Hence the curvature of the Universe is solely determined by the sum of $\Omega_{\rm R}$, $\Omega_{\rm m}$ and Ω_Λ. Since $\Omega_{\rm m}$ as well as $\Omega_\Lambda \gg \Omega_{\rm R}$, $\Omega_{\rm R}$ is sometimes neglected at late times ($\Omega_{\rm R}$ only plays a role some hundred thousand years after the Big Bang).

2.1.4 Distances and redshift

Redshift

The wavelength of photons propagating in the Universe is increased due to the expanding space-time. Observed spectra from distant objects are therefore redshifted. The redshift z of a distant comoving object is defined by the wavelength $\lambda_{\rm e}$ emitted at time $t_{\rm e}$ and the wavelength λ_0 measured by a comoving observer at time t_0:

$$z \equiv \frac{\lambda_0 - \lambda_{\rm e}}{\lambda_{\rm e}}. \tag{2.17}$$

Since light rays travel on null geodesics, $\mathrm{d}s^2 = 0$, it follows $c^2\,\mathrm{d}t^2 = a^2(t)\,\mathrm{d}w^2$, or $c\,\mathrm{d}t = a(t)\,\mathrm{d}w$. Moreover, the comoving distance between the observer and the light-emitter is constant, $w = \text{const}$, hence it follows

$$w = \int_{t_{\rm e}}^{t_0} \frac{c\,\mathrm{d}t}{a(t)} = \text{const}. \tag{2.18}$$

Since changes in t_0 and $t_{\rm e}$ cannot alter the integral (2.18) it follows: $\mathrm{d}t_{\rm e}/\,\mathrm{d}t_0 = a(t_0)/a(t_{\rm e})$. The same applies to wavelength, hence we obtain the relation between redshift and scale factor

$$1 + z = \frac{a(t_0)}{a(t_{\rm e})}. \tag{2.19}$$

The relation (2.19) means that the photons are redshifted according to how much the Universe has expanded since the photons we see here and now were emitted.

Distances

Distances in Euclidean space measured with different methods do not differ from each other. In an expanding Universe described by the Friedmann equations this statement is no longer true. In the following we introduce three important methods of distance measurements.

Proper distance

The proper distance $D_\mathrm{p}(z_1, z_2)$ is defined by the cosmic time a light ray emitted at a redshift of z_2 needs to travel to an observer at $z_1 < z_2$. It is $\mathrm{d}D_\mathrm{p} = -c\,\mathrm{d}t = -c\,\mathrm{d}a\,\dot{a}^{-1} = -c\,\mathrm{d}a\,(aH)^{-1}$. With Eqs. (2.15) and (2.16) we obtain by integration

$$D_\mathrm{p}(z_1, z_2) = \frac{c}{H_0}\int_{a(z_2)}^{a(z_1)} \mathrm{d}a[a^{-1}\Omega_\mathrm{m} + (1 - \Omega_\mathrm{m} - \Omega_\Lambda) + a^2\Omega_\Lambda]^{-1/2}. \tag{2.20}$$

Note that the value of this distance measure is a function of the cosmological parameters Ω_m and Ω_Λ.

Angular diameter distance

The angular diameter distance $D_\mathrm{ang}(z_1, z_2)$ is defined by the ratio of the physical cross section δA of an object at z_2 and the solid angle $\delta\omega$ that an observer at z_1 would see. It follows from

$$\frac{\delta A}{4\pi a^2(z_2) f_\mathrm{K}^2[w(z_1, z_2)]} = \frac{\delta\omega}{4\pi}, \tag{2.21}$$

and $\delta\omega D_\mathrm{ang}^2 = \delta A$:

$$D_\mathrm{ang}(z_1, z_2) = \sqrt{\frac{\delta A}{\delta\omega}} = a(z_2) f_\mathrm{K}[w(z_1, z_2)]. \tag{2.22}$$

The angular diameter distance is the most important distance measure in gravitational lensing (Chapter 3).

Luminosity distance

The luminosity distance $D_\mathrm{lum}(z_1, z_2)$ is defined by the ratio of luminosity L of an object at z_2 and flux S measured by an observer at z_1. It is related to the angular diameter distance through

$$D_\mathrm{lum}(z_1, z_2) = \left(\frac{a(z_1)}{a(z_2)}\right)^2 D_\mathrm{ang}(z_1, z_2). \tag{2.23}$$

2.1.5 Cosmic Microwave Background

About 3.8×10^5 years after the Big Bang (corresponding to a redshift of $z \approx 1100$) the temperature of the Universe dropped to $\sim 3000\,\mathrm{K}$. Around that temperature protons and free electrons started to form neutral hydrogen and the optical depth dropped such that the Universe became transparent for photons. The time of photon decoupling is known as the *(re)combination* or *last scattering* epoch.

Photons, protons and electrons are in equilibrium before recombination, hence the distribution function of the photons follows a perfect black body or Planck spectrum. After the recombination, scattering is unimportant for nearly all photons, therefore the shape of their distribution function is not altered. Due to the expansion of the Universe the photons are redshifted, and the temperature of this relic radiation has dropped to $T = 2.735\,\mathrm{K}$ today. A Planck spectrum should therefore be observable in the microwave range independent of the observing direction.

In the late 1930s and early 1940s several faint interstellar absorption lines were discovered and identified with rotation states of diatomic molecules (e.g. Adams 1941); the rotation state of CN, for instance, corresponds to an "effective temperature of the interstellar space of $\approx 2.7\,\mathrm{K}$" (McKellar 1940). These observations were the first (indirect) measurements of the cosmic microwave background (CMB), however, they were not noticed by cosmologists and were essentially forgotten.

Penzias & Wilson (1965) accidentally detected for the first time the CMB radiation directly with a radio telescope and won for this discovery the 1978 Nobel Prize in physics. They intended to study our own Galaxy with their telescope and measured an excess antenna temperature of $(3.5 \pm 1.0)\,\mathrm{K}$ which they did not expect. This excess antenna temperature was isotropic, unpolarized, and free from time variations and was interpreted by Dicke et al. (1965) as the predicted CMB radiation.

In 1989 the cosmic background explorer (COBE) satellite was launched and measured a perfect black body spectrum (e.g. Mather et al. 1990). Except for the measured dipole anisotropy due to the peculiar motion of the Earth with respect to the CMB and the emission of foreground objects (like the band of our Galaxy), the measured radiation is isotropic, supporting the hypothesis of an isotropic Universe and the Big Bang theory. However, the isotropy is not perfect. Smoot et al. (1992) measured already tiny but statistically significant temperature fluctuations with COBE which could not be attributed to known systematic errors. The anisotropies were interpreted as the imprints of the seeds that eventually grew under the influence of gravity to the observerd present-day structures. John Mather and George Smoot were awarded the 2006 Nobel Prize in physics *for their discovery of the blackbody form and anisotropy of the cosmic microwave background radiation* using COBE data. John Mather was the project manager of COBE and the principal investigator (PI) of the Far Infrared Absolute Spectrophotometer that compares the spectrum of the cosmic microwave background radiation with that from a precise blackbody. George Smoot was the PI of the Differential Microwave Radiometer that measured the anisotropies.

The tiny temperature anisotropies in the CMB are of the order of $\Delta T/T \approx 10^{-5}$ and

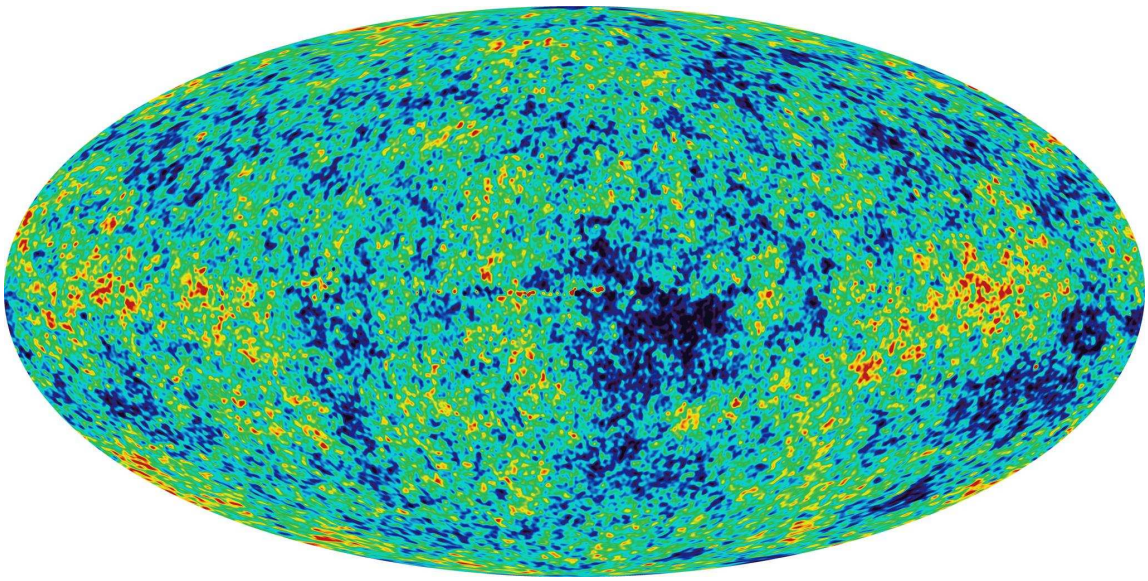

Figure 2.1: Temperature fluctuations of the Cosmic Microwave Background (CMB) of the Universe, as obtained by the WMAP mission. The temperature map is corrected for the dipole anisotropy due to the motion of the earth with respect to the CMB background as well as for foreground contaminations like the radiation of our Galaxy. Red colours indicate regions with warmer temperature than average and blue colour indicate regions cooler than average. The temperature fluctuations are of the order of $\Delta T/T \approx 10^{-5}$. (Figure has been taken from the WMAP mission web page (*http://map.gsfc.nasa.gov*); credit: NASA/WMAP Science Team.)

primarily reflect density, temperature and gravitational potential fluctuations. On large angular scales temperature anisotropies are dominated by fluctuations of the gravitational field of the underlying matter density distribution (Sachs & Wolfe 1967). On scales smaller than the horizon the photon pressure inhibits baryons from falling into the dark matter potential wells and acoustic oscillations are generated. These oscillations are imprinted in the temperature power spectrum and are called 'acoustic peaks', see Fig. 2.8. Their amplitude and position contains a vast amount of cosmological information. In Sect. 2.2.6 we therefore summarise the main results of the cosmological parameter estimates obtained from observations using the Wilkinson Microwave Anisotropy Probe (WMAP), a satellite which measured the temperature anisotropies (Fig. 2.1) with much higher precision than COBE.

2.1.6 What is the Universe made of?

Recent measurements of the CMB combined with supernovae of Type Ia, cosmic shear, and galaxy cluster abundances show that about 75 % of the Universe today is made of the so-called dark energy, and 20 % of cold dark matter. Ordinary baryonic matter, in the form of gas and stars, only makes up 4 %. If these measurements and their interpretation

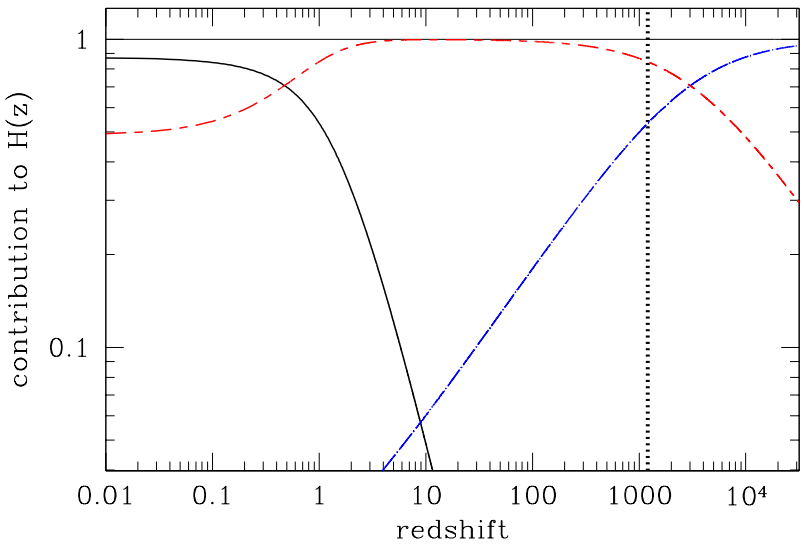

Figure 2.2: Depending on redshift, the expansion of the Universe was either dominated by radiation, dark matter or dark energy. This is expressed by the contribution of the different contents to the Hubble function, $H(z)$, and is calculated by $H_0\,(\Omega_i\,(1+z)^i)^{1/2}/H(z)$, where in this Figure $i = 0$ stands for the dark energy content (black line), $i = 3$ for the total matter content (red line) and $i = 4$ for the radiation content (blue line). The cosmic expansion is radiation-dominated for $z > 3000$, matter-dominated for $z \in [0.45, 3000]$ and dark energy dominated for $z < 0.45$. We used $\Omega_\mathrm{m} = 0.238$, $\Omega_\mathrm{R} = 7.88 \times 10^{-5}$ and $\Omega_\Lambda = 0.762$ (for $h = 0.73$). The dotted vertical line indicate the epoch of last scattering around $z \approx 1100$.

are correct, our Universe is spatially flat ($\Omega_\mathrm{R} + \Omega_\mathrm{m} + \Omega_\Lambda = 1$) and is today dominated by a mysterious dark energy, which causes the cosmic expansion to accelerate.

It is useful to write the Hubble function (2.15) in terms of redshift:

$$H^2(z) = H_0^2 \left[\Omega_\mathrm{R}(1+z)^4 + \Omega_\mathrm{m}(1+z)^3 + (1-\Omega_\mathrm{R}-\Omega_\mathrm{m}-\Omega_\Lambda)(1+z)^2 + \Omega_\Lambda\right]. \qquad (2.24)$$

In the expansion history of the Universe the domination of species changed, as can be inferred from Eq. (2.24). For large redshifts the Hubble function is dominated by the radiation density, Ω_R, for intermediate redshifts by the matter density, Ω_m, and for low redshifts by the dark energy density, Ω_Λ. In Fig. 2.2 the contribution of the different contents of the Universe to the Hubble function are displayed as a function of redshift. For redshifts up to the redshift of matter and radiation equality, $z_\mathrm{eq} = 1/a_\mathrm{eq} - 1 = 23900\,\Omega_\mathrm{m}h^2 \approx 3000$ (for $\Omega_\mathrm{m}h^2 = 0.127$), relativistic particles dominated the expansion of the Universe, then the matter-dominated era started as the expansion slowed down until finally at a redshift of $z \approx 0.45$ dark energy started to dominate, forcing the Universe' expansion to accelerate.

Evidence for dark matter

Zwicky (1933, 1937) discovered in his works that the dispersion of the radial velocities of galaxies in the Coma cluster is much higher than expected if the total mass of the cluster was solely due to the luminous mass of the galaxies. He therefore proposed that most of the total mass of the Coma cluster exists in a non-luminous form, the *dark matter*. Since this first hint of the existence of non-luminous matter several other observations indicate that the total matter content of the Universe is dominated by non-baryonic, non-relativistic cold dark matter (CDM).

The temperature of X-ray gas in nearly relaxed galaxy clusters is a measure of their potential well and hence their mass: the hotter the intra-cluster gas the deeper the potential well of the cluster, so that the gas cannot escape. Many measurements of the X-ray gas temperature in different galaxy clusters confirm the hypothesis of dark matter since the gas is hotter than one would expect if the total cluster mass was only in form of luminous matter.

Another way to directly probe the total mass of a galaxy cluster is gravitational lensing. This method measures similar masses of galaxy clusters as the two former methods and confirms therefore the dark matter hypothesis.

An outstanding example is the merging galaxy cluster 1E0657−558 (Clowe et al. 2004, 2006a; Bradac et al. 2006). Two galaxy clusters collided and the dissipationless stellar components interpenetrated and show now two primary galaxy concentrations (left panel of Fig. 2.3). The intra-cluster gas, however, has been slowed down by ram pressure and is spatially separated from the two mass peaks (right panel of Fig. 2.3). In the absence of dark matter the mass content of the galaxy cluster would mostly be in the form of the intra-cluster gas, hence the weak lensing mass reconstruction would peak on the intra-cluster gas, between the two galaxy clusters. But this is not the case. Clowe et al. (2006a) measure with 8σ significance a spatial offset between the centre of the baryonic mass and the centres of the weak lensing mass peaks. Hence most of the matter in this system is in the form of *dissipationless* dark matter. However, this simple test cannot rule out any modifications of the gravitational force. Modified gravity (MOG) theories, for instance, predict a length dependent scaling of gravity such that the maxima of the surface mass density of the ordinary galaxy matter coincide with the weak lensing peaks (Moffat 2006).

A method to test the dark matter hypothesis on galactic scales is the velocity dispersion of stars in elliptical galaxies and the rotation velocity in spirals. Both are much larger than one would expect if the total mass of the galaxies was solely in form of stars and gas. Hence, dark matter is also needed on galactic scales.

A further, more indirect, evidence for the existence of non-baryonic cold dark matter is inferred from measurements of small-scale CMB anisotropies (Sect. 2.2.6). They cannot be generated solely by baryonic matter since the radiation pressure would dilute baryonic overdensities. Yet dark matter decoupled much earlier from radiation, hence it could clump and form potential wells in which baryons could fall. From the theory of structure formation (Sect. 2.2) large overdensities, like galaxies or galaxy clusters, could therefore never have formed until the present time if dark matter did not exist.

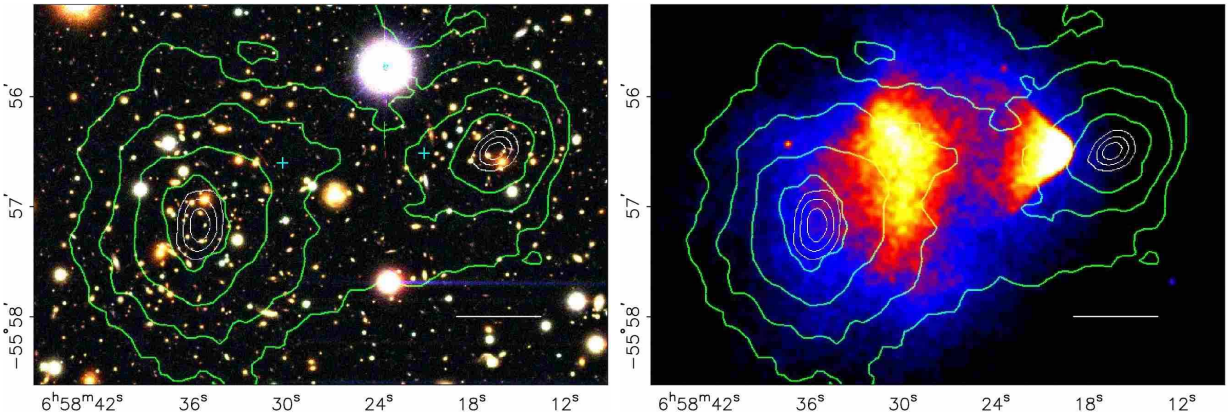

Figure 2.3: The merging galaxy cluster 1E0657−56. *Left panel:* colour composite of the cluster showing the galaxy distribution of cluster and sub-cluster. *Right panel:* Chandra image showing the X-ray emitting plasma and the bow shock. In both panels the green contours indicate the total mass distribution obtained via the weak lensing analysis. The white contours indicate the position error of the weak lensing peaks (1σ, 2σ, 3σ). Figure from Clowe et al. (2006a).

Additionally, measurements of the primordial abundance of helium and deuterium and their comparison with theories of the Big Bang Nucleosynthesis (BBN) indicate that the baryon density, Ω_b, is of the order of 0.04. However, various independent measurements of the total matter density show that it is definitely larger than 0.2. Hence, a large fraction of the total mass content of the Universe is non-baryonic.

Dark matter candidates

Although there are strong indications for dark matter its nature is still unclear. Possible candidates for cold dark matter are non-baryonic weakly interacting massive particles (WIMPs). They would only interact via the weak force and gravity. Theories beyond the standard model of elementary particle physics (e.g. supersymmetry) could explain WIMP-like particles. There are several experiments based on cryogenic light detectors running to search for WIMPS, e.g., the Croyogenic Dark Matter Search (CDMS) or the Cryogenic Rare Event Search with Superconducting Thermometers (CRESST) experiment. However, no WIMP-like particles have been observed yet. Angloher et al. (2005), for instance, give an upper limit of the WIMP-nucleon cross-section, $\sigma_{\nu\mathrm{n}}$: $\sigma_{\nu\mathrm{n}} < 10^{-45}\,\mathrm{m}^2$ for WIMP masses roughly between $30\,\mathrm{GeV}/c^2$ and $1000\,\mathrm{GeV}/c^2$. For comparison: the neutrino-neutron elastic total cross section is $10^{-47}\,\mathrm{m}^2\,(E_\nu/1\,\mathrm{MeV})^2$. The theory of BBN and structure formation give a lower limit of the WIMP masses of at least $1\,\mathrm{MeV}/c^2$, and most probably the WIMP mass is of the order of some hundred GeV/c^2. Large particle colliders will soon reach energies to possibly detect WIMP-like particles in that mass range (e.g. the Large Hadron Collider at CERN).

Other candidates for dark matter, at least on galactic scales, are the so-called massive

compact halo objects (MACHOS), compact massive objects existing in halos of galaxies like white dwarfs, brown dwarfs, neutron stars or black holes (hence baryonic matter; except black holes). However, micro-lensing experiments (MACHO and EROS collaborations) towards the Magellanic Clouds indicate that MACHOS only contribute little to the total matter content of our Galaxy. Afonso et al. (2003), e.g., concluded in their work that objects in the mass range between $M = 2 \times 10^{-7}\, M_{\odot}$ and $1\, M_{\odot}$ cannot contribute more than 25 % of the total halo mass.

Dark energy

The present accelerated expansion of the Universe has been measured for the first time by Riess et al. (1998) and Perlmutter et al. (1999) using measurements of supernovae of Type Ia (SN Ia). SN Ia are explosions of white dwarfs exceeding the maximum mass (Chandrasekhar mass limit). Since they have a common explosion energy, they have a common maximum luminosity and are thus excellent candidates of standard candles. Perlmutter et al. (1999) observed 42 Type Ia supernovae at redshifts between 0.18 and 0.83 and found that they are significantly dimmer than expected for a matter-dominated, decelerating Universe. Furthermore, Riess et al. (2004) studied 16 SN Ia at high redshifts (six of them at $z > 1.25$) and found strong evidence for the transition from cosmic deceleration to cosmic acceleration at $z = 0.46 \pm 0.13$. In addition, many experiments measured the accelerated expansion in a more indirect way (e.g. Seljak et al. 2005; Spergel et al. 2006) and found also very strong indications for a non-vanishing dark energy. However, we still do not know the physical nature of dark energy, and no theoretical model has succeeded to explain it convincingly.

2.2 Structure formation

On small scales the Universe is inhomogeneous. Observationally this has been impressively demonstrated by the 2dF galaxy redshift survey (e.g. Colless et al. 2001) showing the galaxy distribution in a large volume of the Universe, see Fig. 2.4. Clearly visible is that galaxies are not randomly distributed but clustered in galaxy groups and galaxy clusters, the largest collapsed structures in the Universe. They are formed due to the amplification of primordial density fluctuations. Nowadays their mean densities are much larger than the mean density of the Universe. During the last scattering epoch, density perturbations were of the order of 10^{-5}. Hence, in the course of time, density inhomogeneities must have grown dramatically. In this Section we describe the growth of density perturbations in time and their statistical properties.

2.2.1 Linear perturbation theory

Since the Universe is homogeneous and isotropic on large scales the Friedmann equations describe the dynamics of the whole Universe. For scales much smaller than the Hubble radius and weak gravitational fields the growth of structure can be described with Newtonian

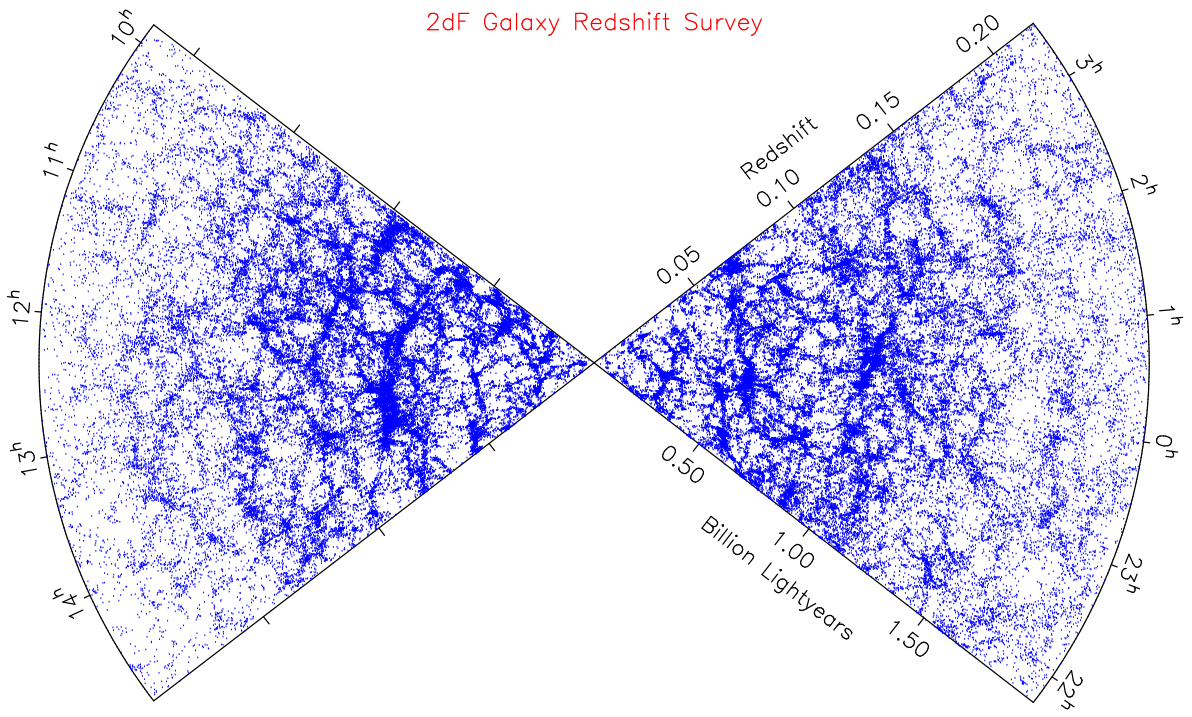

Figure 2.4: Galaxy distribution in redshift space of the complete 2dF redshift survey (2×10^5 galaxies with $\langle z \rangle = 0.11$). The projected map shows the large-scale structure of the Universe, e.g. galaxy clusters, filaments and voids (regions almost without any galaxies). Figure taken from the 2dF galaxy redshift survey web page (*http://www.mso.anu.edu.au/2dFGRS/*).

dynamics. We assume in the following that the matter in the Universe can be described by a perfect fluid with zero pressure (for dissipationless cold dark matter with negligible velocity dispersion this is a reasonable assumption) and density $\rho(\boldsymbol{x}, t)$, where $\boldsymbol{x}$ is the comoving coordinate. The fluid equations in comoving coordinates are (Peebles 1980):

$$\text{Continuity eq.} \qquad \frac{\partial \rho}{\partial t} + 3H\rho + \frac{1}{a}\nabla \cdot (\rho \boldsymbol{v}) = 0 \tag{2.25}$$

$$\text{Euler eq.} \qquad \frac{\partial \boldsymbol{v}}{\partial t} + H\boldsymbol{v} + \frac{1}{a}(\boldsymbol{v} \cdot \nabla)\boldsymbol{v} = -\frac{1}{a}\nabla\Phi \tag{2.26}$$

$$\text{Poisson eq.} \qquad \nabla^2\Phi = 4\pi G\rho a^2 + 3a\frac{\partial^2 a}{\partial t^2}, \tag{2.27}$$

where $\boldsymbol{v}(\boldsymbol{r}/a, t)$ is the peculiar velocity field, defined as proper velocity minus the Hubble flow: $\boldsymbol{v}(\boldsymbol{r}/a, t) = u(\boldsymbol{r}, t) - H\boldsymbol{r}$, and $\boldsymbol{r} = a(t)\boldsymbol{x}$ is the proper coordinate. It is now convenient to define the density contrast

$$\delta(\boldsymbol{x}, t) \equiv \frac{\rho(\boldsymbol{x}, t) - \bar{\rho}(t)}{\bar{\rho}(t)}, \tag{2.28}$$

where $\boldsymbol{x} = \boldsymbol{r}/a$ is the comoving coordinate, and $\bar{\rho}(t)$ is the mean matter density of the Universe at cosmic time t. With $\rho = (\delta + 1)\bar{\rho}$ (see Eq. 2.28) and $\bar{\rho} = \bar{\rho}_0\, a^{-3}$ the continuity equation (2.25) reads

$$\frac{\partial \delta}{\partial t} + \frac{1}{a}\nabla[(1+\delta)\boldsymbol{v}] = 0. \tag{2.29}$$

Using the first Friedmann equation (2.5) and the density contrast (2.28) the Poisson equation (2.27) can be written as

$$\nabla^2\Phi = \frac{3H_0^2\Omega_\mathrm{m}}{2a}\delta. \tag{2.30}$$

In the following we assume $\delta \ll 1$. With this linearisation the Euler equation (2.26) reads

$$\frac{\partial \boldsymbol{v}}{\partial t} + H\boldsymbol{v} = -\frac{1}{a}\nabla\Phi \tag{2.31}$$

and the modified continuity equation (2.29) reads

$$\frac{\partial \delta}{\partial t} + \frac{1}{a}\nabla\boldsymbol{v} = 0. \tag{2.32}$$

Together with the modified Poisson equation (2.30) we can eliminate the peculiar velocity $\boldsymbol{v}$ and gravitational potential Φ. It follows

$$\frac{\partial^2 \delta}{\partial t^2} + 2H\frac{\partial \delta}{\partial t} = \frac{3H_0^2\Omega_\mathrm{m}}{2a^3}\delta. \tag{2.33}$$

Eq. (2.33) makes clear that in linear perturbation theory structures of density perturbations are 'frozen in' in comoving coordinates since Eq. (2.33) does not explicitly contain the spatial coordinate and derivatives with respect to the spatial coordinate. Thus, a general solution to this second-order linear differential equation is given by

$$\delta(\boldsymbol{x}, t) = D_+(t)\delta_+(\boldsymbol{x}) + D_-(t)\delta_-(\boldsymbol{x}). \tag{2.34}$$

The quantities $D_\pm$ are two independent linear solutions of the time dependence in Eq. (2.33), where D_+ increases with time and D_- decreases with time. If both modes were present at some early time, the D_- mode would have died away at some later time. Hence, we neglect D_- in the following. We normalise the *growing mode* or *linear growth factor* D_+ to $D_+(t_0) = 1$ for today. For the density contrast we obtain

$$\delta(\boldsymbol{x}, a) = D_+(a)\delta_0(\boldsymbol{x}), \tag{2.35}$$

where δ_0 would be the present-day density contrast if the growth was exclusively linear until today. The linear growth factor reads

$$D_+(a) \propto \frac{H(a)}{H_0}\int_0^a \mathrm{d}a' \left[1 + \Omega_\mathrm{m}\left(\frac{1}{a'} - 1\right) + \Omega_\Lambda\left(a'^2 - 1\right)\right]^{-3/2}. \tag{2.36}$$

The constant of proportionality is chosen such that the function (2.36) is normalised, $D_+(a=1)=1$. For the special case of an *Einstein-de Sitter* Universe (flat Universe with $\Omega_\mathrm{m}=1$) the constant of proportionality is: $(5/2)\,\Omega_\mathrm{m}$, and the linear growth factor is $D_+ = a = 1/(1+z)$ for $a > a_\mathrm{eq}$. For different (reasonable) cosmologies the linear growth factor only differs slightly from $D_+ = a$.

For density contrasts of the order unity linear theory is not applicable anymore. Then the problem of structure growth cannot be solved analytically, and one has to rely on numerical simulations (see Sect. 2.2.5).

2.2.2 The mass density power spectrum

A characterisation of the statistical properties of the Universe and its evolution in time is given by the autocorrelation function of the density field ξ (henceforth: correlation function) and the related mass density power spectrum P. The correlation function is defined as

$$\xi(\boldsymbol{x}) \equiv \langle \delta(\boldsymbol{x}')\delta(\boldsymbol{x}'+\boldsymbol{x})\rangle, \tag{2.37}$$

where the angular brackets denote the ensemble average. The matter density power spectrum (PS) is the Fourier transform of the correlation function:

$$P_\delta(\boldsymbol{k}) = \int \mathrm{d}^3x\, \xi(\boldsymbol{x}) \exp\left(\mathrm{i}\boldsymbol{k}\boldsymbol{x}\right), \tag{2.38}$$

where $|\boldsymbol{k}|$ is the comoving wave vector, related to length L via $k = 2\pi/L$. The power spectrum describes the amplitude of structure on a given length scale. In an isotropic and homogeneous Universe no direction is preferred, therefore relation (2.38) simplifies to

$$P_\delta(k) = 2\pi \int \mathrm{d}x\, x^2 \frac{\sin kx}{kx} \xi(x). \tag{2.39}$$

The matter density PS is often defined as

$$\langle \hat{\delta}(\boldsymbol{k})\hat{\delta}(\boldsymbol{k}')\rangle = (2\pi)^3 \delta_\mathrm{D}(\boldsymbol{k}-\boldsymbol{k}') P_\delta(k), \tag{2.40}$$

where $\hat{\delta}(\boldsymbol{k})$ is the Fourier transform of the density contrast. Since the Universe is homogeneous, the PS is non-zero only if $\boldsymbol{k} = \boldsymbol{k}'$. Additionally, the Universe is isotropic, hence the PS only depends on the modulus of $\boldsymbol{k}$.

In general the PS does not describe the statistical properties of the random density field unambiguously. Only for Gaussian fluctuations this is the case. As primordial density fluctuations are assumed to be Gaussian (this is confirmed by measurements of the CMB), they are well-defined by the power spectrum. For a full description of the present-day density field, however, also higher-order correlations are needed.

2.2.3 Evolution of the power spectrum

Primordial power spectrum

The amplification of density fluctuations in the linear regime is given by Eq. (2.35). Hence, the time-dependent correlation function reads

$$\xi(x,t) = D_+^2(t)\,\xi(x,t_0) \tag{2.41}$$

and accordingly

$$P(k,t) = D_+^2(t)P(k,t_0) \equiv D_+^2(t)P_0(k), \tag{2.42}$$

where x and k are comoving distance and comoving wavenumber, respectively. The quantity $P_0(k)$ is the linearly evolved power spectrum (PS) that would be the present-day PS if the structure growth was exclusively linear. Within the linear perturbation theory the following statement is therefore correct: if we knew the present-day PS, P_0, we would know the power spectrum, $P(k,t)$, at any time.

But from what did the power spectrum evolve, what was the initial (primordial) PS? For any early time of the Universe prior the time where scales of interest became smaller than the size of the comoving horizon, $R_\mathrm{H} = c/(a\,H(a))$, it is assumed that no scales are preferred. Hence, the primordial power spectrum, P_prim, is given by a simple scale-invariant power law

$$P_\mathrm{prim}(k) = Ak^{n_\mathrm{s}}. \tag{2.43}$$

The slope of the power law (spectral index), n_s, is close to unity (Sect. 2.2.6); for $n_\mathrm{s} = 1$ the PS is called *Harrison-Zel'dovich-spectrum*. The amplitude, A, of the power spectrum is not predicted by any theory and can only be measured, see Sect. 2.2.4.

Transfer function, growth of structure and shape parameter

Relation (2.43) has to be modified since we assumed Newtonian dynamics; we only took the matter-dominated epoch into account, and we assumed a pressureless fluid. The so-called *transfer function*, $T(k)$, is therefore introduced to correct for these effects. Hence the linear and primordial power spectrum are related to each other via

$$P(k) \propto P_\mathrm{prim}(k)\,T^2(k). \tag{2.44}$$

During the radiation and matter-dominated epoch before recombination, baryonic and radiation perturbations smaller than the comoving horizon do not grow and start to oscillate since the radiation pressure counteracts their self-gravitation. Furthermore, the amplitude of fluctuations decreases since photons are diffusing (Silk 1968). This so-called Silk-damping is larger for smaller fluctuations. After recombination, however, the baryons only feel their own gas pressure and fall into the potential wells of the dark matter inhomogeneities. Baryon inhomogeneities now grow on all scales.

During the matter-dominated epoch ($a > a_\mathrm{eq}$) dark matter perturbations grow proportional to a, independent of their length scale. However, for the radiation-dominated

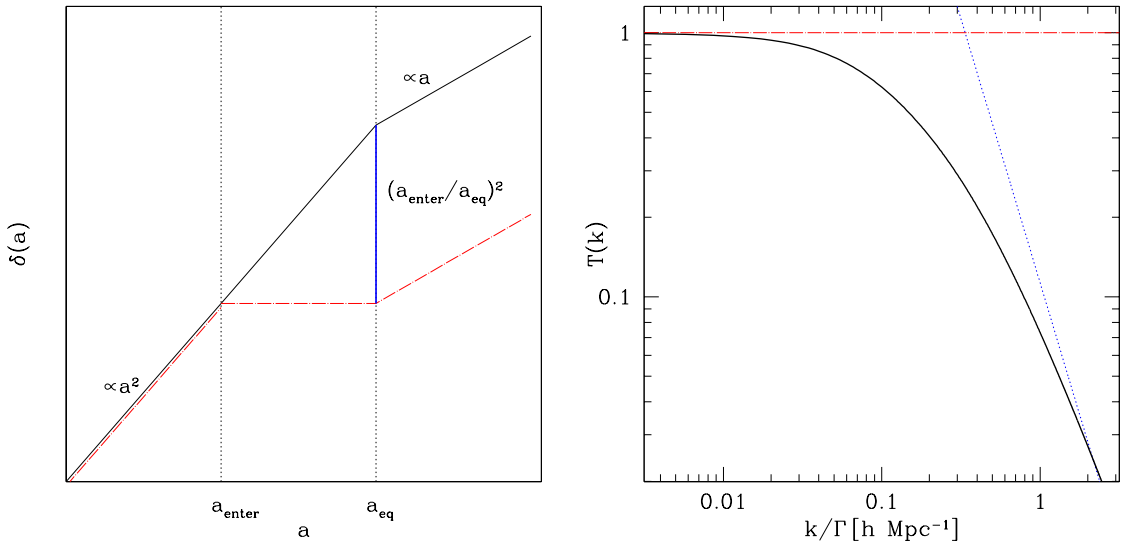

Figure 2.5: *Left panel*: sketch of the suppression of growth. If the density contrast, δ, is larger than the horizon, δ grows with a^2 in the radiation-dominated epoch. If the horizon is getting larger than the size of δ during the radiation-dominated epoch ($a_{\rm enter} < a_{\rm eq}$) the growth of δ is suppressed until the matter-dominated epoch starts. Hence the amplitude of the smaller δ is suppressed by a factor of $(a_{\rm eq}/a_{\rm enter})^2$ in comparison to the larger δ. *Right panel*: fitting formula of the CDM transfer function given in Eq. (2.45) in comparison to $T(k) = 1$ and $T(k) \propto k^{-2}$ (red and blue line, respectively).

epoch the growth of perturbations depends on their length scale. Superhorizon perturbations grow proportional to a^2. Dark matter inhomogeneities smaller than the comoving horizon do not grow via self-gravitation and stagnate due to the fact that the Universe expands too fast (Meszaros 1974). The outcome of this is that small-scale dark matter inhomogeneities which "enter the horizon" during the radiation-dominated epoch do not grow until matter starts to dominate the Universe. In comparison to large inhomogeneities, which "enter the horizon" only during the matter-dominated epoch, the amplitude of the smaller perturbations is *suppressed* by a factor of $(a_{\rm eq}/a_{\rm enter})^2$. A sketch of the suppression of growth is displayed in Fig. 2.5. A characteristic length scale, L_0, is given by the size of the comoving horizon, $R_{\rm H}$, at the redshift, $z_{\rm eq}$, of matter and radiation equality: $L_0 = R_{\rm H} = 12\,(\Omega_{\rm m} h^2)^{-1}\,{\rm Mpc}$. For perturbations that are much larger than L_0 the transfer function reads $T(k) \approx 1$ and the transfer function is $T(k) \approx (kL_0)^{-2}$ for perturbation sizes much smaller than L_0.

The transfer function can be calculated for different CDM cosmologies. In this work we use the fitting formula of the CDM transfer function given in Bardeen et al. (1986)

$$T(q) = \frac{\ln(1+2.34q)}{2.34q}[1+3.89q+(16.1q)^2+(5.46q)^3+(6.71q)^4]^{-1/4}, \qquad (2.45)$$

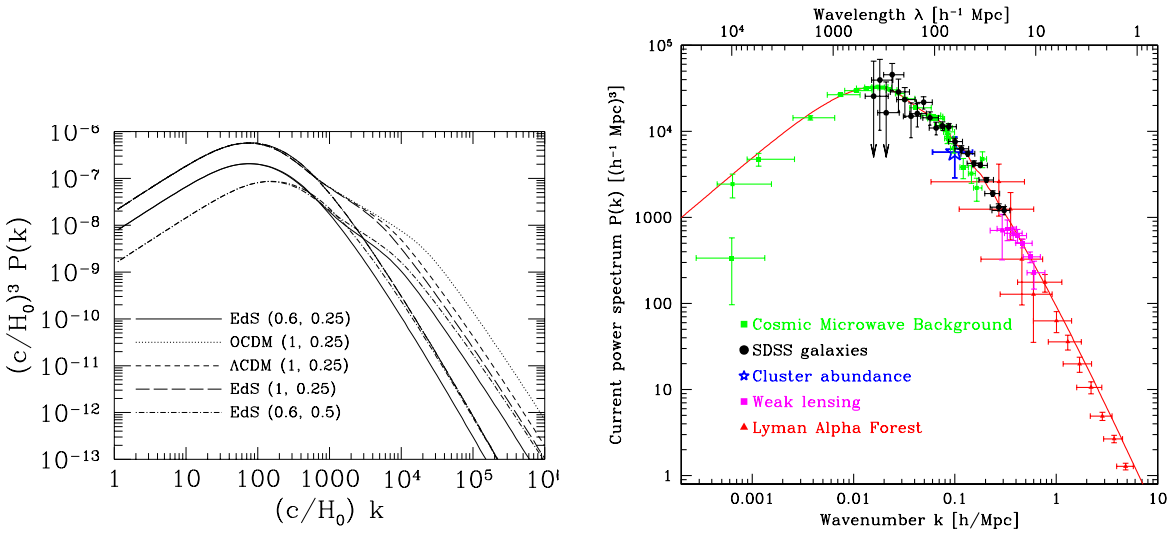

Figure 2.6: *Left panel:* Calculated mass density power spectrum (PS) at current epoch for different cosmological models. Thin lines: linearly extrapolated PS, solid lines: non-linear PS calculated with the Peacock & Dodds (1996) formalism. Values in brackets denote (σ_8, Γ), where EdS: Einstein-de Sitter Universe, OCDM: open Universe with $\Omega_\mathrm{m} = 0.3$, $\Omega_\Lambda = 0$, ΛCDM: Λ dominated Universe with $\Omega_\mathrm{m} = 0.3$, $\Omega_\Lambda = 0.7$. Figure from Meylan et al. (2006). *Right panel:* Measurements of the PS on various scales using different observing methods. On large spatial scales the PS is probed by combined measurements of the CMB (BOOMERANG, MAXIMA, DASI, CBI, VSA, ACBAR and WMAP: Wang et al. 2003; Hinshaw et al. 2003), on intermediate spatial scales by measurements of the CMB, SDSS galaxies (Tegmark et al. 2004) and galaxy clusters (point with error bar reflect spread in the literature). On small spatial scales the PS is probed by cosmic shear (Hoekstra et al. 2002b) and Lyα forest measurements (Gnedin & Hamilton 2002). The location of the points in the diagram depends on the density parameters and for the CMB on the reionisation optical depth, τ (here: $\Omega_\mathrm{m} = 0.28$, $h = 0.72$, $\Omega_\mathrm{b}/\Omega_\mathrm{m} = 0.16$ and $\tau = 0.17$). Figure from Tegmark et al. (2004).

with $q = k/(\Gamma\, h\, \mathrm{Mpc}^{-1})$, where Γ is the *shape parameter*, determining the shape of the transfer function and therefore of the power spectrum. We use in our work

$$\Gamma = \Omega_\mathrm{m}\, h. \tag{2.46}$$

In Fig. 2.5 the transfer function (2.45) is displayed.

2.2.4 Power spectrum normalisation

The shape of the power spectrum (PS) of matter density fluctuations can be predicted for CDM models, its normalisation however can only be determined by observations. A useful definition of the normalisation is given by the dispersion of the linearly extrapolated

present-day density contrast within spheres of radius $R = 8\,h^{-1}\mathrm{Mpc}$:

$$\sigma_8^2 = \langle \delta^2 \rangle_{8\,h^{-1}\mathrm{Mpc}}. \tag{2.47}$$

There are several observational methods to determine the normalisation, σ_8:

- Measurements of temperature fluctuations of the CMB are a powerful way to probe σ_8 as they determine the PS on large to intermediate scales (Spergel et al. 2006).
- The dispersion of the galaxy number count within spheres of $8\,h^{-1}\mathrm{Mpc}$ ($\sigma_{8,\mathrm{g}}^2 \equiv \langle (\Delta n/\bar{n})^2 \rangle_8$) is used to infer the matter PS normalisation (e.g. Tegmark et al. 2004). If galaxies were unbiased tracers of dark matter then we would have $\sigma_8 = \sigma_{8,\mathrm{g}}$. However, since this is not the case it is convenient to define $\sigma_8 = \sigma_{8,\mathrm{g}}/b$, where b is the so-called linear bias factor. The bias factor then has to be determined with other methods (e.g. Simon et al. 2006).
- Since the formation of galaxy cluster-sized matter distributions is dominantly driven by gravitation the cluster mass function is easy to determine theoretically. Hence, the knowledge of the relation between mass and, e.g., X-ray luminosity of galaxy clusters measuring the abundance of X-ray selected galaxy clusters can be used to constrain σ_8 (e.g. Henry 2004; Bahcall et al. 2003; Reiprich & Böhringer 2002).
- Weak lensing of the large-scale structure (cosmic shear) is a powerful way to determine σ_8 as it directly measures the total matter PS in the local Universe and is independent of any assumptions on the ratio between dark and luminous matter. We discuss this method and its results in detail in Sects. 3.2 and 6.3.
- The lumpiness of the Lyα forest in quasar spectra can be used to infer σ_8 since it determines the PS on very small scales (e.g. Viel & Haehnelt 2006; Viel et al. 2006).

In Fig. 2.6 different measurements of the matter power spectrum, $P(k)$, probing different scales are displayed. Within the error bars various independent observations nicely agree with theoretical predictions over a large range of scales.

2.2.5 Beyond linear perturbation theory

The density contrast of galaxies and galaxy clusters is much larger than unity. Hence, linear perturbation theory is not applicable anymore on these scales and cannot explain the formation of galaxies and galaxy clusters. Although there are theories like the spherical collapse model that analytically describe the non-linear evolution of density perturbations due to gravitational collapse, these theories only describe special cases of structure formation. To obtain detailed theoretical predictions of the growth of density perturbations in time and their statistical properties, numerical simulations of structure growth are carried out. Since the Universe is dominated by dark energy (which, however, does not cluster) and cold dark matter, it is sufficient to consider the gravitational force. The largest N-body

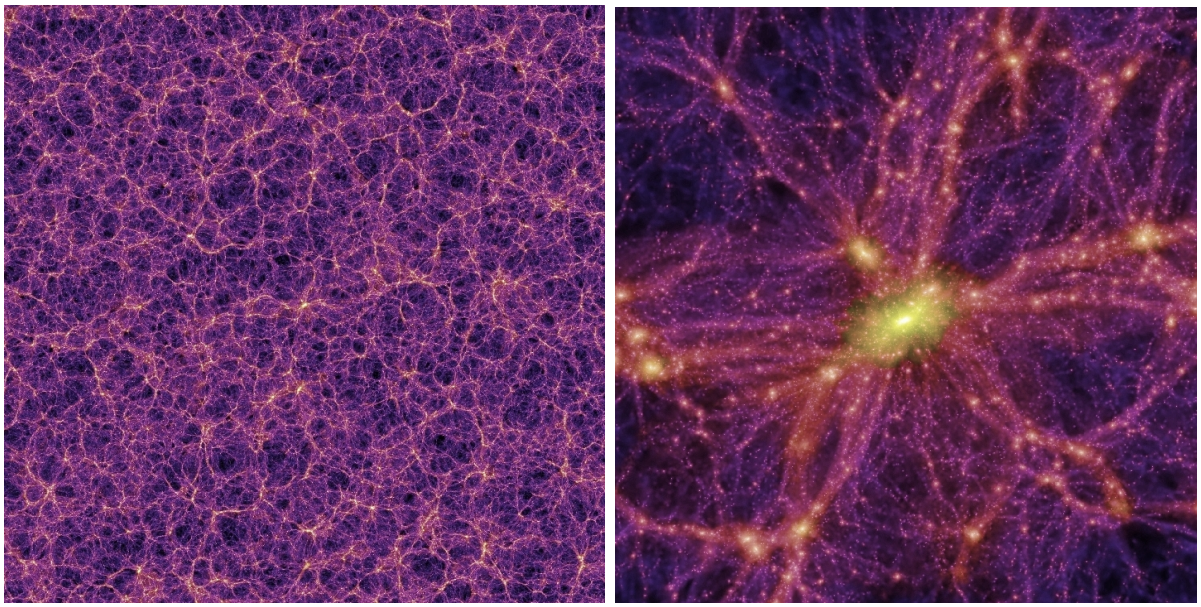

Figure 2.7: *Left panel*: A projection of a 15 Mpc/h thick slice through the density field of the Millennium Run. The size of the box is approximately 1 Gpc and the redshift is $z = 0$. The dark matter is concentrated into a web-like distribution of filaments that intersect at dense nodes where great clusters of galaxies are expected to form and become visible. *Right panel*: A zoom in of the centre of the left panel by a factor of 16. Shown is a huge cluster of galaxies. The size of the box is approximately 60 Mpc. Figure has been taken from the MPG press release, 2005 (*http://www.mpa-garching.mpg.de/galform/press/*); credit: Springel et al. (2005).

simulation today is the Millennium Run (Springel et al. 2005) with $\Omega_{\rm m} = 0.25$, $\Omega_\Lambda = 0.75$, $\sigma_8 = 0.9$ and $h = 0.73$. The volume of this huge simulation is $(500\,h^{-1}\,\mathrm{Mpc})^3$, where about 10^{10} particles with masses of $8.6 \times 10^8\,h^{-1}\,M_\odot$ are traced. With this simulation it is possible to study the statistical properties of the LSS, to obtain the power spectrum in a wide k-range, to study the time evolution of a large number of galaxy clusters and galaxy halos and their substructure. A projection of a 15 Mpc/h thick slice and a zoom-in are displayed in Fig. 2.7.

2.2.6 Cosmological parameters with WMAP

After COBE and several balloon experiments (e.g. BOOMERANG, MAXIMA, DASI) the Wilkinson Microwave Anisotropy Probe (WMAP) was launched in 2001 to measure the temperature (see Fig. 2.1) and polarization anisotropies of the cosmic microwave background radiation in the complete sky. After three years of data accumulation, data processing, temperature and polarisation analyses (Jarosik et al. 2006; Hinshaw et al. 2006; Page et al. 2006), the *WMAP Three Year Results: Implications for Cosmology* paper was published by Spergel et al. (2006). We summarise in the following some results of this

paper since the accuracy of most of the cosmological parameter estimates are without competition for the next few years and the parameter estimates act as reference for ours.

In comparison to the WMAP first year results (Spergel et al. 2003) the WMAP three year data have been significantly improved. A better beam model and foreground subtraction has been applied. Due to the longer integration time the statistical errors of the temperature (TT), temperature-polarisation (TE) and polarisation (EE) power spectrum have been reduced considerably. The signal of the polarisation power spectrum is now measured significantly and is included in the cosmological parameter estimate. The temperature power spectrum is now cosmic variance limited up to $l = 400$ and the signal-to-noise ratio is larger than one up to $l = 850$. In Fig. 2.8 the measured angular power spectra are displayed.

The main cosmological results are as follows. Assuming that the primordial fluctuations are adiabatic and the primordial power spectrum follows a power law with slope n_s, the WMAP data set all by itself requires dark matter. In addition, n_s is significantly lower than the scale-invariant spectrum independently predicted by Harrison, Zel'dovich and Peebles ($n_\mathrm{s} = 1$). With an additional prior of the Hubble constant larger than $40\,\mathrm{km\,s^{-1}\,Mpc^{-1}}$ the WMAP data set requires dark energy. The WMAP data set places significant constraints on the curvature of the Universe since the positions of the acoustic peaks in the temperature power spectrum strongly depend on it. It follows a narrow degeneracy surface in the Ω_m-Ω_Λ-plane. The best fit is a *non-flat* Universe model with $\Omega_\mathrm{m} = 0.42$, $\Omega_\Lambda = 0.63$, $\Omega_\mathrm{K} = -0.04$, $H_0 = 55\,\mathrm{km\,s^{-1}\,Mpc^{-1}}$. However, combining the WMAP data set with other measurements the curvature is consistent with zero.

The following parameter estimates are therefore based on the motivated assumption of a flat Universe. The constraint on the matter power spectrum amplitude is $\sigma_8 = 0.744^{+0.050}_{-0.060}$, the total matter density is $\Omega_\mathrm{m} = 0.238^{+0.030}_{-0.041}$, the baryon density is $\Omega_\mathrm{b}\,h^2 = 0.0223^{+0.0007}_{-0.0009}$ and the dark energy density is $\Omega_\Lambda = 1 - \Omega_\mathrm{m} = 0.762^{+0.030}_{-0.041}$. The constraint on the Hubble constant is $H_0 = 73.4^{+2.8}_{-3.8}\,\mathrm{km\,s^{-1}\,Mpc^{-1}}$. The measurement of the EE power spectrum eliminates a large region of parameter space with a large optical depth, τ, and a large value of n_s. The preferred value for the optical depth is $\tau = 0.088^{+0.028}_{-0.034}$, where the redshift at the reionisation epoch is $z_\mathrm{reion} = 10.9^{+2.7}_{-2.3}$ (the reionisation epoch is the period of the Universe where the neutral gas is reionised by the first stars and active galactic nuclei) corresponding to the cosmic age, $t_\mathrm{reion} = 365\,\mathrm{Myr}$. The preferred value for the slope of the initial power spectrum is $n_\mathrm{s} = 0.951^{+0.015}_{-0.019}$. There exist strong degeneracies between σ_8, τ, and n_s since these parameters essentially move the temperature fluctuation spectrum up and down and only mildly alter its shape, and not at all for σ_8 (Dodelson & Efstathiou 2004). Since the additional measurement of the EE power spectrum for the WMAP three year result yielded significant lower values of τ and n_s in comparison to the first year result, one might think this also alters σ_8. However, this seems not to be the case. The larger σ_8 the larger the power on all scales, and a larger n_s causes a tilt of the power spectrum resulting in more power on small scales. But the larger τ, the *smaller* the power on small scales ($l > 20$) since more free electrons are present and thus more CMB photons are scattered and the primordial anisotropies washed out. Thus, τ and n_s are counteracting and σ_8 is not strongly affected. Nevertheless, the σ_8-value of the WMAP three year result

Table 2.1: Constraints on cosmological parameters (assuming flatness) from WMAP data only, joint constraints from WMAP and other CMB experiments measuring small scale temperature fluctuations and joint constraints from WMAP and a cosmic shear analysis of the CFHT Legacy Survey. Table from Spergel et al. (2006).

Parameter	WMAP Only	WMAP +CBI+VSA	WMAP+ACBAR +BOOMERanG	WMAP +CFHTLS
$100\,\Omega_{\rm b}h^2$	$2.233^{+0.072}_{-0.091}$	$2.212^{+0.066}_{-0.084}$	$2.231^{+0.070}_{-0.088}$	$2.247^{+0.064}_{-0.082}$
$\Omega_{\rm m}h^2$	$0.1268^{+0.0072}_{-0.0095}$	$0.1233^{+0.0070}_{-0.0086}$	$0.1259^{+0.0077}_{-0.0095}$	$0.1410^{+0.0042}_{-0.017}$
h	$0.734^{+0.028}_{-0.038}$	$0.743^{+0.027}_{-0.037}$	$0.739^{+0.028}_{-0.038}$	$0.686^{+0.017}_{-0.024}$
τ	$0.088^{+0.028}_{-0.034}$	$0.088^{+0.027}_{-0.033}$	$0.088^{+0.030}_{-0.033}$	$0.088^{+0.021}_{-0.031}$
$n_{\rm s}$	$0.951^{+0.015}_{-0.019}$	$0.947^{+0.014}_{-0.017}$	$0.951^{+0.015}_{-0.020}$	$0.950^{+0.015}_{-0.019}$
σ_8	$0.744^{+0.050}_{-0.060}$	$0.722^{+0.043}_{-0.053}$	$0.739^{+0.047}_{-0.059}$	$0.826^{+0.023}_{-0.035}$
$\Omega_{\rm m}$	$0.238^{+0.030}_{-0.041}$	$0.226^{+0.026}_{-0.036}$	$0.233^{+0.029}_{-0.041}$	$0.301^{+0.018}_{-0.031}$

is significantly lower compared to the first year result ($\sigma_8^{\rm 1st\,yr} = 0.92 \pm 0.10$). The main reason is that the third peak in the TT power spectrum is now much lower, hence $\Omega_{\rm m}$ is lower and consequently σ_8 since it implies a less structure growth at late times.

In table 2.1 we give an overview of some constraints on cosmological parameters obtained from WMAP only and joint constraints from WMAP and other experiments. Note the large differences between the joint constraints on $\Omega_{\rm m}$ and σ_8 from WMAP and the CFHTLS lensing data (Hoekstra et al. 2005; Semboloni et al. 2006). Since the lensing constraints on $\Omega_{\rm m}$ and σ_8 are significantly wider than those of WMAP the combination favours larger values of $\Omega_{\rm m}$ and σ_8. Additionally, the error bars of the joint constraints of WMAP and CFHTLS are much smaller compared to combinations of WMAP with non-lensing experiments since the cosmic shear constraints are nearly orthogonal to the CMB degeneracies (see introduction).

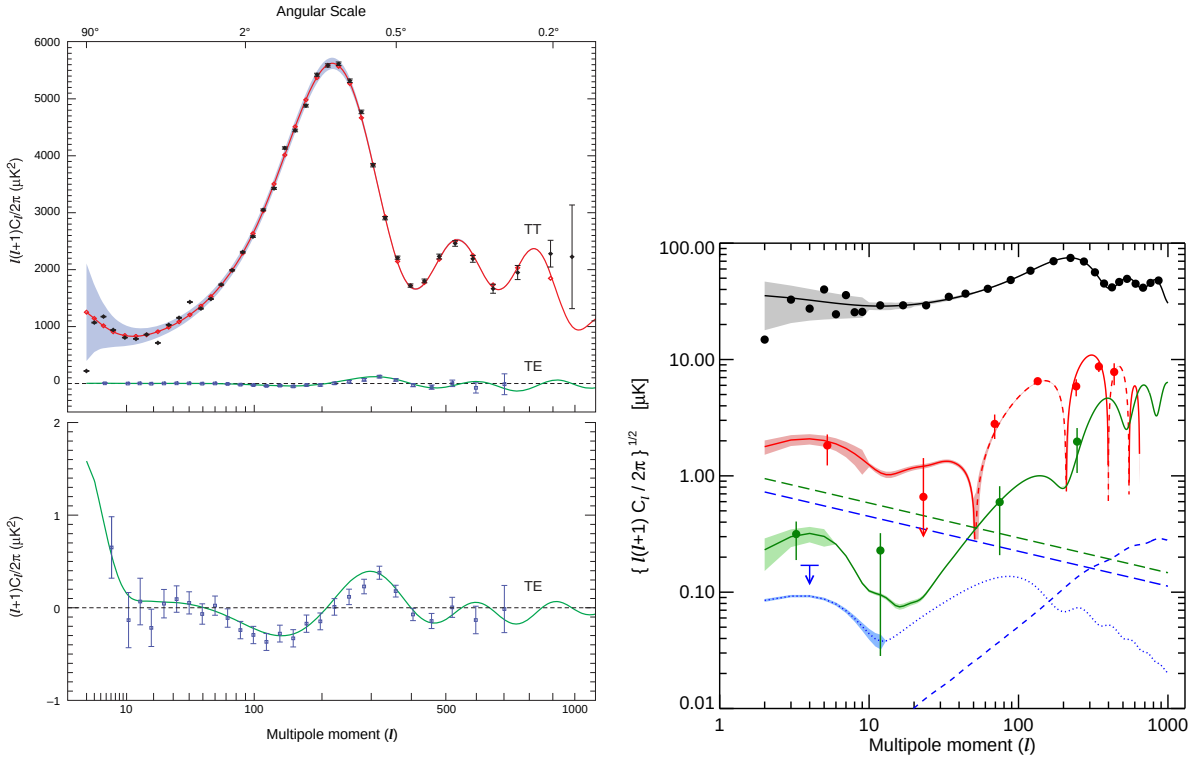

Figure 2.8: *Left panel*: upper panel: Angular TT (black diamonds) and angular TE (blue boxes) power spectrum. The red and green lines are flat ΛCDM Universe fits. The blue shaded area enclosing the line is the binned $1\,\sigma$ cosmic variance error. Lower panel: angular power spectrum TE. Figure from Hinshaw et al. (2006). *Right panel*: Angular power spectra TT (black), TE (red), EE (green); the lines in corresponding colours are flat ΛCDM Universe fits. The dashed line of the TE spectrum are regions of anticorrelation. The shaded areas enclosing the lines are the binned $1\,\sigma$ cosmic variance error. WMAP can only limit the BB signal (blue arrow: $1\,\sigma$ limit for $l \in [2, 10]$, the blue dotted curve is a model). Figure from Page et al. (2006); credit: NASA/WMAP Science Team.

Chapter 3

Weak lensing and cosmic shear

The gravitational lensing effect describes the impact of any kind of matter on light bundles and their trajectories. A light bundle of a distant object (source) is deflected by the gravitational potential of an intervening mass concentration (gravitational lens) such that the apparent source position, shape and flux differs from an undeflected source image.

First, we will discuss the basic principle of gravitational lensing assuming a single deflector like a galaxy or galaxy cluster. We focus on *weak* gravitational lensing i.e. lensing with only small magnifications and shape distortions (shear) of galaxy images. Assuming a random distribution of galaxy orientations in the case of no lensing, a coherent alignment of galaxy ellipticities could indicate a mass concentration. To quantify this alignment we introduce the aperture mass statistics which we use to search for galaxy clusters.

Second, we discuss the weak gravitational lensing effect induced by the tidal gravitational field of the large-scale structure of the Universe, also called *cosmic shear*. In this case, light bundles of distant sources are continuously deflected by the tidal field of multiple gravitational lenses along the line-of-sight. Hence, the simple assumption of a single deflector breaks down. We therefore present a more general treatment of the light propagation and deflection in the inhomogeneous Universe and show how galaxy images are altered in this framework. We derive relations between shear correlations and the projected matter density power spectrum and discuss the required estimators for these correlations to perform a cosmic shear analysis of our data set.

This Chapter is organised as follows. We present some basic concepts and definitions of gravitational lensing in Sects. 3.1.1 and 3.1.2. In Sect. 3.1.3 we give the relation between lensing and measurable quantities concentrating on weak lensing. We introduce the aperture mass statistics in Sect. 3.1.4 and briefly summarise our cluster search findings (see Hetterscheidt et al. 2005; Schirmer et al. 2006). In Sect. 3.2 we discuss in detail the theory of cosmic shear by presenting the light propagation through the inhomogeneous Universe (Sect. 3.2.1) and the relation between the projected three-dimensional mass density power spectrum and shear estimators (Sect. 3.2.2). In Sect. 3.2.3 we present the different shear estimators in practice. We end this Chapter by giving an overview of the influcene of cosmological parameters on the convergence power spectrum (Sect. 3.2.4). A derivation of gravitational lensing from General Relativity can be found in Schneider et al. (1992). A

thorough description of weak lensing and cosmic shear can be found, e.g., in Bartelmann & Schneider (2001); Van Waerbeke & Mellier (2003); Meylan et al. (2006).

3.1 Weak gravitational lensing

3.1.1 Thin lens approximation

We first consider the special case of gravitational lensing by a spherically symmetric lens of mass M. Assuming that the gravitational field strength of the lens is small, the deflection angle $\hat{\boldsymbol{\alpha}}$ induced by the lens is predicted by General Relativity:

$$\hat{\boldsymbol{\alpha}} = \frac{4GM}{c^2} \frac{\boldsymbol{\xi}}{|\boldsymbol{\xi}|^2}, \tag{3.1}$$

where $\boldsymbol{\xi}$ is the so-called impact parameter of the light ray which is assumed to be much larger than the Schwarzschild radius of the lens, $\xi \gg R_\mathrm{s} = 2GM/c^2$, and the light ray is outside the mass distribution of the lens. The deflection angle given in Eq. (3.1) is just twice the deflection angle predicted from Newtonian gravity. Measurements of gravitational light deflection of stars positioned close to the Sun during solar eclipses have therefore been used to confirm General Relativity, see the pioneering workings of e.g. Eddington (1919, 1920).

We are interested here in gravitational lensing by extended objects, where the lens is assumed to be *thin*, i.e. is much smaller than the distances between observer-lens and lens-source. In a first step we rewrite the deflection angle in Eq. (3.1) as a linear superposition of deflections caused by individual, point-like lenses of mass m_i:

$$\hat{\boldsymbol{\alpha}} = \frac{4G}{c^2} \sum_i m_i \frac{\boldsymbol{\xi} - \boldsymbol{\xi}_i}{|\boldsymbol{\xi} - \boldsymbol{\xi}_i|^2}, \tag{3.2}$$

where $\boldsymbol{\xi} - \boldsymbol{\xi}_i$ is the impact paramter relative to the lens i. We now consider a continuous mass distribution, ρ, acting as a thin lens, so we can project the mass distribution onto the lens plane that is orthogonal to the line-of-sight. The obtained two-dimensional mass distribution is called surface mass density and is given by

$$\Sigma(\boldsymbol{\xi}) = \int \rho(\boldsymbol{\xi}, z)\, \mathrm{d}z. \tag{3.3}$$

The deflection angle $\hat{\boldsymbol{\alpha}}$ of the continuous mass distribtion is then given by

$$\hat{\boldsymbol{\alpha}}(\boldsymbol{\xi}) = \frac{4G}{c^2} \int \mathrm{d}^2\xi'\, \Sigma(\boldsymbol{\xi}') \, \frac{(\boldsymbol{\xi} - \boldsymbol{\xi}')}{|\boldsymbol{\xi} - \boldsymbol{\xi}'|^2}. \tag{3.4}$$

3.1.2 The lens equation

The lens equation relates the true position, $\boldsymbol{\eta}$, of a source in the source plane and the observed position, $\boldsymbol{\xi}$, in the lens plane (an illustration of the lens geometry is displayed in Fig. 3.1). We assume that only one mass concentration is located between source and observer and the extension of the mass distribution is small compared to the separation between lens-observer (D_d) and lens-source (D_ds). Then the slightly bent light ray can be approximated by a straight line having a kink in the lens plane. Applying the theorem on intersecting lines on the geometrical configuration of observer, lens- and source plane, the lens equation is obtained:

$$\boldsymbol{\eta} = \frac{D_\mathrm{s}}{D_\mathrm{d}}\boldsymbol{\xi} - D_\mathrm{ds}\,\hat{\boldsymbol{\alpha}}(\boldsymbol{\xi}), \tag{3.5}$$

where $D_\mathrm{s}, D_\mathrm{d}$ and D_ds are angular diameter distances; note that in general $D_\mathrm{ds} \neq D_\mathrm{s} - D_\mathrm{d}$ (Sect. 2.1.4). The relation (3.5) describes a mapping of the lens plane onto the source plane. Introducing the angles $\boldsymbol{\beta} = \boldsymbol{\eta}/D_\mathrm{s}$, $\boldsymbol{\theta} = \boldsymbol{\xi}/D_\mathrm{d}$ and the scaled deflection angle $\alpha(\boldsymbol{\theta}) = D_\mathrm{ds}\,\hat{\boldsymbol{\alpha}}(D_\mathrm{d}\,\boldsymbol{\theta})/D_\mathrm{s}$, the lens equation can be written in angular coordinates:

$$\boldsymbol{\beta} = \boldsymbol{\theta} - \boldsymbol{\alpha}(\boldsymbol{\theta}). \tag{3.6}$$

The scaled deflection angle can be transformed to (see Eq. 3.4)

$$\boldsymbol{\alpha}(\boldsymbol{\theta}) = \frac{1}{\pi}\int \mathrm{d}^2\theta' \kappa(\boldsymbol{\theta}')\frac{\boldsymbol{\theta}-\boldsymbol{\theta}'}{|\boldsymbol{\theta}-\boldsymbol{\theta}'|^2}, \tag{3.7}$$

where we introduce the dimensionless surface mass density or convergence κ:

$$\kappa(\boldsymbol{\theta}) \equiv \frac{\Sigma(\boldsymbol{\theta})}{\Sigma_\mathrm{crit}}. \tag{3.8}$$

The critical surface mass density, Σ_crit, is given by

$$\Sigma_\mathrm{crit} = \frac{c^2}{4\pi G}\frac{D_\mathrm{s}}{D_\mathrm{d}D_\mathrm{ds}}, \tag{3.9}$$

and is a characteristic parameter that separates strong and weak gravitational lensing. In the case of $\kappa \ll 1$ the lensing effect is weak, for $\kappa \approx 1$ the effect is strong. In Fig. 3.2 and Fig 3.3 we give illustrations of strong and weak lensing. We introduce the deflection potential, the two-dimensional gravitational potential of the convergence:

$$\psi(\boldsymbol{\theta}) \equiv \frac{1}{\pi}\int \mathrm{d}^2\theta'\,\kappa(\boldsymbol{\theta}')\ln|\boldsymbol{\theta}-\boldsymbol{\theta}'|. \tag{3.10}$$

The deflection angle, $\boldsymbol{\alpha}$, then follows from the potential (3.10) by calculating the gradient: $\boldsymbol{\alpha}(\boldsymbol{\theta}) = \nabla\psi(\boldsymbol{\theta})$. Since $\nabla^2\ln|\boldsymbol{\theta}| = 2\pi\delta_\mathrm{D}(\boldsymbol{\theta})$, where δ_D is the two-dimensional Dirac delta function, we obtain the Poisson equation in two dimensions

$$\nabla^2\psi = 2\kappa(\boldsymbol{\theta}). \tag{3.11}$$

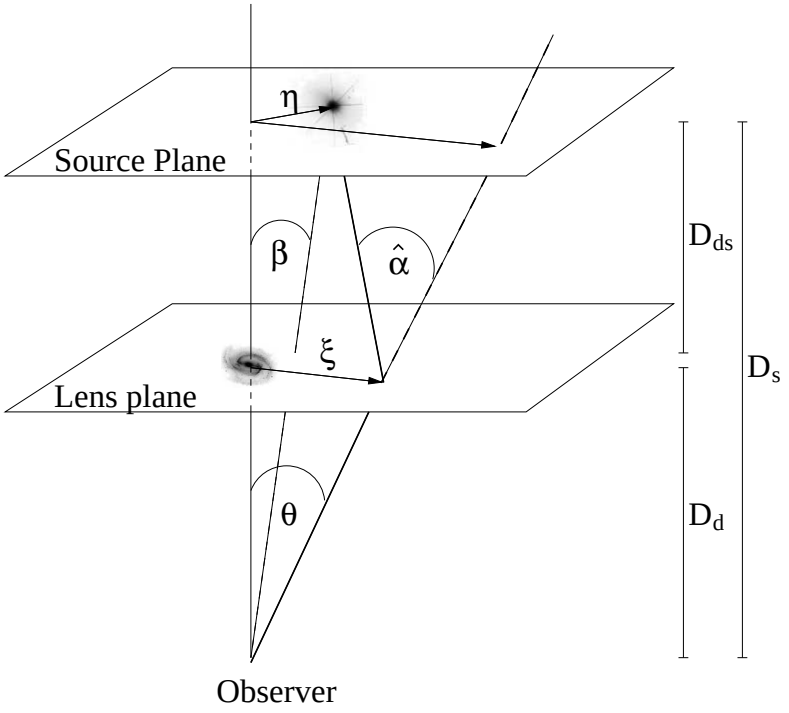

Figure 3.1: Gravitational lens system of observer, lens and source plane. The planes are perpendicular to the optical axis which is defined by the observer and the centre of mass of the lens. The galaxy in the lens plane at an angular diameter distance D_d from the observer symbolises the mass distribution acting as a gravitational lens. Light rays from a background source at the position $\boldsymbol{\eta}$ in the source plane at a distance D_s from the observer undergo a deflection by the mass distribution of an angle $\hat{\boldsymbol{\alpha}}$. With a lens, the observer sees the image of the source at the apparent position $\boldsymbol{\xi}$ in the lens plane with an angle of $\boldsymbol{\theta}$ to the optical axis. The angle $\boldsymbol{\beta}$ is the unlensed angular position of the source in the source plane. The distance between the lens and the source plane is D_ds. Figure by J. Hartlap.

Hence the convergence κ can be obtained by differentiating the deflection potential. The most important quantity in the theory of weak gravitational lensing, the complex shear γ, is obtained in a similar way:

$$\gamma_1(\boldsymbol{\theta}) = \frac{1}{2}(\psi_{,11} - \psi_{,22}), \quad \gamma_2(\boldsymbol{\theta}) = \psi_{,12} = \psi_{,21}, \quad \gamma = \gamma_1 + \mathrm{i}\gamma_2. \tag{3.12}$$

Gravitational lenses not only alter the apparent position of a source but also its shape, since light bundles are deflected differentially. Defining $I_\mathrm{s}(\boldsymbol{\beta})$ as the surface brightness distribution in the source plane, the observed surface brightness distribution $I(\boldsymbol{\theta})$ in the lens plane can be written as

$$I(\boldsymbol{\theta}) = I_\mathrm{s}[\boldsymbol{\beta}(\boldsymbol{\theta})], \tag{3.13}$$

since gravitational lensing conserves the surface brightness. If the source is small compared to the scale on which the lens properties vary, the lens mapping can be linearised locally.

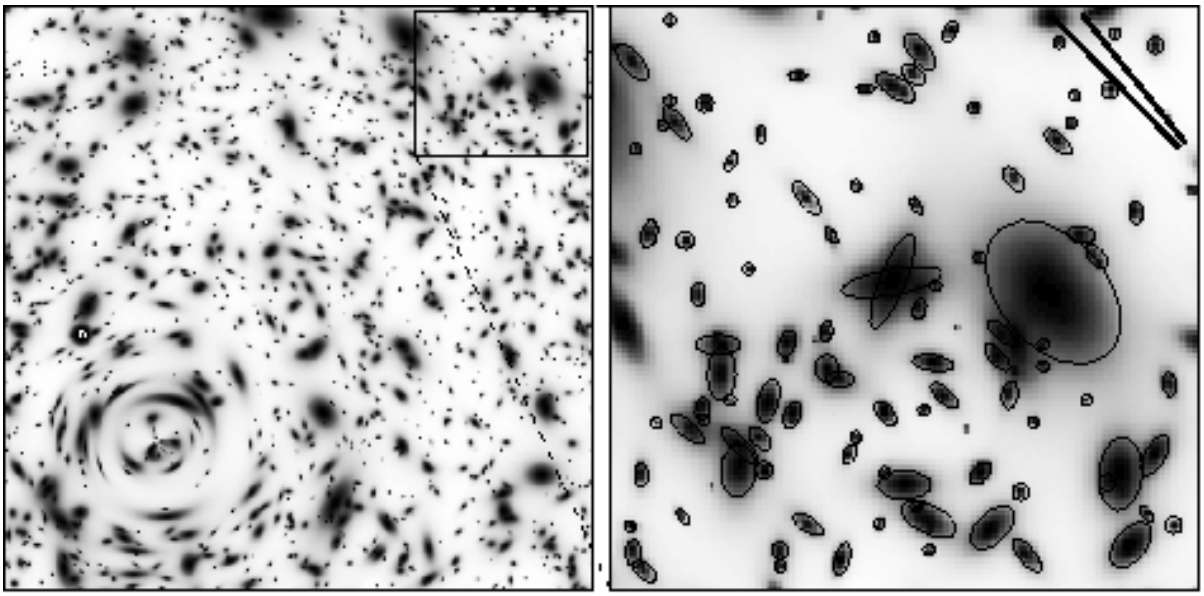

Figure 3.2: Difference between strong and weak gravitational lensing. *Left panel*: randomly placed and oriented background galaxies with an average redshift of $\langle z \rangle = 1.0$. These galaxies are sheared by a singular isothermal sphere (SIS), a spherical mass distribution with a density profile of $\rho(r) \propto \sigma^2/r^2$, where the velocity dispersion of the self-gravitating particles is here $\sigma = 1300\,\mathrm{km\,s^{-1}}$. The SIS is placed at $z = 0.15$. Close to the SIS-centre the galaxies are strongly distorted tangentially (giant arcs). With a larger distance to the SIS-centre the shear signal decreases. *Right panel*: zoom in of a part of the left panel that is far away from the lens centre. The contours around the galaxies indicate their measured ellipticity. The distortion of individual galaxies is not visible and the shear signal is much less than their intrinsic ellipticity. To obtain nonetheless a shear signal one has to average over a large number of galaxies. The lower black line indicates the true orientation of the shear caused by the SIS. The upper black line indicates the orientation determined by averaging over the 92 galaxies in the zoom in. Figure from Mellier (1999).

A Taylor expansion of $\boldsymbol{\beta}(\boldsymbol{\theta})$ at a position $\boldsymbol{\theta} = \boldsymbol{\theta}_0$ yields the locally linearised lens equation,

$$\boldsymbol{\beta} = \boldsymbol{\beta}(\boldsymbol{\theta}_0) + \frac{\partial \boldsymbol{\beta}}{\partial \boldsymbol{\theta}}\Big|_{\boldsymbol{\theta}=\boldsymbol{\theta}_0}(\boldsymbol{\theta} - \boldsymbol{\theta}_0) = \boldsymbol{\beta}_0 + A(\boldsymbol{\theta}_0)(\boldsymbol{\theta} - \boldsymbol{\theta}_0), \tag{3.14}$$

where A is the Jacobian matrix given by

$$A(\boldsymbol{\theta}) = \frac{\partial \boldsymbol{\beta}}{\partial \boldsymbol{\theta}} = \frac{\partial}{\partial \boldsymbol{\theta}}[\boldsymbol{\theta} - \boldsymbol{\alpha}(\boldsymbol{\theta})] = \delta_{ij} - \frac{\partial^2}{\partial\theta_i \partial\theta_j}\psi. \tag{3.15}$$

In such a case the distortion (3.13) can be written as

$$I(\boldsymbol{\theta}) = I_\mathrm{s}[\boldsymbol{\beta}_0 + A(\boldsymbol{\theta}_0)(\boldsymbol{\theta} - \boldsymbol{\theta}_0)], \tag{3.16}$$

Figure 3.3: One of the most spectacular gravitational lens system: the galaxy cluster RX J1347−1145. The image has been obtained with the Advanced Camera for Surveys (ACS) of the Hubble Space Telescope (HST). RX J1347−1145 is the most X-ray luminous galaxy cluster known and is clearly acting as a gravitational lens; many arcs and arclets are visible. Credit: Thomas Erben and Tim Schrabback.

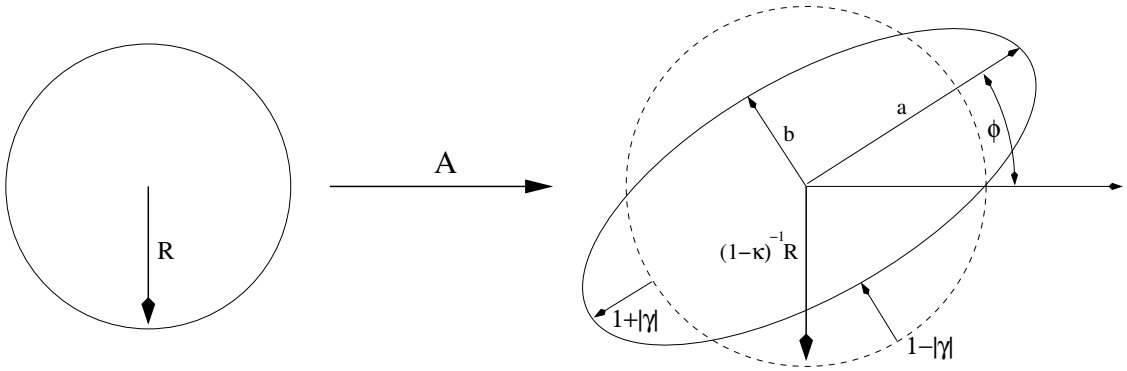

Figure 3.4: Mapping of a circular source onto an ellipse by the Jacobian matrix A. Illustrated is the influence of the convergence, κ, and shear, γ, on the circular source with radius R. The convergence magnifies the source by $1/(1-\kappa)$ and the shear distorts the source to an ellipse with axis ratio b/a, whereas the orientation of the ellipse depends on the phase of the shear.

using Eq. (3.14). The Jacobian matrix can be expressed by means of the convergence and shear:

$$A(\boldsymbol{\theta}) = \begin{pmatrix} 1-\kappa-\gamma_1 & -\gamma_2 \\ -\gamma_2 & 1-\kappa+\gamma_1 \end{pmatrix}. \tag{3.17}$$

The matrix can be decomposed into:

$$A(\boldsymbol{\theta}) = (1-\kappa)\begin{pmatrix} 1 & 0 \\ 0 & 1 \end{pmatrix} - |\gamma|\begin{pmatrix} \cos 2\phi & \sin 2\phi \\ \sin 2\phi & -\cos 2\phi \end{pmatrix}, \tag{3.18}$$

where we used $\gamma = |\gamma|\exp(2\mathrm{i}\phi)$. In Fig. 3.4 we visualise the effect of the local transformation given by the Jacobian matrix. A circular light source is isotropically magnified by the convergence and is anisotropically distorted into an ellipse by the shear, where the minor and major axis of the ellipse is

$$b = \frac{1}{1-\kappa+|\gamma|} \qquad \text{and} \qquad a = \frac{1}{1-\kappa-|\gamma|}, \tag{3.19}$$

respectively. Here, we assumed that $\kappa + |\gamma| < 1$. The angle ϕ describes the orientation of the ellipse with respect to the θ_1-axis.

3.1.3 Shear and observables

Weak gravitational lensing induces small distortions of galaxy images. To quantify this effect we measure the light distribution of a galaxy. In the following we use the surface

brightness distribution, $I(\boldsymbol{\theta})$, to describe the shape of a galaxy image. We first define the centre of an isolated galaxy image as

$$\bar{\boldsymbol{\theta}} \equiv \frac{\int \mathrm{d}^2\theta\, q_I[I(\boldsymbol{\theta})]\boldsymbol{\theta}}{\int \mathrm{d}^2\theta\, q_I[I(\boldsymbol{\theta})]}, \tag{3.20}$$

where $q_I[I(\boldsymbol{\theta})]$ is a filter function. Additionally, we define the tensor of second brightness moments (e.g. Blandford et al. 1991):

$$Q_{ij} \equiv \frac{\int \mathrm{d}^2\theta\, q_I[I(\boldsymbol{\theta})](\theta_i - \bar{\theta}_i)(\theta_j - \bar{\theta}_j)}{\int \mathrm{d}^2\theta\, q_I[I(\boldsymbol{\theta})]}; \quad i,j \in \{1,2\}. \tag{3.21}$$

Note that the area of an image is given by the trace of Q_{ij}. For circular images it follows: $Q_{11} = Q_{22}$ and $Q_{12} = 0 = Q_{21}$. The shape of an image is characterised by the complex ellipticity χ defined by means of the tensor of second brightness moments,

$$\chi \equiv \frac{Q_{11} - Q_{22} + 2\mathrm{i}Q_{12}}{Q_{11} + Q_{22}}. \tag{3.22}$$

For elliptical isophotes with axis ratios of $b/a = r \leq 1$ the ellipticity reads

$$\chi = \frac{1 - r^2}{1 + r^2}\mathrm{e}^{2\mathrm{i}\phi}, \tag{3.23}$$

where ϕ is the angle between the abscissa and semi-major axis.

Relations between source and image ellipticities

In analogy to Eq. (3.21) we define the tensor of second brightness moments for the unlensed source:

$$Q^{\mathrm{s}}_{ij} \equiv \frac{\int \mathrm{d}^2\beta\, q_I[I_{\mathrm{s}}(\boldsymbol{\beta})](\beta_i - \bar{\beta}_i)(\beta_j - \bar{\beta}_j)}{\int \mathrm{d}^2\beta\, q_I[I_{\mathrm{s}}(\boldsymbol{\beta})]}. \tag{3.24}$$

The transformation between source and lens plane is given by $\mathrm{d}^2\beta = \det A\, \mathrm{d}^2\theta$, and the locally linearised lens equation was $\boldsymbol{\beta} - \bar{\boldsymbol{\beta}} = A(\bar{\boldsymbol{\theta}})\,(\boldsymbol{\theta} - \bar{\boldsymbol{\theta}})$ (see Eq. 3.14). With this we obtain a relation between the surface brightness tensor in the lens and source plane since the surface brightness is conserved (Eq. 3.13):

$$Q^s = AQA^T = AQA, \tag{3.25}$$

where A^T is the transpose of the Jacobian matrix, and $A = A^T$.

From that relation the transformation between the ellipticity of the source and the lens plane follows

$$\chi^{\mathrm{s}} = \frac{\chi - 2g + |g|^2\chi^*}{1 + |g|^2 - 2\mathrm{Re}(g\chi^*)}, \tag{3.26}$$

where 'Re' is the real part and '*' stands for complex conjugation. In Eq. (3.26) we introduced the reduced shear

$$g(\boldsymbol{\theta}) = \frac{\gamma(\boldsymbol{\theta})}{1-\kappa(\boldsymbol{\theta})}. \tag{3.27}$$

The transformation of the galaxy ellipticities only depends on the reduced shear, hence the reduced shear or functions of it are the only quantities that can be obtained from ellipticity measurements, see Eq. (3.26). This can also be seen by rewriting Eq. (3.17) to

$$A(\boldsymbol{\theta}) = (1-\kappa)\begin{pmatrix} 1-g_1 & -g_2 \\ -g_2 & 1+g_1 \end{pmatrix}. \tag{3.28}$$

A further useful definition of the complex ellipticity is given by

$$\epsilon \equiv \frac{Q_{11}-Q_{22}+2\mathrm{i}Q_{12}}{Q_{11}+Q_{22}+2(Q_{11}Q_{22}-Q_{12}^2)^{1/2}}. \tag{3.29}$$

Like in Eq. (3.23), we can rewrite the ellipticity:

$$\epsilon = \frac{1-r}{1+r}\mathrm{e}^{2\mathrm{i}\phi}, \tag{3.30}$$

where the phase of ϵ is the same as for χ. The transformation between the ellipticity of the source and the lens plane is then given by

$$\epsilon^{\mathrm{s}} = \begin{cases} \frac{\epsilon-g}{1-g^*\epsilon}; & |g| \leq 1 \\ \frac{1-g\epsilon^*}{\epsilon^*-g^*}; & |g| > 1. \end{cases} \tag{3.31}$$

The relation between ϵ and χ is

$$\epsilon = \frac{\chi}{1+(1-|\chi|^2)^{1/2}} \quad \text{and} \quad \chi = \frac{2\epsilon}{1+|\epsilon|^2}, \tag{3.32}$$

respectively.

A relation between shear and ellipticity

The reduced shear is in principle computable if the intrinsic ellipticities of the source galaxies are known, see Eqs. (3.26) and (3.31). However, we cannot measure the intrinsic ellipticity since images of distant source galaxies are always sheared. To exploit the observed ellipticities of galaxies nonetheless we consider the following. In the case of the weak gravitational lensing effect the convergence is much smaller than unity as is the reduced shear, which is then approximately the same as the shear:

$$\kappa \ll 1, \quad |\gamma| \ll 1, \quad |g| \ll 1 \quad \Rightarrow \quad g \approx \gamma. \tag{3.33}$$

With this, Eqs. (3.26) and (3.31) simplify to:

$$\chi^{\mathrm{s}} \approx \chi - 2g \approx \chi - 2\gamma \tag{3.34}$$

and

$$\epsilon^{\mathrm{s}} \approx \epsilon - g \approx \epsilon - \gamma. \tag{3.35}$$

The most fundamental assumption for all weak lensing studies is that *the intrinsic orientation of galaxies is random.* It follows that the ensemble average of the ellipticity vanishes,

$$\langle \chi^{\mathrm{s}} \rangle = 0 = \langle \epsilon^{\mathrm{s}} \rangle, \tag{3.36}$$

and hence

$$\gamma = \frac{1}{2}\langle \chi \rangle, \qquad \gamma = \langle \epsilon \rangle, \tag{3.37}$$

see Eqs. (3.34) and (3.35). The average ellipticity of an ensemble of galaxies is an unbiased estimator of the local shear field. Hence, the measured galaxy ellipticity is an unbiased, however very noisy, estimator of the local (reduced) shear:

$$\gamma \approx \epsilon, \qquad \gamma \approx \frac{1}{2}\chi. \tag{3.38}$$

The signal-to-noise ratio of a local shear field, when averaging over N galaxies, is given by

$$S/N = \frac{|\langle \epsilon \rangle| \sqrt{N}}{\sigma_\epsilon}, \tag{3.39}$$

where σ_ϵ is the galaxy ellipticity dispersion. Thus, the S/N increases with an increasing number of background sources.

Note that by averaging Eq. (3.31) directly over the intrinsic galaxy orientations without assuming weak shape distortions one obtains the more general equations: $\langle \epsilon \rangle = g$, if $|g| \leq 1$ and $\langle \epsilon \rangle = 1/g^*$, if $|g| > 1$ (Schramm & Kayser 1995; Seitz & Schneider 1997). In general the expectation value of the ellipticity definition of χ, however, explicitly depends on the intrinsic ellipticity distribution of the sources and is not simply related to g (Schneider & Seitz 1995). Hence, in the general case it is convenient to use the ellipticity definition (3.29) rather than (3.22). However, in the weak lensing regime both definitions can be used interchangeably.

3.1.4 The aperture mass statistics

Weak gravitational lensing provides an opportunity to measure the (projected) mass distribution without making any assumptions about its baryonic content. Aside from the analysis of already known mass concentrations like galaxy clusters, weak lensing techniques can be used to perform a blind search for hitherto unknown mass concentrations. Assuming a random distribution of galaxy orientations in the case of no lensing, a coherent alignment of galaxy ellipticities could indicate a mass concentration. A quantitative way

to measure this alignment is the so-called aperture mass ($M_{\rm ap}$) statistics (Schneider 1996). In this Section we introduce the $M_{\rm ap}$-statistics and briefly summarise our cluster search findings using this weak lensing method (Hetterscheidt et al. 2005; Schirmer et al. 2006). Additionally, the aperture mass will play an important role for cosmic shear analyses, see Sect. 3.2.

The aperture mass

The aperture mass, $M_{\rm ap}$ is defined as the spatially filtered projected mass distribution, κ, inside a circular aperture of angular radius θ_0 at a position $\boldsymbol{\zeta}$,

$$M_{\rm ap}(\boldsymbol{\zeta}) \equiv \int \mathrm{d}^2\theta\, \kappa(\boldsymbol{\theta})\, U(|\boldsymbol{\theta}-\boldsymbol{\zeta}|), \tag{3.40}$$

where U is a radially symmetric continuous weight function. Using a compensated filter function of radius θ_0,

$$\int_0^{\theta_0} \mathrm{d}\theta\, \theta\, U(\theta) = 0, \tag{3.41}$$

one can express $M_{\rm ap}$ in terms of the tangential shear $\gamma_{\rm t}$

$$M_{\rm ap}(\boldsymbol{\zeta}) = \int \mathrm{d}^2\theta\, \gamma_{\rm t}(\boldsymbol{\theta};\boldsymbol{\zeta})\, Q(|\boldsymbol{\theta}-\boldsymbol{\zeta}|), \tag{3.42}$$

where the observable quantity

$$\gamma_{\rm t}(\boldsymbol{\theta};\boldsymbol{\zeta}) = -\mathrm{Re}\left[\gamma(\boldsymbol{\theta})\mathrm{e}^{-2\mathrm{i}\phi}\right] \tag{3.43}$$

is the tangential component of the shear at the relative position $\boldsymbol{\theta}-\boldsymbol{\zeta} = |\boldsymbol{\theta}-\boldsymbol{\zeta}|(\cos\phi, \sin\phi)$, with ϕ being the polar angle of $\boldsymbol{\theta}-\boldsymbol{\zeta}$. The filter functions Q and U are related through

$$Q(\vartheta) = \left[\frac{2}{\vartheta^2}\int_0^{\vartheta} \mathrm{d}\vartheta'\, \vartheta'\, U(\vartheta')\right] - U(\vartheta). \tag{3.44}$$

In Schneider et al. (1998) a family of polynomial filter functions which fulfil the conditions (3.41) and (3.44) were primarily introduced for cosmic shear analyses (Sect. 3.2). Throughout the work we use the simplest one,

$$U(\theta;\theta_0) = \frac{9}{\pi\,\theta_0^2}\left[1-\left(\frac{\theta}{\theta_0}\right)^2\right]\left[\frac{1}{3}-\left(\frac{\theta}{\theta_0}\right)^2\right], \tag{3.45}$$

which corresponds to

$$Q(\theta;\theta_0) = \frac{6}{\pi\,\theta_0^2}\left(\frac{\theta}{\theta_0}\right)^2\left[1-\left(\frac{\theta}{\theta_0}\right)^2\right], \tag{3.46}$$

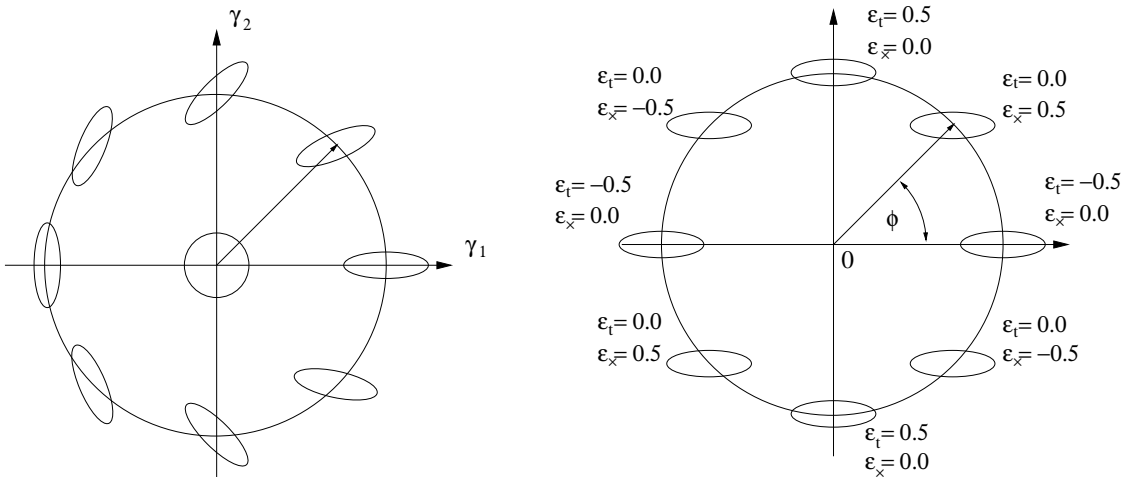

Figure 3.5: *Left panel:* The orientation of the shear of a galaxy illustrated by an ellipse in the local coordinate system attached to the galaxy. *Right panel:* The tangential and cross component of the galaxy ellipticity, ϵ, with $\epsilon_1 = 0.5$ and $\epsilon_2 = 0.0$ and various directions ϕ with respect to a reference point 0. Note that the ellipticity is invariant by a rotation of π and not 2π.

where θ is the projected angular separation from the aperture centre and θ_0 is the filter radius. In the right panel of Fig. 3.6 the aperture filter function Q is displayed. We define in analogy to Eq. (3.42) the cross aperture mass:

$$M_\perp(\boldsymbol{\zeta}) = \int \mathrm{d}^2\theta\, \gamma_\times(\boldsymbol{\theta};\boldsymbol{\zeta})\, Q(|\boldsymbol{\theta}-\boldsymbol{\zeta}|), \tag{3.47}$$

where

$$\gamma_\times(\boldsymbol{\theta};\boldsymbol{\zeta}) = -\mathrm{Im}\left[\gamma(\boldsymbol{\theta})\mathrm{e}^{-2\mathrm{i}\phi}\right] \tag{3.48}$$

is the cross component of the shear. In Fig. 3.5 the tangential and cross components of the shear relative to the direction defined by ϕ are illustrated. For circular-symmetric mass concentrations the shear at any point will be oriented tangentially towards its centre. In this case the cross aperture should be exactly zero.

Applying the M_{ap}-statistics to images

The aperture mass can be used to search for cluster-sized mass concentrations. It is straightforward to construct an unbiased estimator M'_{ap} for the integral (3.42) by a discrete sum over observed galaxy ellipticities ϵ_{t}. Considering the coordinate origin to be at the centre of the aperture, the estimator reads

$$M'_{\mathrm{ap}} = \frac{1}{n}\sum_{i=1}^{N} \epsilon_{\mathrm{t}}(\boldsymbol{\theta}_i) Q(\theta_i;\theta_0), \tag{3.49}$$

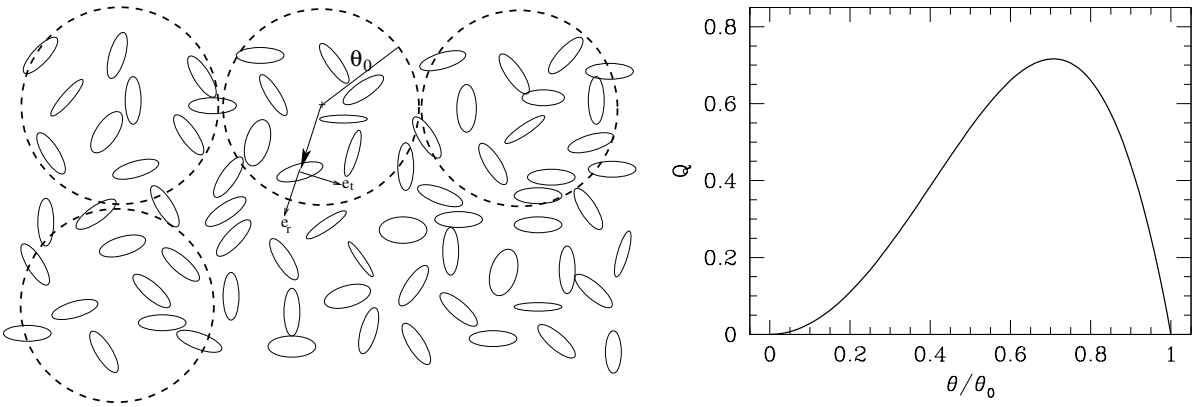

Figure 3.6: *Left panel:* an aperture mass map can be obtained from measured galaxy ellipticities by placing a regular grid on the data field (in the same way the shear and aperture mass dispersion can be obtained, see Sect. 3.2.2). The galaxy ellipticities are then smoothed within an aperture of radius θ_0, where each grid point is an aperture centre. The smoothing function is the filter function, Q, given in Eq. (3.46) (its profile is displayed in the *right panel*). The $(e_\mathrm{r}, e_\mathrm{t})$ coordinate system attached to one galaxy in the left panel is the local frame of that galaxy. The galaxy ellipticity components can be projected onto the axis to estimate the tangential and radial shear.

where N is the number of galaxies and $n = N/2\pi\theta_0^2$ is the number density of galaxies within the circular aperture of radius θ_0. The tangential ellipticity $\epsilon_\mathrm{t} = -\mathrm{Re}[\epsilon(\boldsymbol{\theta})\exp(-2\mathrm{i}\phi)]$ is an unbiased estimator of the tangential shear (Eq. 3.38). The signal-to-noise ratio (S/N) for the aperture mass is given analytically by

$$(S/N)(\boldsymbol{\xi}) = \frac{\sqrt{2}}{\sigma_\epsilon} \frac{\sum_i \epsilon_\mathrm{t}(\boldsymbol{\theta}_i;\boldsymbol{\xi})\, Q(\theta_i;\theta_0)}{\sqrt{\sum_i Q^2(\theta_i;\theta_0)}}, \tag{3.50}$$

where σ_ϵ is the intrinsic ellipticity dispersion.

Placing a grid over the data field and calculating the signal-to-noise ratio for each grid point $\boldsymbol{\xi}$ results into a two-dimensional S/N-aperture mass map, where mass concentrations should reveal themselves as high S/N peaks. S/N-maps are created for various filter radii, θ_0, since the S/N is maximal if the filter radius matches the extend of a mass concentration.

The filter function (3.46) is not optimised for cluster search. Schneider (1996) showed that for a given mass, redshift of the lens and redshift distribution of the background sources the largest S/N is reached if the filter function Q follows the tangential shear profile of the lens. Schirmer (2004) realised this idea and introduced an improved filter function which was intensively tested in Hetterscheidt et al. (2005). Additionally, we analysed in that work 50 randomly selected deep, blank VLT fields applying the M_ap-statistics with the improved filter function. The I-band images cover a total area of $0.64\,\mathrm{deg}^2$ and were taken under superb seeing conditions (average seeing of $\approx 0\farcs6$) resulting in a mean galaxy number density of $n = 26\,\mathrm{arcmin}^{-2}$. This was one of the first systematic galaxy cluster

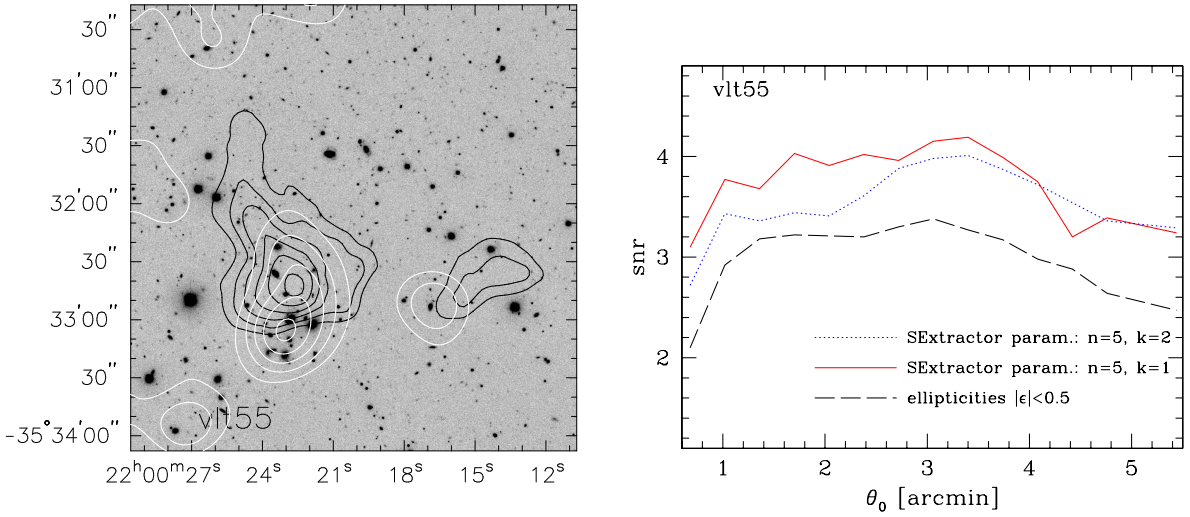

Figure 3.7: *Left panel:* Magnified image of one VLT-field in which we detected a significant lensing signal ($S/N \approx 4.3$). The $M_{\rm ap}$ contours are black (S/N: 1.5, 2.0, 2.5, 3.0, 3.5, 4.0) and the light distribution contours are white (S/N: 1.0, 2.0, 3.0, 4.0, 5.0). The concentration of luminous galaxies is clearly visible. *Right panel:* Maximum S/N (here: snr) of the cluster candidate shown in the left panel and its dependence on filter radius θ_0 for different `SExtractor` parameter settings ($n = 5$ contiguous pixels, $k = 1\sigma$ and $k = 2\sigma$ above the smoothed sky background, respectively). The S/N should be stable for different filter radii and different `SExtractor` parameter settings to substantiate the presumption of the candidate to be a real cluster. To exclude that the S/N of the $M_{\rm ap}$-signal is dominated by only a small fraction of galaxies with high ellipticities we also show a $M_{\rm ap}$-analysis for which we exclude ellipticities with $|\epsilon| > 0.5$ (dashed line). Figures from Hetterscheidt et al. (2005).

searches using weak lensing. We found five significant $M_{\rm ap}$-peaks which coincide with an overdensity of the light distribution. These detections are excellent candidates for possible galaxy clusters and need a spectroscopic follow-up observation to clarify their nature. In the left panel of Fig. 3.7 we display the most promising candidate. In the right panel of the same Figure we present the results of two criteria applied to the most promising candidate to substantiate or weaken the presumption of it to be a real galaxy cluster.

In Schirmer et al. (2006) we applied the $M_{\rm ap}$ method to the 30 times larger GaBoDS data set (the GaBoDS is described in Sect. 4.1) and found 158 high signal-to-noise $M_{\rm ap}$-peaks, half of them beeing 'dark clumps' with no luminous counterparts.

3.2 Cosmic shear

Up to now we only considered the weak gravitational lensing effect of single, localised mass concentrations. This approximation holds for cases where the mass concentrations are massive objects like galaxy clusters since they dominate the integrated mass along the line-

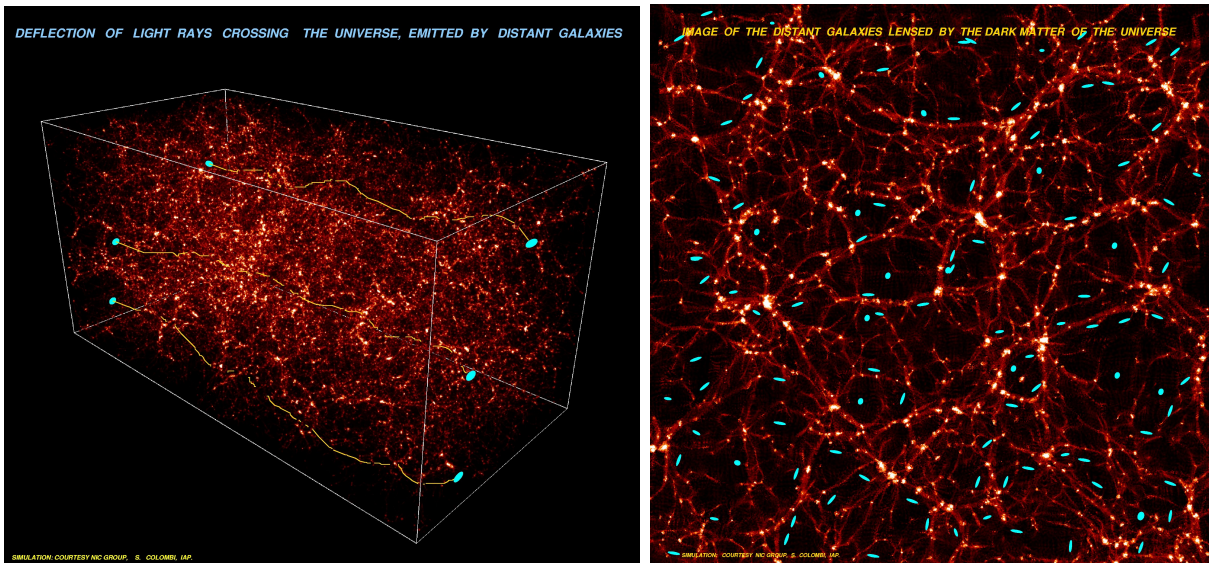

Figure 3.8: *Left panel*: numerical N-body simulation of the dark matter distribution in the Universe by S. Colombi. The box represents a distance of about 300 Mpc, brighter regions have a higher dark matter density than darker regions. The three blue ellipses at the left end of the box represent three distant galaxies. Light rays from those galaxies propagate through the Universe and are weakly deflected and distorted by the gravitational field of the intervening dark matter inhomogeneities. The three blue ellipses at the right side of the box indicate the slightly distorted images of the three distant galaxies. *Right panel*: a projection of the N-body simulation. The blue elongated disks are images of distant galaxies that are distorted due to the gravitational lensing of the dark matter distribution of the N-body simulation (distortions are highly exaggerated). The lensed images of background galaxies are aligned with the filaments of dark matter. (Figures taken from the CFHT press release, 2000, *http://www.cfht.hawaii.edu/News/Lensing/#IC*.)

of-sight to lensed background sources. In general, however, light bundles of distant galaxies are continuously deflected by the tidal gravitational field of the LSS of the Universe inducing weak shape and size distortions of galaxy images (Fig. 3.8). This weak gravitational lensing effect by the LSS is called *cosmic shear*. Analysing second-order statistics of the shear field, like two-point correlations of the image distortions, yields valuable information on the statistical properties of the (projected) LSS, and thus on cosmological parameters. In this Section we derive a relation between the convergence and the density contrast as well as a relation between the 3D mass density power spectrum P_δ, and the convergence power spectrum P_κ which in turn is related to observable shear estimators.

3.2.1 Light propagation through the inhomogeneous Universe

In this Section we present an outline of the derivation of the convergence given that light bundles are now assumed to be continuously deflected by the three-dimensional mass distribution between a background galaxy population and an observer. We assume in the

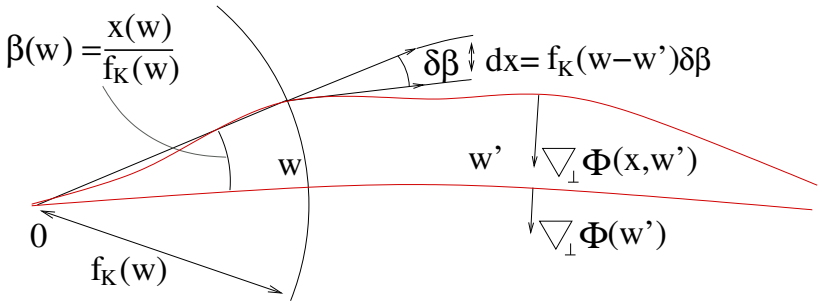

Figure 3.9: A sketch of two light rays. The upper one is propagating through the inhomogeneous Universe, the lower one is assumed to be only influenced by the homogeneous and isotropic background cosmology. For details see text. Figure by T. Schrabback.

following that the gravitational potential of the intervening LSS is weak, $|\Phi| \ll c^2$, and that the largest structures along the line-of-sight are much smaller than the curvature scale of the Universe. To derive an equation of motion for a light ray propagating through the inhomogeneous Universe we consider the situation displayed in Fig. 3.9. Two light rays are observed at the observer's position $\mathbf{0}$ and are separated by an angle of $\boldsymbol{\theta}$, with $|\boldsymbol{\theta}| \ll 1$. One light ray is exclusively influenced by the homogeneous and isotropic background cosmology, the other one is additionally perturbed by the LSS. The comoving separation vector $\boldsymbol{x}(\boldsymbol{\theta}, w)$ between the two light rays at the comoving radial distance w is given by $\boldsymbol{x}(\boldsymbol{\theta}, w) = f_\mathrm{K}(w)\,\boldsymbol{\beta}(\boldsymbol{\theta}, w)$. Here $\boldsymbol{\beta}(\boldsymbol{\theta}, w)$ is the angular separation between the two light rays an observer would measure without a lensing effect. The propagation equation describing the evolution of the comoving separation vector $\boldsymbol{x}(\boldsymbol{\theta}, w)$ is then given by

$$\frac{\mathrm{d}^2\boldsymbol{x}}{\mathrm{d}w^2} + K\,\boldsymbol{x} = -\frac{2}{c^2}\nabla_\perp \Phi\left(\boldsymbol{x}(\boldsymbol{\theta}, w), w\right), \tag{3.51}$$

where K is the spatial curvature of the Universe, $\nabla_\perp = (\partial/\partial x_1, \partial/\partial x_2)$ is the transverse comoving gradient operator, i.e., the two-dimensional gradient in the plane perpendicular to the corresponding light ray. A thorough derivation of Eq. (3.51) is given in Bartelmann & Schneider (2001). The homogeneous part of this equation is given by

$$\frac{\mathrm{d}^2\boldsymbol{x}}{\mathrm{d}w^2} + K\,\boldsymbol{x} = 0 \tag{3.52}$$

and describes the propagation of a light ray in the homogeneous and isotropic Friedmann Universe (Sect. 2.1.2). The solution of Eq. (3.52) with initial conditions $\boldsymbol{x}(w = 0) = 0$ and $\mathrm{d}\boldsymbol{x}/\,\mathrm{d}w(w = 0) = \boldsymbol{\theta}$ reads $\boldsymbol{x}(\boldsymbol{\theta}, w) = f_\mathrm{K}(w)\,\boldsymbol{\theta}$, where the latter equation is the definition of the comoving angular diameter distance.

The solution in the inhomogeneous case (Eq. 3.51) is formally given by

$$\boldsymbol{x}(\boldsymbol{\theta}, w) = f_\mathrm{K}(w)\,\boldsymbol{\theta} - \frac{2}{c^2}\int_0^w \mathrm{d}w'\, f_\mathrm{K}(w - w')\left[\nabla_\perp \Phi(\boldsymbol{x}(\boldsymbol{\theta}, \boldsymbol{w'}), w') - \nabla_\perp \Phi^{(0)}(w)\right]. \tag{3.53}$$

In a homogenous and isotropic Universe we obtain trivially $\boldsymbol{\beta} = \boldsymbol{\theta}$ since the perturbing potential Φ in Eq. (3.53) is zero and we have $\boldsymbol{x}(\boldsymbol{\theta}, w) = f_{\rm K}(w)\,\boldsymbol{\theta}$. In analogy with standard lens theory we can now calculate the Jacobian matrix (e.g., Bartelmann & Schneider 2001)

$$A_{ij}(\boldsymbol{\theta}, w) = \frac{\partial \beta_i}{\partial \theta_j} = \frac{1}{f_{\rm K}(w)} \frac{\partial}{\partial \theta_j} x_i(\boldsymbol{\theta}, w) \tag{3.54}$$

$$= \delta_{ij} - \frac{2}{c^2} \int_0^w {\rm d}w' \, \frac{f_{\rm K}(w-w') f_{\rm K}(w')}{f_{\rm K}(w)} \frac{\partial^2}{\partial x_i \partial x_k} \Phi(\boldsymbol{x}(\boldsymbol{\theta}, w'))\, A_{kj} \tag{3.55}$$

$$\approx \delta_{ij} - \frac{2}{c^2} \int_0^w {\rm d}w' \, \frac{f_{\rm K}(w-w') f_{\rm K}(w')}{f_{\rm K}(w)} \frac{\partial^2}{\partial x_i \partial x_j} \Phi(\boldsymbol{x} = f_{\rm K}(w')\boldsymbol{\theta}, w'), \tag{3.56}$$

where we used the chain rule in Eq. (3.55). On the right hand side of Eq. (3.56) we used the Born approximation since the expected deflection angles are small: we replaced the light ray path, $\boldsymbol{x}$, by the unperturbed light ray path, $f_{\rm K}(w')\boldsymbol{\theta}$, and replaced the Jacobian matrix A_{kj} by the Jacobian matrix in the absence of lensing, δ_{kj}. Note that $\nabla_\perp \Phi^{(0)}(w)$ does not depend on $\boldsymbol{\theta}$. We define the deflection potential

$$\psi(\boldsymbol{\theta}, w) \equiv \frac{2}{c^2} \int_0^w {\rm d}w' \, \frac{f_K(w-w')}{f_K(w) f_K(w')}\, \Phi\left(f_K(w')\boldsymbol{\theta}, w'\right), \tag{3.57}$$

where

$$A_{ij} = \delta_{ij} - \frac{\partial^2 \psi}{\partial \theta_i \partial \theta_j} \tag{3.58}$$

holds like in the case of the thin lens approximation. In analogy to Eqs. (3.11) and (3.12) the effective convergence is defined for cosmic shear,

$$\kappa = \frac{1}{2} \left(\frac{\partial^2}{\partial \theta_1^2} + \frac{\partial^2}{\partial \theta_2^2} \right) \psi \tag{3.59}$$

and likewise the shear

$$\gamma = \frac{1}{2} \left(\frac{\partial^2}{\partial \theta_1^2} - \frac{\partial^2}{\partial \theta_2^2} \right) \psi + {\rm i} \frac{\partial}{\partial \theta_2} \psi. \tag{3.60}$$

The convergence is then given by

$$\kappa(\boldsymbol{\theta}, w) = \frac{1}{2}(\psi_{,11} + \psi_{,22}) = \frac{1}{c^2} \int_0^w {\rm d}w' \, \frac{f_{\rm K}(w-w') f_{\rm K}(w')}{f_{\rm K}(w)} \left(\frac{\partial^2}{\partial x_1^2} + \frac{\partial^2}{\partial x_2^2} \right) \Phi(f_{\rm K}(w')\boldsymbol{\theta}, w'). \tag{3.61}$$

Using the three-dimensional Poisson equation in comoving coordinates (see Eq. 2.30)

$$\Delta \Phi = \frac{3 H_0^2 \Omega_{\rm m}}{2} \frac{\delta}{a} \tag{3.62}$$

we can express the convergence, κ, in terms of the three-dimensional (3D) matter density contrast, δ

$$\kappa(\boldsymbol{\theta}, w) = \frac{3 H_0^2 \Omega_{\rm m}}{2c^2} \int_0^w {\rm d}w' \, \frac{f_{\rm K}(w-w') f_{\rm K}(w')}{f_{\rm K}(w)} \, \frac{\delta(f_{\rm K}(w')\boldsymbol{\theta}, w')}{a(w')}, \tag{3.63}$$

where the line-of-sight integration of $\partial^2/\partial x_3^2$ is on average zero.

Up to now, we only considered a fixed source redshift corresponding to the comoving source distance w. If the sources are distributed between the observer and the comoving horizon, with a source distribution $p(w)$, given in practice by the (normalised) redshift distribution, $p_z(z)$, then the surface mass density needs to be averaged over $p_w(w)\,\mathrm{d}w = p_z(z)\,\mathrm{d}z$:

$$\kappa(\boldsymbol{\theta}) = \int_0^{w_\mathrm{h}} \mathrm{d}w\, p_w(w)\kappa(\boldsymbol{\theta}, w) = \frac{3H_0^2\Omega_\mathrm{m}}{2c^2} \int_0^{w_\mathrm{h}} \mathrm{d}w\, g(w) f_\mathrm{K}(w) \frac{\delta(f_\mathrm{K}(w)\boldsymbol{\theta}, w)}{a(w)}, \tag{3.64}$$

where we have introduced the effective source redshift weighting function

$$g(w) \equiv \int_w^{w_h} \mathrm{d}w'\, p_w(w') \frac{f_\mathrm{K}(w'-w)}{f_\mathrm{K}(w')}, \tag{3.65}$$

with w_h being the comoving distance to the horizon. The redshift distribution is often parameterised by

$$p_z(z) = \frac{\beta}{\Gamma[(1+\alpha)/\beta] z_0} \left(\frac{z}{z_0}\right)^\alpha \exp\left[-\left(\frac{z}{z_0}\right)^\beta\right]. \tag{3.66}$$

The shape of the distribution is determined by α and β, z_0 is a characteristic redshift and Γ is the Gamma-function.

3.2.2 Relation between the convergence power spectrum and shear estimators

The convergence power spectrum

The convergence given in Eq. (3.64) is a projection of the 3D matter density contrast, δ. We now relate the power spectrum of the convergence, P_κ, to the 3D matter density power spectrum, P_δ, using Limber's equation (Limber 1953). Assuming that δ is a homogeneous and isotropic random field, then two different projections are given by

$$g_i(\boldsymbol{\theta}) = \int_0^{w_\mathrm{h}} \mathrm{d}w\, q_i(w) \delta(f_\mathrm{K}(w)\boldsymbol{\theta}, w) \tag{3.67}$$

and are also (two-dimensional) homogeneous and isotropic random fields. The q_i are weight functions, with $i = 1, 2$. Limber's equation now states that the cross power spectrum of the two projections is given by

$$P_{12}(l) = \int \mathrm{d}w\, \frac{q_1(w) q_2(w)}{f_\mathrm{K}^2(w)} P_\delta\left(\frac{l}{f_\mathrm{K}(w)}; w\right); \tag{3.68}$$

see Kaiser (1992, 1998).

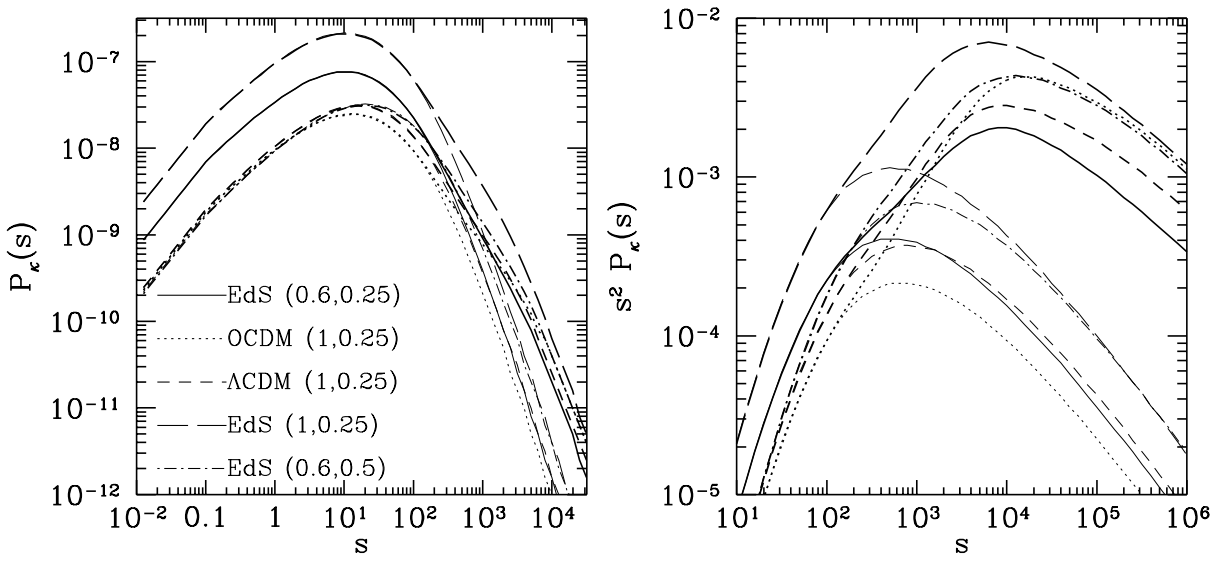

Figure 3.10: Power spectrum of the convergence $P_\kappa(l = s)$ (*left panel*) and its dimensionless form $l^2\,P_\kappa(l = s)$ (*right panel*) for various cosmologies (abbreviations given in Fig. 2.6). Thin lines: linear structure growth, solid lines: non-linear structure growth (based on the model of Peacock & Dodds 1996). The mean of the redshift distribution (Eq. 3.66) is assumed to be $\langle z\rangle = 1.5$. For angular scales below $\approx 30\,\mathrm{arcmin}$, corresponding to wave numbers larger than $l \approx 200$, the non-linear structure growth strongly increases the power. Figures from Schneider et al. (1998).

We now choose $q_1(w) = q_2(w) = (3/2)(H_0/c)^2\,\Omega_\mathrm{m}\,g(w)\,f_\mathrm{K}(w)/a(w)$ and obtain the convergence power spectrum (e.g. Kaiser 1998; Schneider et al. 1998):

$$P_\kappa(l) = \frac{9H_0^4\Omega_\mathrm{m}^2}{4c^4}\int_0^{w_\mathrm{H}} \mathrm{d}w\,\frac{g^2(w)}{a^2(w)}P_\delta\left(k = \frac{l}{f_K(w)}; w\right), \tag{3.69}$$

where a is the cosmic scale factor and g is the weighting function accounting for the source redshift distribution of galaxies, see Eq. (3.65). In Fig. 3.10 we display the convergence power spectrum $P_\kappa(l)$ and its dimensionless form $l^2\,P_\kappa(l)$ for various cosmologies. Observations yielding P_κ can therefore be used to determine constraints on P_δ. Furthermore, the amplitude and shape of P_κ depend on the cosmological model. Hence, knowing P_κ or quantities related to it can be used to determine constraints on cosmological parameters.

Second-order cosmic shear measures

The convergence power spectrum can be written as:

$$\langle\hat\kappa(\boldsymbol{l})\hat\kappa(\boldsymbol{l}')\rangle = 4\pi^2\delta_\mathrm{D}(\boldsymbol{l}-\boldsymbol{l}')P_\kappa(l), \tag{3.70}$$

in analogy to Eq. (2.40), where $\hat\kappa(\boldsymbol{l})$ is the Fourier transform of $\kappa(\boldsymbol{\theta})$:

$$\hat\kappa(\boldsymbol{l}) = \int \mathrm{d}^2\theta\,\kappa(\boldsymbol{\theta})\exp\left(-\mathrm{i}\boldsymbol{\theta}\cdot\boldsymbol{l}\right), \tag{3.71}$$

and l is the modulus of the two-dimensional wave vector. Blandford et al. (1991) showed that the two-point correlation functions of the convergence and shear are identical:

$$\langle\kappa(\boldsymbol{\theta})\kappa(\boldsymbol{\theta}')\rangle = \langle\gamma(\boldsymbol{\theta})\gamma(\boldsymbol{\theta}')\rangle. \tag{3.72}$$

Hence, the convergence power spectrum can directly be estimated from the shear two-point correlation function.

All statistical quantities of the cosmic shear field which are quadratic in shear, the so-called second-order cosmic shear statistics, yield information about the convergence power spectrum, P_κ, and are fully described by P_κ. We use in this work the following second-order statistics to estimate cosmological parameters: the shear two-point correlation functions ξ_+, ξ_- and the aperture mass dispersion $\langle M_{\rm ap}^2\rangle$ (Sect. 3.1.4). For completeness we also give the equation for the shear dispersion, $\langle\gamma^2\rangle$. All quantities are linearly related to the convergence power spectrum P_κ by

$$\xi_+(\theta_0) = \frac{1}{2\pi}\int_0^\infty {\rm d}l\, l P_\kappa(l) W_{\xi_+}(l\theta_0), \tag{3.73}$$

$$\xi_-(\theta_0) = \frac{1}{2\pi}\int_0^\infty {\rm d}l\, l P_\kappa(l) W_{\xi_-}(l\theta_0), \tag{3.74}$$

$$\langle M_{\rm ap}^2\rangle(\theta_0) = \frac{1}{2\pi}\int_0^\infty {\rm d}l\, l P_\kappa(l) W_{\rm ap}(l\theta_0), \tag{3.75}$$

$$\langle\gamma^2\rangle(\theta_0) = \frac{1}{2\pi}\int_0^\infty {\rm d}l\, l P_\kappa(l) W_{\rm TH}(l\theta_0), \tag{3.76}$$

with

$$W_{\xi_+}(\eta) = J_0(\eta), \quad W_{\xi_-}(\eta) = J_4(\eta), \quad W_{\rm TH}(\eta) = 4\frac{J_1^2(\eta)}{\eta^2}, \quad W_{\rm ap}(\eta) = 576\frac{J_4^2(\eta)}{\eta^4}, \tag{3.77}$$

where J_n denotes the $n^{\rm th}$-order Bessel function of the first kind (e.g., Kaiser 1992; Schneider et al. 1998). Note that in general $W_{\rm ap}$ depends on the choice of the filter function U in Eq. (3.40). We chose U given in Eq. (3.45).

The shear two-point correlation functions ξ_+ and ξ_-

The shear two-point correlation functions are directly related to the observable quantities $\gamma_{\rm t} = -{\rm Re}[\gamma\exp(-2{\rm i}\phi)]$ and $\gamma_\times = -{\rm Im}[\gamma\exp(-2{\rm i}\phi)]$ (see Eqs. 3.43, 3.48) of a galaxy pair, where ϕ is the polar angle of their separation vector $\boldsymbol{\theta}$:

$$\xi_\pm(\theta) = \langle\gamma_{\rm t}\gamma_{\rm t}\rangle(\theta) \pm \langle\gamma_\times\gamma_\times\rangle(\theta). \tag{3.78}$$

Another quantity is defined by

$$\xi_\times(\theta) = \langle\gamma_{\rm t}\gamma_\times\rangle(\theta). \tag{3.79}$$

Due to parity invariance the correlation function, $\xi_\times$ is expected to vanish since under parity transformation $\gamma_{\rm t} \to \gamma_{\rm t}$ and $\gamma_\times \to -\gamma_\times$.

The aperture mass dispersion $\langle M_{\rm ap}^2 \rangle$

The aperture mass dispersion can directly be obtained from the observed images, for example, by placing a regular grid on the data field (Sect. 3.1.4). For each grid point the aperture mass, $M_{\rm ap}$, can be measured within an aperture of radius θ_0, and then the dispersion $\langle M_{\rm ap}^2 \rangle$ can be calculated for various filter radii, see Fig. 3.6. This yields information about the convergence power spectrum. Since the filter function $W_{\rm ap}$ in Eq. (3.75) is very localised (see left panel of Fig. 3.11) the shape of the aperture mass dispersion as a function of the filter radius is similar to that of the convergence power spectrum (Bartelmann & Schneider 1999). Hence, $\langle M_{\rm ap}^2 \rangle$ yields localised information of P_κ at a scale of $l \approx 5/\theta_0$. This can be seen in the right panel of Fig. 3.11, where we display $\langle M_{\rm ap}^2 \rangle^{1/2}$ for various comological models. However, the high resolution of the convergence power spectrum, corresponding to a narrow range of wave numbers l, has the disadvantage that the S/N of $\langle M_{\rm ap}^2 \rangle$ is smaller than, e.g., the shear dispersion. We use in this work $\langle M_{\rm ap}^2 \rangle$ nontheless since it has the nice property to reveal possible systematics in the data, see below. Furthermore, neighbouring data points in a $\langle M_{\rm ap}^2 \rangle$-$\theta$ plot are much less correlated than in the case of other cosmic shear statistical measures.

The shear dispersion $\langle \gamma^2 \rangle$

The shear dispersion can be obtained in a similar way as aperture mass dispersion: by placing a regular grid on the data field, where for every grid point the average shear is calculated within a circular aperture of radius θ_0. The shear dispersion is then calculated for various filter radii.

The top-hat filter in Eq. (3.76) is very broad, hence the shear dispersion for a given angular scale θ_0 depends on the convergence power spectrum over a wide range of l. This results into more power in comparison with $\langle M_{\rm ap}^2 \rangle$, in particular on small scales, as can be seen in the right panel of Fig. 3.11.

Interrelations between $\langle M_{\rm ap}^2 \rangle$, $\langle \gamma^2 \rangle$ and $\xi_\pm$

As outlined in the last paragraphs the aperture mass and shear dispersion can directly be obtained from the observed images by placing apertures. However, with this method it is impossible to obtain unbiased estimates for $\langle M_{\rm ap}^2 \rangle$ and $\langle \gamma^2 \rangle$ because of gaps, holes and borders in the data fields. We therefore calculate the dispersions, $\langle \gamma^2 \rangle$ and $\langle M_{\rm ap}^2 \rangle$, directly in terms of the shear two-point correlation functions $\xi_\pm$.

To do so we first invert the relations (3.73) and (3.74) using the orthonomality realtion of the Bessel functions:

$$P_\kappa(l) = 2\pi \int_0^\infty {\rm d}\theta\, \theta \xi_+(\theta) J_0(l\theta) = 2\pi \int_0^\infty {\rm d}\theta\, \theta \xi_-(\theta) J_4(l\theta). \tag{3.80}$$

The shear dispersion is then obtained by inserting Eq. (3.80) into Eq. (3.76):

$$\langle \gamma^2 \rangle(\theta_0) = \int \frac{{\rm d}\theta\, \theta}{\theta_0^2} \xi_+(\theta) S_+\left(\frac{\theta}{\theta_0}\right) = \int \frac{{\rm d}\theta\, \theta}{\theta_0^2} \xi_-(\theta) S_-\left(\frac{\theta}{\theta_0}\right), \tag{3.81}$$

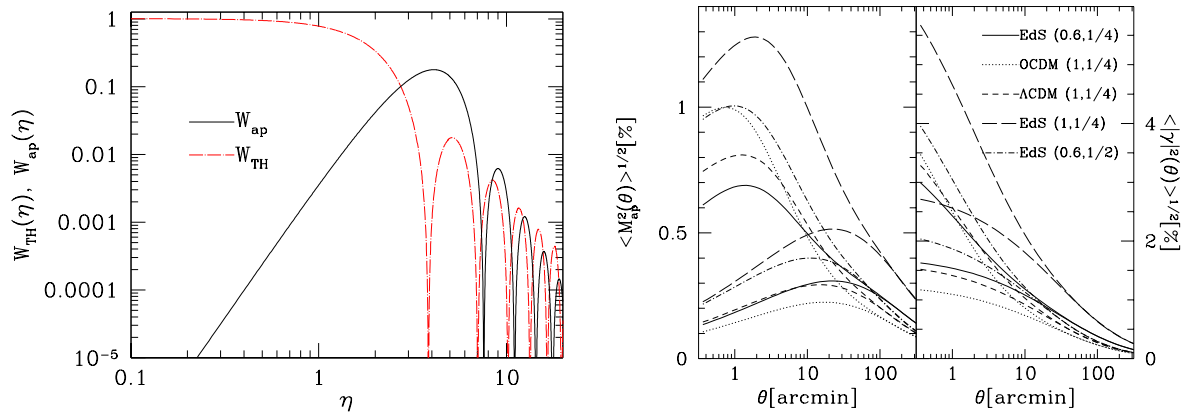

Figure 3.11: *Left panel:* filter function for the aperture mass dispersion, $W_{\rm ap}$, and for the shear dispersion, $W_{\rm TH}$. *Right panel:* Square root of the aperture mass dispersion $\langle M_{\rm ap}^2\rangle$ (P_κ is filtered with $W_{\rm ap}$, see Eq. 3.75) and shear dispersion $\langle\gamma^2\rangle$ (P_κ is filtered with $W_{\rm TH}$, see Eq. 3.76) for various cosmologies (abbreviations given in Fig. 2.6). Right Figure from Schneider et al. (1998).

with

$$S_+ = \frac{1}{\pi}\left[4\arccos\left(\frac{x}{2}\right) - x\sqrt{4-x^2}\right]\mathrm{H}(2-x) \tag{3.82}$$

and

$$S_- = \frac{x\sqrt{4-x^2}(6-x^2) - 8(3-x^2)\arcsin(x/2)}{\pi x^4}\mathrm{H}(2-x) + \frac{4(x^2-3)}{x^4}\mathrm{H}(x-2), \tag{3.83}$$

where H denotes the Heaviside step function. The relation between the aperture mass dispersion and the shear two-point correlation function is obtained by inserting Eq. (3.80) into Eq. (3.75):

$$\langle M_{\rm ap}^2\rangle(\theta_0) = \int \frac{\mathrm{d}\theta\,\theta}{\theta_0^2}\xi_+(\theta)\,T_+\left(\frac{\theta}{\theta_0}\right) = \int \frac{\mathrm{d}\theta\,\theta}{\theta_0^2}\xi_-(\theta)\,T_-\left(\frac{\theta}{\theta_0}\right). \tag{3.84}$$

The functions $T_\pm$ again depend on the choice of the filter function U in Eq. (3.40). We chose U given in Eq. (3.45). In this case $T_\pm$ can be expressed analytically (Schneider et al. 2002):

$$T_-(x) = \frac{192}{35\pi}x^3\left(1-\frac{x^2}{4}\right)^{7/2} \tag{3.85}$$

and

$$T_+(x) = \frac{6(2-15x^2)}{5}\left[1-\frac{2}{\pi}\arcsin\left(\frac{x}{2}\right)\right] + \frac{x\sqrt{4-x^2}}{100\pi}\left(120+2320x^2-754x^4+132x^6-9x^8\right). \tag{3.86}$$

Both functions vanish for $x > 2$. Thus $\langle M_{\rm ap}^2\rangle$ can be obtained directly from the correlation functions $\xi_\pm$ in a finite interval. The filter functions $T_\pm$ and $S_\pm$ are displayed in the left panel of Fig. 3.12.

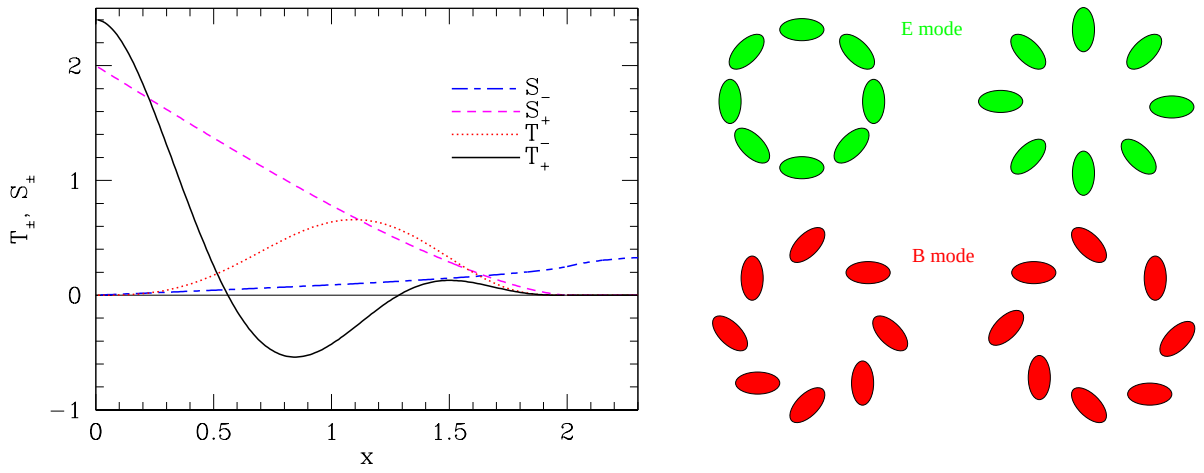

Figure 3.12: *Left panel*: Filter functions $T_\pm$ and $S_\pm$. Note that S_- does not vanish for $x > 2$. *Right panel*: Sketch of the E-mode pattern (curl-free mode) as it shows up for a mass overdensity (*upper left*: tangential alignment) or underdensity (*upper right*: radial alignment). The B-mode pattern (curl mode) cannot be generated by lensing. Right Figure from Van Waerbeke & Mellier (2003).

E- and B-modes

Since the shear field γ is a two-component quantity and is obtained from the one-component scalar potential ψ, the two components of γ are not independent of each other. Consider the definition of the gradient field Schneider et al. (e.g., 2002)

$$\boldsymbol{u} \equiv \nabla\kappa = \begin{pmatrix} \gamma_{1,1} + \gamma_{2,2} \\ \gamma_{1,2} - \gamma_{2,1} \end{pmatrix}.$$

The gradient field $\boldsymbol{u}$ is expected to be curl-free (E-mode) for pure lensing. However, due to noise in the data, insufficient PSF anisotropy correction (Sect. 5.3), artefacts of the data reduction and intrinsic alignment of source galaxies (see Sect. 6.4.2 for a detailed discussion of these effects) a curl component (B-mode) can arise. Hence, for a shear field estimated from real data, the convergence κ acquires a non-vanishing imaginary part. We decompose the convergence into an E- and B-mode (Fig. 3.12):

$$\nabla^2\kappa = \nabla^2\kappa_\mathrm{E} + \mathrm{i}\nabla^2\kappa_\mathrm{B} = \nabla\cdot\boldsymbol{u} + \mathrm{i}\nabla\times\boldsymbol{u}, \tag{3.87}$$

with $\nabla\times\boldsymbol{u} = u_{2,1} - u_{1,2}$. We now define in full analogy with the pure lensing case the E/B-modes of the complex deflection potential $\psi(\boldsymbol{\theta}) = \psi^\mathrm{E}(\boldsymbol{\theta}) + \mathrm{i}\psi^\mathrm{B}(\boldsymbol{\theta})$ so that $\nabla^2\psi = 2\kappa$. With this the shear can be calculated as usual: $\gamma = (\psi_{,11} - \psi_{,22})/2 + \mathrm{i}\psi_{,12}$. Using the E- and B-mode convergences we can construct the E- and B-mode power spectra, P^E and P^B, where the convergence power spectrum is given by

$$P_\kappa(l) = P_\mathrm{E}(l) + P_\mathrm{B}(l). \tag{3.88}$$

If B-modes are present, the relations of the cosmic shear two-point statistics are altered. The relations between the shear two-point correlation function, aperture mass dispersion and the E- and B-mode power spectra are then given by (Crittenden et al. 2002; Schneider et al. 2002):

$$\xi_+(\theta_0) = \frac{1}{2\pi}\int_0^\infty \mathrm{d}l\, l[P_\mathrm{E}(l) + P_\mathrm{B}(l)]W_{\xi_+}(l\theta_0), \tag{3.89}$$

$$\xi_-(\theta_0) = \frac{1}{2\pi}\int_0^\infty \mathrm{d}l\, l[P_\mathrm{E}(l) + P_\mathrm{B}(l)]W_{\xi_-}(l\theta_0), \tag{3.90}$$

$$\langle M_\mathrm{ap}^2\rangle(\theta_0) = \frac{1}{2\pi}\int_0^\infty \mathrm{d}l\, lP_\mathrm{E}(l)W_\mathrm{ap}(l\theta_0), \tag{3.91}$$

$$\langle M_\perp^2\rangle(\theta_0) = \frac{1}{2\pi}\int_0^\infty \mathrm{d}l\, lP_\mathrm{B}(l)W_\mathrm{ap}(l\theta_0). \tag{3.92}$$

Thus, $\langle M_\mathrm{ap}^2\rangle$ is sensitive to E-modes only and $\langle M_\perp^2\rangle$ to B-modes only. By contrast, $\xi_\pm$ is a mixture of E- and B-modes.

As in the pure lensing case, the aperture mass dispersion can be calculated from the shear two-point correlation functions, $\xi_\pm$ (Schneider et al. 2002):

$$\langle M_\mathrm{ap}^2\rangle(\theta_0) = \frac{1}{2}\int \frac{\mathrm{d}\theta\,\theta}{\theta_0^2}\left[\xi_+(\theta)\,T_+\left(\frac{\theta}{\theta_0}\right) + \xi_-(\theta)\,T_-\left(\frac{\theta}{\theta_0}\right)\right], \tag{3.93}$$

$$\langle M_\perp^2\rangle(\theta_0) = \frac{1}{2}\int \frac{\mathrm{d}\theta\,\theta}{\theta_0^2}\left[\xi_+(\theta)\,T_+\left(\frac{\theta}{\theta_0}\right) - \xi_-(\theta)\,T_-\left(\frac{\theta}{\theta_0}\right)\right]. \tag{3.94}$$

Ideally, gravitational lensing cannot generate B-modes. Hence, measuring a significant B-mode signal could indicate remaining systematic effects in the data. In this work we utilise the aperture mass dispersion to separate E- and B-modes because the integral in Eqs. (3.93) and (3.94) are calculated in a finite region ($T_\pm$ vanish for $\theta > 2\theta_0$). Throughout this work we use the expressions $\langle M_\mathrm{ap}^2\rangle$ and 'E' interchangeably as well as $\langle M_\perp^2\rangle$ and 'B'.

Another quantity defined by

$$\langle M_\times^2\rangle(\theta_0) = \int \frac{\mathrm{d}\theta\,\theta}{\theta_0^2}\,\xi_\times(\theta)\,T_-\left(\frac{\theta}{\theta_0}\right) \tag{3.95}$$

can be used as an indicator for systematics since $\xi_\times$ and hence $\langle M_\times^2\rangle$ are expected to vanish (Eq. 3.79). We choose T_- in Eq. (3.95) because it has no change of sign in contrast to T_+.

3.2.3 Shear estimators in practice

In this Section we give the connection to the real world, i.e. we specify practical unbiased estimators of the two-point correlation functions (3.78) and the aperture mass dispersion (3.93) and (3.94). Since the measured ellipticities, ϵ, of galaxies are unbiased estimators of

the local shear, γ (see Eq. 3.38) the estimators of the two-point shear correlation functions in practice are

$$\hat{\xi}_{\pm}(\theta) = \frac{\sum_{i,j}^{N} w_i w_j (\epsilon_{\mathrm{t},i}\epsilon_{\mathrm{t},j} \pm \epsilon_{\times,i}\epsilon_{\times,j})\Delta_{ij}(\theta)}{\sum_{i,j}^{N} w_i w_j \Delta_{ij}(\theta)}, \tag{3.96}$$

with

$$\Delta_{ij}(\theta) = \begin{cases} 1, & \theta - \Delta\theta/2 \leq |\theta_i - \theta_j| < \theta + \Delta\theta/2 \\ 0, & \text{otherwise,} \end{cases} \tag{3.97}$$

where ϵ_{t} and $\epsilon_{\times}$ are the tangential and cross components of the corrected galaxy ellipticities and w_i is the weighting factor (details of the correction and weighting scheme can be found in Sect. 5.3). All pairs of background galaxies within a distance between $\theta - \Delta\theta/2$ and $\theta + \Delta\theta/2$ are considered, where $\Delta\theta$ is the angular width of the bin. Accordingly, the practical estimators of the aperture mass dispersion are

$$\hat{M}(\theta_0) = \frac{\Delta\theta}{2\theta_0^2} \sum_{n=1}^{2m} \theta_n \left[\hat{\xi}_+(\theta_n)\, T_+\left(\frac{\theta_n}{\theta_0}\right) + \hat{\xi}_-(\theta_n)\, T_-\left(\frac{\theta_n}{\theta_0}\right) \right], \tag{3.98}$$

$$\hat{M}_{\perp}(\theta_0) = \frac{\Delta\theta}{2\theta_0^2} \sum_{n=1}^{2m} \theta_n \left[\hat{\xi}_+(\theta_n)\, T_+\left(\frac{\theta_n}{\theta_0}\right) - \hat{\xi}_-(\theta_n)\, T_-\left(\frac{\theta_n}{\theta_0}\right) \right], \tag{3.99}$$

$$\hat{M}_{\times}(\theta_0) = \frac{\Delta\theta}{\theta_0^2} \sum_{n=1}^{2m} \theta_n\, \hat{\xi}_{\times}(\theta_n)\, T_-\left(\frac{\theta_n}{\theta_0}\right), \tag{3.100}$$

with the centre of the bins $\theta_n = (n-1/2)\Delta\theta$ and the aperture radius θ_0 which is an integer multiple of the bin width, $\theta_0 = m\,\Delta\theta$. With the given shear estimators at hand we can now extract the cosmic shear signal from the data.

3.2.4 Cosmic shear signal and cosmological parameters

With the theoretical background of this and Chapter 2 we are now able to compare cosmic shear measurements with theoretical predictions. The cosmic shear signal, i.e. the signal of the aperture mass dispersion and shear two-point correlation function, is directly related to the convergence power spectrum, which in turn depends on the cosmological model, parameterised by the mass density power spectrum normalisation, σ_8, the total matter density, Ω_{m}, the source redshift distribution, $p(z)$, the shape parameter, Γ, the slope of the initial power spectrum, n_{s}, and the dark energy density, Ω_Λ.

The parameters Ω_{m}, σ_8, and the mean redshift of the source redshift distribution, $\langle z \rangle$, cause a change of the amplitude of the convergence power spectrum, where the amplitude is higher the larger the parameters are (if all other parameters are fixed). A larger σ_8 directly increases the amplitude of the 3D mass density power spectrum on all scales and thus the amplitude of the convergence power spectrum. A larger Ω_{m} also increases the amplitude since gravitational lensing not only depends on the relative density contrast, $\delta = \Delta\rho/\rho$, but on $\Delta\rho$ (see the prefactor in Eq. 3.69). Furthermore, a larger $\langle z \rangle$ increases the cosmic

shear signal since high-redshift galaxies are deflected along a longer path through the LSS of the Universe, and the lens efficiency (Eq. 3.65) depends on the factor $f_{\rm K}(w-w')/f_{\rm K}(w')$ which increases for sources at higher redshift.

The parameters Γ, $n_{\rm s}$ and Ω_Λ cause a tilt of the power spectrum (PS) if all other parameters are fixed. A larger Γ cause a shift of the convergence PS to larger wave numbers since the argument of the transfer function is nomalised by Γ. Hence, the PS seems to be tilted since the amplitude of the convergence PS is larger on small scales and lower on large scales. A larger Ω_Λ cause a slight shift of the convergence PS to smaller wave numbers, hence the PS seems to be tilted since the amplitude is smaller on small scales and larger on large scales. A larger $n_{\rm s}$ cause a tilt of the convergence power spectrum such that on larger scales the amplitude is higher. Since the behaviour of the convergence power spectrum is similar for different parameter changes these parameters are highly degenerate, see Sect. 6.4 and, e.g., Fig. 6.11.

Chapter 4

Data, data reduction & data quality

During the last few years astronomers have been confronted with large data sets that are obtained with multi-chip CCD cameras which lead to new challenges in the data reduction process. Single CCDs of a large mosaic detector array are never perfectly aligned and equally sensitive. Hence, the data reduction process of multi-chip cameras is non-trivial. An example is the Wide Field Imager camera of the MPG/ESO 2.2m telescope (hereafter we refer to it as WFI@2.2m). It was fully operational in the beginning of 1999 but only 35 refereed papers based on WFI@2.2m data were published until the end of 2002, although WFI@2.2m is one of the most requested telescopes of the European Southern Observatory (ESO). To cope with the large data sets of multi-chip cameras we therefore developed a nearly fully automatic imaging pipeline for an efficient processing of them. Since the main science driver is weak gravitational lensing studies the pipeline is optimised for deep empty field observations in order to measure the shape of faint galaxies as accurately as possible.

In the first part of the Chapter we present the Garching-Bonn Deep Survey (GaBoDS) data set obtained with the WFI@2.2m. This large high-quality data set consists of 61 wide field images and is mainly obtained via a virtual survey, meaning that it was collected from the ESO archive. In the second part we describe the data reduction process of the GaBoDS. The fully reduced images are used in the following Chapter to create galaxy catalogues for the cosmic shear analysis. Finally, we describe in the third part the implementation of a basic quality check on the reduced images.

This Chapter is organised as follows. We first give an overview of the data set analysed in this thesis starting in Sect. 4.1.1 with the description of the Wide Field Imager instrument. In Sect. 4.1.2 we delineate the characteristics of the large deep multi-colour data set obtained with the wide-field instrument also with regard to the following weak lensing analysis. At the end of this Chapter the data reduction process (Sect. 4.2) and the quality control of the final images (Sect. 4.3) are elucidated in detail.

Parts of Sect. 4.1 have been published in Hetterscheidt et al. (2006), GaBoDS: The Garching-Bonn Deep Survey: VI. Cosmic shear analysis, astro-ph/0606571.
A large part of Sect. 4.3 has been published in Erben et al. (2005), GaBoDS: The Garching-Bonn Deep Survey: IV. Methods for the image reduction of multi-chip cameras.

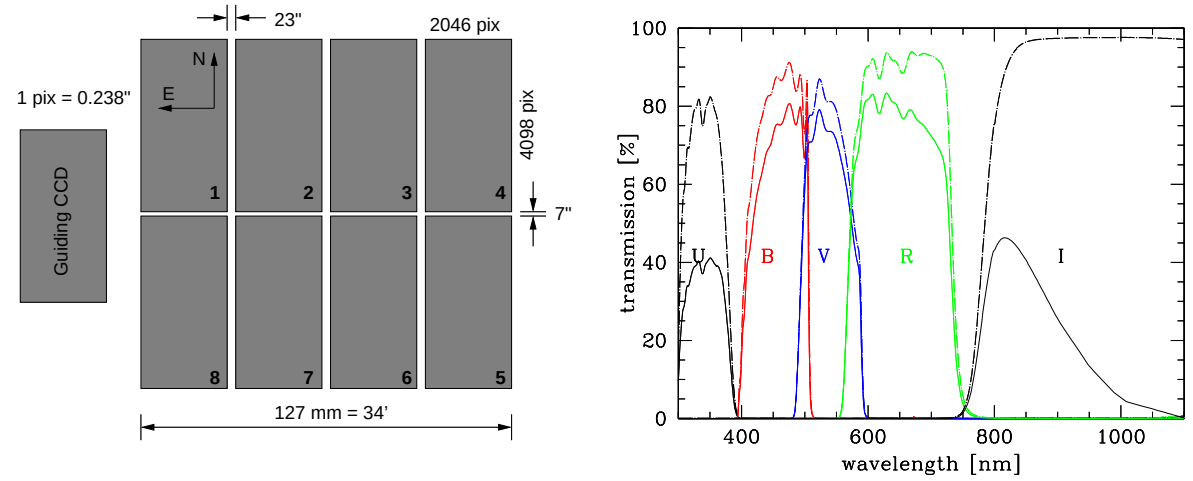

Figure 4.1: *Left panel:* CCD layout of WFI@2.2m (not to scale). *Right panel:* Broadband filters for WFI@2.2m. Dot-dashed lines: Filter transmission. Solid lines: Instrumental response (including filter, CCD and telescope) in different filters. Left Figure from Erben et al. (2005).

4.1 The Data

4.1.1 The Wide Field Imager

The Garching-Bonn Deep Survey (GaBoDS) data set was observed with the Wide Field Imager which is mounted at the Cassegrain focus of the MPG/ESO 2.2m telescope on La Silla, Chile. It is a mosaic camera consisting of eight $2\,\mathrm{k} \times 4\,\mathrm{k}$ CCDs with a pixel size of $15\,\mu\mathrm{m}$. The pixel scale is $0\farcs238$ and the total field-of-view in the sky is $34' \times 33'$. The CCD layout is shown in the left panel of Fig. 4.1 (note the gaps between single CCDs). The telescope layout is such that it allows a flat focal plane. Therefore the PSF properties over the whole field-of-view are excellent which is especially important for weak lensing analyses. The instrument characteristic is optimal for observations in the wavelength range from UV to near IR. Since we use in our work multi-colour data, we give an overview of the different broadband filters in the right panel of Fig. 4.1. For a more detailed description of the Wide Field Imager we refer to Baade (2002).

4.1.2 The GaBoDS data set

For our cosmic shear analysis we use the GaBoDS data set which consists of 61 deep high-quality R-band WFI images. The WFI camera shows gaps between the single CCDs. To have a uniform image coverage of the exposed sky, often a dither pattern (offset of the telescope between different exposures) is applied. Due to that the effective field-of-view of the camera can be as large as $40' \times 40'$. Each of the WFI images observed with dither pattern ($\approx 70\,\%$ of all fields) therefore cover an area of about $0.35\,\mathrm{deg}^2$. However, for the

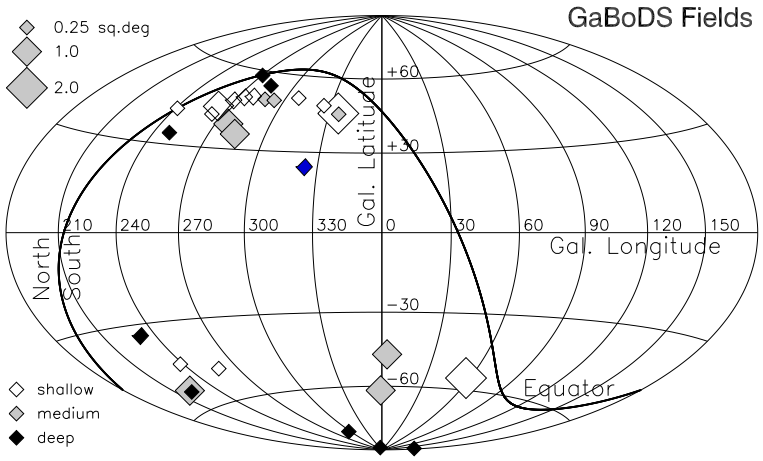

Figure 4.2: Sketch of the field distribution in the sky (adapted from Schirmer et al. 2003).

following cosmic shear analysis we exclude the edges of the images since the anisotropy of the seeing disc is larger there and would bias our cosmic shear results. This exclusion has only a small effect on the total number density of background sources. The resulting effective area is $0.25\,\mathrm{deg}^2$ per field, hence, the 61 WFI images roughly correspond to $15\,\mathrm{deg}^2$.

About 80 % of the data were obtained by a virtual survey (ASTROVIRTEL project[1,2]), meaning that the data set was collected from the ESO archive. For data mining the archive, the search engine `querator`[3] was developed by Pierfederici (2001) to address the needs of astronomers looking for multicolor imaging data. We selected the fields by four criteria: (1) the exposure time was at least 3.5 ks, (2) the seeing was better than ≈ 1 arcsec, (3) the field was not affected by bright foreground objects and (4) neither the field nor adjacent fields contained previously known very massive structures. For further details of the data mining of the ESO archive we refer to Schirmer et al. (2003). The rest of the data set was obtained by own observations (table 4.1 & 4.2). The data set is heterogeneous with respect to the (aperture) limiting magnitude m_{lim}, defined as

$$m_{\mathrm{lim}} = z_{\mathrm{p}} - 2.5\,\log\left(\sqrt{N_{\mathrm{pix}}}\,\sigma_{\mathrm{sky}}\right), \tag{4.1}$$

where z_{p} is the photometric zero point of the image considered (see Sect. 4.2.3), N_{pix} is the number of pixels within an aperture, and σ^2_{sky} is the pixel-to-pixel dispersion of the sky background. The limiting magnitudes in the R-band range between 25.0 mag and 26.5 mag for a sky level noise of $\sigma^2_{\mathrm{sky}} = 5$ measured in a circular aperture of $2''$ radius. Furthermore,

[1]ASTROVIRTEL cycle 2: Erben et al.,Gravitational lensing studies in randomly distributed, high galactic latitude fields

[2]http://www.stecf.org/astrovirtel

[3]http://archive.eso.org/querator

the seeing ranges between $0\farcs75$ and $1\farcs20$, the images were observed with different strategies (dithering/no dithering), and for the co-addition process we used different programmes (`EISdrizzle` and `SWarp`, see Sect. 4.2.4). In table 4.2 we give an overview of the different images. Some of the fields form small patches in the sky comprising areas from 0.25 up to 2 square degrees. The different patches represent 29 different lines-of-sight, where their positions are randomly distributed on the southern hemisphere at high galactic latitudes (Figs. 4.2, B.1 and B.2).

The survey is separated into six data sets mainly depending on the source of the data (table 4.1 and 4.2) to better trace possible systematic errors in our cosmic shear analysis resulting from, e.g., observing strategy. Note that the ESO Distant Cluster Survey (EDisCS, White et al. 2005; Clowe et al. 2006b) data set contains distant galaxy clusters ($z = 0.5...0.8$) that have been originally identified in the Las Campanas Distant Cluster Survey (LCDCS) using a surface brightness enhancement method (Gonzalez et al. 2001) and confirmed using the red cluster sequence (White et al. 2005). Since we perform our lensing analysis with those objects lying in the magnitude interval $R \in [21.5, 24.5]$, we are presumably not sensitive to those high-redshift clusters. We assume in the following that these fields do not bias our cosmic shear survey significantly towards high-density regions. We discuss this in more detail in Sect. 6.4.2.

Additionally, we use the ESO Deep-Public-Survey (henceforth: DPS), a sub-set of GaBoDS, which was mainly carried out by the ESO Imaging Survey (EIS) team. The DPS is a deep multi-colour imaging survey and was obtained with the standard *UBVRI* broad-band filters. The DPS comprises 10 fields, corresponding to $2.5\,\mathrm{deg}^2$, where at least three colours are observed (table 4.2). For seven fields of the DPS *UBVRI*-band observations are available. This corresponds to $1.75\,\mathrm{deg}^2$ and yields photometric redshift information for 8% of the lensing galaxies considered for the cosmic shear analysis. For the data processing description and data quality we refer to Hildebrandt et al. (2006).

4.2 Data Reduction

Reducing observations taken by multi-chip CCD cameras presents new challenges in terms of the quantity of data which must be processed. The total amount of raw CCD mosaic frames reduced for this work contains several terabytes of data. During the reduction process, however, more disc space must be available to edit these CCD frames in a proper and secure way. We reduced the data with a nearly fully automatic, parallel working imaging pipeline that we developed for a homogeneous and efficient processing of large data sets. The pipeline splits the raw science and calibration CCD mosaics into single chips, which are then processed individually by individual computers, nodes, of a computer cluster. The processing of the individual chips contains the basic data reduction: overscan-correction, master bias subtraction, flat-fielding with skyflats and superflats and defringing (Fig. 4.6). The next processes like astrometric and photometric calibration and co-addition can partly not be parallelised and are done on the master computer. In the following all processing steps are elucidated in detail.

Table 4.1: Data code, depth of the fields (time t of all co-added exposures), total field area, effective number density of galaxies $n_{\rm eff}$ (to calculate $n_{\rm eff}$, the weighting factor of individual galaxies is taken into account, see Eq. 5.19) and data source (see table 4.2 for details of individual fields). Key: ‡: fields are rejected for the final cosmic shear analysis.

code	depth t [ks]	area [deg^2]	$n_{\rm eff}$ [$'^{-2}$]	Data source	Comments
COMBO	$10<t<56$	1.25	16.5	COMBO-17	
OWN	$7.0<t<22$	3.25	12.0	own obs., MPE IR group, ESO archive	
DEEP	$3.9<t<9.3$	3.25	11.5	EIS + own obs.	multicolor data, co-addition with `swarp`
B8	$4.2<t<7.5$	2.5	11.5	ASTROVIRTEL	no dithering
C0‡	$4.0<t<4.8$	2.0	10.0	ASTROVIRTEL	no dithering
CL	$t=3.6$	3.0	12.0	EDisCS	cluster candidates

4.2.1 Basic data reduction

Bias subtraction

Even a zero second integration exposure has a non-zero count rate due to read-out noise. To avoid negative numbers in the output image, CCD electronics are set up to provide a positive offset value, called the bias. For each image we perform an overall estimate for the bias. We first consider pixels of the so-called overscan region. This region is a 50 pixel wide strip at the edges of the CCD detector. There are no physical pixels in the overscan region. Instead the CCD is read out 50 times without moving charges. We add for each line all pixel values in the overscan region, reject the lowest and highest values and estimate a straight mean from the rest. This mean is then subtracted from the corresponding pixel line of the total image. After this correction, we remove the overscan regions of the images. To correct for spatially varying bias patterns in the flat or science images, we median combine, with outlier rejection, several overscan-corrected bias exposures to create a *master bias* for each CCD frame. This *master bias* is subtracted from each individual science and calibration exposure.

Skyflats

Individual signatures on the CCD chips, like varying illumination across the field-of-view and pixel-to-pixel variations in the CCD response, present in the science frames have to be removed. To this end, we take several twilight exposures that are uniformly illuminated (skyflat). We overscan-correct the skyflats and subsequently subtract the master bias from them. We rescale the skyflats to a common value, and we then pixel-wise median combine

Table 4.2: List of all fields of the GaBoDS survey. The observing time, $t_{\rm obs}$, corresponds to the R-band observation, N is the number of galaxies per field in the final catalogue in the magnitude range $R \in [21.5, 24.5]$ and $2\,r_{\rm h}$ is twice the measured half light radius of stars in arcseconds.

name	RA (J2000)	DEC (J2000)	$t_{\rm obs}$[ksec]	N	$2\,r_{\rm h}['']$	data source	code	colours
A901	149.07771	−10.02734	18.1	19513	0.75	COMBO-17	COMBO	R
AXAF	53.13344	−27.82255	57.2	19639	0.90	COMBO-17	COMBO	$UBVRI$
FDF	16.44541	−25.85742	11.8	19169	0.86	COMBO-17	COMBO	R
S11	175.74860	−1.73458	21.5	18855	0.84	COMBO-17	COMBO	R
SGP	11.49852	−29.61047	20.0	21465	0.85	COMBO-17	COMBO	R
CAPO_DF	186.03787	−13.10764	13.0	16014	0.97	ESO archive	OWN	R
NDF	181.36237	−7.65226	21.8	14146	0.93	ME IR group	OWN	R
SHARC2	76.3333	−28.81805	11.4	19101	0.86	own obs.	OWN	R
F17_P1	216.41916	−34.69460	10.0	10345	1.13	own obs.	OWN	R
F17_P3	217.02611	−34.69463	10.0	14135	0.77	own obs.	OWN	R
A1347_P1	175.25702	−25.51474	13.5	10330	0.76	own obs.	OWN	R
A1347_P2	175.79254	−25.50918	7.5	13738	0.91	own obs.	OWN	R
A1347_P3	175.23976	−25.00933	7.0	15581	0.89	own obs.	OWN	R
A1347_P4	175.79459	−24.99836	8.0	13665	1.07	own obs.	OWN	R
F4_P1	321.65611	−40.25193	9.5	16135	0.93	own obs.	OWN	R
F4_P2	321.71942	−39.76761	7.0	14103	1.06	own obs.	OWN	R
F4_P3	322.32389	−39.72689	10.0	16348	0.87	own obs.	OWN	R
F4_P4	322.32389	−39.72689	7.5	12943	1.10	own obs.	OWN	R
Deep1a	343.79506	−40.19886	7.2	16131	1.00	EIS	DEEP	$UBVRI$
Deep1b	343.058572	−40.22481	3.9	9806	1.30	EIS	DEEP	$UBVRI$
Deep1c	342.328125	−40.20702	3.9	13354	1.03	EIS	DEEP	VRI
Deep1e	341.96679	−39.52874	9.0	13374	1.05	EIS	DEEP	URI
Deep2a	54.372223	−27.81551	6.0	14785	1.00	EIS	DEEP	R
Deep2b	53.746626	−27.80862	5.1	10177	1.20	EIS	DEEP	$UBVRI$
Deep2d	52.506344	−27.81774	3.0	9745	1.20	EIS	DEEP	R
DEEP2e	53.12291	−27.30467	7.5	16768	0.97	own obs.	DEEP	R
DEEP2f	53.66995	−27.32400	7.0	14494	1.10	own obs.	DEEP	R
Deep3a	171.24559	−21.68289	7.2	14130	0.91	EIS	DEEP	$UBVRI$
Deep3b	170.66159	−21.70969	9.3	14905	0.92	EIS	DEEP	$UBVRI$
Deep3c	170.01909	−21.69960	9.0	15606	0.90	EIS	DEEP	$UBVRI$
Deep3d	169.42875	−25.85742	9.3	14134	0.80	own obs.	DEEP	$BVRI$
AM1	58.81181	−49.667762	7.5	14956	0.99	ASTROVIRTEL	B8	R
B8p0	340.34886	−9.59009	7.2	13299	0.87	ASTROVIRTEL	B8	R
B8p1	340.346051	−9.08957	4.5	13654	0.87	ASTROVIRTEL	B8	R
B8p2	340.345309	−8.58963	5.4	13308	0.87	ASTROVIRTEL	B8	R
B8p3	340.345149	−8.08951	5.4	13834	0.89	ASTROVIRTEL	B8	R
B8m1	340.34884	−10.08953	4.5	12401	0.90	ASTROVIRTEL	B8	R
B8m2	340.348548	−10.58954	5.4	12864	0.89	ASTROVIRTEL	B8	R
B8m3	340.346888	−11.08857	5.4	14397	0.99	ASTROVIRTEL	B8	R
Comparison	65.307669	−36.28380	5.3	14882	1.02	ASTROVIRTEL	B8	R
Pal3	151.432117	−0.00344	4.2	12608	1.07	ASTROVIRTEL	B8	R
C0400	214.360609	−12.25356	4.8	11857	0.90	ASTROVIRTEL	C0	R
C04m1	214.727417	−12.75342	4.0	10536	0.94	ASTROVIRTEL	C0	R
C04m2	214.478576	−13.25319	4.0	11292	0.89	ASTROVIRTEL	C0	R
C04m3	215.318002	−13.75352	4.0	13170	0.85	ASTROVIRTEL	C0	R
C04m4	215.111423	−14.25337	4.0	11872	0.88	ASTROVIRTEL	C0	R
C04p1	214.726983	−11.75319	4.0	11760	0.92	ASTROVIRTEL	C0	R
C04p2	214.727266	−11.25366	4.0	11093	0.90	ASTROVIRTEL	C0	R
C04p3	215.098018	−10.75340	4.0	13702	0.85	ASTROVIRTEL	C0	R
CL1037-1243	159.444072	−12.75499	3.6	13210	1.03	EDisCS	CL	R
CL1040-1155	160.139300	−11.96379	3.6	13451	0.99	EDisCS	CL	R
CL1054-1146	163.581888	−11.81304	3.6	12263	1.00	EDisCS	CL	R
CL1054-1245	163.647353	−12.79700	3.6	15420	0.90	EDisCS	CL	R
CL1059-1253	164.755650	−12.92051	3.6	12778	1.05	EDisCS	CL	R
CL1119-1129	169.784677	−11.52558	3.6	13635	0.99	EDisCS	CL	R
CL1138-1133	174.508878	−11.59953	3.6	16748	0.93	EDisCS	CL	R
CL1202-1224	180.645603	−12.44172	3.6	14935	0.97	EDisCS	CL	R
Cl1216-1201	184.170966	−12.06268	3.6	17472	0.75	EDisCS	CL	R
Cl1301-1139	195.467853	−11.63099	3.6	13975	0.96	EDisCS	CL	R
CL1353-1137	208.306268	−11.59813	3.6	15281	0.90	EDisCS	CL	R
CL1420-1236	215.066773	−12.64986	3.6	11223	1.04	EDisCS	CL	R

them with outlier rejection, like pixels affected by stars (bright stars are detected even in twilight) or cosmic rays to form a *master skyflat*. Due to the dithering of individual exposures (offsetting the telescope between single exposures by an amount which is typically larger than the gaps between the CCDs of the camera), stars and cosmic rays appear at different positions on the image and are interpreted as outliers. We then normalise the *master skyflats* to unity (i.e., we divide each pixel by the median of all CCD *master skyflat* pixels) and divide the science frames by the *normalised master skyflat* to get in the ideal case a uniform sky background across each chip. Skyflats have to be taken for all filters, because the sensitivity of the CCD chips is wavelength-dependent.

Superflats

Since the *normalised master skyflats* have a median of unity, the different gains of the different science frames are still present after the flat-fielding step. Furthermore, the flat-fielded science frames show a varying sky-background up to 3-4% over the total field-of-view, depending on sky brightness and filter in use. We therefore create a superflat directly from the already flat-fielded science exposures, if there is a sufficient number of science exposures at hand (typically more than a dozen) and if the dither pattern was significantly larger than the largest object in the field, so each pixel of the camera will see the sky-background several times. All flat-fielded science exposures from a given *run* (a *run* is a time interval for which the instrument or ambient conditions are stable; for R-band usually 2-3 nights, for I-band a few hours) are median combined, again with rejection of outliers yielding the so called *unsmoothed superflat*. Pixels affected by stars or galaxies are detected with `SExtractor` and masked out before combination, preventing them from affecting the *unsmoothed superflat*. In cases where all input pixels are masked, the output pixel is set to the median value of the object-subtracted and flat-fielded science frame. The result is then heavily smoothed by creating a *background* image using `SExtractor` with the `SExtractor` parameter BACK_SIZE=90. In an area of BACK_SIZE × BACK_SIZE the mean and dispersion of all pixel values are calculated, where pixels that deviate more than $3\,\sigma$ from the mean are rejected. This procedure is repeated until all pixel values are within $\pm 3\,\sigma$. The background image is then a bi-cubic spline to all mean pixel values of the corresponding areas. The smoothed image yields an illumination correction image or *smoothed superflat* for every chip. All science frames are then divided by the *smoothed superflat*. Typical science images taken in the broad band filters *UBVRI* are then flat up to 1% over the whole mosaic. In Fig. 4.3 the effects of master bias subtraction, flat-fielding and superflat-fielding are displayed for a V-band exposure from WFI@2.2m.

Defringing

Science images can suffer from the so-called fringe pattern which shows up as spatially quickly varying, wave-like structures on the CCDs, see Fig. 4.4. The fringe pattern is caused by a thin-film interference effect in the detector. If the optical depth of photons in the silicon layer is larger than twice the thickness of this layer, the photons can be reflected

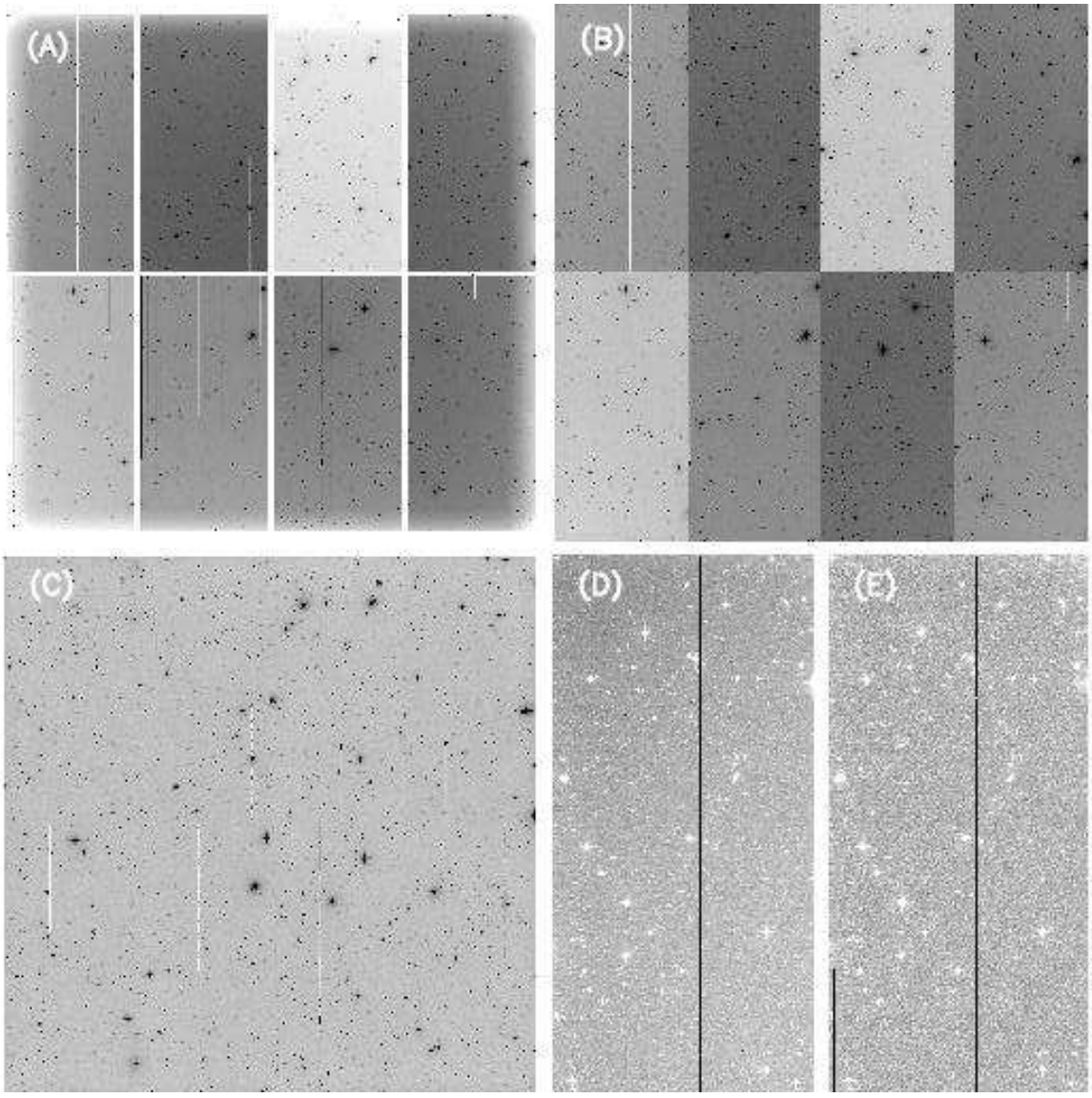

Figure 4.3: Basic data reduction of a V-band exposure from WFI@2.2m. *Panel (A):* raw image, *panel (B):* result after *master bias* and *master skyflat* correction. The procedure of flat-fielding takes out small-scale variations but leaves large-scale residuals of up to 3% of the sky background on the scale of the CCD [*panel (D)*]. The large-scale residuals and the differences in the sky count-rate are removed after flat-fielding with the *smoothed superflat*. A flatness of 1% of the sky background is obtained over the entire mosaic in most of the cases [*panels (C)* and *(E)*]. Figure from Erben et al. (2005).

off the gain structure back to the top surface and then back into the silicon layer. These photons then interfere with other photons destructively or constructively, which results in an increased or reduced additive illumination (Howell 2000). This illumination varies across the detector, depending on the thickness of the silicon layer and the angle with which the photons strike the mosaic. In addition, the amplitude of the fringe pattern varies with time, because the amplitude strongly depends on sky brightness, cloud coverage, position on the sky and airmass.

These unwanted additive structures need to be subtracted from the data. This is done by calculating a fringe model for every superflat-fielded science frame. The fringe model is obtained by subtracting the *smoothed superflat* from the *unsmoothed superflat*. The fringing-corrected (defringed) science frame is then obtained by subtracting the scaled fringe model from the science frame. The fringe model for every CCD chip has to be scaled since the amplitude of the fringes scales with the sky background. The scale factor is given by the median value of the corresponding science frame divided by the median value of the *unsmoothed superflat*. In order to have a fringe model with a sufficiently low pixel-to-pixel noise, one has to combine more than approximately 10 science frames to form the *unsmoothed superflat*. If not, the pixel-to-pixel noise can be larger than the fringing amplitude and would introduce more noise into the individual defringed images than without fringing correction. Furthermore, the science frames should be taken in a short period of time to avoid the time dependent amplitude variation of the fringe pattern.

Since the interference is wavelength dependent, using different filters result in different fringe patterns. For the WFI@2.2m camera fringing is not present in UBV and for R-band data is of the order of a few percent as compared to the sky background. In the redder I-band the fringing patterns are more pronounced and show amplitude variations depending on night sky conditions (brightness, cloud coverage), the position on the sky and the airmass and is therefore more difficult to remove. In Fig. 4.4 the fringing correction in WFI@2.2m I-band data is displayed. In the case of our GaBoDS and DPS data sets the method described removes the fringes in the R-band well below 0.1 % of the sky background. This is also the case for I-band data if a very good superflat can be constructed.

Masking and creation of a basic weighting map

Besides the fringing pattern as a source of large-scale background variations, there are other unwanted effects of non-Gaussian nature seen in the CCD images, affecting a proper determination of the weighting factor (Sect. 4.2.4). These unwanted effects have to be masked out and downweighted to zero to form the *bad pixel map*, b, where b is zero or unity.

Examples of these large-scale defects are satellite tracks, reflections from moon light or bright stars inside and outside of the WFI field due to the filter in use or retaining jigs, which are often seen in images as stripes or elongated rings. Some examples are shown in Fig. 4.5. Only small areas of the total WFI field are affected by these random features. These defects do not show up in all exposures of a dither sequence and have to be masked out by hand utilising the *polygon* option of the `ds9` visualisation programme. These masks

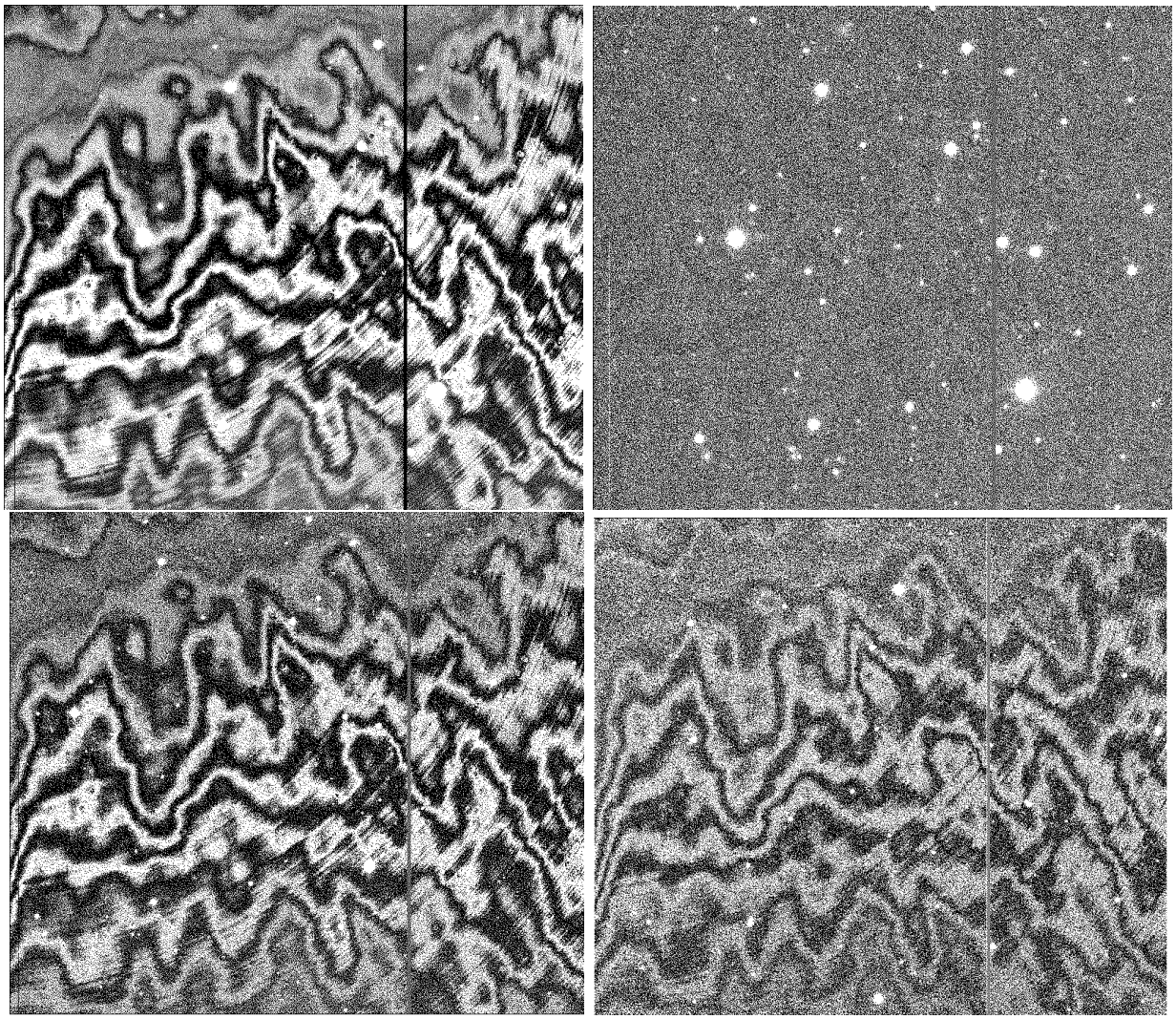

Figure 4.4: Fringing correction in WFI@2.2m I-band data. *Upper left panel:* science frame taken during stable, photometric conditions before fringing correction, *upper right panel:* science frame after fringing correction, *lower left panel:* same science frame, this time taken during non-photometric conditions, *lower right panel:* frame after correction. For non-photometric WFI@2.2m observations in I-band the fringing correction is not satisfactory. Credit: T. Erben.

or *bad pixel maps* are necessary for the weight creation as these areas obtain a zero weight for the later co-addition. Other effects can be detected automatically and get also a zero weight:

- Every chip contains 'hot' and 'cold' pixels, which always have high and low charge values, respectively, independent of the illumination. It can be possible that a whole column is affected in such a way. These pixels can be detected most effectively by *dark frames* and unsmoothed superflats, defining a threshold. All pixels with a value above or below the threshold are considered to be bad pixels. *Dark frames* are exposures with a closed shutter that contain the read-out noise and the accumulated thermic dark current of the CCD.

- In single exposures there are pixels affected by cosmic rays, which are detected with `SExtractor` with a special filter for cosmic ray detection generated with EYE (Bertin 2001; Nonino et al. 1999).

- There are also saturated pixels, which are detected by applying a pixel value threshold to the science frames (see above).

A basic weighting map is constructed such that simply every pixel in a single exposure i gets the value of the normalised skyflat as a weight ws_i. The basic weighting map is then modified with the *bad pixel map* in such a way that every pixel of a single exposure i has now the value of the normalised skyflat multiplied with the *bad pixel map*: $W_i = ws_i \times b_i$.

Sky background subtraction

Before the final co-addition, all images are brought to the same background level by subtracting the night sky. To this end, we utilise `SExtractor` to detect large-scale objects having at least 50 adjacent pixels with $1.5\,\sigma$ above the sky background in the superflat-fielded science frames and replace them by the mode of the unaffected pixels. From this image we create a background image using `SExtractor` with the `SEctractor` parameter BACK_SIZE=90. It serves as a model for the sky background and is subtracted from the original science frame.

4.2.2 Astrometric calibration

For multi-chip cameras like WFI@2.2m the astrometric solution is difficult to calculate, because stable field distortions occur: single chips can be rotated and shifted with respect to each other and can be tilted against the focal plane, see Fig. 4.7. Furthermore, unstable field distortions occur from temperature fluctuations of the telescope, and varying geometrical distortions of the telescope due to gravity since the observed targets have different zenith angles. Hence, the spherically curved sky is mapped in a *non-linear* way into the tangential plane of the camera having a large field-of-view. The *internal* astrometric accuracy (the accuracy with which the misalignment of the CCD chips with respect to each other can be

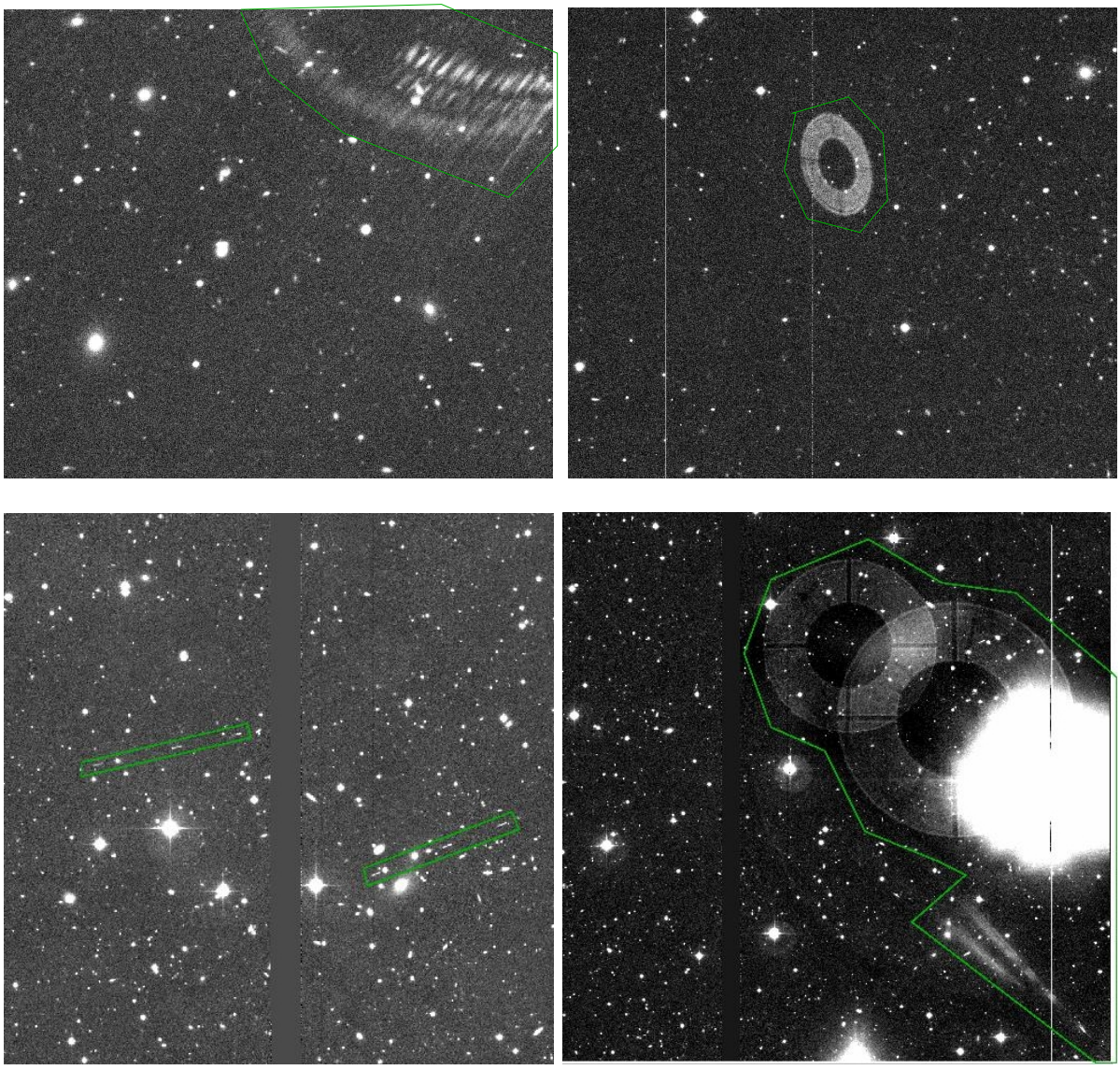

Figure 4.5: Examples of large-scale defects. *Upper left:* reflections from bright objects outside the WFI@2.2m field. *Lower left:* satellite track, *upper right:* 'ghost' image, a reflection from a bright star at the filter onto the CCD chip. All such features are typically unique to individual exposures and do not appear in subsequent, sufficiently dithered exposures. *Lower right:* reflections from a bright star inside the WFI@2.2m field (here: image not dithered). All described defects are detected by eye and are masked by hand using the *polygon* option of the `ds9` visualisation programme (green line). The masked regions are set to zero to prevent that they enter the final image co-addition.

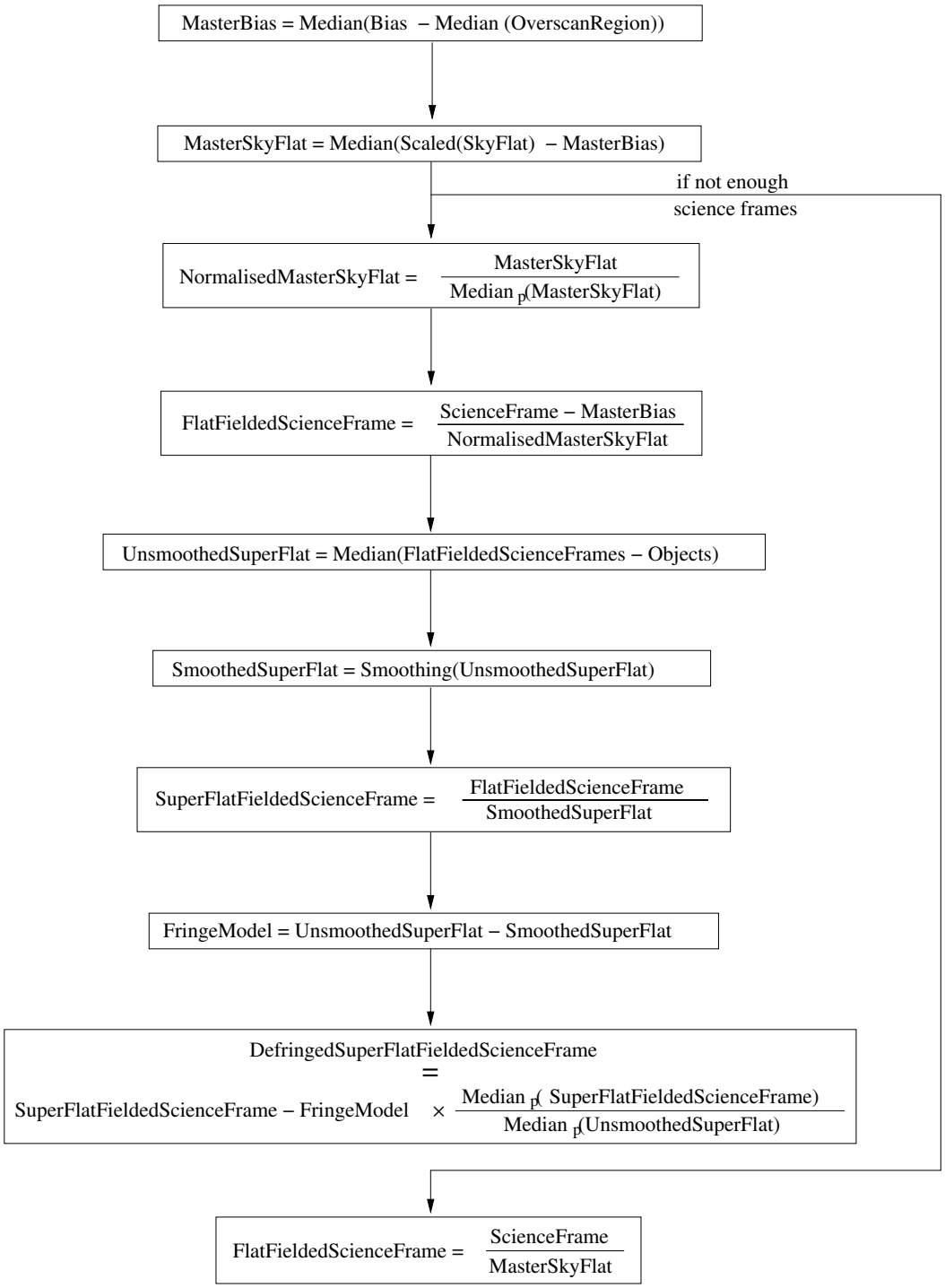

Figure 4.6: Flow-chart of the basic data reduction. The operator `Median`() denotes a pixel-wise median combination of several exposures, whereas $\texttt{Median}_p()$ denotes a median combination of all pixels of an exposure (both combinations with outlier rejection). All other operators are self-explanatory.

corrected) must be very high for weak lensing studies. We therefore directed our attention to the astrometric calibration and tested the accuracy intensively with respect to weak lensing studies (for test details see Erben et al. 2005). In the following we describe the astrometric calibration which is a two step procedure.

Single shift astrometric solution

For the astrometric calibration we utilise a catalogue of unsaturated objects with a high signal-to-noise ratio. We extract the objects with `SExtractor`, where they typically consist of five contiguous pixels that are five sigma above the sky background. With these parameter settings we obtain about three to six objects per square arcminute for empty field observations at high-galactic latitudes. In a first step, we use these objects to calculate a simple shift astrometric solution for each exposure, where we use the USNO-A2 catalogue (Monet et al. 1998) as a reference.

Full astrometric solution

The simple zero-order solution is only a first approximation and we use it to derive a general solution. In a second step, we use the `Astrometrix` package to calculate a two-dimensional third-order polynomial describing the astrometric distortions for each image. Especially the detected objects in the overlap regions are important since they are used to calculate the *internal* solution. The reference catalogue is then used by `Astrometrix` to fix the *external* solution with respect to the absolute sky coordinate system. The *internal* solution is typically accurate to $\approx 20\,\mathrm{mas}$, whereas the *external* solution is limited by the accuracy of the reference catalogue which is of the order of 250 mas.

4.2.3 Photometric calibration

Absolute photometric calibration using standard stars

To perform the absolute photometric calibration, images of standard stars (standard images) are observed in the same night as the science images. The standard images are reduced in a similar way as the science images. We derive an astrometric solution for the standard images, create standard star catalogues, and match them with the photometric standard star catalogues from Landolt (1992) or Stetson (2000). Then we fit the following equation to the matched standard stars:

$$m - m_{\mathrm{WFI}} = ZP + e_{\mathrm{c}} * a_{\mathrm{m}} + c_{\mathrm{t}} * c_{\mathrm{i}}, \tag{4.2}$$

where m is the given magnitude of the reference star and c_{i} is the given colour index, e.g. $(B-V)$. The quantity m_{WFI} is the measured magnitude on the reduced standard image (we use here the `SExtractor` parameter MAG_AUTO) and a_{m} is the measured airmass, where airmass is defined as the path length through the atmosphere of a light ray of an extraterrestrial source with respect to that of a source located at the zenith. The fit

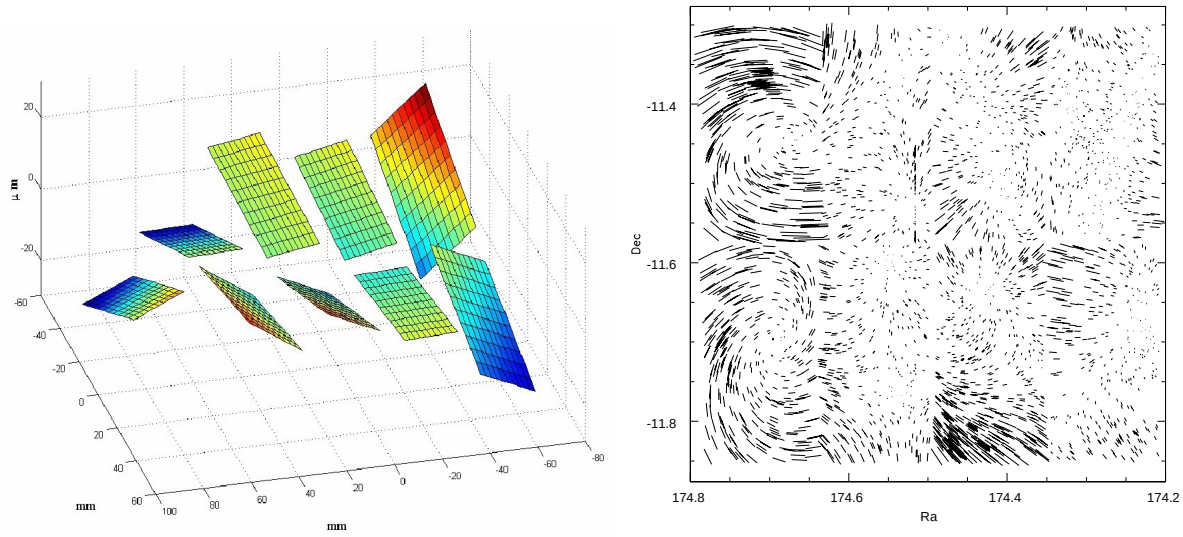

Figure 4.7: *Left panel:* WFI topography: tilt of the CCDs. Figure from the WFI@2.2m homepage (*http://www.ls.eso.org/lasilla/sciops/2p2/E2p2M/WFI/docs/WFInutshell.html*). *Right panel:* Difference in object position between a single-shift astrometric solution of the whole mosaic and a second-order astrometric solution for every chip. The two left CCDs are rotated with respect to the whole mosaic. The largest sticks correspond to $\approx 1\farcs5$. Right Figure from Erben et al. (2005).

parameter ZP is the absolute zero point of a night, $e_{\rm c}$ is the extinction coefficient and $c_{\rm t}$ is the colour term (accounting for the different stellar colours). To obtain the best-fit parameters we perform the fit simultaneously for all CCD chips. The photometric zero points of individual chips agree to within 0.01-0.03 mag.

Relative photometric calibration and external photometric solution

Since science exposures are usually taken under different photometric conditions, we perform an internal photometric calibration to scale all exposures to a common zero point. To perform an adequate photometry of multi-chip images we apply the following least-square minimization procedure (Koranyi et al. 1998). To determine the relative photometric zero point for all exposures, we compare the instrumental magnitudes of all objects located in the overlap regions of single exposures. Let k and l be two overlapping images with N number of common objects. In the first step, the noise weighted mean deviation $\bar{M}_{k,l}$ of the magnitudes K_i and L_i of all $i = 1, ..., N$ objects in the overlap region of two chips, k and l is calculated,

$$\bar{M}_{k,l} = \frac{\sum_{i=1}^{N} w_i(K_i - L_i)}{\sum_{i=1}^{N} w_i}, \tag{4.3}$$

with $w_i = (\sigma_{K,i}^2 + \sigma_{L,i}^2)^{-1}$, where $\sigma_{K,i}$ and $\sigma_{L,i}$ are the errors of the measured magnitudes K_i and L_i. In the next step the relative zero points ZP_m of all $N_{\rm over}$ overlapping CCD chips are calculated such that χ^2 is minimized with respect to ZP_m,

$$\chi^2 = \sum_{k,l}^{N_{\rm over}} [\bar{M}_{k,l} - (ZP_k - ZP_l)]^2. \tag{4.4}$$

To make the system non-degenerate, the constraint $\sum_k ZP_k = 0$ has to be fulfilled. This procedure offers a self-consistent relative photometric calibration of multi-chip images with overlap due to dithering.

After the relative photometric calibration we calculate the external photometric solution to relate the measured count rates to a photometric system, see Dietrich (2006).

4.2.4 Co-addition and weight creation

Pre co-addition quality control

Before the co-addition, we create quality control plots of the single science frames like seeing distribution of the frames, sky relative zero point, sky background (this allows us to identify exposures taken during twilight or unfavourable moon phases), their standard deviation and PSF ellipticity distribution of the mean ellipticity value from all stars within an exposure. These control plots allow us to select the images that enter the final co-addition process, see Fig. 4.8 as an example.

Co-addition and weight creation

The final co-addition of the sky subtracted science frames and creation of the weighting map of the DPS data set is done with `SWarp`, a TERAPIX[4] software module (Bertin et al. 2002; Bertin 2002). For the rest of the GaBoDS data set we utilise `EISdrizzle`, a specific version of the IRAF package `drizzle` (Fruchter & Hook 2002). Since the co-addition method of a simple pixel-shift from different exposures on top of each other is not accurate enough `SWarp` and `EISdrizzle` perform a sub-pixel co-addition. This is done by mapping an input pixel grid onto a finer output grid. All individual exposures are remapped onto the output grid taking into account the full astrometric solution.

Erben et al. (2005) and Schirmer (2004) showed that the size of the PSF using `EISdrizzle` is $\approx 5\,\%$ larger than the PSF size using `SWarp`. Additionally, images co-added with `EISdrizzle` show correlated noise, in contrast to that co-added with `SWarp`. However, the PSF anisotropy patterns and the measured ellipticities of faint galaxies show no significant differences using `EISdrizzle` or `SWarp`.

For the co-addition the sky background noise $\sigma_{{\rm sky},i}$ is determined with `SExtractor`, and the flux scale f_i with which the science frame has to be scaled to a consistent photometric

[4]available at http://terapix.iap.fr/soft/

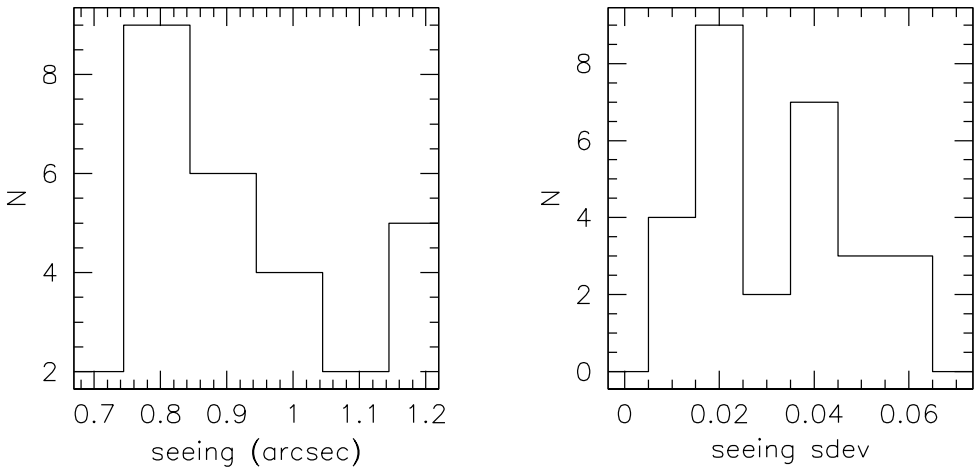

Figure 4.8: Example of pre co-addition quality control plots for 28 *R*-band science frames. *Left panel:* seeing distribution of the frames, where the seeing value of an exposure is estimated from the mean seeing in the individual chips. *Right panel:* seeing standard deviation within an exposure calculated from the eight mean seeing values of the individual chips. The *R*-band is the primary band for weak lensing analysis and we typically co-add frames with a seeing value less than 1 arcsec.

zero point ZP_i and to a fixed exposure time $t_i = 1\,\mathrm{s}$ is calculated,

$$f_i = 10^{ZP_i/2.5}/t_i. \tag{4.5}$$

The weighting factor $w_{\sigma\mathrm{f},i}$ due to $\sigma_{\mathrm{sky},i}$ and f_i is then given by

$$w_{\sigma\mathrm{f},i} = 1/(\sigma^2_{\mathrm{sky},i}\, f_i). \tag{4.6}$$

With this we can create an individual weighting map for every chip in the WFI mosaic, if every pixel of an exposure gets a weighting factor w_i of

$$w_i = w_{\sigma\mathrm{f},i} \times W_i, \tag{4.7}$$

where W_i is the value of the basic weighting map. The output pixel value of the co-added science image of N single science exposures with a pixel value of I_i is given by

$$I_{\mathrm{out}} = \frac{\sum_{i=1}^{N} w_i\, f_i\, I_i}{\sum_{i=1}^{N} w_i}, \tag{4.8}$$

taking into account that the noise is also scaled with the flux scale f_i. The pixel value I_i represents the part of the input pixel that is mapped onto the corresponding output pixel.

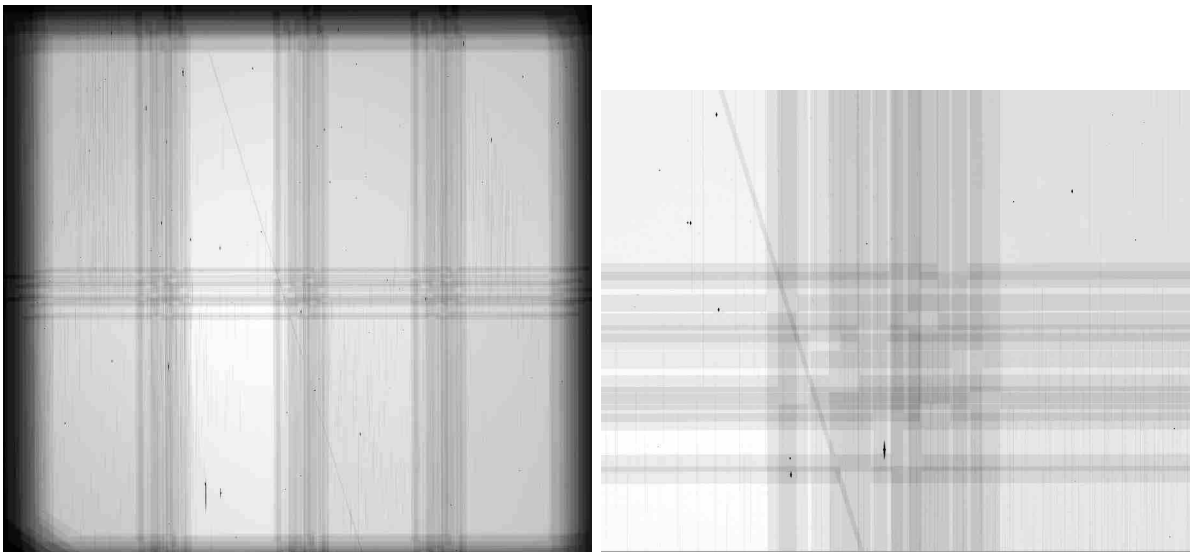

Figure 4.9: *Left panel:* weight map, *right panel:* zoom-in to its centre. We obtain the weight map by co-adding the normalised skyflats, where we set all defects to zero as we do for the science images. The weight map characterises the complex noise properties of a co-added science image. The lighter the colour, the higher the relative weight of the pixel. The darker regions at the positions where different chips meet have about half the weight of well-covered regions. Different weights between regions where the same number of input images have contributed show intrinsic sensitivity variations. The noise structure is complex and cannot be taken into account appropriately without the weight map. These maps are used by `SExtractor` for object detection (see Fig. 4.10) and for noise calculations. Using the weight map for simple object detections, one does in principle not need to cut the outermost regions of the co-added images where the noise is considerably higher than in the inner regions, see Fig. 4.10. As we will see in the next Chapter, we do so nevertheless since the PSF anisotropy is much higher near the image borders which would otherwise bias our cosmic shear measurements. Figure from Erben et al. (2005).

The output pixel value of the weighting map is simply

$$W = \sum_{i=1}^{N} w_i. \tag{4.9}$$

The co-added weight map provides a full characterisation of the relative noise properties for each science image pixel. When estimating a threshold for object detection or for estimating errors based on pixel noise (for instance object flux) the weighting map is taken into account. Fig. 4.9 displays an example of a co-added weight map and Fig. 4.10 its merits for object detection with `SExtractor`.

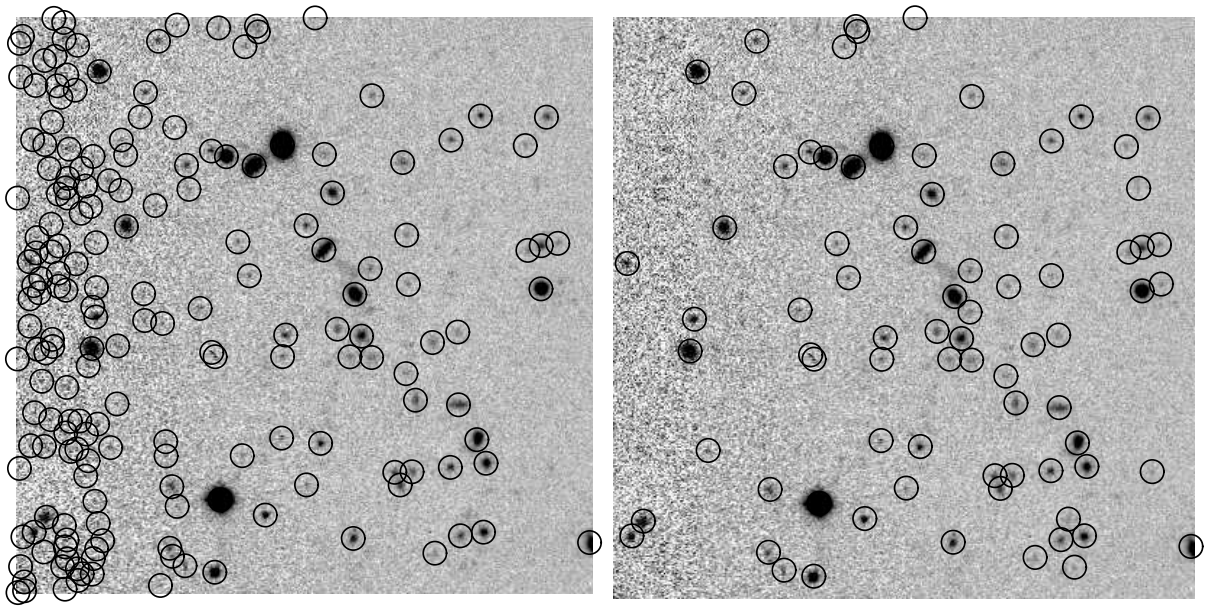

Figure 4.10: Objects detected with `SExtractor` in the same mosaic (with an area of $95'' \times 95''$) without (*left*) and with (*right*) a weight map as an additional `SExtractor` argument. The number of spurious detections in high-noise regions is obviously large if no weight image is used as an additional input. Figure from Erben et al. (2005).

4.3 Data quality control of co-added images

In this Section we describe the implementation of an automatic first quality check on our co-added mosaics. Basic tests on extracted object catalogues, like galaxy counts and the check on the clustering of sources are done without any user interaction and are performed for each individual pointing and filter (results for the DPS are shown under *http://marvin.astro.uni-bonn.de/DPS*).

4.3.1 Galaxy counts

The programme `SExtractor` is used to create a raw catalogue of objects in the final co-added image that consist of at least 3 contiguous pixels (DETECT_MINAREA=3) with a flux 2σ above the flux of the sky-background (DETECT_THRESH=2). The source extraction is done on a filtered image; we use a normalised Gaussian filter with a full width half maximum of 4.0 pixels (FILTER_NAME=gauss_4.0_7x7.conv). This conservative threshold is chosen in order to minimise the number of spurious detections. In the following, we use the `SExtractor` parameters MAG_AUTO (a Kron-like elliptical aperture magnitude) for magnitudes and FLUX_RADIUS for the half-light radius. `SExtractor` calculates the FLUX_RADIUS in such a way that a circle is placed around the center of a detected objected and the total flux is measured. The radius of the circle in which only half of the total flux is measured is called FLUX_RADIUS. To create a galaxy catalogue, the

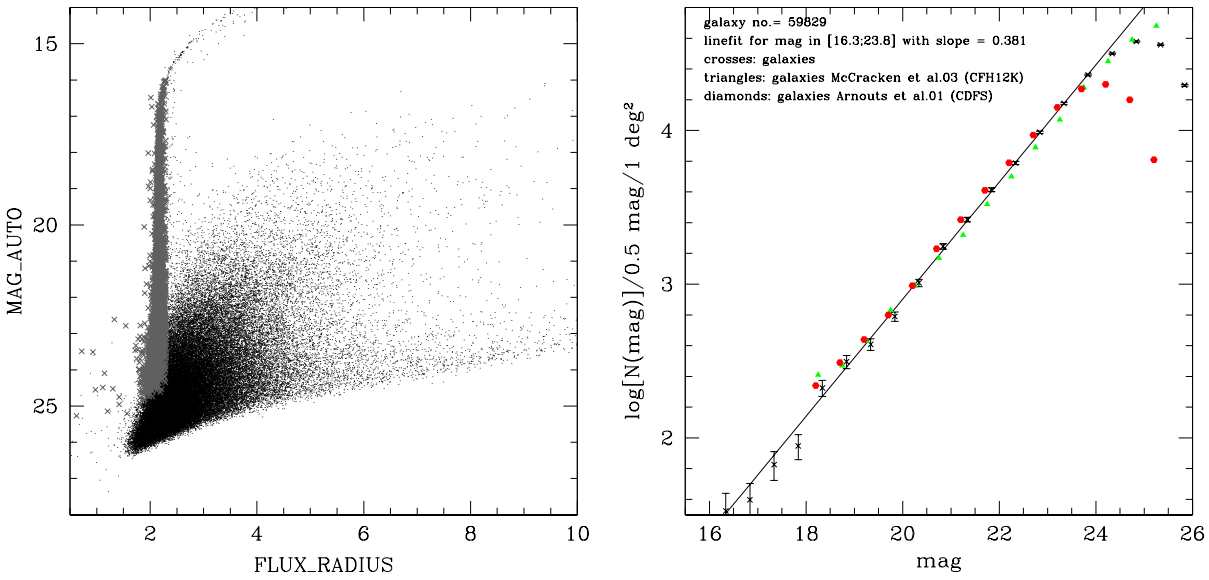

Figure 4.11: *Left panel:* Magnitude vs. half-light radius plot from our reduction of the Chandra Deep Field South (CDFS; see Giavalisco et al. 2004). Grey crosses: stars; they appear as a vertical branch in the plot and are selected by the CLASS_STAR parameter and FLUX_RADIUS (half-light radius), see text. Dots: extended sources. *Right panel:* Logarithmic galaxy counts in 0.5 mag bins per one square degree of the CDFS. The error bars are due to Poisson noise; the line fit is an error-weighted linear regression in a magnitude range between the saturation and the limiting magnitude (here: $R \in [16.3, 23.8]$). For the normalisation of the area we take into account that each detected object occupies an area in which fainter objects cannot be detected. As a comparison to our galaxy counts we also plot the galaxy number counts from the CFH12K-VIRMOS deep field (McCracken et al. 2003). For the CDFS we also plot the number counts from Arnouts et al. (2001). Figure from Erben et al. (2005).

`SExtractor` parameter CLASS_STAR in combination with the half-light radius is used; saturated objects are rejected. By default we define every object which has CLASS_STAR less than 0.95 as a galaxy. Note that this parameter depends on seeing. A simple check of this selection is a magnitude over half-light radius plot. All stars have approximately the same half-light radius and therefore show up as a vertical branch in this plot, see Fig. 4.11.

We count the number of galaxies in 0.5 mag wide bins per one square degree. To normalise the area to one square degree, we take into account that each object occupies an area in which fainter objects can not be detected. For this correction we use the `SExtractor` parameter ISO0, which is the isophotal area above the analysis threshold. We note that in the case of empty fields this effect is negligible. An error-weighted linear regression to the logarithmic galaxy counts is performed in a given magnitude range and the slope, $\mathrm{d}\log N/\mathrm{d}\,\mathrm{mag}$ determined. Weak lensing analyses are typically performed on deep empty fields, therefore we perform the fit in the range $\mathrm{mag} \in [16, 23.5]$. We routinely compare

our galaxy counts and the slope $\mathrm{d}\log N/\mathrm{d}\,\mathrm{mag}$ with those of McCracken et al. (2003), see right panel of Fig. 4.11 as example. We refer to our web site *http://marvin.astro.uni-bonn.de/DPS* for the number count plots of all individual images of the DPS data set. With this comparison, a rough test of the magnitude zero point and the limiting magnitude (the magnitude value, where the count rate differs from the linear fit) can be performed. If the magnitude zero point is correct, the slope and the counts in each bin should be comparable to former galaxy counts.

4.3.2 Clustering of extended sources

The two-point correlation function ω

A further commonly used test for the quality of the co-added image is the clustering of sources. For that purpose we use the two-point angular correlation function, $\omega(\theta)$, where $\omega(\theta)\delta\theta$ is the excess probability of finding a pair separated by an angle between θ and $\theta + \delta\theta$, see for instance Peacock (1999). We estimate this quantity by creating a large number of random catalogues (by default 40 mock catalogues are created) and count the pairs within the data catalogue, DD, within the random catalogue, RR, and between the data and random catalogues, DR. The estimator for $\omega(\theta)$, proposed by Landy & Szalay (1993), is

$$\omega(\theta) = \frac{DD - 2DR + RR}{RR} \tag{4.10}$$

and is used in the following. The random fields must have the same geometry as the data field. Therefore we calculate an obscuration mask out from the number density of extracted sources as follows. A mesh with 512×512 mesh cells is placed on top of a data field and the number of objects in each cell is counted. Then the cell count matrix is smoothed with a Gaussian kernel of about 512/60 cells FWHM, and all matrix elements lower than a given fraction of the mean number of galaxies inside a cell are defined as a masked region (we use 75% as default but varying this parameter between 50% and 80% does not change the results significantly). The borders of a field, bright stars, and part of their halos are masked automatically by this method (see Fig. 4.12).

To maximise computational speed, we perform our calculations by creating an index tree for galaxy positions as explained in Zhang & Pen (2004). In the framework of our automatic data quality control we count the galaxy pairs for the individual images in only 14 logarithmic angular bins. All generated plots of the DPS data set are shown on our web site, *http://marvin.astro.uni-bonn.de/DPS*. The error bars in our check-plots for each angular bin are simply estimated by Poisson noise and are a lower limit to the uncertainty in $\omega(\theta)$.

As an example we present the two-point angular correlation function of galaxies in our R-band reductions for 11 WFI-fields in the EIS Deep Public Survey (EIS DPS). For an exact comparison we use in this case 2000 linear bins which are logarithmically rebinned. It is known that the correlation function $\omega(\theta)$ can be approximated by a power law over a large range (see for instance Davis & Peebles 1983; Norberg et al. 2001; Zehavi et al. 2002, 2004).

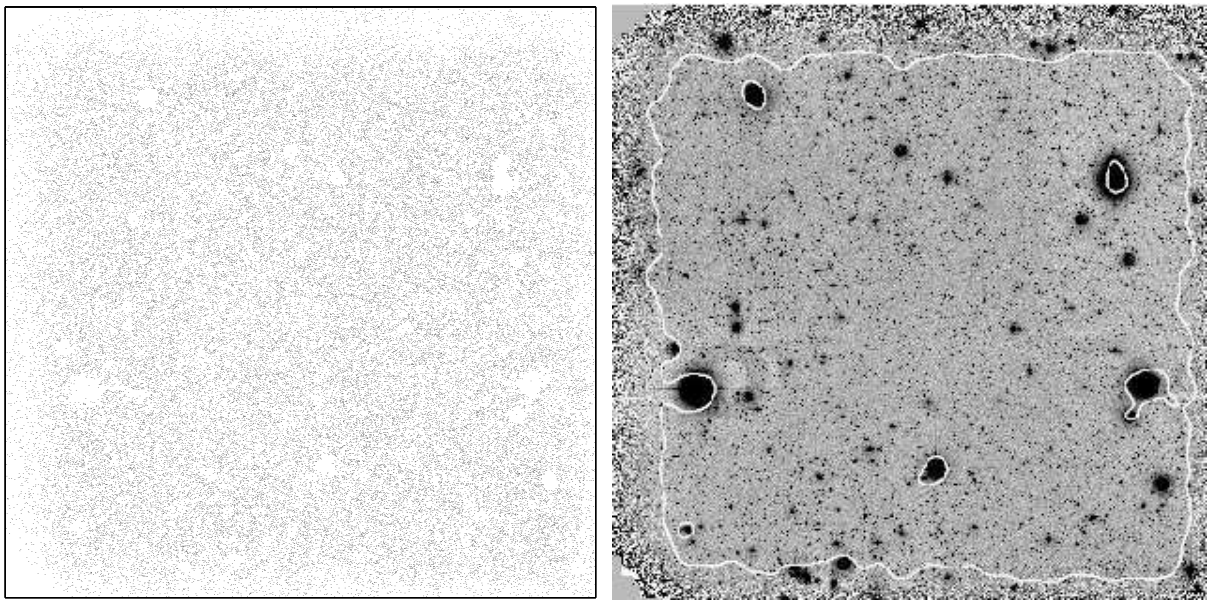

Figure 4.12: Obscuration mask for the CDFS. *Left panel:* Distribution of detected sources. *Right panel:* FITS image of the CDFS. White contours indicate masked region. In deep fields, our automatic obscuration mask based on object density variations reliably marks large-scale astronomical sources and noisy borders which would significantly influence the area of our correlation function analysis. This approach turned out to be sufficient for quality check purposes. Figure from Erben et al. (2005).

For three different magnitude bins we therefore fitted a power law, $\omega(\theta) = A_1\,\theta^{-\delta} - C$, to the data, where $A_1 = A(\theta = 1')$ is the clustering amplitude at $\theta = 1'$ and δ is the power-law index. The so-called integral constraint C (see for instance Groth & Peebles 1977; Roche et al. 1993) systematically reduces the angular correlation due to an uncertainty about the mean number density of sources, which is the larger the smaller the field under consideration. The integral constraint only becomes important for large fields at larger scales ($\theta > 2'$). We therefore neglect the integral constraint and perform the fit for small scales ($\theta < 2'$). The results are shown in Fig. 4.13.

The aperture number count dispersion $\langle N^2 \rangle$

The results from our clustering analysis can be cross-checked by considering the aperture number count dispersion $\langle N^2 \rangle(\theta)$. It is directly related to the angular correlation function $\omega(\theta)$ by

$$\langle N^2 \rangle(\theta) = \int \mathrm{d}\vartheta\, \frac{\vartheta}{\theta^2}\, \omega(\vartheta)\, T_+ \left(\frac{\vartheta}{\theta^2} \right), \tag{4.11}$$

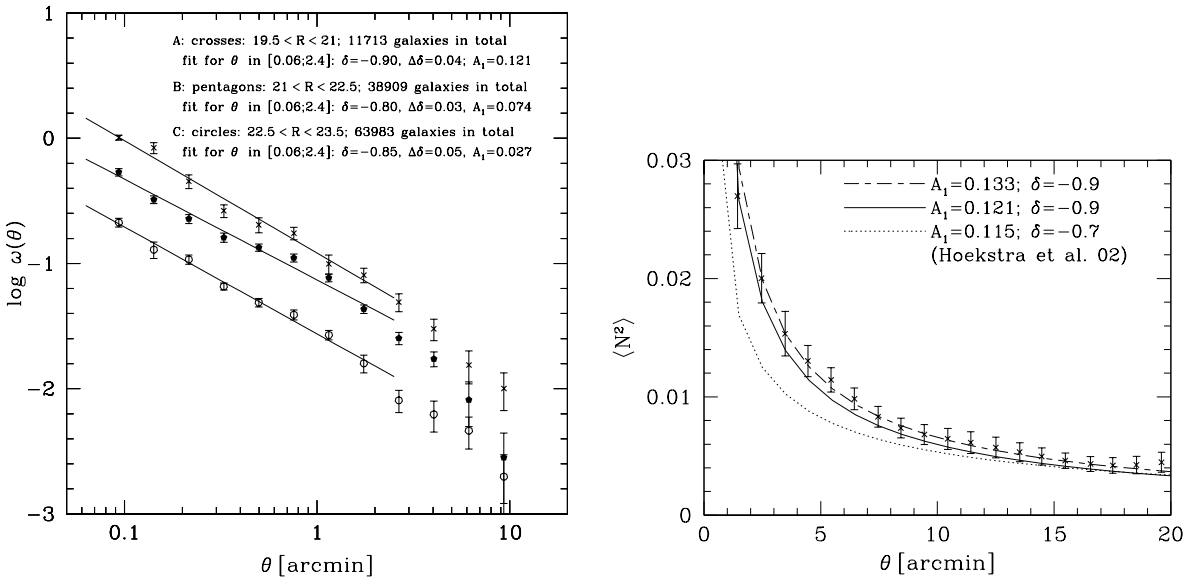

Figure 4.13: *Left panel:* the two-point angular correlation function of galaxies for different magnitude bins, for 11 R-band WFI-fields in the DPS. We show the logarithm of the amplitude, $\log\,\omega(\theta)$, as a function of the angular separation θ in arcmin. Here the error bar in each bin is due to the field-to-field variance. We perform a simple error-weighted linear regression in the angular interval $\theta \in [4'', 2'\,]$ (where the integral constraint is negligible) to determine the slope δ and the amplitude $A_1 = \omega(\theta = 1')$. *Right panel:* the aperture number count dispersion $\langle N^2_{\rm obs}\rangle(\theta)$ as a function of angular scale θ in arcmin for 11 WFI-fields in the magnitude interval $R \in [19.5, 21]$. The error bars on the function $\langle N^2\rangle(\theta)$ are due to the field-to-field variance of the 11 fields. Note that the points are correlated. The lines display the function $\langle N^2_{\rm fit}\rangle(\theta)$ assuming a power law for the angular two-point correlation function of the form $\omega(\theta) = A_1\,\theta^{-\delta}$ for different parameters $A_1 = \omega(\theta = 1')$ and δ. Solid line: $\langle N^2_{\rm fit}\rangle(\theta)$ calculated for the fit parameter obtained from the angular correlation function (see Fig. 4.13); dotted line: comparison with $\langle N^2\rangle(\theta)$ calculated for the fit parameters determined by Hoekstra et al. (2002a); dashed line: best fit to $\langle N^2\rangle(\theta)$. Figure from Erben et al. (2005).

where T_+ is given in Eq. (3.86). As pointed out by Hoekstra et al. (2002a) $\langle N^2\rangle$ has the nice property of being independent of the integral constraint C, because

$$C \int {\rm d}\vartheta\, \frac{\vartheta}{\theta^2}\, T_+\left(\frac{\vartheta}{\theta^2}\right) = 0. \tag{4.12}$$

To compare the slope δ and amplitude A_1 of the fitted power law to the measured $\omega(\theta)$ of the previous Section (Fig. 4.13), $\langle N^2\rangle(\theta)$ is calculated for the power law, $\omega(\theta) = A_1\,\theta^{-\delta}$ using Eq. (4.11). We obtain,

$$\langle N^2\rangle(\theta) = \int {\rm d}\vartheta\, \frac{\vartheta}{\theta^2}\, A_1\theta^{-\delta}\, T_+\left(\frac{\vartheta}{\theta^2}\right) = f(\delta)\, A_1\theta^{-\delta}, \tag{4.13}$$

where the function $f(\delta)$ can be approximated within a few percent accuracy for $\delta \in [0, 1.6]$ by

$$f(\delta) \approx 0.0051\delta^{11.55} + 0.2769\delta^{3.95} + 0.2838\delta^{1.25} \tag{4.14}$$

(Simon 2005). With this notion we estimate the clustering amplitude A_1 and the power law index δ of the correlation function $\omega(\theta)$ by fitting a power law $A_1'\theta^{-\delta}$ to the aperture number count dispersion $\langle N_{\rm obs}^2 \rangle(\theta)$ and by using the transformation $A_1 = A_1'/f(\delta)$.

As an example of the cross-check we use the measured $\omega(\theta)$ for the magnitude interval $R \in [19.5, 21]$ from the 11 WFI-fields of the last Section to calculate $\langle N_{\rm obs}^2 \rangle(\theta)$, see Fig. 4.13. The results show that the slope δ obtained from the power-law fit of the angular correlation function $\omega(\theta)$ is correct. The amplitude A_1, however, seems, with $A_1 = 0.121$, to be a bit smaller compared to the $\langle N^2 \rangle(\theta)$-fit; this small discrepancy can easily arise due to the fact that $\langle N_{\rm obs}^2 \rangle(\theta)$ is calculated using $\omega(\theta)$ over the entire θ-range and that the ω-fit is slightly influenced by the integral constraint. As a comparison, Fig. 4.13 displays the function $\langle N^2 \rangle(\theta)$ for the fit parameters determined by Hoekstra et al. (2002a) for $R_{\rm C}$-band data of the same magnitude range. Note that this can only be a rough comparison, because of different source extraction algorithms and slightly different R-band filter.

We performed these first quality checks on the co-added mosaics of the DPS. A comparison of the basic galaxy count test of the DPS with other surveys shows no significant deviation. The same is true for the check on the clustering of sources. Hence, the data quality of our co-added images is good.

Chapter 5

From measured surface brightness to unbiased shear estimates

Images of distant galaxies which are sheared due to the weak gravitational lensing effect are additionally distorted by telescope effects and the turbulent atmosphere of the Earth. In the first part of this Chapter we elucidate in detail these unwanted but unavoidable distortion effects of images observed with ground-based telescopes and answer the question of how gravitational shear estimates can be obtained from measured surface brightness of faint background galaxies. We therefore describe the so-called KSB method by Kaiser, Squires and Broadhurst (1995) and its improvement KSB+ by Luppino & Kaiser (1997) and Hoekstra et al. (1998) which we use to correct for PSF distortions and to obtain unbiased shear estimates. Then we describe its practical implementation, where we focus on the galaxy catalogue creation of the GaBoDS data set for the subsequent science application.

There are more methods in use to recover shear, for instance, the shapelets method by Refregier (2003) and Refregier & Bacon (2003), the Bernstein & Jarvis (2002) algorithm and im2shape by Bridle et al. (2001). Not only the methods are diverse, but also their practical implementation. The Shear TEsting Programme (hereafter: STEP), a collaborative project to improve the accuracy and reliability of all weak lensing measurements was therefore initiated in 2004 (first results can be found in Heymans et al. 2006a; Massey et al. 2006). We summarise in this Chapter some tests and comparisons of methods and their implementations of 16 different weak lensing groups.

This Chapter is organised as follows. First the distortions of the intrinsic surface brightness of an observed image by the telescope and atmosphere are described (Sect. 5.1). We then focus in Sect. 5.2 on the KSB algorithm to obtain unbiased shear estimates from noisy, pixelised galaxy images. We describe the practical implementation of the KSB algorithm in our weak lensing pipeline and the catalogue creation for our following cosmic shear analysis in Sect. 5.3. In Sect. 5.4 we discuss the most important results of STEP 1 and STEP 2 and the changes made to our pipeline due to the lessons we have learnt from STEP.

A large part of Sect. 5.3 has been published in Hetterscheidt et al. (2006), GaBoDS: The Garching-Bonn Deep Survey, VI. Cosmic shear analysis, astro-ph/0606571.

A part of Sect. 5.4 has been published in Heymans et al. (2006a), The Shear TEsting Programme 1: Weak lensing analysis of simulated ground-based observations, and Massey et al. (2006), The Shear TEsting Programme 2: Factors affecting high precision weak lensing analyses, astro-ph/0608643.

5.1 The point spread function

Light bundles of an observed point source (like a star) are never focused perfectly on a CCD chip. They get diffracted in the optical system of the telescope. The main reasons for this are the aperture of the telescope, the edges of the mirrors and the mounting supports of the secondary mirror. These diffraction images of point sources are called telescope 'point spread function' (hereafter: telescope PSF). A perfect telescope in space would then only be diffraction limited. In addition, the telescope PSF suffers from optical aberration: for instance the mirror deviates from the optimal parabolic form, or there is an offset between primary and secondary mirror compared to the optical axis, or the whole CCD chip is not in focus. For ground-based telescopes the light beam gets additionally distorted by turbulence and convective motions in the dome and telescope due to temperature gradients. These can produce a large and anisotropic telescope PSF. However, the major problem for ground-based observations is the atmosphere of the Earth. The atmosphere is not homogeneous, but consists of turbulence cells with different densities and therefore different refraction indices. A beam of light gets deflected by these moving atmospheric turbulence cells. The image of a star is therefore smeared to a disc on the time-integrating CCD chip. A two-dimensional Gaussian function is an adequate approximation of the intensity distribution on the CCD of the so-called seeing disc or (total) PSF. The full width at half-maximum (FWHM) of the PSF for good, stable atmospheric conditions at the best astronomical sites is of the order of one arcsecond or less.

Mathematically the distortion of images by these effects can be described as a convolution of the intrinsic surface brightness $I^{\rm intr}(\boldsymbol{\theta})$ of an object and the PSF $P(\boldsymbol{\theta})$ which describes the brightness distribution of a point source on the CCD. The observed surface brightness $I^{\rm obs}(\boldsymbol{\theta})$ of an arbitrary object is then given by

$$I^{\rm obs}(\boldsymbol{\theta}) = \int {\rm d}^2\vartheta\, I^{\rm intr}(\boldsymbol{\vartheta}) P(\boldsymbol{\theta}-\boldsymbol{\vartheta}). \tag{5.1}$$

The PSF P can be measured from stars as they are intrinsically point like, $I^{\rm intr}_{\rm star}(\vartheta) = \delta(\vartheta)$. It follows from Eq. (5.1) $I^{\rm obs}_{\rm star} = P$. As the typical size of faint background galaxy images used for weak lensing analyses is of the order of 0.5 arcsec, the size of the PSF should be at most equal to or less than 1 arcsec to correct for PSF distortions. Therefore the atmospheric conditions must be excellent for ground-based weak lensing studies in order to obtain reasonably good shear estimates from faint background galaxies. In Fig. 5.1 the images of the core of the galaxy M100 taken with a space (with and without optical aberration) and a ground-based telescope are compared and the effect of an imperfect optics and the influence of the atmosphere are nicely illustrated.

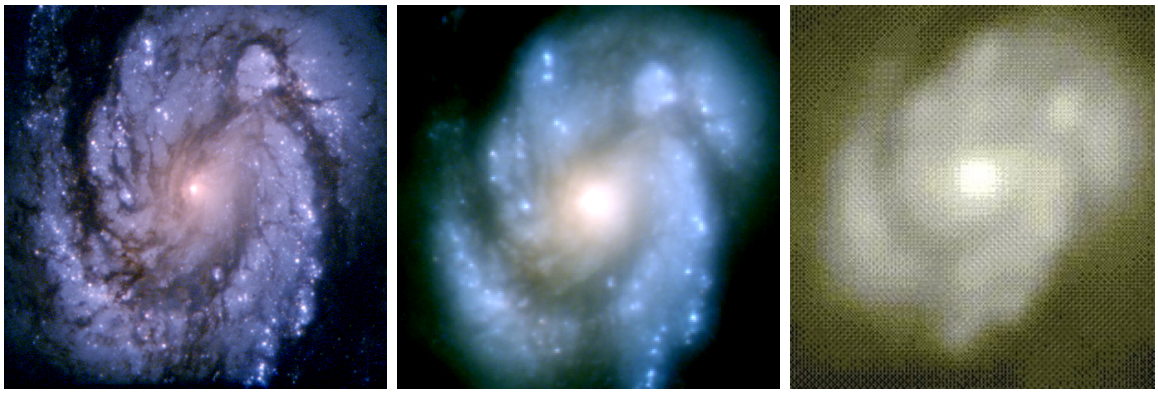

Figure 5.1: Influence of the telescope and atmospheric PSF on the image of the core of the galaxy M100. *Left:* image taken by the Wide Field Planetary Camera 2 (WFPC-2) of the Hubble Space Telescope (HST) in its high-resolution channel on December 31, 1993. The image was taken after the service mission to correct for optical aberration of the 2.4 m primary mirror. *Middle:* same image, but taken with the WFPC-1 of the HST in wide-field mode on November 27, 1993, a few days prior to the service mission. Clearly visible is the influence of the telescope PSF on the image (in this case an imperfect optic: optical aberration). *Right:* R-band image from the same region of M100 (a little rotated to the prior ones) taken with the Kitt Peak 2.1 m telescope with a seeing of one arcsecond. The strong influence of the smearing effect of the atmosphere on the galaxy image is clearly visible. Credit for the two left Figures: NASA, STScI (*http://hubblesite.org/newscenter/newsdesk/archive/releases/1994/01/*). Right Figure by Bill Keel of the University of Alabama (*http://www.seds.org/messier/more/m100_comp.html*).

5.2 Recovering gravitational shear

The influence of the PSF on the sheared image of a faint background galaxy is not the only problem that hampers the proper determination of the gravitational shear. Also the pixelisation of the CCD chips and the noise due to the sky background complicate the shape determination of mostly small-sized galaxy images (which often only comprise a few pixels, see Fig. 5.2). In this Section we therefore elucidate in detail how gravitational shear can be recovered from noisy, pixelised and PSF-influenced faint galaxy images.

5.2.1 The KSB algorithm

In principle, the PSF effects can be corrected for if the size and the shape of the PSF and its variation across the whole field-of-view can be measured and sampled properly. Kaiser, Squires & Broadhurst (hereafter KSB) developed in 1995 an algorithm which was significantly improved by Luppino & Kaiser (1997), to correct for PSF smearing and its anisotropy and to recover shear estimates from measured ellipticities. We give a thorough derivation of the KSB algorithm in App. A.

Within the framework of weak gravitational lensing, the shape of an object is usually

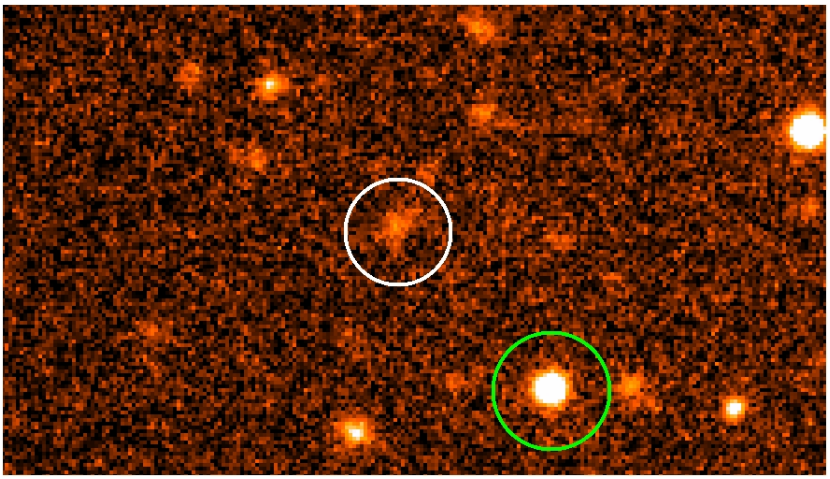

Figure 5.2: A typical clip of an image that is analysed. It shows noisy and pixelised images of faint galaxies (e.g., *left circle*), and a typical star for PSF anisotropy correction (*right circle*). Due to the sky background noise it is impossible to perform an easy deconvolution to obtain the lensed surface brightness.

described by its ellipticity χ,

$$\chi = \chi_1 + \mathrm{i}\chi_2 = \frac{Q_{11} - Q_{22}}{\mathrm{tr}\, Q_{ij}} + \mathrm{i}\frac{2Q_{12}}{\mathrm{tr}Q_{ij}}, \tag{5.2}$$

calculated from the quadrupole moments Q_{ij} of the surface brightness $I(\boldsymbol{\theta})$,

$$Q_{ij} = \int \mathrm{d}^2\theta\, (\theta_i - \bar{\theta}_i)(\theta_j - \bar{\theta}_j)\, I(\boldsymbol{\theta}), \tag{5.3}$$

where $\bar{\boldsymbol{\theta}}$ is the object centre.

The integral in Eq. (5.3) formally extends to infinity and is not applicable in practice, because the sky background noise will dominate the observed surface brightness $I^{\mathrm{obs}}(\boldsymbol{\theta})$ of the considered object at a given distance from its centre, or other objects will contribute to $I^{\mathrm{obs}}(\boldsymbol{\theta})$. Therefore a weighting function W is introduced which downweights the noise-dominated surface brightness several half-light radii away from the object centre. In the KSB algorithm the ellipticity parameter χ is calculated from weighted quadrupole moments,

$$Q_{ij} = \int \mathrm{d}^2\theta\, (\theta_i - \bar{\theta}_i)(\theta_j - \bar{\theta}_j)\, I(\boldsymbol{\theta})\, W\left(\left|\boldsymbol{\theta} - \bar{\boldsymbol{\theta}}\right|\right), \tag{5.4}$$

where we choose a Gaussian weighting function

$$W\left(\left|\boldsymbol{\theta} - \bar{\boldsymbol{\theta}}\right|\right) = \frac{1}{2\pi\sigma^2}\exp\left(-\frac{|\boldsymbol{\theta} - \bar{\boldsymbol{\theta}}|^2}{2\sigma^2}\right) \tag{5.5}$$

with a scale length σ equal to the half-light radius, r_h, of the object considered. The centre is defined as

$$\bar{\boldsymbol{\theta}} \equiv \frac{\int \mathrm{d}^2\theta\, W(\theta)\, \boldsymbol{\theta}\, I(\boldsymbol{\theta})}{\int \mathrm{d}^2\theta\, W(\theta)\, I(\boldsymbol{\theta})}. \tag{5.6}$$

For the following consideration we assume that the PSF P can be decomposed into an isotropic part P^iso which is defined as the azimuthal average over P and a small anisotropic part q,

$$P(\boldsymbol{\vartheta}) = \int \mathrm{d}^2\varphi\, q(\boldsymbol{\varphi}) P^\mathrm{iso}(\boldsymbol{\vartheta} - \boldsymbol{\varphi}), \tag{5.7}$$

where P^iso and q are normalised to unity (see Eq. A.5).

In the weak lensing regime the relation between the observed image ellipticity, the intrinsic ellipticity and the local reduced shear is given by (Sect. 3.1.3):

$$\chi^\mathrm{obs} = \chi^\mathrm{s} + 2\, g. \tag{5.8}$$

However, due to the weighting function introduced in the definition of the quadrupole moments (Eq. 5.4) the simple relation (5.8) no longer holds. It now reads

$$\chi^\mathrm{iso} = \hat{\chi} + P^\mathrm{sh}\, g, \tag{5.9}$$

where P^sh is the shear polarisability tensor, χ^iso is the observed ellipticity convolved with P^iso, and $\hat{\chi}$ is an ellipticity for which $\langle\hat{\chi}\rangle = 0$ still holds. The last statement is of course not obvious but part of the rather technical derivation of the KSB algorithm. We refer the reader to App. A, where we introduce the quantities χ^iso and $\hat{\chi}$ in a more proper way. The response of the image ellipticity on the anisotropy part of the PSF q is given by

$$\chi^\mathrm{iso} = \hat{\chi}^0 + P^\mathrm{sh}\, g + P^\mathrm{sm}\, q, \tag{5.10}$$

where P^sm is the smear polarisability tensor, and $\hat{\chi}^0$ is an ellipticity for which again $\langle\hat{\chi}^0\rangle = 0$ still holds (App. A). The smear polarisability tensor describes the isotropic smearing. Its size decreases for larger images since it is proportional to $1/\mathrm{tr}Q^\mathrm{obs}$ (App. A). This is expected because the ellipticities of larger images are less affected by a PSF anisotropy than those of smaller images. The smear polarisability also affects the shear polarisability in the following way:

$$P^\mathrm{sh} \quad \rightarrow \quad P^\mathrm{g} = P^\mathrm{sh} - P^\mathrm{sm}(P^{\mathrm{sm}*})^{-1} P^{\mathrm{sh}*}, \tag{5.11}$$

where $P^{\mathrm{sm}*}$, $P^{\mathrm{sh}*}$ are measured on stellar-sized objects. The quantity P^g can be interpreted as the response of the image ellipticity to the shear in the presence of the PSF smearing.

The final relation between the observed image ellipticity, the intrinsic ellipticity and the local reduced shear, including the effects of the weighting function and anisotropic PSF, is then given by

$$\chi^\mathrm{obs} = \hat{\chi}^0 + P^\mathrm{g}\, g + P^\mathrm{sm}\, q. \tag{5.12}$$

Note that $P^{\rm g}$ and $P^{\rm sm}$ in Eq. (5.12) are calculated from third- and fourth-order moments of the observed light distribution (App. A), hence from the data itself.

Assuming that the intrinsic orientation of galaxies is random we finally obtain an unbiased estimate of of the reduced shear g,

$$\langle g \rangle = \langle (P^{\rm g})^{-1} (\chi^{\rm obs} - P^{\rm sm} q) \rangle. \tag{5.13}$$

In order to apply relation (5.13), the anisotropy term q has to be known. It can be determined from the shape of stellar images. Since stars are point-like and unaffected by lensing, their isotropically smeared images have zero ellipticity. Hence, we obtain:

$$q^* = (P^{\rm sm*})^{-1}\, \chi^{\rm obs*}. \tag{5.14}$$

In general, the PSF is a function of image position, but can only be measured at the star position. However, the PSF correction has to be applied to galaxies. Assuming that the PSF varies smoothly over the total field-of-view, q can be determined for a set of stars, and approximated by a low-order two-dimensional polynomial across the data field. With this polynomial fit it is then possible to estimate the anisotropy kernel q by the value of the polynomial function at the position of galaxies.

In the weak lensing regime the reduced shear can be estimated by the shear, $\gamma \approx g$, so that Eq. (5.13) provides a noisy but unbiased estimate of the shear γ,

$$\gamma \approx (P^{\rm g})^{-1} \chi^{\rm aniso}, \tag{5.15}$$

where $\chi^{\rm aniso} = \chi^{\rm obs} - P^{\rm sm} q$ is the anisotropy-corrected ellipticity.

5.3 Catalogue creation & practical implementation of the KSB algorithm

The KSB algorithm is currently most widely used to obtain shear estimates from real data. However, different implementation of the algorithm give different results in shear estimates and therefore in the determination of cosmological parameters. In this Section we describe our catalogue creation, catalogue filtering, implementation of the KSB algorithm and weighting scheme. All these different steps are performed by a nearly fully automatic pipeline.

Raw catalogue

We utilise the programme `SExtractor` (Bertin & Arnouts 1996) to create a raw catalogue of objects (source galaxy candidates). The final co-added image is first smoothed with a Gaussian kernel of 2.5 pixel FWHM (FILTER_NAME: gauss_2.5_5x5.conv). Then objects are extracted which consist of at least $N = 5$ contiguous pixels (`SExtractor` parameter 'DETECT_MINAREA') with a flux greater than $k = 1.5\,\sigma$ above the sky level

noise (`SExtractor` parameter 'DETECT_THRESH'). With these rather conservative parameters we reduce the number of noise detections and increase the reliability of shape measurements. For the object detection the co-added WEIGHT image is taken into account as an additional `SExtractor` argument. It provides a full characterisation of the relative noise properties for each science image pixel and therefore lowers the probability to detect pure noise objects (see Sect. 4.2.4, Fig. 4.9 and Fig. 4.10). In addition, we set BACK_TYPE=MANUAL and BACK_VALUE=0 (our co-added images are sky subtracted). In this way `SExtractor` does not model halos around bright objects as sky background. It turns out that this effectively reduces spurious detections of objects in the proximity of bright stars or within their halos.

Calculation of quadrupole moments, Q_{ij} and centroid, $\bar{\boldsymbol{\theta}}$

The raw catalogue is transfered to the programme `analyseldac`, an adjusted version of N. Kaisers `imcat`, which measures the quadrupole moments of each object detected with `SExtractor`. Additionally, it calculates the object's centre, ellipticities, and tensors needed for the KSB algorithm (like $P^{\rm sm}$ or $P^{\rm sh}$). Due to pixelisation, the continuous integrals in Eqs. (5.4) and (5.6) are now transformed into discrete sums,

$$Q_{ij} = \sum_{|\theta-\bar{\theta}|<\theta_{\rm max}} \Delta\theta^2\,(\theta_i-\bar{\theta}_i)(\theta_j-\bar{\theta}_j)\,I(\boldsymbol{\theta})\,W\left(\left|\boldsymbol{\theta}-\bar{\boldsymbol{\theta}}\right|^2\right) \tag{5.16}$$

and

$$\bar{\boldsymbol{\theta}} = \frac{\sum_{|\theta-\bar{\theta}|<\theta_{\rm max}} \Delta\theta^2\,W(|\boldsymbol{\theta}-\bar{\boldsymbol{\theta}}|)\,\boldsymbol{\theta}\,I(\boldsymbol{\theta})}{\sum_{|\theta-\bar{\theta}|<\theta_{\rm max}} \Delta\theta^2\,W(|\boldsymbol{\theta}-\bar{\boldsymbol{\theta}}|)\,I(\boldsymbol{\theta})}, \tag{5.17}$$

where θ is measured, in pixel units, from the source centroid $\bar{\boldsymbol{\theta}}$. Note that we subdivide the pixel grid given by the camera into a four times finer pixel grid to obtain a more accurate description surface brightness by interpolation. Hence the quantity $\Delta\theta$ in Eq. (5.17) is given by $\Delta\theta = 0.25\,$pixel. The object centre $\bar{\boldsymbol{\theta}}$ is determined by iteratively solving Eq. (5.17), where the starting point is the `SExtractor` centroid. The scale in the Gaussian weighting function, W, is the half-light radius, $r_{\rm h}$, which we choose to be equal to the `SExtractor` parameter FLUX_RADIUS. The quadrupole moments, Q_{ij}, are calculated from all pixels for which $|\boldsymbol{\theta}-\bar{\boldsymbol{\theta}}| < \theta_{\rm max} = 3\,r_{\rm h}$. For non integer pixel values of the position $\boldsymbol{\theta}$, the surface brightness $I(\theta_i,\theta_j)$, known at pixel positions, is estimated from a linear interpolation over the four nearest pixels to (θ_i,θ_j).

PSF-anisotropy correction

As pointed out in Sect. 5.2.1, the anisotropy term q has to be known at the position of the galaxies in order to apply relation (A.59). For the PSF-anisotropy correction we utilise images of stars which are intrinsically point-like and unaffected by lensing, hence they trace the PSF (Eq. 5.1). All stellar images have almost the same half-light radius (corresponding to the half-light radius of the PSF) and therefore show up as a vertical

branch in a magnitude against half-light radius plot, see Fig. 4.11. Stars which have a brightness of $R = 0.5$ magnitudes fainter than saturated stars and which are well above the crowded faint magnitude region which contains a mixture of faint stars, galaxies and noise detections are selected. Using this sample of bright, unsaturated stars, we measure q^* with a Gaussian filter scale matched to the size of the galaxy image to be corrected. Hoekstra et al. (1998) proposed this matched PSF-anisotropy correction scheme for space-based data. It turned out in STEP 2 (Massey et al. 2006, Sect. 5.4.3) that this also improves the results for ground-based data.

In the case of the WFI@2.2m instrument the PSF anisotropy of the co-added images is rather small and varies smoothly over the total field-of-view. Discontinuities in the PSF anisotropy are largely absent across chip borders (demonstrated in Schirmer et al. 2003; Schirmer 2004; Erben et al. 2005). Hence, we utilise the programme `anisotropy` to perform a second- or third-order two-dimensional polynomial fit to q^* with $3.2\,\sigma$-clipping as a function of position over the entire field-of-view. The σ-clipping effectively excludes stars with very noisy shape measurements that do not trace the PSF anisotropy. With this fit it is possible to estimate the anisotropy kernel, q^*, at the position of the galaxies. A basic analysis of PSF anisotropy properties of the GaBoDS data set is given in Schirmer et al. (2006). Note that this anisotropy correction method is not perfect as the PSF is only measured at the position of stars, and a polynomial *interpolation* is used to estimate the PSF anisotropy at the position of galaxies. However, our fields comprises several hundreds to some thousands of stars used for the anisotropy correction, so that the PSF is sampled very well. As an example the anisotropy correction of the DPS field Deep3b is shown in Fig. 5.3.

For future cosmic shear analyses aiming at high precision constraints for cosmological parameters this PSF anisotropy correction method we apply must be improved. Recently Jarvis & Jain (2004) have introduced a promising correction algorithm, the so-called principal component analysis. With this method the dominant PSF anisotropy patterns are identified from a large number of exposures and are used to model the PSF. In this way, the PSF anisotropy correction does no longer depend on the number density of stars per field, but by the stacked number density of stars across all fields of the survey.

Calculation of $P^{\rm g}$

The $P^{\rm g}$ tensor calculated as in Eq. (A.57) is an extremely noisy quantity. The diagonal elements of all tensors with which $P^{\rm g}$ is calculated ($P^{\rm sh}$, $P^{\rm sm}$, $P^{\rm sh*}$, $P^{\rm sm*}$) are mostly dominant by a factor of 10 compared to the off-diagonal elements and they are approximately equal, so that we can estimate $P^{\rm g}$ by $P^{\rm g}_{\rm s}\mathbb{I}$, with $\mathbb{I}$ being the unit matrix, and

$$P^{\rm g}_{\rm s} = \frac{1}{2}\left\{\mathrm{tr}(P^{\rm sh}) - \frac{\mathrm{tr}(P^{\rm sh*})}{\mathrm{tr}(P^{\rm sm*})}\,\mathrm{tr}(P^{\rm sm})\right\}, \tag{5.18}$$

see Erben et al. (2001). De facto, in the absence of a PSF and weight function the elements of $P^{\rm g}$ would be: $P^{\rm g}_{11} = P^{\rm g}_{22} = 2$ and $P^{\rm g}_{12} = P^{\rm g}_{21} = 0$.

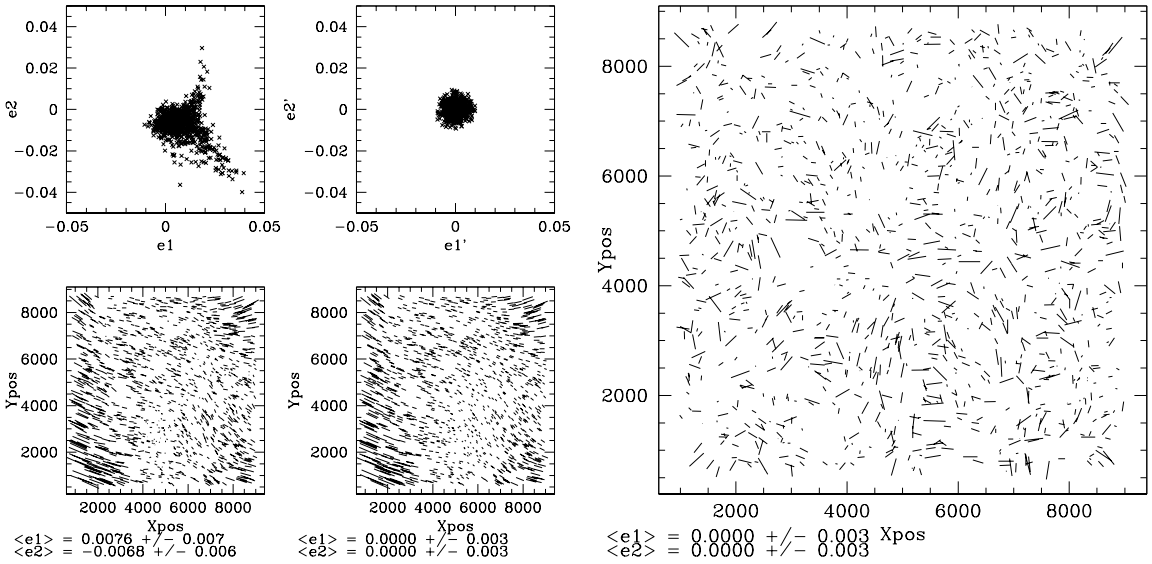

Figure 5.3: Example of a PSF anisotropy correction for field Deep3b. *Upper left panel*: the uncorrected ellipticity components, $e_\alpha = \chi^*_\alpha$, of stars are plotted against each other. Below this panel the uncorrected stellar ellipticity is shown as a function of position. *Upper middle panel*: the corrected stellar ellipticity components $e^{\rm corr}_\alpha = \chi^{\rm corr}_\alpha = {\rm tr}(P^{\rm sm*})\, q^*_\alpha$ are plotted. Below this panel the ellipticity values $e'_\alpha = \chi^{\rm poly}$ of the fitted polynomial at the position of stars are shown. For the anisotropy correction a low-order 2 D polynomial fit with a $3\,\sigma$ clipping has been performed over the whole field to 1179 stars with the following selection criteria: $r_{\rm h} \in [1.7, 2.1]$, $R \in [16.4, 20.6]$, and the edges are cut-off (Xpos $\in [1000, 9000]$, Ypos $\in [600, 8700]$). *Right panel*: residual ellipticity pattern of stars after anisotropy correction, $(e_\alpha - e^{\rm corr}_\alpha)$(Xpos, Ypos). The largest sticks are $\approx 1\%$.

The stellar smear and shear polarisability tensors $P^{\rm sm*}$ and $P^{\rm sh*}$ depend in practice on the choice of the smoothing scale, $\sigma = r^*_{\rm h}$, in the weight function (Hoekstra et al. 1998, App. A). We calculate them for a set of 10 different smoothing scales $r^*_{\rm h}$. The tensors $P^{\rm sm*}$ and $P^{\rm sh*}$ are then calculated for the closest match of the galaxy size, $r_{\rm h}$, with the smoothing scale, $r^*_{\rm h}$.

Additionally, the quantity ${\rm tr}(P^{\rm sm*})/{\rm tr}(P^{\rm sh*})$ varies smoothly over the total field-of-view. Although the variations across the field are small (at the $\pm 10\,\%$ level), it is not negligible for our aimed high precision cosmic shear analysis and should be taken into account. We therefore perform a fifth-order polynomial fit as a function of position to ${\rm tr}(P^{\rm sm*})/{\rm tr}(P^{\rm sh*})$. For $P^{\rm g}$ we finally use the raw, unsmoothed values because Erben et al. (2001) pointed out that fitting or calculating means does not improve the shear estimates.

However, as we will see in Sect. 5.4.2, the off-diagonal elements of $P^{\rm g}$ are not always much smaller than the diagonal elements. Neglecting them leads to an underestimation of the shear. Hence, our final shear estimate is given by $\gamma_{\rm corr} = \gamma / f_{\rm cal}$, where γ is calculated according to Eq. (5.15) and $f_{\rm cal} = 0.88$ is a calibration factor obtained from `skymaker` and

shapelet simulations (STEP 1 and 2).

Catalogue filtering

All objects for which problems concerning the determination of shape or centroid position occur are rejected (e.g., objects near the border, with negative total flux, with negative $Q_{11} + Q_{22}$, with negative semi-major and/or semi-minor axis, or when the iterative centroid determination is not stable after a given number of steps). In addition, we only use those objects with a half-light radius which is larger than that measured for stars. The raw, unsmoothed values of P^{g} are extremely noisy and can be close to zero or negative, so that the PSF-corrected galaxy images can have unphysical ellipticities. Therefore we reject all objects having a modulus of the ellipticity (after PSF correction) of more than 1.0.

To obtain a more homogeneous data set, with respect to the completeness of the object catalogue of individual fields, the raw background galaxy catalogues are compiled from objects in the `SExtractor` isophotal magnitude interval $R \in [21.5, 24.5]$. In this magnitude range we are confident to obtain reasonable photometric redshift estimates for most of the lensing galaxies in the individual DPS fields so that we have a reliable redshift distribution for all lensed galaxies. The mean of the redshift distribution is determined in Sect. 6.3.3 to be $\bar{z} = 0.78$. In the given magnitude range we obtain a number density of source galaxies of $n = 16\,\mathrm{arcmin}^{-2}$. However, if we take the weighting factor of individual galaxies (Eq. 5.19) into account, we obtain an effective number density of $n_{\mathrm{eff}} = 12.5\,\mathrm{arcmin}^{-2}$. We defined $n_{\mathrm{eff}} \equiv n \times w(R)/w(R = 21.5\,\mathrm{mag})$, with $w(R)$ being the magnitude dependent weighting factor. Since it is lower for fainter than for brighter galaxies, the effective number density n_{eff} is lower than the number density n.

In the left panel of Fig. 5.4 the galaxy number counts of the final GaBoDS catalogues are displayed for three different exposure time intervals. The distributions are approximately equal below $R < 24.5$, independent of the exposure time.

Weighting

Each shear value of a galaxy image is weighted according to its noise level in the following way. For each galaxy the next 12 neighbours are identified in the magnitude-half-light radius plane and the variance, σ_e^2, of the ellipticity distribution of this sub-sample is calculated (for more details about this technique see Erben et al. 2001). The variance, σ_e^2, gives an indication of the noise level of the galaxy's shear value. From σ_e^2 we then determine the weighting factor, w_i, as

$$w_i = \frac{1}{\sigma_e^2 + \bar{\sigma}^2}, \tag{5.19}$$

where $\bar{\sigma}^2 = 0.16$ is the variance of the unlensed galaxies (estimated from the total PSF-corrected galaxy sample). In the right panel of Fig. 5.4 the mean weighting factor is displayed as a function of magnitude. In comparison to Hoekstra et al. (2005) the average relative weight is almost the same in the given magnitude interval, although they use a completely different weighting scheme.

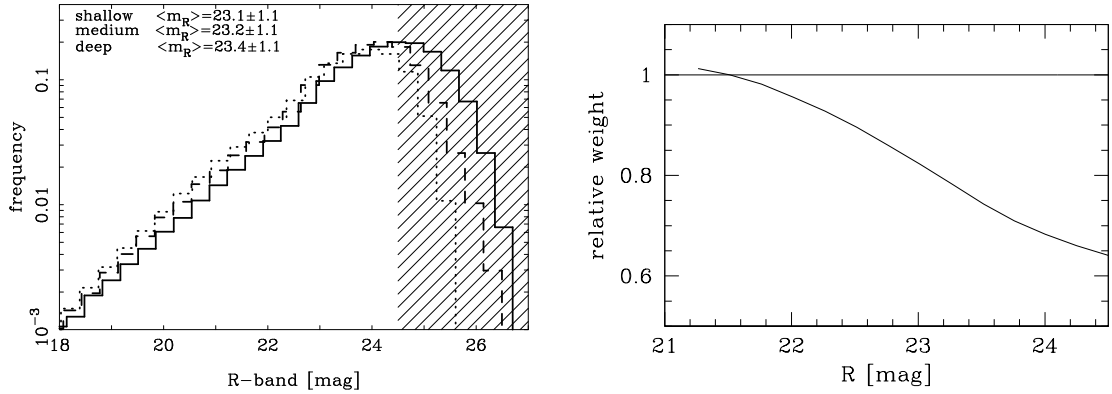

Figure 5.4: *Left panel:* galaxy counts in R-band magnitude of the GaBoDS for three different exposure time intervals. Solid line: deep ($10\,\mathrm{ks} < t < 56\,\mathrm{ks}$), dashed line: medium ($7\,\mathrm{ks} < t < 10\,\mathrm{ks}$), dotted line: shallow ($3.6\,\mathrm{ks} < t < 7\,\mathrm{ks}$). All distribution functions are normalised by area between $18 < R < 24.5$. Galaxies with $R > 24.5$ (shaded area) are not considered in this work. *Right panel:* average weighting factor calculated from all galaxies as a function of magnitude. The weighting factors are calculated with Eq. (5.19) such that galaxies with a magnitude of $R = 21.5$ have a weight of 1. Figure from Hetterscheidt et al. (2006).

5.4 STEP

Weak lensing by the LSS induces percent level correlations in the ellipticities of galaxies which are an order of magnitude lower than correlations induced by the anisotropic PSF. Therefore a precise PSF correction method has to be applied to the data to obtain reliable shear estimates, in particular with regard to future large surveys that will reduce the statistical error on shear measurements to the 2 % level and less. Since different PSF correction methods and their various implementations give different results in the shear estimates, the Shear TEsting Programme (henceforth: STEP) was initiated in order to compare weak lensing pipelines of different groups and to improve the accuracy and the reliability of future weak lensing measurements, see Heymans et al. (2006a).

In this Section we first give a summary of STEP 1, a blind test of ground-based `skymaker` simulations, in particular with regard to our weak lensing pipeline. We then describe the changes made to our pipeline to improve the shear estimate and show the impact on the STEP 1 results. In the end the results of STEP 2, a blind test of ground-based *shapelet* simulations (morphology of galaxies is more realistic compared to STEP 1) are presented.

5.4.1 STEP 1

We present in this Section the results of STEP 1, a blind analysis of synthetic `skymaker` images to recover the unknown shear, and discuss them in the view of our pipeline. This blind analysis has been performed by 13 different weak lensing groups using different PSF correction methods and different implementations of them. All groups and their imple-

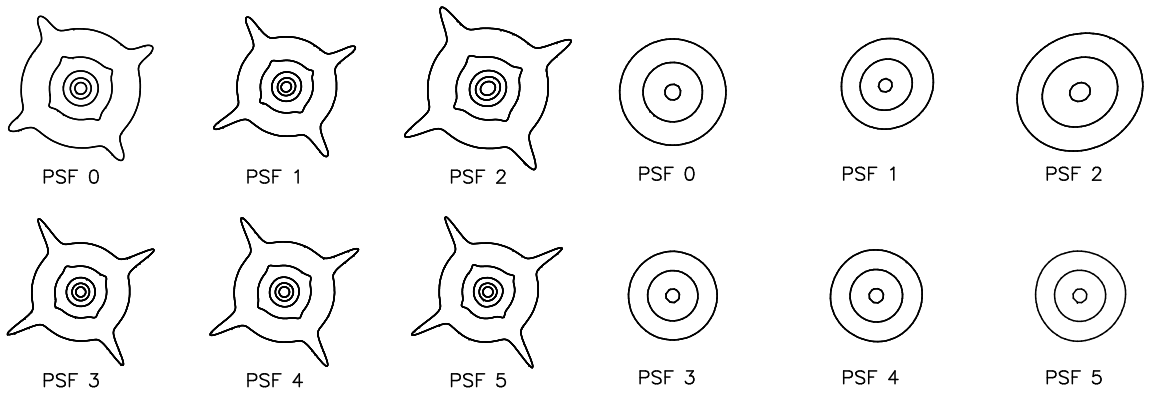

Figure 5.5: STEP 1 PSF models (see table 5.2). *Left panel:* Extended intensity contours of the PSF models; contour levels from outward to inward: 0.003 %, 0.03 %, 0.3 %, 3 % and 25 % of the peak intensity. *Right panel:* Core intensity contours of the different PSF models; contour levels from outward to inward: 3 %, 25 % and 90 % of the peak intensity. Figure from Heymans et al. (2006a).

mented methods are listed in table 5.1.

`Skymaker` simulations

For six different PSF models and five different applied shears, 64 images each were created. Each image has a size of 4096×4096 pixels. We used the programme `stuff` to create the input galaxy catalogue, and the programme `skymaker` to create the synthetic images. Both programmes have been developed by Emmanuel Bertin. A short description of these programmes can be found in Erben et al. (2001). The number density of galaxies $n_{\rm gal}$ and stars $n_{\rm star}$ in each image is approximately $n_{\rm gal} \approx 15\,{\rm arcmin}^{-2}$ and $n_{\rm star} \approx 10\,{\rm arcmin}^{-2}$, respectively.

The combination of 6 different PSF types and 5 different shears yields 30 different data sets. Within a data set, however, the sky noise level of the simulations, the position and morphology of each galaxy and the applied shear is constant for all 64 images. The applied shear values are as follows: $\gamma_1^{\rm true} = (0.0, 0.005, 0.01, 0.05, 0.1)$ and $\gamma_2^{\rm true} = 0.0$; the different PSF models are listed in table 5.2 and shown in Fig. 5.5. For each image the PSF is uniform over the entire field. For a more detailed description of the simulations we refer to Heymans et al. (2006a).

Calibration bias

All groups analysed the simulations without knowing the applied shear values beforehand (exception: LV who created the simulations and knew the input shear). In the following, the residuals of the measured shear γ_1 to the known input shear $\gamma_1^{\rm true}$ from a possible poor

Table 5.1: table of author (group), key and method. The methods and/or implementations are given in the cited papers, where KSB+ is an improvement of KSB by Hoekstra et al. (1998) and Luppino & Kaiser (1997). The average shear calibration bias (see below) is given in the columns named STEP 1 and STEP 2. The errors are the $1\,\sigma$ variance of the different PSF models and shear components. A short description of each method and implementation can be found in Heymans et al. (2006a).

Author (group)	Key	Method	STEP 1	STEP 2
J. Berge	JB	Shapelets		0.006 ± 0.047
		(Massey & Refregier 2005)		
Bridle & Hudelot	SB	Im2shape (Bridle et al. 2001)	-0.048 ± 0.027	
M. L. Brown	MB	KSB+ (Bacon et al. 2000)	-0.071 ± 0.015	
D. Clowe	C1	KSB+	-0.100 ± 0.018	-0.121 ± 0.048
	C2	KSB+	-0.084 ± 0.018	-0.077 ± 0.04
H. Dahle	HD	K2K (Kaiser 2000)	$+0.219 \pm 0.036$	
M. Hetterscheidt	MH	KSB+ (Erben et al. 2001)	-0.161 ± 0.014	$+0.034 \pm 0.031$
C. Heymans	CH	KSB+	-0.032 ± 0.028	
H. Hoekstra	HH	KSB+	-0.015 ± 0.006	-0.018 ± 0.018
M. Jarvis	MJ	Bernstein & Jarvis (2002)	$+0.002 \pm 0.027$	-0.017 ± 0.015
		Rounding kernel method		-0.015 ± 0.018
K. Kuijken	KK	Shapelets to 12^{th} order	-0.106 ± 0.021	-0.031 ± 0.016
		Kuijken (2006)		
R. Mandelbaum	RM	Reglens (Hirata & Seljak 2002)		-0.025 ± 0.021
V. Margoniner	VM	Wittman et al. (2001)	-0.164 ± 0.028	
R. Nakajima	RN	Bernstein & Jarvis (2002)	-0.011 ± 0.011	-0.045 ± 0.020
		Deconvolution fitting method		
Paulin-Henriksson	SP	KSB+		-0.089 ± 0.037
M. Schirmer	MS	KSB+ (Erben et al. 2001)		-0.157 ± 0.036
		with tensor		-0.041 ± 0.050
T. Schrabback	TS	KSB+ (Erben et al. 2001)	-0.167 ± 0.011	-0.017 ± 0.027
		+ modifications		
E. Sembolini	ES	KSB+		-0.163 ± 0.045
		+ modifications		$+0.031 \pm 0.072$
L. Van Waerbeke	LV	KSB+	-0.068 ± 0.025	

Table 5.2: The STEP 1 `skymaker` simulations are convolved with the given series of uniform PSF models. The PSF models are a realistic representation of PSF distortions seen in ground-based observations. The FWHM of all PSF types is 0.″9.

PSF	PSF type	Ellipticity
0	no anisotropy	0.00
1	coma	~ 0.04
2	jitter, tracking error	~ 0.08
3	defocus	~ 0.00
4	astigmatism	~ 0.00
5	triangular (trefoil)	0.00

PSF correction are analysed. For each group and PSF model the best fit parameters to

$$\Delta\gamma = \gamma_1 - \gamma_1^{\rm true} = q(\gamma_1^{\rm true})^2 + m\gamma_1^{\rm true} + c_1 \tag{5.20}$$

are determined. The fit parameter q is a measure for a possible non-linear response of the PSF correction method to the input shear. The linear dependence m of the PSF correction residual $\Delta\gamma$ on the input shear is, in the following, called calibration bias. If the PSF correction residual is a constant due to shot noise or PSF correction systematics, c_1 does not vanish. In the cases where q is close to zero a new, linear fit is performed. For all simulations $\gamma_2^{\rm true}$ is zero. Thus we calculate for all PSF models $c_2 = \langle\gamma_2\rangle$. For all groups the calibration bias m and the fit parameter q depend only weakly on the PSF model. Therefore the average calibration bias $\langle m\rangle$ and non-linear response $\langle q\rangle$ are calculated for all PSF models. The value of $\langle c_i\rangle$ is consistent with shot noise at the 0.1 % level for all groups, with the highest residuals measured for PSF type 1 and 2. As a measure of PSF correction systematics/residuals the variance $\sigma_{\rm c}^2$ of c_1 and c_2 is introduced.

The results are shown in the left panel of Fig. 5.6. All groups, except HD, underestimate the shear. In addition, RN, MJ and HD show a non-linear response of their method to the input shear. Even though most of the groups are using KSB+ the spread of shear estimates is quite large (between 2 % and 16 % underestimation).

In the following we focus on our pipeline; we refer to Heymans et al. (2006a) for a more detailed discussion of the results of the other groups. The calibration bias of our "old" pipeline used in STEP 1 is $\langle m\rangle = -0.161 \pm 0.014$, so we underestimate the shear by 16 % and the PSF systematics are $\sigma_{\rm c} = 0.0008$. Note that we described in Sect. 5.3 the modified pipeline used for our cosmic shear analysis. In table 5.4 we give a brief comparison between both.

Selection bias

The most important assumption in weak lensing is that the average unsheared source ellipticity $\langle e^{\rm s}\rangle$ is zero. Therefore we focus in this Section on the selection bias which can

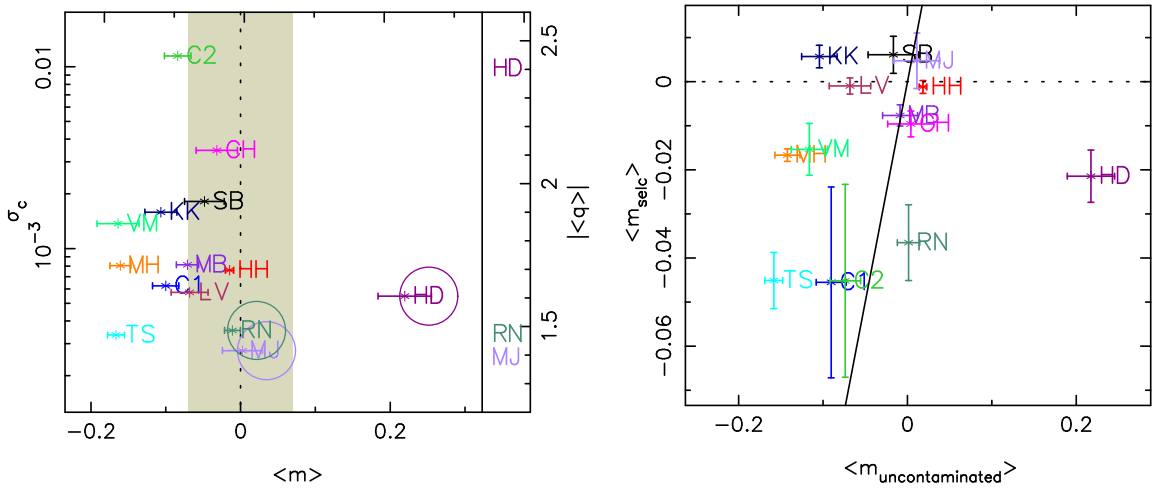

Figure 5.6: Overview of the calibration and selection bias of the different methods and implementations. *Left panel*: calibration bias $\langle m \rangle$, PSF residuals σ_c and non-linearity $\langle q \rangle$ for each author (keys see table 5.1). Points surrounded by a circle have a non-linear response on the used PSF-correction method, $q \neq 0$, and are separated by the vertical line. Points in the shaded area have less than 7 % calibration bias. All groups that measured cosmic shear resulting in cosmological parameters estimates before STEP 1 have a calibration bias of less than 7 %. *Right panel*: comparison of the selection bias $\langle m_{\rm selec} \rangle$ with the calibration bias obtained from a catalogue cleansed from false detections and stellar contamination, $\langle m_{\rm uncontaminated} \rangle$. Figure from Heymans et al. (2006a).

alter $\langle \epsilon^{\rm s} \rangle$. Selection bias can, for instance, arise from source extraction if the extracted galaxies are preferentially oriented in the same direction as the PSF anisotropy, see Kaiser (2000). Furthermore, selection criteria after source extraction can bias $\langle \epsilon^{\rm s} \rangle$ if the selection has a dependence on galaxy shape. To quantify the selection bias we measure $\langle \epsilon^{\rm s} \rangle$ from the galaxy sample cleansed from false detections. As in the last paragraph, we determine the best fit parameters for each author and PSF model to

$$\begin{aligned} \langle \epsilon_1^{\rm s} \rangle_{\rm selc} &= m_{\rm selc} \gamma_1^{\rm true} + c_1^{\rm s} \\ \langle e_2^{\rm s} \rangle_{\rm selc} &= c_2^{\rm s}. \end{aligned} \tag{5.21}$$

We calculate the mean $\langle m_{\rm selc} \rangle$ over the different PSF models as a measure of the shear-dependent selection bias, and the variance $(\sigma_c^{\rm s})^2$ of $c_1^{\rm s}$ and $c_2^{\rm s}$ as a measure of PSF anisotropy-dependent selection bias. The selection bias is displayed in the right panel of Fig. 5.6. For our pipeline the shear-dependent selection bias, $\langle m_{\rm selc} \rangle$, is small with $\approx 1.7\,\%$.

As in the last paragraph we now calculate, with Eq. (5.20), $\langle m_{\rm uncontaminated} \rangle$ using the shear catalogue cleansed of false detections and stellar contamination. For our pipeline the stellar contamination is 4 %, and there is no contamination of false objects, resulting in $\langle m_{\rm uncontaminated} \rangle = -0.142 \pm 0.015$. Comparing $\langle m_{\rm uncontaminated} \rangle$ with $\langle m \rangle$ obtained in the last paragraph, the impact of false detections and stellar contamination can be quantified

to $\langle m \rangle - \langle m_{\rm uncontaminated} \rangle = -0.02$, meaning that a small part of the calibration bias is due to stellar contamination.

In Fig. 5.6 the results are shown. We conclude that for many cases where the points do not fall on the 1 : 1 line (meaning $\langle m_{\rm selc} \rangle \neq \langle m_{\rm uncontaminated} \rangle$) the calibration bias does not solely result from a selection bias, as for our pipeline where $\langle m_{\rm selc} \rangle = -0.017 \pm 0.001$.

Weight bias

To obtain the weight bias $m_{\rm weight}$ we perform a linear fit to the difference of the unweighted average $\langle \epsilon_1^{\rm s} \rangle_{\rm selc}$ and the weighted average $\langle \epsilon_1^{\rm s} \rangle'_{\rm selc}$ as a function of input shear $\gamma_1^{\rm true}$,

$$\langle \epsilon_1^{\rm s} \rangle_{\rm selc} - \langle \epsilon_1^{\rm s} \rangle'_{\rm selc} = m_{\rm weight}\, \gamma_1^{\rm true} + c_1^{\rm w}. \tag{5.22}$$

For all groups the fitting parameter $c_1^{\rm w}$ is consistent with zero. All weighting schemes introduce a bias, but less than 4 %, so that the calibration bias is not solely due to the weight bias. However, our pipeline introduces a weighting bias of about 3 %, resulting from a weighting scheme that is not adequate for a constant shear.

5.4.2 Improvement of the pipeline

In this Section we describe the changes we have made to our pipeline to reduce the calibration bias.

Weighting

The weighting scheme used for the STEP 1 analysis, see Sect. 5.3, Eq. (5.23) is not applicable for a constant shear across the field and introduces the measured weight bias of 3 %. We therefore changed the weighting scheme to that proposed by Hoekstra et al. (2000). For bright and large galaxies the error on the shape measurement is dominated by the intrinsic ellipticity, for fainter and smaller galaxies the shot-noise increases the uncertainty in the shape determination. The weight w is the inverse of the variance of the shear estimate (5.15):

$$w = \frac{{\rm tr}^2(P^{\rm g})}{\sigma_\epsilon^2\, {\rm tr}^2(P^{\rm g}) + \langle \Delta\chi^2 \rangle} \tag{5.23}$$

where σ_ϵ^2 is the ellipticity dispersion of the corrected galaxies and $\langle \Delta\chi^2 \rangle = \langle \Delta\chi_1^2 + \Delta\chi_2^2 \rangle$ is the error on the observed ellipticity measurements,

$$\langle \Delta\chi_1^2 \rangle = \frac{1}{(Q_{11}+Q_{22})^2}[(1-\chi_1)^2\langle \Delta Q_{11}^2 \rangle + (1+\chi_1)^2\langle \Delta Q_{22}^2 \rangle - 2(1-\chi_1^2)\langle \Delta Q_{12}^2 \rangle] \tag{5.24}$$

and

$$\begin{aligned}\langle \Delta\chi_2^2 \rangle = \frac{1}{(Q_{11}+Q_{22})^2}[&\chi_2^2(\langle \Delta Q_{11}^2 \rangle + \langle \Delta Q_{22}^2 \rangle) + (4+2\chi_2^2)\langle \Delta Q_{12}^2 \rangle \\ &- 4\chi_2(\langle \Delta Q_{11}\Delta Q_{12} \rangle + \langle \Delta Q_{22}\Delta Q_{12} \rangle)].\end{aligned} \tag{5.25}$$

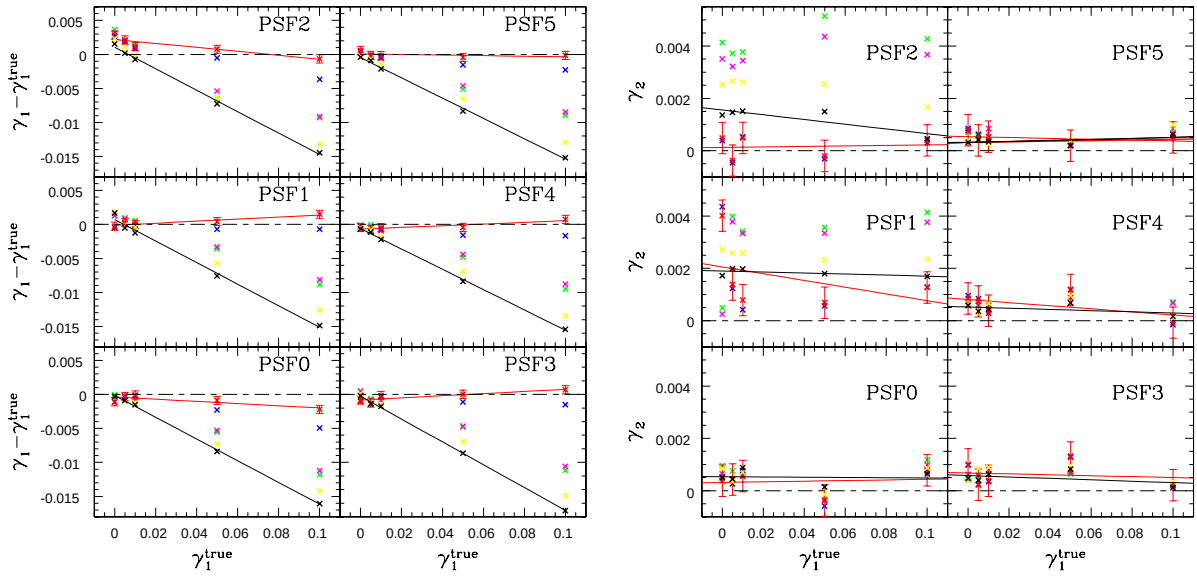

Figure 5.7: Shear estimates of γ_1 (*left*) and γ_2 (*right*) as a function of the input shear $\gamma_{1,2}^{true}$ for different PSF models and different implementations of the KSB-pipeline. Black crosses: 'old' pipeline used for the STEP 1 analysis. Yellow crosses: 'old' pipeline with a less conservative filtering of the final shear estimate: $|\gamma| < 1.0$. Green crosses: 'old' pipeline with the 'new' weighting scheme given by Eq. (5.23) and $|\gamma| < 1.0$. Pink crosses: 'old' pipeline with the new weighting scheme and $|\gamma| < 1.4$. Blue crosses: full tensor correction instead of using the trace of P^g, with $|\gamma| < 0.8$. Red crosses: full tensor correction, with $|\gamma| < 1.4$.

An outline of the derivation of Eqs. (5.23)-(5.25) is given in the Appendix of Hoekstra et al. (2000). With this 'new' weighting scheme the weighting bias in the STEP 1 analysis is zero.

Note that we use the weight given in Eq. (5.19) instead of Eq. (5.23) for our following cosmic shear analysis of the GaBoDS.

P^g calculation I

The calibration bias measured in STEP 1 is partly due to the weight and selection bias and due to contamination with pure noise objects and stars. We use the STEP 1 simulations to show how large the different effects for our pipeline are, see Fig. 5.7. Since we restricted the final shear estimate to $|\gamma| < 0.8$, it is definitely biased. Here γ is calculated with Eqs. (5.15) and (5.18). Changing the filtering to $|\gamma| < 1.0$ reduce the calibration bias from $\sim 16\,\%$ to $\sim 14\,\%$. Changing the weighting scheme from Eq. (5.19) to Eq. (5.23) the calibration bias decreases from $\sim 14\,\%$ to $\sim 11\,\%$. A further changing of the filtering to $|\gamma| < 1.4$ only mildly reduces the bias by about one percentage, however, it also increases the variance of the ellipticity distribution and thus the noise of the shear estimate. Despite the changes, we still underestimate the shear on average by about $11\,\%$. To correct for this

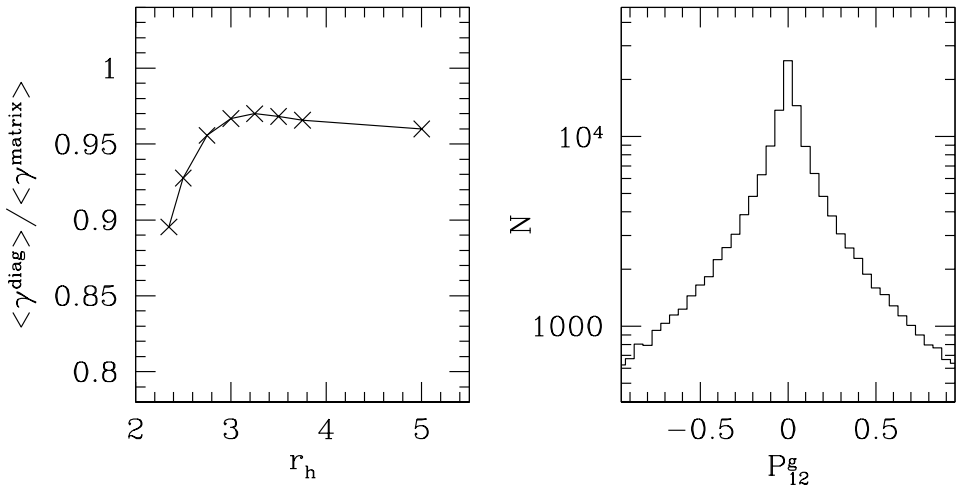

Figure 5.8: Full tensor correction versus trace correction (STEP 1 data set: PSF3, $\gamma = 0.1$). Note that the full tensor correction yields on average an unbiased estimate of the shear. *Left*: ratio of the average shear estimates obtained with the full tensor correction and the trace correction (see Eq. 5.27) as a function of half-light radius. Applying the trace correction results into an underestimate of the average shear. *Right*: Number count of the off-diagonal element $P^{\rm g}_{12}$ as a function of its value.

PSF independent robust underestimation of the shear, we introduce a calibration factor $c_{\rm f}$:

$$\gamma_{\rm corr} = \gamma / c_{\rm f}, \quad \text{with} \quad c_{\rm f} = 0.88. \tag{5.26}$$

P^g calculation II

As a different approach we do not use the trace estimation of P^g (see Eq. 5.18) but use the full tensor calculation to obtain unbiased shear estimates. The major part of the calibration bias vanishes when re-analysing the STEP 1 data set using the full tensor approach. If we restrict the shear estimates (the fully corrected ellipticities) to $|\gamma| < 0.8$ we still underestimate the shear, but only slightly $\langle m \rangle \approx -0.025$. If we use the filter $|\gamma| < 1.4$ the calibration bias vanishes totally. This result is not unexpected since $P^{\rm g}$ and its inverse have the following form:

$$P^{\rm g} = \begin{pmatrix} P^{\rm g}_{11} & P^{\rm g}_{12} \\ P^{\rm g}_{21} & P^{\rm g}_{22} \end{pmatrix}; \quad (P^{\rm g})^{-1} = \frac{1}{P^{\rm g}_{11}P^{\rm g}_{22} - P^{\rm g}_{12}P^{\rm g}_{21}} \begin{pmatrix} P^{\rm g}_{22} & -P^{\rm g}_{12} \\ -P^{\rm g}_{21} & P^{\rm g}_{11} \end{pmatrix}.$$

The shear $\gamma^{\rm matrix}$ is then

$$\gamma^{\rm matrix} = (P^{\rm g})^{-1}\chi = \frac{1}{P^{\rm g}_{11}P^{\rm g}_{22} - P^{\rm g}_{12}P^{\rm g}_{21}} \begin{pmatrix} P^{\rm g}_{22}\,\chi_1 - P^{\rm g}_{21}\,\chi_2 \\ P^{\rm g}_{11}\,\chi_2 - P^{\rm g}_{12}\,\chi_1 \end{pmatrix},$$

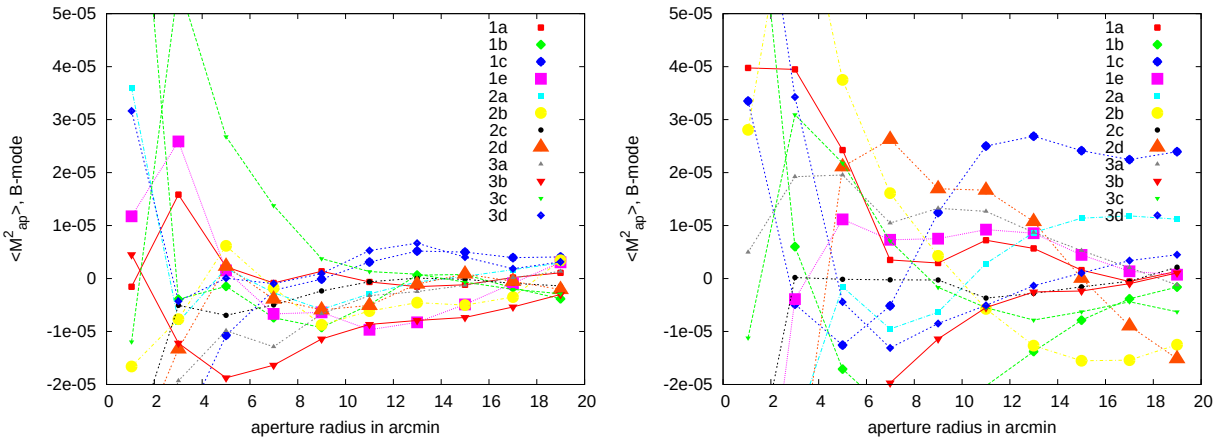

Figure 5.9: *Left panel*: B-modes of all DPS fields obtained from galaxies corrected with the trace of the $P^{\rm g}$ tensor, see Eq. (5.18). *Right panel*: B-modes from the same galaxies as in the left panel but corrected with the full $P^{\rm g}$ tensor. The full tensor correction introduces much more noise in the final result.

where χ is the anisotropy-corrected galaxy ellipticity. The shear $\gamma^{\rm diag}$, only calculated with the trace of $P^{\rm g}$, is given by

$$\gamma^{\rm diag} = \frac{2}{P^{\rm g}_{11} + P^{\rm g}_{22}} \begin{pmatrix} \chi_1 \\ \chi_2 \end{pmatrix}.$$

Since the expectation value of $P^{\rm g}_{12}$, $P^{\rm g}_{21}$ and χ_2 is zero, the ratio of $\langle\gamma_1^{\rm diag}\rangle$ to $\langle\gamma_1^{\rm matrix}\rangle$ is

$$\frac{\langle\gamma^{\rm diag}\rangle}{\langle\gamma^{\rm matrix}\rangle} = \frac{\sum_{i=1}^{N} 2/(P^{\rm g}_{11,i} + P^{\rm g}_{22,i})}{\sum_{i=1}^{N} P^{\rm g}_{22,i}/(P^{\rm g}_{11,i}P^{\rm g}_{22,i} - P^{\rm g}_{12,i}P^{\rm g}_{21,i})}, \tag{5.27}$$

where N is the number of galaxies. If $P^{\rm g}_{12}P^{\rm g}_{21}$ was much smaller than $P^{\rm g}_{11}P^{\rm g}_{22}$ and $P^{\rm g}_{11} \approx P^{\rm g}_{22}$, as assumed in Eq. (5.18), then the right-hand side of Eq. (5.27) would simply be unity and no bias would be present. However, this is not the case. We calculated the ratio given in Eq. (5.27) for a STEP 1 data set (PSF3, $\gamma = 0.1$), where the full tensor approach yielded on average an unbiased shear estimate. For most of the galaxies $P^{\rm g}_{12}$ and $P^{\rm g}_{21}$ are close to zero (right panel of Fig. 5.8). However, for a significant galaxy fraction the off-diagonal elements are of the same order of magnitude as the diagonal elements, hence the ratio in Eq. (5.27) is smaller than unity (left panel of Fig. 5.8). The shear is on average underestimated by about 5 % if the off-diagonal elements are simply not considered and the trace correction is used instead of the full tensor correction. For galaxies with smaller half-light radii, which are noisier, the shear is even more strongly underestimated (about 10 %). Since the full tensor correction unfortunately introduces much more noise in the final cosmic shear signal (Fig. 5.9) we do not use this approach henceforth.

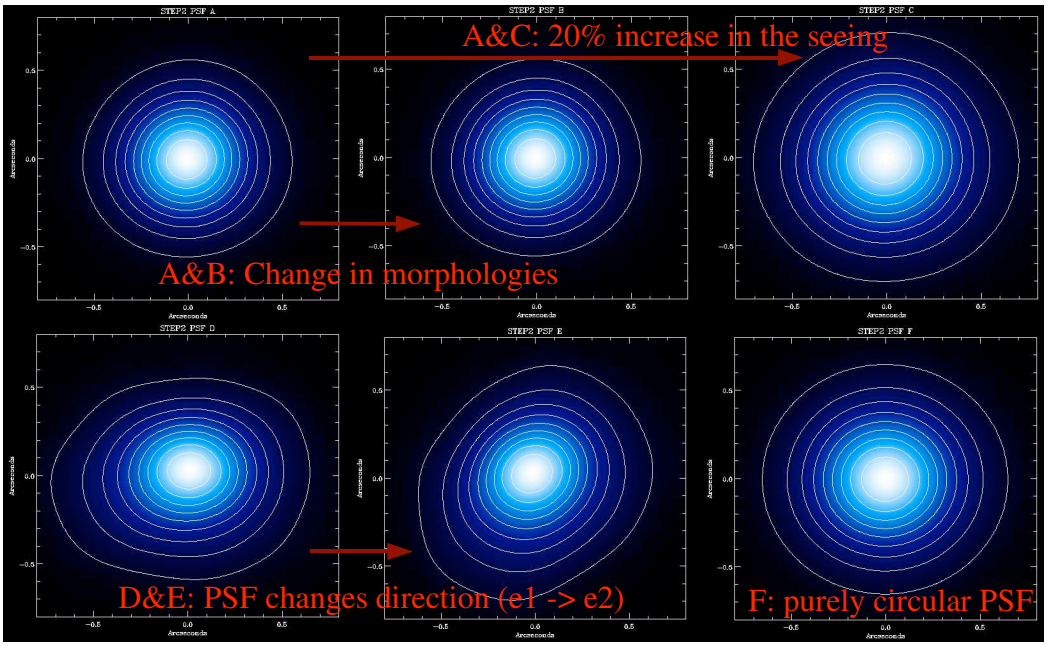

Figure 5.10: Intensity contours of the different PSF models of the STEP 2 simulations (see table 5.3). Figure from Massey et al. (2006).

5.4.3 STEP 2

In this Section we present the results of STEP 2, a blind analysis of synthetic shapelets images to recover the unknown shear, and discuss them in the view of our pipeline. This blind analysis has been performed by 12 different weak lensing groups using different shape measurement, PSF correction methods and different implementations of their methods, see table 5.1.

Shapelet simulations

For 6 different PSF models (see table 5.2 and Fig. 5.10), 128 2100 × 2100 pixel (the pixel scale is $0\farcs2$) images were created. The first image in each set is not sheared, the next 63 are sheared by a random amount chosen with a flat probability distribution function with $\gamma^{\mathrm{true}} \in [0, 0.06]$. Furthermore, in contrast to STEP 1, the orientation of the input shear relative to the pixel grid is random from image to image. The simulated images are very similar to deep r-band images taken under good seeing conditions with the Suprime-Cam camera of the Subaru telescope. They were created with a new version of the Massey et al. (2004) image simulation pipeline, where their morphology is much more complex in comparison to the `skymaker` galaxies since they include spiral arms, dust lanes and small-scale substructure. To keep the analysis of the simulations simple, the noise level, the input shear and the PSF do not vary as a function of position within an image.

However, to reduce the noise induced by the intrinsic ellipticity of galaxies, the sky is

Table 5.3: The *shapelet* simulations are convolved with this series of PSF models. The PSF models are a realistic representation of PSF distortions seen in ground-based observations (like the Subaru telescope).

Image set	PSF description	Galaxy type
A	typical Subaru PSF ($\approx 0\farcs6$)	shapelets
B	typical Subaru PSF ($\approx 0\farcs6$)	pure exponential
C	enlarged Subaru PSF ($\approx 0\farcs8$)	shapelets
D	elliptical PSF (aligned along x axis)	shapelets
E	elliptical PSF (aligned along $+45°$ direction)	shapelets
F	circularly symmetric Subaru PSF	shapelets

artificially rotated by 90° for the next 64 images before the galaxy images are convolved with the same PSF and sheared by the same amount as before. This procedure flips the sign of their intrinsic ellipticities. All 128 images in each data set are analysed independently to quantify the rms shear from different populations of galaxies. To obtain the calibration of shear measurement methods, we calculate the average of $\epsilon^{\rm obs}_{\rm unrotated} = \epsilon^{\rm intr} + \gamma^{\rm true}$ and $\epsilon^{\rm obs}_{\rm rotated} = -\epsilon^{\rm intr} + \gamma^{\rm true}$ from the unrotated and rotated version of a galaxy. The intrinsic shape noise $\epsilon^{\rm intr}$ cancels to first order so that we are left with measurement noise and possible biases in the shear estimations. For a more detailed description of the simulations we refer to Massey et al. (2006).

Calibration bias

As in STEP 1, all groups analysed the shapelet simulations without knowing the applied shear values beforehand. In the following, the residuals of the measured shear γ_1, γ_2 to the known input shear $\gamma_1^{\rm true}$, $\gamma_2^{\rm true}$ induced by a possible poor PSF correction are analysed. For each group and PSF model, the best fit parameters to

$$\langle\gamma_1\rangle - \gamma_1^{\rm true} = m_1\gamma_1^{\rm true} + c_1 \tag{5.28}$$

$$\langle\gamma_2\rangle - \gamma_2^{\rm true} = m_2\gamma_2^{\rm true} + c_2 \tag{5.29}$$

are determined, where $\langle\gamma_{1,2}\rangle$ is the mean shear measured within each image and $\gamma_{1,2}^{\rm true}$ is the input shear. Since the calibration bias is typically equal for the rotated and unrotated galaxy images, $m_i = (m_i^{\rm unrot} + m_i^{\rm rot})/2$ is calculated. For the residual shear calibration it is $c_i^{\rm rot} \approx -c_i^{\rm unrot}$, and we define $c_i = c_i^{\rm rot} - c_i^{\rm unrot}$. The total average calibration bias $\langle m\rangle$ and residual shear calibration $\langle c\rangle$ are calculated for both shear components and all PSF models.

The average result for all groups are shown in Fig. 5.11, where C1, SP, MS1 and ES1 are not plotted since their results are extremely off. Note that the size of both panels in that Figure corresponds to the size of the shaded region in Fig. 5.6. In addition, we give

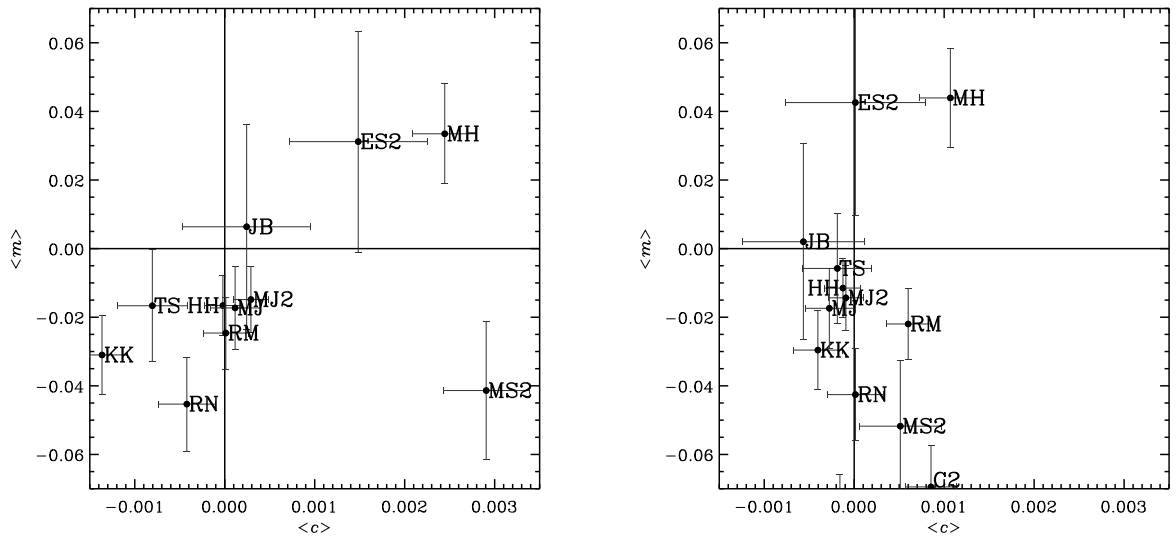

Figure 5.11: Overview of the shear calibration bias and PSF residuals of the different methods and implementations (keys see table 5.1). *Left panel*: calibration bias $\langle m \rangle$ and PSF residuals σ_c averaged over both shear components and all sets of images. *Right panel*: same as in the left panel but only averaged over PSF models A,B,C and F, to avoid the highly anisotropic PSFs. Figure from Massey et al. (2006).

$\langle m \rangle$ in table 5.1. All groups, except ES2 and us, underestimate the shear. The spread of shear estimates is significantly lower compared to STEP 1. The maximum shear calibration bias is less than 5 % for most of the groups (the bias in the analysis of C1, SP, MS1 and ES1 is much higher and is not considered here).

In the following we focus on our pipeline; we refer to Massey et al. (2006) for a more detailed discussion of the results of the other groups. In Fig. 5.12 we display our results of the calibration bias $\langle m \rangle$ and PSF residual c for each PSF model and shear component. We overestimate the shear most strongly (7.5 %) where the galaxy images type is a pure exponential. For the realistic galaxy types only the calibration bias is 2.5 %. The PSF residual is strongest for the anisotropic PSF models.

The calibration bias of the "old" pipeline used in STEP 1 (Sect. 5.4.1) was $\langle m \rangle = -0.161 \pm 0.014$, so we underestimate the shear by 16 %, and the PSF systematics were $\sigma_c = 0.0008$. After our changes we overestimate the shear by about (3.4 ± 3.1) % ($1\,\sigma$ variance of the different PSF models and shear components). Considering only the realistic galaxy types the bias is reduced even more, down to 2.5 %. Note, however, that for every PSF model the bias should vanish and not only the average bias. Only if there is no bias in the shear estimate for any "artificial" PSF we can hope that shear estimates in "real" data influenced by "real" PSFs are unbiased!

Bias dependence on magnitude and shapelet size

Up to now we only considered the mean shear from a large population of galaxies within a PSF model. However, it is possible to measure the mean shear correctly, but to underestimate or overestimate the shear in different populations. For weak lensing analyses different populations are often created from galaxies within different magnitude and size bins to exclude noisy objects and to obtain redshift distributions with different mean redshifts. The STEP 2 results reveal a shear calibration bias that depends strongly on the magnitude of galaxies and mildly on their size, independent of the image set and shear component: the fainter and smaller the galaxy images the more the shear is underestimated (Fig. 5.13). Especially for galaxies with $mag > 15$ the shear is strongly underestimated. This strong deterioration of the shear estimate is observed with all KSB implementations and other methods that are otherwise robust (Massey et al. 2006). A reason could be the strong measurement noise for faint and small galaxy images which is additionally blown-up during the non-linear correction process. A further reason for the gradual magnitude trend of the shear calibration bias might be caused by the evolution of the intrinsic morphology distribution as a function of redshift. This trend is least pronounced for image set B in which the galaxy ellipticities do not evolve.

The bias dependence on magnitude is a serious problem since cosmic shear analyses not only rely on unbiased shear estimates but also on unbiased redshift distributions. Fainter galaxies have a higher mean redshift, hence they are sheared more strongly. However, if the shear estimate of faint galaxies is biased, the effective redshift distribution of source galaxies is also altered. Especially for shear tomography analyses (shear cross-correlation analyses of galaxies in different redshift bins), aiming at revealing the LSS of the Universe as a function of redshift, magnitude dependence will be a serious problem. Hence the causes of the strong magnitude trend must be studied in more detail with further, more simple STEP simulations.

For most of the image sets the PSF residuals show no clear magnitude dependence. However, for the image sets D and E, which are anisotropically distorted, this is not the case. For image set D and E the PSF residuals of γ_1 and γ_2 are smaller for larger shapelet sizes since smaller galaxies are more affected by a PSF anisotropy (Sect. 5.2.1).

A further improvement of the pipeline: $P^{\mathrm{sm}*}$ and $P^{\mathrm{sh}*}$ correction.

The pipeline used by TS (Schrabback et al. 2006) and ours are based on the KSB+ implementation of Erben et al. (2001). The main difference is the measurement of the anisotropy kernel q. Since the PSF residuals are significantly higher for the anisotropic PSF models in our case we change it to that implemented by TS: We now measure q^* with a Gaussian filter scale matched to the size of the galaxy image to be corrected and not with a fixed filter scale (Sect. 5.3).

A further difference is the $P^{\mathrm{sm}*}/P^{\mathrm{sh}*}$-correction. Before the anisotropy correction is performed we calculate the diagonal elements of $P^{\mathrm{sm}*}/P^{\mathrm{sh}*}$ from a number of stars selected from the $mag - r_{\mathrm{h}}$ plot (Fig. 4.11). They show a mild dependence on field position. We

Table 5.4: A brief comparison between the modified and "old" pipeline. Both pipelines are based on the KSB algorithm outlined in the text. The changes made to the pipeline are based on results given in Heymans et al. (2006a) and Massey et al. (2006). Key: †: this changes were made after STEP 2. ‡: the quantity γ is the final shear estimate calculated with Eqs. (5.15) and (5.18).

modified pipeline	"old" pipeline
anisotropy measurement†: q^* matched with a Gaussian filter scaled to the size of the galaxy image to be corrected	fixed Gaussian filter scale
$P^{\rm g}$ correction†: $P^{\rm sm*}/P^{\rm sh*}$ matched with a Gaussian filter scaled to the size of the galaxy to be corrected + polynomial fit to $P^{\rm sm*}/P^{\rm sh*}$ as a function of position.	fixed Gaussian filter scale no interpolation
cuts: $\lvert\gamma\rvert < 1.0^{\ddagger}$ $\mathrm{tr}[P^{\rm g}] > 0.05$	 $\lvert\gamma\rvert < 0.8^{\ddagger}$ $\mathrm{tr}[P^{\rm g}] > 0$
calibration factor $\gamma_{\rm corr} = \gamma/0.88$	No calibration factor

therefore measure the diagonal elements of $P^{\rm sm*}/P^{\rm sh*}$ for different filter scales $r_{\rm h}$ and perform a fourth-order two-dimensional polynomial fit to $P^{\rm sm*}/P^{\rm sh*}$ as a function of position. With the polynomial fit it is possible to calculate $P^{\rm sm*}/P^{\rm sh*}$ at the position of galaxies. However, an improvement of the shear estimate due to the changed $P^{\rm sm*}/P^{\rm sh*}$ calculation can unfortunately not be tested in detail with STEP 1 & 2, because the PSF pattern of the simulations are constant over the field-of-view.

In table 5.4 a brief overview of the pipeline prior STEP 1 ("old" pipeline) and after STEP 2 (modified pipeline, used for the catalogue creation) is given.

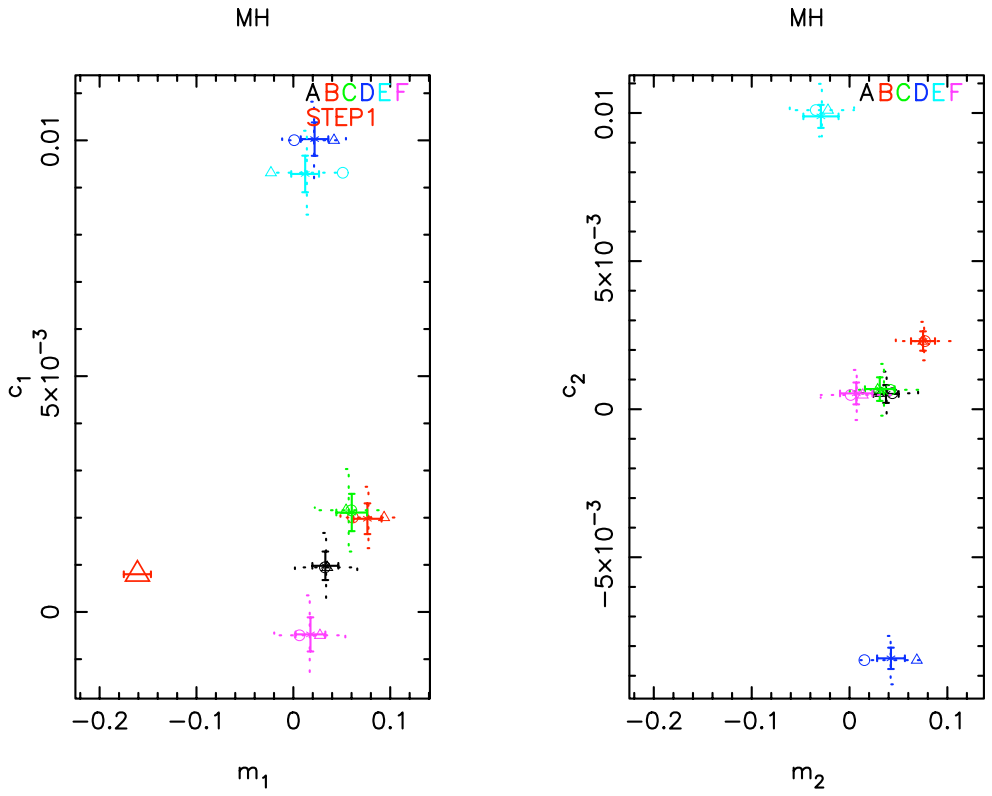

Figure 5.12: Calibration bias $\langle m \rangle$ and PSF residual c for each PSF model and shear component. Image set A: the shear is overestimated by 3.7 % ($3\,\sigma$) for both components. Image set C: the γ_1 component is slightly overestimated by 3.4 % ($2\,\sigma$) but γ_2 is stronger overestimated by 3.4 % ($4\,\sigma$). Image set B: the shear is strongly overestimated by 7.7 % ($6\,\sigma$). Image set D: the γ_1 component is overestimated by 2.5 % ($2\,\sigma$) and γ_2 by 4.6 % ($3\,\sigma$). Image set E: there is no significant calibration bias of γ_1 but a slight underestimation of γ_2 by 2.9 % ($1.5\,\sigma$). Image set F: no significant calibration bias. The PSF residuals are negligible for all image sets but D and E (both highly anisotropic): in both the PSF residuals of γ_1 are strongly positive with $c_1 \approx 0.01$. The PSF residual of γ_1 in image set E is strongly positive with $c_1 \approx 0.01$ but strongly negative for image set D. Figure by R. Massey and C. Heymans.

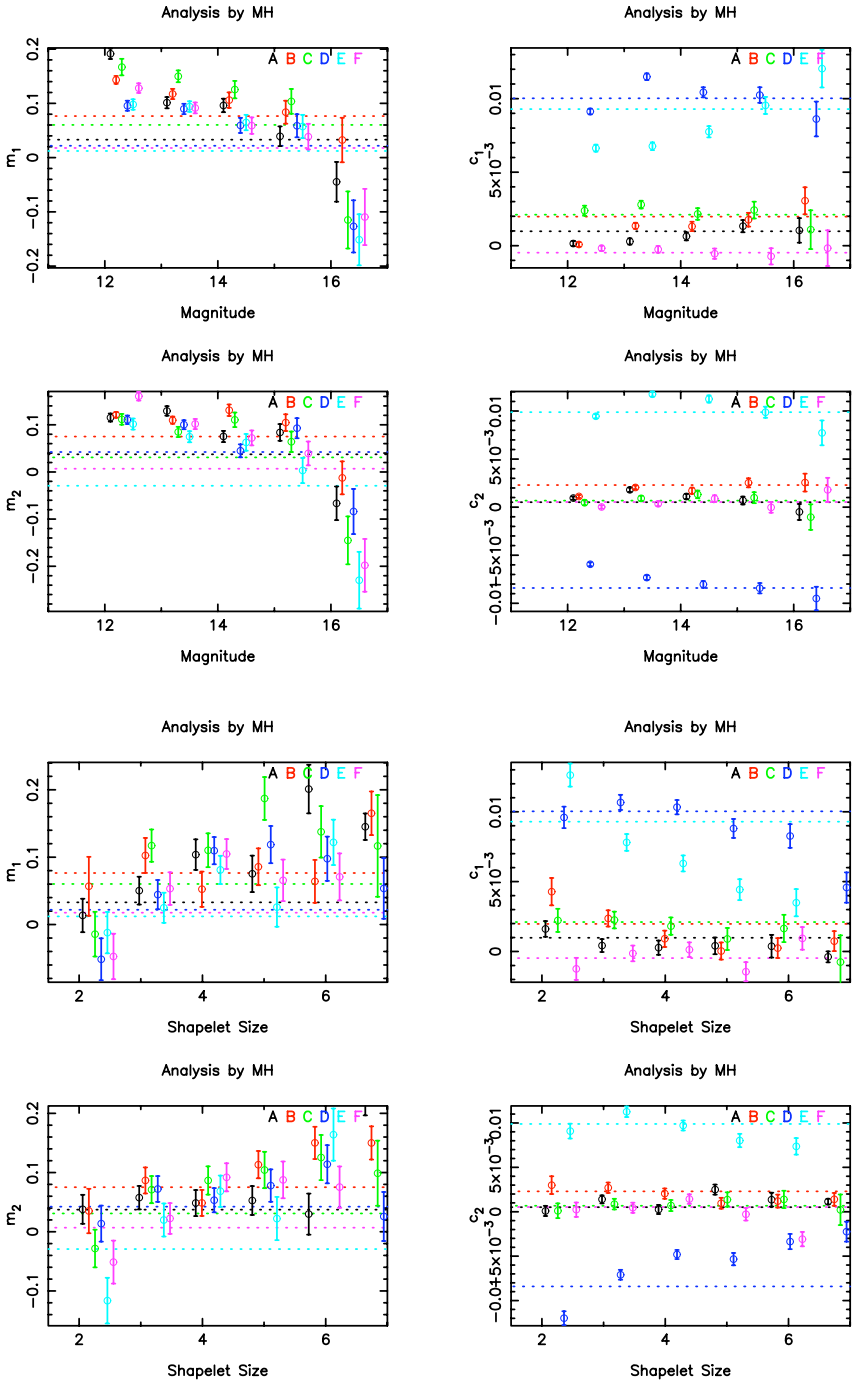

Figure 5.13: Shear calibration bias and PSF residuals as a function of magnitude and shapelet size (size of the galaxy image). Magnitude and shapelet size are in arbitrary units. The shear calibration bias strongly depends on the magnitude, independent of the image set and shear component: the fainter the galaxies the more the shear is underestimated. For the PSF residuals there is no clear magnitude dependence visible. The dependence of the calibration bias on shapelet size is not so pronounced as it is for the magnitude dependence. For most of the PSF models the calibration bias is slightly higher for larger shapelet size independent of the shear component. For the image sets D and E (they are strongly anisotropic) the PSF residuals of γ_1 are smaller for larger shapelet sizes, and for image set D vice versa. Figure by R. Massey and C. Heymans.

Chapter 6

Cosmic shear analysis

Measuring cosmic shear is a powerful way to explore the statistical properties of the LSS of the Universe. Since cosmic shear is independent of any assumptions on the relation between dark and luminous matter it has become an important tool to measure cosmological parameters. In particular, the cosmic shear signal is sensitive on the amplitude of density fluctuations of the LSS which is mainly characterised by the matter density $\Omega_{\rm m}$ and the mass power spectrum normalisation σ_8.

It has only been in recent years that groups have begun to use this method. The first cosmic shear measurements were published in the beginning of 2000 (Bacon et al. 2000; Van Waerbeke et al. 2000; Kaiser et al. 2000; Wittman et al. 2000). Although some constraints on cosmological parameters were obtained from these measurements, their statistical errors (due to the small areas of the surveys $\sim 1\,\mathrm{deg}^2$) and systematic errors were large. More recently, several groups have published cosmic shear analyses of larger survey areas ($\sim 10\,\mathrm{deg}^2$) and/or deeper fields to obtain smaller statistical errors. Additionally, they discuss the influence of systematic errors on the cosmic shear signal (e.g. Maoli et al. 2001; Van Waerbeke et al. 2001, 2002, 2005; Rhodes et al. 2001, 2004; Refregier et al. 2002; Hamana et al. 2003; Bacon et al. 2003; Hoekstra et al. 2002b; Brown et al. 2003; Massey et al. 2005; Jarvis et al. 2003, 2005; Heymans et al. 2005).

We are now entering a new phase of wide-field surveys which are wider and/or deeper so that systematic errors may begin to dominate over statistical errors. The validity of results from cosmic shear surveys depends strongly on the treatment of systematic errors. Many groups have therefore been working on the problem of reducing systematic errors in cosmic shear measurements and have presented its impact on cosmological parameter estimates. Hoekstra (2004) and Van Waerbeke et al. (2005) discussed the influence of an imperfect PSF-anisotropy correction on the cosmic shear signal. The impact of the redshift distribution sampling error has recently been studied by Ma et al. (2006) and Van Waerbeke et al. (2006). A further, more fundamental, source of bias is the correlation between the weak gravitational shear of distant galaxies and the intrinsic shape of foreground galaxies (e.g. Hirata & Seljak 2004; Heymans et al. 2006b). In addition, the STEP project discussed in Sect. 5.4 has been initiated in mid 2004 (first results in Heymans et al. 2006a).

In this Chapter we first present the results from a test of our pipeline using synthetic

images. Specifically we present the influence of the changes we have made to it on the cosmic shear signal due to the lessons we have learnt so far from STEP. We then present a cosmic shear analysis and data validation of the Garching-Bonn Deep Survey in the magnitude interval $R \in [21.5, 24.5]$. We measure the two-point shear correlation functions to calculate the aperture mass dispersion, and apply both statistics and further tests to the data set to check for possible systematic errors. In contrast to many other cosmic shear surveys we measure the redshift distribution from *lensing* galaxies from $1.75\,\mathrm{deg}^2$ of *UBVRI*-band data of the DPS, a sub-sample of GaBoDS and not from an external redshift sample. Combining the cosmic shear signal with the measured photometric redshift distribution we determine constraints for the matter density Ω_m, the mass power spectrum normalisation σ_8 and the dark energy density Ω_Λ. As a result we obtain $\sigma_8 = 0.80 \pm 0.10$ ($1\,\sigma$ statistical error) for $\Omega_\mathrm{m} = 0.30$ assuming a flat Universe with negligible baryon content and marginalising over the Hubble parameter and the uncertainties in the fitted redshift distribution. Finally, we discuss several possible sources of systematic errors in the results of our cosmological parameter estimate.

This Chapter is organised as follows. We present tests of our pipeline by analysing synthetic images in Sect. 6.1. In Sect. 6.2 we elucidate in detail the different tests on the systematics in our data. In Sect. 6.3 we give the results from our cosmic shear analysis and present the cosmological parameter estimates. For that we employed the so-called Monte Carlo Markov Chain (MCMC), an efficient technique to estimate the posterior likelihood. In addition, we discuss several possible sources of systematic errors.

A large part of this Chapter has been published in Hetterscheidt et al. (2006), GaBoDS: The Garching-Bonn Deep Survey: VI. Cosmic shear analysis, astro-ph/0606571.

6.1 Cosmic shear analysis of synthetic images

In this Section we present the results from tests of our pipeline. For simplicity we divide our pipeline into two parts: (1) the part concerning the PSF correction and shear estimate (Sect. 5.3) and (2) the part which measures the two-point correlation function and calculates the aperture mass dispersion (Sect. 3.2.3). In addition, we investigate the impact of the changes we have made to part (1) of our pipeline (see table 5.4) on the cosmic shear signal due to the lessons we have learnt so far from STEP (Sect. 5.4).

We perform a cosmic shear analysis of twelve synthetic WFI sized images created from ray tracing through ΛCDM N-body simulations ($\Omega_\Lambda = 0.7$, $\Omega_0 = 0.3$, $\sigma_8 = 0.9$, $h = 0.7$) using the E- and B-mode decomposition of the M_ap-statistics (Sect. 3.2.2). These simulations were kindly made available by Takashi Hamana [details see Hamana et al. (2004)]. We create twelve initial catalogues of randomly distributed galaxies using the programme `stuff`[1] (E. Bertin). The galaxies are assumed to be at a fixed redshift $z = 1$, and are sheared according to the shear map of the ray-tracing simulations. In the following these galaxy catalogues are called *input catalogues*.

[1] Available at: http://terapix.iap.fr/cplt/oldSite/soft/stuff/

The input catalogues are used to create synthetic images using the programme `skymaker`[2] by E. Bertin. A short description is given in Erben et al. (2001). Twelve $30' \times 30'$ images resulting in a $3\,\mathrm{deg}^2$ survey are obtained for the twelve input catalogues. These images are treated in exactly the same way as real data (like object detection, PSF correction, same cuts, weighting), see Sect. 5.3. The resulting galaxy catalogues are called *output catalogues*.

To exclude the effect of false detections we only take into account those objects which are present in both, input and output catalogues. To obtain a similar number density in comparison to the real data we perform a similar magnitude cut: $mag \in [21.5, 24.5]$. The mean ellipticity dispersion of the galaxies of the input and output catalogues is $\sigma_\epsilon = 0.32$ and the mean galaxy number density is $n = 15\,\mathrm{arcmin}^{-2}$. For a more detailed description of the image creation, galaxy morphology and magnitude distribution we refer the reader to Hetterscheidt et al. (2005) and Erben et al. (2001).

6.1.1 Noise-free case

To neglect the intrinsic shape of galaxies we perform a cosmic shear analysis of the input catalogue for intrinsically round objects using the aperture mass statistics. The results are given in the left panel of Fig. 6.1. The displayed ΛCDM prediction is based on the Peacock & Dodds (1996) model of the non-linear power spectrum. The cosmic shear signal is in excellent agreement with the theoretical prediction for $\theta > 2\,\mathrm{arcmin}$. Hence we conclude that part (2) of the pipeline measures the two-point correlation function and calculates the aperture mass dispersion accurately, and does not create artificial B-modes.

For angular scales smaller than two arcminutes the E- and B-mode signals are significantly smaller than expected. This effect is explained and quantified in Kilbinger et al. (2006). The measured two-point correlation functions, $\xi_\pm$, are set to zero for small angular scales (here we choose the same value as for the observations: $\theta_0 < 6\,\mathrm{arcsec}$) because close galaxy pairs are rejected. This lack of shear correlation measurements on small scales results in a mixing of E- and B-modes.

Note that for angular scales larger than two arcminutes the marginal difference between the theoretical prediction and simulations can easily arise from cosmic variance due to the fact that we only use $3\,\mathrm{deg}^2$ from the numerical simulations.

6.1.2 Realistic case

Using the "old" pipeline the shear measurements of simple `skymaker` simulations yielded, on average, an underestimation of the shear by $\sim 15\,\%$ (STEP 1, see Heymans et al. 2006a, and Sect. 5.4.1). With our (modified) pipeline we are currently able to recover the shear with less than $\approx 3\,\%$ calibration bias (depending on the PSF model). This has been checked with a second set of more realistic simulations (shapelets) (STEP 2, see Massey et al. 2006,

[2]Available at: http://terapix.iap.fr/cplt/oldSite/soft/skymaker/

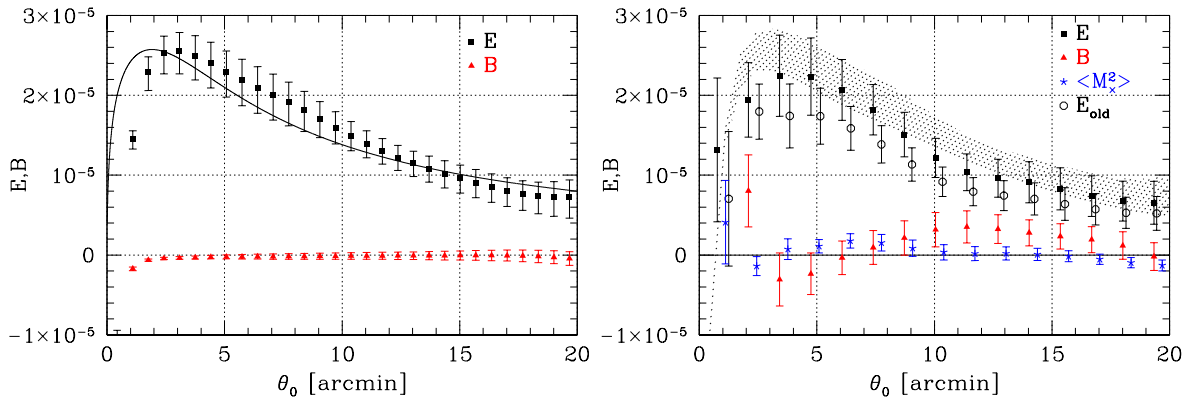

Figure 6.1: *Left panel:* noise-free case: cosmic shear analysis of the input catalogue. The number density of background sources is $n = 15\,\mathrm{arcmin}^{-2}$, and the sources are intrinsically round. The signal in each bin is the average of the 12 fields, where the statistical weight for each field is unity; the error bars are obtained by bootstrapping, see Sect. 6.3.1, and are highly correlated. Displayed is the aperture mass dispersion (E- and B-modes). The line is a ΛCDM prediction assuming $\Omega_\mathrm{m} = 0.3$, $\Omega_\Lambda = 0.7$, $\Gamma = 0.21$ and $\sigma_8 = 0.9$ (Peacock & Dodds model of the power spectrum), where all background sources are at a fixed redshift of $z_\mathrm{source} = 1$. *Right panel:* realistic case: cosmic shear analysis of the output catalogue. The same objects are used as in the left panel. Shaded area: $1\,\sigma$ range of the signal in the left panel. Displayed are the aperture mass dispersion (E- and B-modes) and $\langle M_\times^2 \rangle$. In addition, the $\mathrm{E_{old}}$-mode signal obtained via the "old" pipeline prior STEP 1 is displayed. Figure from Hetterscheidt et al. (2006).

and Sect. 5.4.3). A short comparison between the modified and "old" pipeline is given in table 5.4.

The same analysis as in Sect. 6.1.1 is performed for the output catalogue. We present the results of the analysis done with the two different pipelines, prior and after the changes we have made to our pipeline due to STEP 1 and 2. Both results are compared with the expected signal of the noise-free case, see right panel of Fig. 6.1. Clearly visible is the improvement of the modified compared to the "old" pipeline. However, we still slightly underestimate the cosmic shear signal with the modified pipeline by a few percent. In addition, our pipeline does not create significant artificial B-modes (note that the error bars in Fig. 6.1 are strongly correlated and the B-mode signal varies around zero).

We conclude that with our updated cosmic shear pipeline we estimate the shear in an unbiased way and calculate various cosmic shear statistics within the currently attainable accuracy, without any systematics.

6.2 Dealing with systematics in the GaBoDS data

In this Section we describe various tests to discover systematic errors in our data set. First we present four simple and quick quality checks of the data. Second, we present a powerful standard test for systematics, the cross-correlation between uncorrected stars

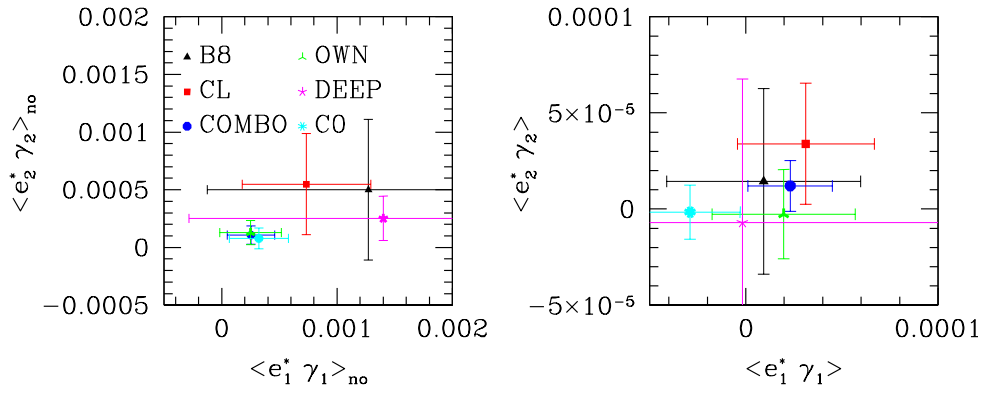

Figure 6.2: Test of the anisotropy correction in the magnitude range $R \in [21.5, 24.5]$ using Eq. (6.1). We average over the fields within a data set. The error bars are due to field-to-field variance. *Left panel:* before anisotropy correction; *right panel:* after anisotropy correction. Note the drastic change of scale. Figure from Hetterscheidt et al. (2006).

and anisotropy corrected galaxies (Bacon et al. 2003). All tests described basically provide checks on the quality of the PSF anisotropy correction. However, to test the smearing correction (i.e. the correction for the PSF size) we have to rely on simulations. For that purpose the discussed STEP project has been initiated.

6.2.1 Four basic quality tests

I. Shear - PSF anisotropy

We calculate the average

$$\langle e_{1,2}^{*,\mathrm{pol}}\, \gamma_{1,2} \rangle = \frac{1}{N} \sum_{i=1}^{N} e_{1,2}^{*,\mathrm{pol}}(\boldsymbol{\theta}_i)\, \gamma_{1,2}(\boldsymbol{\theta}_i) \tag{6.1}$$

before and after anisotropy correction. The quantities $\gamma_{1,2}$ are the shear components of all N galaxies in a GaBoDS field, and $e_{1,2}^{*,\mathrm{pol}}$ are the components of the polynomial fit function (see Sect. 5.3) at the position $\boldsymbol{\theta}_i$ of the galaxy. Since $e_{1,2}^{*,\mathrm{pol}}$ should be zero on average and uncorrelated with $\gamma_{1,2}$, $\langle e_{1,2}^{*,\mathrm{pol}}\, \gamma_{1,2} \rangle$ should vanish after the anisotropy correction. This simple test can therefore be used to reveal a possible imperfect anisotropy correction.

The result is displayed in Fig. 6.2, where we average over the fields within a data set. The average of all data sets is consistent with zero after anisotropy correction. Furthermore, it is reduced by at least a factor of 20 by applying the anisotropy correction.

II. Average shear

We calculate the average shear $\langle \gamma_i \rangle$ for each component, i, of all galaxies in the magnitude bin $R \in [21.5, 24.5]$ for each GaBoDS-field, before and after anisotropy correction, see

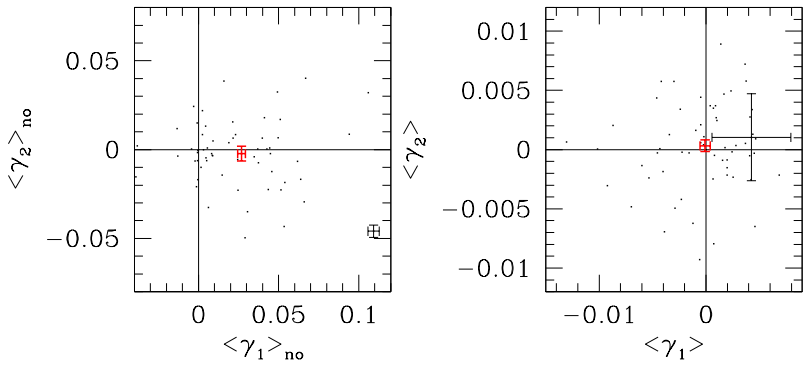

Figure 6.3: Average shear components of all galaxies in the considered magnitude bin $R \in [21.5, 24.5]$ calculated for all GaBoDS fields before (*left panel*) and after anisotropy correction (*right panel*). Because of clarity we only plot one error bar for a single field (thin lines). The average of all fields is plotted with a solid error bar. Note the drastic change of scale. Figure from Hetterscheidt et al. (2006).

Fig. 6.3. For most of the fields the average shear values, $\langle\gamma_{1,2}\rangle$, are significantly different from zero before the anisotropy correction and γ_1 is on average significantly larger than zero. The scatter is strongly reduced after anisotropy correction. For most of the fields the average shear is consistent with zero. In addition, the total average shear of all fields is consistent with zero at the $1\,\sigma$ level.

III. Average shear in bins

A further simple test of residual systematics is given by the average shear in bins with and without PSF-anisotropy correction. The galaxies are sorted according to the increasing value of the PSF-anisotropy (value of the polynomial fit function at the galaxy position). Thereafter we bin the sorted galaxy catalogue such that each bin contains an equal large number of galaxies. We then calculate for each bin two different average shear estimates: one is the fully PSF corrected shear estimate, the other one is not PSF-anisotropy corrected. The former one should not be correlated with the PSF-anisotropy, The latter one, however, should show a strong dependence on the PSF-anisotropy. We show in Fig. 6.4 exemplarily the results for two fields. The anisotropy correction works well for the AM1-field whereas the C04p1-field shows still a bias in both shear components after the anisotropy correction (see table 4.2 for details of individual fields).

IV. E- and B-modes of stars

In order to estimate the amount of residual systematics in the data set, we utilise the stars used for the anisotropy correction. Therefore the correlation functions $\xi_\pm$ are measured for them before and after the anisotropy correction and the corresponding E- and B-modes ($\langle M_{\rm ap}^2\rangle$ and $\langle M_\perp^2\rangle$) are calculated. The results are presented in Fig. 6.5. After the

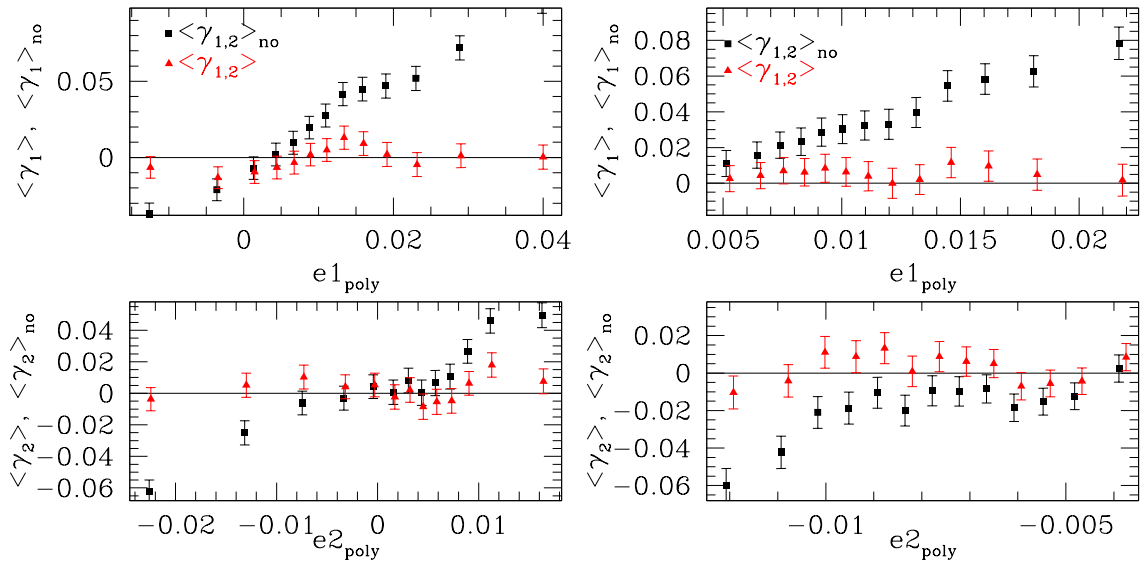

Figure 6.4: Averaged shear components versus the ellipticity components of the PSF at the galaxy position (polynomial value) with and without anisotropy correction. *Left two panels:* AM1-field; *right two panels:* C04p1-field. The γ_1 component of the C04p1-field is still significantly larger then zero after the anisotropy correction. Figure from Hetterscheidt et al. (2006).

anisotropy correction we still measure a significant signal which is, however, ten times lower than before correction and about ten times lower than the expected cosmic shear signal.

Notable is the significantly larger E- than B-mode signal of uncorrected stars indicating that on average the PSF-anisotropy pattern influences the E-mode signal of galaxies more strongly than the B-mode signal.

6.2.2 Cross-correlation of galaxies and stars

The $\xi^+_{\rm SYS}$ estimator

A powerful way to estimate the amount of systematics left in the cosmic shear signal (like an insufficient PSF anisotropy correction) is given by the cross-correlation of uncorrected ellipticities of stars and PSF-corrected ellipticities of galaxies (Brown et al. 2003; Bacon et al. 2003). Since we use the correlation functions $\xi_\pm$ to estimate cosmological parameters we propose a similar estimator:

$$\xi^+_{\rm SYS}(\theta) \equiv \sum_{i=1}^{N_{\rm f}} \frac{\langle \epsilon^* \gamma \rangle_i^+(\theta)\, |\langle \epsilon^* \gamma \rangle_i^+(\theta)|}{\langle |\epsilon^*|^2 \rangle_i(\theta)}\, W_i(\theta), \tag{6.2}$$

where $N_{\rm f}$ is the total number of fields, $\langle |\epsilon^*|^2 \rangle_i$ is the auto-correlation function of stars and W_i is the statistical weight of a single field obtained by bootstrapping on galaxy basis, see

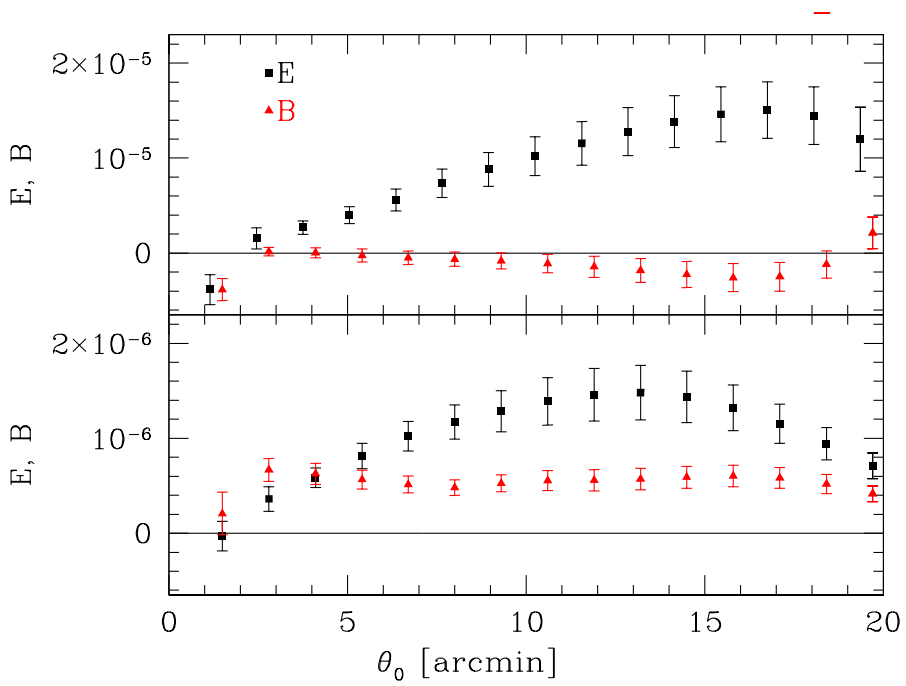

Figure 6.5: E and B-modes of uncorrected (*upper panel*) and anisotropy corrected stars (*lower panel*). The signal of the corrected stars is significantly inconsistent with zero. Note, however, the cosmic shear signal is about 10 times larger. Figure from Hetterscheidt et al. (2006).

Sect. 6.3.1. The cross-correlation function is given by

$$\langle \epsilon^* \gamma \rangle^{\pm}(\theta) = \frac{\sum_{i,j}^{N} w_i^* w_j^{\rm gal} (\epsilon^*_{{\rm t},i} \gamma_{{\rm t},j} \pm \epsilon^*_{\times,i} \gamma_{\times,j}) \Delta_{ij}(\theta)}{\sum_{i,j}^{N} w_i^* w_j^{\rm gal} \Delta_{ij}(\theta)}, \tag{6.3}$$

where N is the number of star-galaxy pairs, and Δ_{ij} is given in Eq. (3.97). We set $w_i^* = 1$ and calculate $w_j^{\rm gal}$ with Eq. (5.19). The quantity ϵ^* is the uncorrected stellar ellipticity and γ is the shear estimate of the galaxies.

The cross-correlation estimator proposed by Bacon et al. (2003) cannot become negative. It is therefore not directly comperable to the cosmic shear signal which can become negative. The definition of $\xi^+_{\rm SYS}$ overcomes this limitation since it takes into account that ξ_+ can be negative for individual fields (the nominator in Eq. 6.3 can be negative).

Hence, in combination with the normalisation of the auto-correlation function of stars, $\xi^+_{\rm SYS}$ is directly comparable to the signal, ξ_+. The results are displayed in the right panel of Fig. 6.8. The cosmic shear signal ξ_+ is about 10 times larger than the cross-correlation signal $\xi^+_{\rm SYS}$. We conclude that our way to correct for the PSF anisotropy is sufficient to obtain a clean cosmic shear signal using the two-point shear correlation function.

The $M_{\rm cross;E}$ and $M_{\rm cross;B}$ estimators

We calculate the two-point cross-correlation function $\langle\epsilon^*\gamma\rangle^{\pm}(\theta)$ for every field using Eq. (6.3). The two-point correlation function $\xi_{\pm}$ in Eq. (3.93) and Eq. (3.94) are then replaced by the cross-correlation functions $\langle\epsilon^*\gamma\rangle^{\pm}(\theta)$. For the average value we obtain

$$M_{\rm cross;E} \equiv \langle M_{\rm ap}^* M_{\rm ap}^{\rm gal}\rangle(\theta) = \frac{\sum_{i=1}^{N_{\rm f}} \langle M_{\rm ap}^* M_{\rm ap}^{\rm gal}\rangle_i(\theta)\, W_i(\theta)}{\sum_{i=1}^{N_{\rm f}} W_i(\theta)} \tag{6.4}$$

and

$$M_{\rm cross;B} \equiv \langle M_{\times}^* M_{\times}^{\rm gal}\rangle(\theta) = \frac{\sum_{i=1}^{N_{\rm f}} \langle M_{\times}^* M_{\times}^{\rm gal}\rangle_i(\theta)\, W_i(\theta)}{\sum_{i=1}^{N_{\rm f}} W_i(\theta)}, \tag{6.5}$$

respectively. The quantity $N_{\rm f}$ is the total number of fields and W_i is the statistical weight of a single field obtained by bootstrapping on galaxy basis, see Sect. 6.3.1. The results are displayed in Fig. 6.7 and 6.8 for the different data sets and for the total data set, respectively. The cross-correlation signal, $M_{\rm cross;E}$, is significantly non-zero for the C0-fields and shows the same characteristic as the E-mode signal. Hence our anisotropy correction seems to work only insufficiently for these fields. The C0-fields were observed without dithering. It is therefore possible that the PSF anisotropy variation from chip to chip is too large to be corrected for completely using the poynomial interpolation method. On the other hand, the B8-fields were also observed without dithering and do not show a significant $M_{\rm cross;E}$-signal. A further investigation is necessary to clarify the reason for the measured systematics in the C0-fields.

Note that, in contrast to Semboloni et al. (2006), a function similar to $\xi_{\rm SYS}^{+}$ (a function normalised with the auto-correlation of stars, $\langle|M^*|^2\rangle$) is not calculated for $M_{\rm ap}$. This is because in our case we analyse single fields which are shallower and smaller in size, hence the $M_{\rm ap}$ auto-correlation function of stars is very noisy and can have zero-crossings.

6.3 Cosmic shear analysis of the GaBoDS

6.3.1 Error estimates and field weights

Bootstrapping on galaxy basis

To obtain the statistical weights of $\langle M_{\rm ap}^2\rangle$ and $\xi_{\pm}$ for each field i and angular bin j we make 200 bootstrap samples of the galaxy catalogue as follows. We randomly draw $N_{\rm gal}$ times galaxies from the galaxy catalogue for each field i with putting back (where $N_{\rm gal}$ is the total number of galaxies in the field i) and place them at the same position with the same orientation as before. For each bootstrap sample, $\langle M_{\rm ap}^2\rangle_{ij}$ and $\xi_{\pm,ij}$ are calculated for each angular bin j. The statistical error for each field and bin is then the bootstrapping variance σ_{ij}^2.

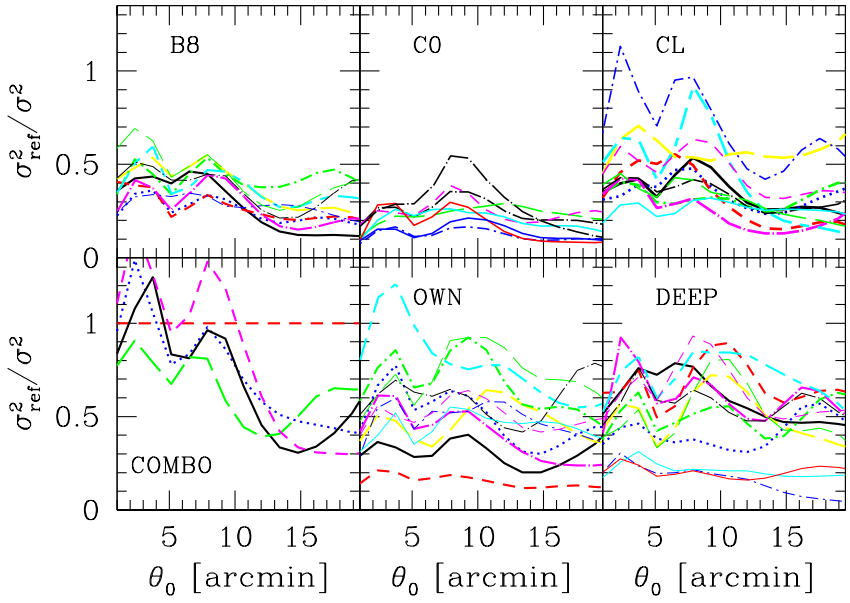

Figure 6.6: Relative statistical weights of the GaBoDS fields versus the aperture radius θ_0 obtained via bootstrapping on galaxy basis. The COMBO field SGP is chosen as a reference field since it is one of the deepest. Figure from Hetterscheidt et al. (2006).

The average measurement signal of the total survey in each bin j is calculated as

$$\langle M_{\rm ap}^2 \rangle_j = \frac{\sum_{i=1}^{N_{\rm f}} \langle M_{\rm ap}^2 \rangle_{ij} \, W_{ij}}{\sum_{i=1}^{N_{\rm f}} W_{ij}} \quad \text{and} \tag{6.6}$$

$$\xi_{\pm;j} = \frac{\sum_{i=1}^{N_{\rm f}} \xi_{\pm;ij} \, W_{ij}}{\sum_{i=1}^{N_{\rm f}} W_{ij}}, \tag{6.7}$$

where $N_{\rm f}$ is the total number of fields. As weight W_{ij} we use the reciprocal bootstrapping variance $W_{ij} = 1/\sigma_{ij}^2$. In Fig. 6.6 the relative statistical weights of the GaBoDS fields calculated for $\langle M_{\rm ap}^2 \rangle$ versus the angular bin (aperture radius θ_0) are displayed. The statistical weights of fields with a low number density of galaxies are lower than of those with a high number density, as expected. This can also be seen in the upper and lower left panels of Fig. B.3 (App. B) where the square root of the variance, σ_{ij} is plotted for two fields with different number densities (FDF-field: 1.9×10^4 galaxies and C04p3-field: 1.3×10^4 galaxies). Clearly visible are also the large error bars for small angular scales since the number of pairs is small for them.

Bootstrapping on field basis

The measurement error of the combined signal for each angular bin j is obtained by 2000 bootstrap samples of the field sample as follows. We randomly draw $N_{\rm f}$ times fields out

of the field sample with putting back. This bootstrap sample is combined according to Eqs. (6.6) and (6.7). With the 2000 bootstrap samples we estimate the probability distribution function (PDF) of the statistical errors in the combined signal including cosmic variance and obtain covariances of the errors for the final analyses. With the PDF we obtain for each angular bin j the error of the combined signal by calculating the 68 % confidence intervals about the mean. For equal weights the calculated $1\,\sigma$ variance in each bin is comparable to the usual field-to-field variance in each bin as the PDF of the bootstrap sample is almost symmetric in our case.

6.3.2 Cosmic shear signal

A powerful way to reveal possible systematic errors is the application of the aperture mass statistics as it provides an unambiguous splitting of E- and B-modes (Sect. 3.2.2). The presence of a non-vanishing B-mode is a good indicator for systematic errors arising, for instance, from an imperfect anisotropy correction. However, Kilbinger et al. (2006) found in their work a mixing of E- and B-modes if a cut-off in $\xi_\pm$ on small angular scales is performed. According to Kilbinger et al. (2006) the deviation of the biased E- and B-modes (the E- and B-modes are smaller due to the cut-off) from the true E- and B-mode signal is only 1 % for angular scales up to 4 arcmin for a cut-off in $\xi_\pm$ at 6 arcsec. In our work we calculate $\langle M_{\rm ap}^2 \rangle$ from $\xi_\pm$ in the interval $[6'', 40']$. For the parameter estimate we only consider the E-mode signal from angular scales larger than 4 arcmin (see below), so the bias described is negligible. Schneider & Kilbinger (2006) overcome the general problem and introduce the ring-statistics which unambiguously splits E- and B-modes in any case.

At this stage it is worth mentioning that B-modes can also arise from the intrinsic alignment of galaxies (e.g. Heavens et al. 2000; Crittenden et al. 2001) which could be removed, in principle, by using redshift information (King & Schneider 2003; Heymans & Heavens 2003). Another possible source of B-modes is the intrinsic shape-shear correlation (Heymans et al. 2006b, see also Sect. 6.4.2). They performed in their work a cosmic shear analysis of a large ΛCDM N-body simulation assuming a simple galaxy model and found a weakly negative B-mode. In addition, B-modes can arise from clustering of galaxies from which the shear is measured (Schneider et al. 2002). All three sources of B-modes combined are probably not significant as the statistical errors are still quite large. In Sect. 6.4.2 we discuss in detail the contamination of the E-mode signal by the intrinsic alignment and the intrinsic shape-shear correlation of galaxies which can be much larger and significant.

As pointed out in Sect. 4.1.2 we split our data into six different sets depending on the data source. The data is heterogeneous with respect to the seeing conditions, observing strategy and other characteristics. Thus splitting of the data into different sets allows us to reveal potential systematics depending on the data source. In Fig. 6.7 the average E- and B-mode signal and the average signal of the cross-correlation between uncorrected stars and PSF corrected galaxies for E- and B-modes, $M_{\rm cross;E}$ and $M_{\rm cross;B}$, of the different data sets are displayed. In particular the cross-correlation signal, $M_{\rm cross;E}$, of the C0-fields is significantly non-zero and shows the same characteristic as the E-mode signal. In addition, the B-modes within the interval $\theta_0 \in [2', 7']$ are significantly larger than zero, hence we

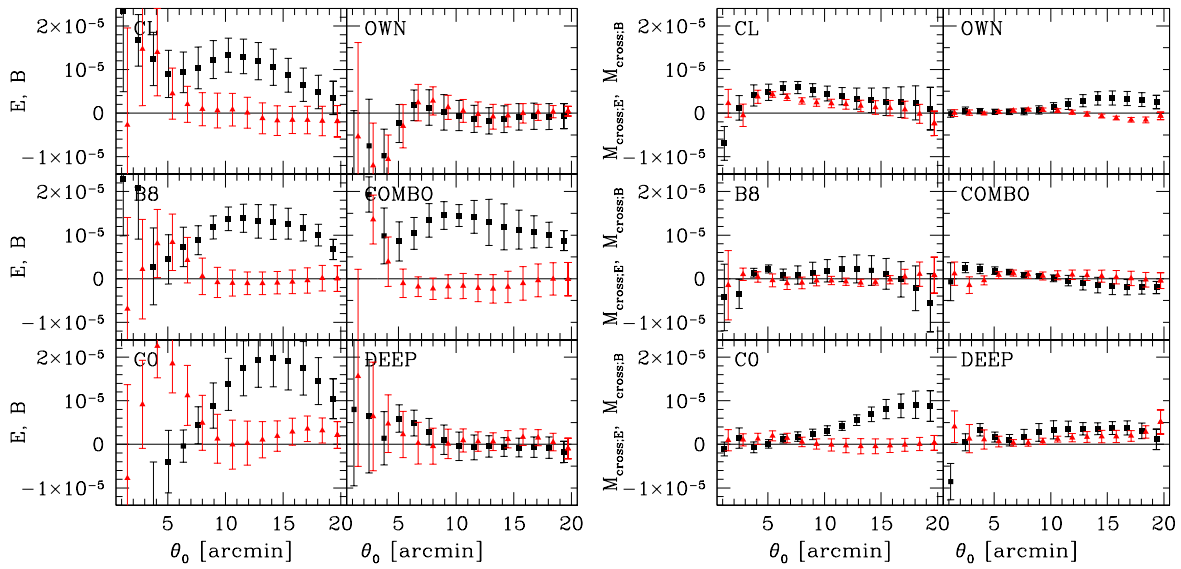

Figure 6.7: Measurements of the aperture mass statistics in the R-band for all six data sets. *Left panel :* E-mode (squares) and B-mode (triangles). *Right panel:* $M_{\rm cross;E}$ (squares) and $M_{\rm cross;B}$ (triangles). For clarity, E- and B-mode points are slightly offset. Figure from Hetterscheidt et al. (2006).

exclude those fields from our final analysis.

By excluding the C0-fields we obtain, in the magnitude range $R \in [21.5, 24.5]$, 7.8×10^5 galaxies, corresponding to a number density of $n = 16\,\mathrm{arcmin}^{-2}$. Taking into account the weights of individual galaxies this results in an effective number density of source galaxies of $n_{\rm eff} = 12.5\,\mathrm{arcmin}^{-2}$, see Sect. 5.3. In Fig. 6.8 the average E-mode, B-mode, $\langle M_\times^2 \rangle$ and the average signal of the cross-correlation between uncorrected stars and PSF corrected galaxies of all fields, except the excluded C0-fields, are displayed.

The average B-mode is consistent with zero within the $1\,\sigma$-range for $\theta_0 > 4\,\mathrm{arcmin}$, and the cross-correlation between uncorrected stars and corrected galaxies, $M_{\rm cross;B}$, is consistent with zero as well. Hence the anisotropy correction method does not create an artificial B-mode. In addition, the $\langle M_\times^2 \rangle$-signal is consistent with zero indicating a clean data set, free from any systematic errors. The cross-correlation signal, $M_{\rm cross;E}$, however, is about $1\,\sigma$ to $2\,\sigma$ larger than zero for $\theta_0 > 5\,\mathrm{arcmin}$ and $3\,\sigma$ for $\theta_0 \in [3', 5']$. This suggests that the PSF-anisotropy correction is not perfect and biases the E-mode even though the B-mode is consistent with zero. However, as mentioned before, $M_{\rm cross;E}$ and $M_{\rm cross;B}$ are not normalised with the auto-correlation function of stars, so $M_{\rm cross;E}$ is not directly comparable with the lensing signal itself. Therefore it is hard to judge how large the possible impact of systematics on the E-mode signal really is.

Taking into account the B-mode, the $\langle M_\times^2 \rangle$ and the cross-correlation signals $M_{\rm cross;E}$ and $M_{\rm cross;B}$ we conclude that the influence of systematics on the calculated E-mode is negligible on angular scales larger than four arcminutes within the currently attainable accuracy. For

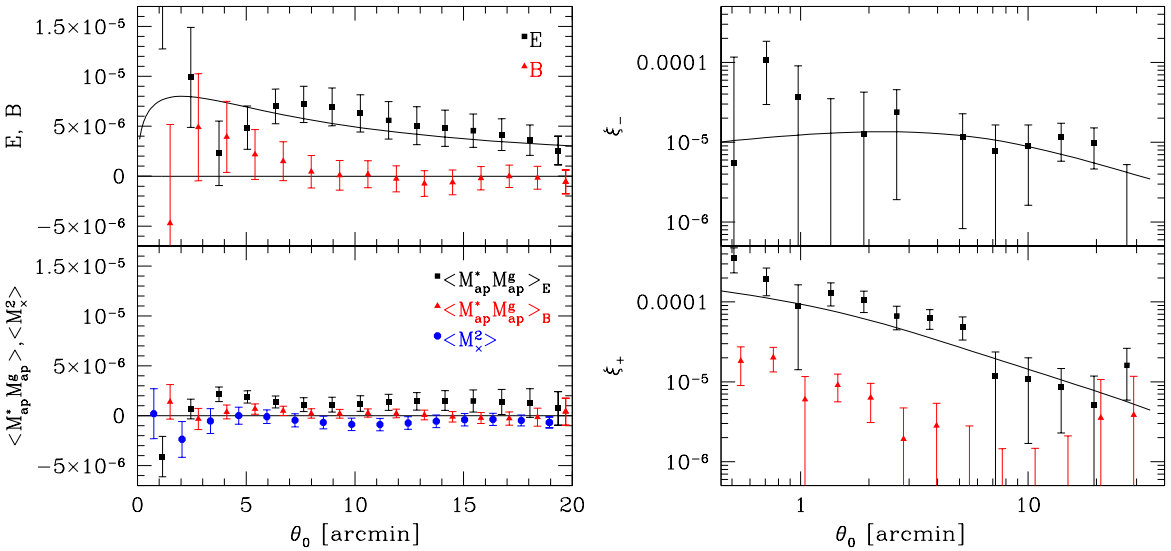

Figure 6.8: *Left panel:* Various measurements of the aperture mass statistics of 52 GaBoDS fields (the C0 fields are excluded, see text) in the R-band ($\approx 13\,\mathrm{deg}^2$). All galaxies in the magnitude range $R \in [21.5, 24.5]$ are used for the cosmic shear analysis. The total number of galaxies is $\approx 7.8\times10^5$ corresponding to an effective number density of $n_{\rm eff} = 12.5\,\mathrm{arcmin}^{-2}$. Upper panel: E- and B-mode decomposition of the $M_{\rm ap}$-signal. The line is a ΛCDM prediction assuming $\Omega_{\rm m} = 0.3$, $\Omega_\Lambda = 0.7$, $\Gamma = 0.21$ and $\sigma_8 = 0.9$; the redshift distribution function is given by Eq. (6.8). For clarity the B-mode points are slightly offset to the right. Lower panel: Cross-correlation between uncorrected stars- and corrected galaxies for E- and B-modes and $\langle M_\times^2\rangle$. For clarity the $\langle M_\times^2\rangle$- and $\langle M_\times^* M_\times^{\rm gal}\rangle$-points are slightly offset to the left and right, respectively. *Right panel:* Measured two-point correlation functions ξ_+ and ξ_-. In the lower panel $\xi^+_{\rm SYS}$ (see Eq. 6.2) is plotted (triangles). The line is a ΛCDM prediction (same parameters as in the left panel). Figure from Hetterscheidt et al. (2006).

scales below four arcminutes the B-mode is slightly positive (about $1\,\sigma$) and the $M_{\rm cross;E}$-signal has its maximum. For this reason, we exclude in our further $\langle M_{\rm ap}^2\rangle$-analysis scales below four arcminutes.

In Fig. 6.8 the average ξ_--, ξ_+- and $\xi^+_{\rm SYS}$-signals of all fields, except the excluded C0-fields, are plotted. The $\xi^+_{\rm SYS}$-signal is at least a factor of 10 smaller than the ξ_+-signal so we conclude that the two-point shear correlation function is not significantly influenced by an imperfect anisotropy correction.

Both, the aperture mass dispersion (in the interval $\theta_0 \in [4', 20']$) and the two-point shear correlation function (in the interval $\theta_0 \in [0'.8, 33']$) are used in the following to estimate cosmological parameters.

6.3.3 Photometric redshifts

The GaBoDS data set includes $2\,\mathrm{deg}^2$ of deep *UBVRI*-band observations from the DPS, which yields photometric redshift information for about 8% of the objects considered for the cosmic shear analysis. The redshift catalogue was obtained using the `hyper-z` public software developed by Bolzonella et al. (2000). Note that for our quantitative cosmic shear analysis we are not interested in the individual galaxy redshifts but in the redshift distribution of the whole galaxy sample.

Comparison with VVDS and GOODS-MUSIC sample

For the Chandra Deep Field South (CDFS, name in our paper: AXAF), a database of spectroscopically observed objects from the VIMOS-VLT-Deep-Survey (VVDS, Le Fevre et al. 2004) exists. In addition, the Great Observatories Origins Deep Survey-MUltiwavelength Southern Infrared Catalogue (GOODS-MUSIC, Grazian et al. 2006) sample is publicly available. It is centred on the CDFS (left panel of Fig. 6.9) and comprises 14847 objects with reliable, high-quality photo-z estimates.

For the photometric redshift estimate we used the observed galaxy templates by Coleman et al. (1980) (CWW templates) and the synthetic galaxy templates derived from the library of Bruzual & Charlot (1993) (BC templates). The synthetic galaxy templates yield a smaller scatter in the difference between photometric and VVDS-spectroscopic redshifts for galaxies with magnitudes $R < 23$. However, the redshift distribution of galaxies in the magnitude interval $R \in [21.5, 24.5]$, obtained with the observed galaxy templates, matches the redshift distribution obtained from the GOODS-MUSIC sample slightly better than that obtained with synthetic galaxy templates. The number of catastrophic outliers around $z = 3.6$ is much lower for the CWW than for the BC templates (right panel of Fig. 6.9).

A comparison between the redshifts of 500 VVDS-objects and photometric redshifts obtained with `hyper-z`, in the considered magnitude interval $R \in [21.5, 24.5]$, reveals a systematic underestimation of the photometric redshifts of $0.055\,(1+\langle z\rangle)$. This is corrected for in an ad-hoc manner by adding $0.055\,(1 + \langle z\rangle)$ to each photo-z of a galaxy.

Estimate of the redshift distribution

To estimate the redshift distribution of the background sources we associate the redshift catalogue with the lensing catalogue. In this way the weighting of individual galaxies (see Eq. 5.19) is taken into account in the estimate of the redshift distribution. In addition, we only take those photometric redshift estimates into account with a `hyper-z` 68 %-confidence interval smaller than $0.55\,(1 + z)$. With this cut we exclude objects with highly uncertain redshift estimates which are also galaxies with a low signal-to-noise ratio in R-band, see Fig. 6.10.

We obtain 6.2×10^4 objects with accurate photometric redshifts corresponding to 70 % of the DPS-lensing objects and about 8 % of all lensing objects. With these objects we estimate a redshift distribution of the DPS-lensing galaxies in the given magnitude bin. To acquire a smooth redshift distribution for all galaxies of the GaBoDS galaxy lensing

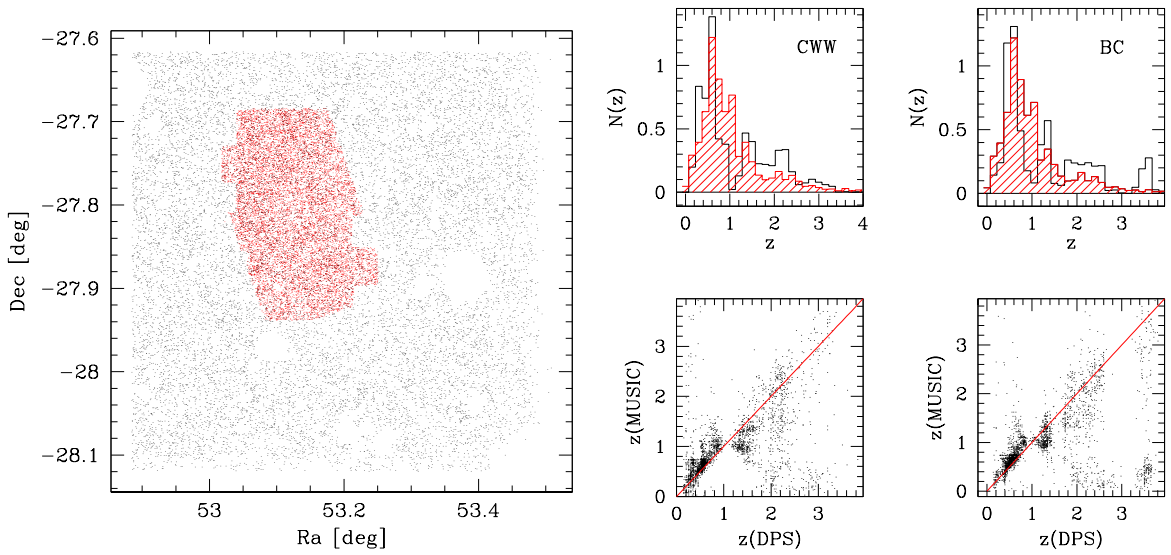

Figure 6.9: *Left panel:* Positions of lensing galaxies with photo-z information in the AXAF field (black) and galaxies with photo-z information from the GOODS-MUSIC sample (red). *Right panels:* Comparison of our DPS-photo-z estimates with those of the GOODS-MUSIC sample for the observed (CWW, left panels) and synthetic (BC, right panels) templates. The red line in the lower panels is the one-to-one relation. Upper panels: photo-z of the DPS (black histograms) and photo-z of the GOODS-MUSIC sample (red shaded histogram).

catalogue, we fit the following distribution function $p_{\rm fit}$, introduced by Brodwin et al. (2006), to the measured redshift distribution,

$$p_{\rm fit}(z) = A\,\left[p_1(z)\,H(z_{\rm t}-z) + p_2(z)\,H(z-z_{\rm t})\right], \tag{6.8}$$

where H denotes the Heaviside step function,

$$p_1(z) = \left(\frac{z}{z_0}\right)^{\alpha} \exp\left[-\left(\frac{z}{z_0}\right)^{\beta}\right] \tag{6.9}$$

and

$$p_2(z) = \exp\left[\left(\frac{z_{\rm t}}{z_1}\right)^{\gamma} - \left(\frac{z}{z_1}\right)^{\gamma}\right] p_1(z_{\rm t}); \tag{6.10}$$

the normalisation A is obtained by

$$\int_0^{z_{\rm t}} {\rm d}z\, p_1(z) + \int_{z_{\rm t}}^{3} {\rm d}z\, p_2(z) = 1. \tag{6.11}$$

The fit function was binned in the same way as the measured distribution. For $z_{\rm t} = 1$ we minimise χ^2 and obtain as best-fit parameters $z_0 = 0.27 \pm 0.14$, $\alpha = 2.84 \pm 0.96$, $\beta = 1.40 \pm 0.37$, $\gamma = 2.34 \pm 0.53$ and $z_1 = 2.16 \pm 0.22$ which results in a mean redshift of $\bar{z} = 0.78$. The errors given are $1\,\sigma$ statistical uncertainties.

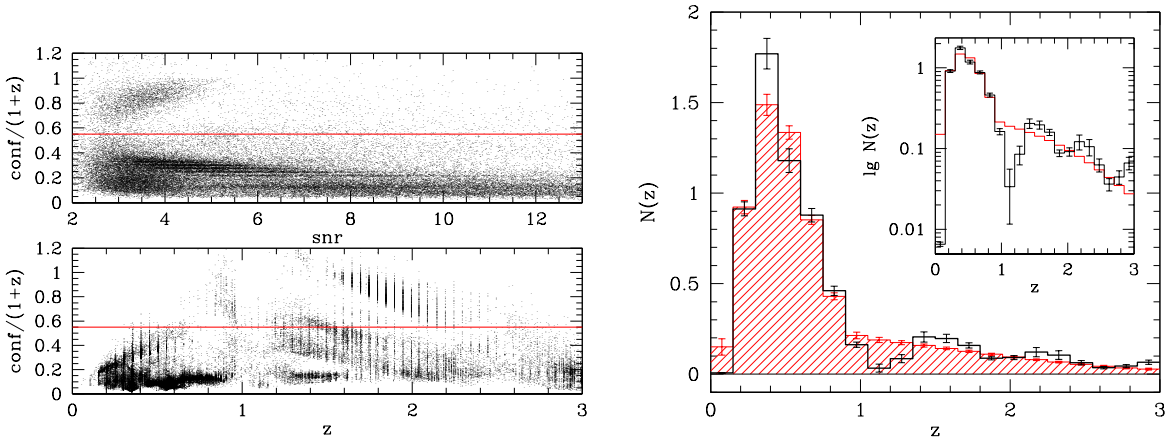

Figure 6.10: *Upper left panel*: Relative `hyper-z` 68 %-confidence interval, conf/(1+z), of lensing galaxies and its dependence on the signal-to-noise ratio (snr) in the R-band. *Lower left panel*: Relative confidence interval and its dependence on photometric redshift z. The vertical line indicates the cut described in the text. *Right panel:* Normalised number density of galaxies as a function of photometric redshift. Solid black histogram: measured redshifts; red shaded histogram: fit given by Eq. (6.8). The photometric redshifts are obtained from 7 WFI fields of the DPS (with 5 broadband filters: *UBVRI*) for 6.2×10^4 objects ($\approx 70\%$ of the lensing objects) in the magnitude interval $R \in [21.5, 24.5]$. To better display the tail of the distribution we plot inside the diagram a logarithmic plot of $N(z)$. The error bars are the field-to-field variance of the 7 WFI fields. Figure from Hetterscheidt et al. (2006).

In the right panel of Fig. 6.10 the redshift distribution of the DPS galaxy subsample in the magnitude interval $R \in [21.5, 24.5]$ is displayed. Note the dip at $z = 1.1$ in the observed redshift distribution (such a dip can also be seen in the photo-z distribution measured by Semboloni et al. 2006). This dip is present in the estimated redshift distributions of each DPS field, yet not for the GOODS-MUSIC sample which comprises infrared bands (Fig. 6.9). We assume that this is a systematic effect due to (1) the lack of infrared information and (2) the lack of a large spectroscopic calibration sample. To obtain the best-fit parameters of the redshift distribution we therefore downweighted this redshift bin.

A more proper way to determine the redshift distribution from the photometric redshift estimates would be to deconvolve the latter with the width of the phot-z uncertainties. However, the corresponding change in the "true" redshift distribution would be fairly small, yielding a correction factor which is much smaller than the statistical uncertainties of the shear measurements. We have therefore not attempted such a deconvolution and do not consider this negligible bias of the redshift distribution in the following error estimate of σ_8 (Sect. 6.4.2).

6.3.4 Estimate of cosmological parameters

The measured cosmic shear signal is related to the dark matter density power spectrum, which in turn depends on cosmological parameters and the source redshift distribution (Sect. 3.2). To estimate the parameters $\boldsymbol{\alpha} = (z_0, z_1, \alpha, \beta, \gamma, \sigma_8, \Omega_\mathrm{m}, h, \Omega_\Lambda)$ from our measured data vector $\boldsymbol{d}$ (either the binned $\langle M_\mathrm{ap}^2 \rangle$- or $\xi_\pm$-values) we use the generalised likelihood. The probability distribution function (PDF) of the model parameters $\boldsymbol{\alpha}$ given the p-dimensional data vector $\boldsymbol{d}$ is called the posterior PDF $P(\boldsymbol{\alpha}|\boldsymbol{d})$. It is obtained using Bayes theorem as follows

$$P(\boldsymbol{\alpha}|\boldsymbol{d}) \propto P_\mathrm{prior}(\boldsymbol{\alpha}) P(\boldsymbol{d}|\boldsymbol{\alpha}), \tag{6.12}$$

where $P(\boldsymbol{d}|\boldsymbol{\alpha})$ is the usual likelihood function and $P_\mathrm{prior}(\boldsymbol{\alpha})$ is a prior of $\boldsymbol{\alpha}$. We define $\boldsymbol{m}(\boldsymbol{\alpha})$ as the p-dimensional model vector. Assuming that the noise residual $\boldsymbol{n} = \boldsymbol{d} - \boldsymbol{m}$ obeys Gaussian statistics the log-likelihood function reads

$$\ln P(\boldsymbol{d}|\boldsymbol{\alpha}) = -\frac{1}{2}(\boldsymbol{d} - \boldsymbol{m})^t C^{-1} (\boldsymbol{d} - \boldsymbol{m}) + \mathrm{const.} \tag{6.13}$$

An unbiased estimator of the inverse covariance matrix is given by

$$C^{-1} = \frac{N_\mathrm{f} - p - 2}{N_\mathrm{f} - 1} \tilde{C}^{-1}, \tag{6.14}$$

where p is the size of the data vector (in our case the number of angular bins, with $p = 15$), and N_f is the number of statistical independent data vectors (in our case the number of fields, $N_\mathrm{f} = 52$). Without the factor, $(N_\mathrm{f} - p - 2)/(N_\mathrm{f} - 1)$, the error contours would be underestimated and strongly depend on the number of bins, p. For a detailed discussion of how to obtain unbiased estimates of inverse covariance matrices, we refer to Hartlap et al. (2006). The quantity

$$\tilde{C}_{ij} = \frac{1}{N_\mathrm{boot} - 1} \sum_{l=1}^{N_\mathrm{boot}} (d_i^{(l)} - \bar{d}_i)(d_j^{(l)} - \bar{d}_j) \tag{6.15}$$

is the estimated noise covariance matrix with the angular bins $i, j \in \{1, 2, ..., p\}$. The quantity $\bar{d}$ is the average signal of all fields in the considered bin, see Eqs. (6.6) and (6.7), and $N_\mathrm{boot} = 2000$ is the number of bootstrap samples on field basis (Sect. 6.3.1).

In many other works on cosmic shear the covariance matrix is computed analytically (especially for those cosmic shear surveys consisting of a large contiguous field). The covariance matrix is decomposed as $\tilde{C} = C_\mathrm{n} + C_\mathrm{s}$, where C_n is the statistical noise and C_s is the cosmic variance covariance matrix. The cosmic variance covariance matrix is then computed according to Schneider et al. (2002) assuming a fiducial cosmological model and an effective survey area. Note that in contrast to this approach we estimate our covariance matrix *directly from the data* without any further assumptions. This is possible as our fields are widely separated in the sky; hence they are statistically independent.

To calculate the model vector $\boldsymbol{m}(\boldsymbol{\alpha})$, we have to specify the dark matter density power spectrum. Our measurements probe scales which are affected by the non-linear growth of

structure. We calculate the non-linear power spectrum using the fitting formula proposed by Peacock & Dodds (1996). The fitting formula is based on a semi-analytical prescription for the evolution of the dark matter power spectrum. Although this formula is relatively simple it reproduces the main features of the standard cosmological model and is accurate enough for our purposes, considering the large statistical errors of our measurements. To estimate cosmological parameters we assumed two simple ΛCDM models:

- **A**: a flat Universe: $\Omega_\mathrm{m} + \Omega_\Lambda = 1$ and
- **B**: a Λ-Universe with Ω_Λ, $\Omega_\mathrm{m} \in [0, 1.5]$.

For both models we assumed a negligible baryon content (the shape parameter is given by $\Gamma = \Omega_\mathrm{m}\, h$ and the transfer function is given in Bardeen et al. 1986) and a primordial spectral index of $n_\mathrm{s} = 1$. The remaining free parameters in our following likelihood analyses are therefore:

- the five fit parameters of the redshift distribution $(z_0, z_1, \alpha, \beta, \gamma)$ with the constraint from our obseved redshift distribution,
- Hubble constant with a constraint of $h = 0.7 \pm 0.07$ (supported by the HST key project),
- mass power spectrum normalisation σ_8,
- matter density with the constraint $\Omega_\mathrm{m} \geq 0$,
- in addition for model **B**: Ω_Λ.

To apply Eq. (6.12) we have to specify the probability function of the priors, $P_\mathrm{prior}(\boldsymbol{\alpha})$. It is given by a multivariate Gaussian distribution

$$P_\mathrm{prior}(\boldsymbol{\alpha}) \propto \exp\left\{-\frac{1}{2}(\boldsymbol{\alpha} - \bar{\boldsymbol{\alpha}})^t C^{-1}_\mathrm{prior}(\boldsymbol{\alpha} - \bar{\boldsymbol{\alpha}})\right\}. \tag{6.16}$$

The correlation between the five fit parameters of the redshift distribution is taken into account in the prior covariance matrix, C_prior.

The Monte Carlo Markov Chain method

We do not evaluate the likelihood function on a grid. It would be eight- or nine-dimensional in our case ($\sigma_8, \Omega_\mathrm{m}, h$ or $\sigma_8, \Omega_\mathrm{m}, h, \Omega_\Lambda$, depending on model **A** or **B**, and the five fit parameter of the redshift distribution) and would therefore be too time consuming. The Monte Carlo Markov Chain (MCMC) technique overcomes this computational limitation. The likelihood function is no longer evaluated at fixed positions in the parameter space but at randomly selected positions along the Markov Chain.

The MCMC code in our work is based on the Metropolis-Hastings algorithm, see Metropolis et al. (1953) and Hastings (1970), or Tereno et al. (2005) for recent implementations to estimate cosmological parameters. It performs a random walk through the parameter space $S_i = (\alpha_1^{(i)}, ..., \alpha_{8/9}^{(i)})$ with $i \in [1, N_\mathrm{s}]$ (N_s is the number of accepted steps). The starting point, S_0, can be somewhere in the parameter space. We choose it to be close to the expected likelihood maximum. Then a candidate for the next step S_{i+1} is drawn. We use for the jump within the parameter space from the position S_i to the position of the candidate S_{i+1} a proposal PDF $Q(S_i, S_{i+1})$. For each iteration i a model candidate S_{i+1} is randomly *generated* by $Q(S_i, S_{i+1})$, where S_{i+1} depends on the current model S_i. In general the choice of the proposal function is free. To achieve convergence in a reasonable time we choose, as in Tereno et al. (2005), a multivariate Gaussian distribution

$$Q(S_i, S_{i+1}) \propto \exp\left\{-\frac{1}{2}[S_i - S_{i+1}]^t M^{-1}[S_i - S_{i+1}]\right\}. \tag{6.17}$$

For M we choose during a pre-phase (first 1000 steps along the chain) the Fisher matrix F_{ij} at the position S_0, the given starting point:

$$F_{ij} = F_{ij}^{\mathrm{prior}} + \sum_{k,l} \frac{\partial m_k}{\partial \alpha_i}[C^{-1}]_{kl}\frac{\partial m_l}{\partial \alpha_j} \tag{6.18}$$

where

$$F_{ij}^{\mathrm{prior}} = \frac{\partial^2}{\partial \alpha_i \partial \alpha_j} \ln P_{\mathrm{prior}}(\boldsymbol{\alpha}) \tag{6.19}$$

is the Fisher matrix of the priors. After the pre-phase we replace M by the covariance matrix, $\mathrm{cov}(\alpha_i, \alpha_j)$, of the parameters estimated from the first 1000 steps.

The value S_{i+1} is then *accepted* if the following inequalities are fulfilled, either

$$P(S_{i+1}|\boldsymbol{d}) \geq P(S_i|\boldsymbol{d}) \quad \text{or} \quad \frac{P(S_{i+1}|\boldsymbol{d})}{P(S_i|\boldsymbol{d})} \geq x\,\frac{Q(S_i, S_{i+1})}{Q(S_{i+1}, S_i)}, \tag{6.20}$$

where $x \in [0, 1]$ is a random number drawn from a uniform distribution. If the candidate is accepted we move to S_{i+1} and repeat the procedure. Since Q in Eq. (6.17) satisfies $Q(S_i, S_{i+1}) = Q(S_{i+1}, S_i)$, Eq. (6.20) simplifies to $P(S_{i+1}|\boldsymbol{d})/P(S_i|\boldsymbol{d}) \geq x$.

Usually several independent MCMCs are started. For every chain the first S_i values are rejected (burn-in phase) until the MCMCs have forgotten about their initial start position. In this way a possible bias due to the starting position is avoided. To estimate the size of the burn-in phase we use the Gelman & Rubin test (Gelman & Rubin 1992). We first calculate the variance for each parameter inside every chain k: $\sigma_{\alpha,k}^2$, and then the average variance of all chains: $\bar{\sigma}_\alpha^2 = (1/k)\sum_k \sigma_{\alpha,k}^2$. Next we calculate the average of each parameter inside each chain, and then the variance of all averages: $\sigma_{\bar{\alpha}}^2$. The average and variance inside each chain is calculated using only S_i, with $i \in [n, 2n]$. For $n \to \infty$ both variances, $\sigma_{\bar{\alpha}}^2$ and $\bar{\sigma}_\alpha^2$, converge to the same value. Therefore the ratio

$$R = \frac{\sigma_{\bar{\alpha}}^2}{\bar{\sigma}_\alpha^2} + \frac{n}{n-1} \tag{6.21}$$

Table 6.1: Joint constraints on Ω_m and σ_8 from our cosmic shear analysis using the two-point shear-correlation function and the aperture mass dispersion. Results from model **A** in which we assume $\Omega_\Lambda + \Omega_\mathrm{m} = 1$, $\Gamma = \Omega_\mathrm{m}\, h$, $n = 1$, $\Omega_\mathrm{m} \in [0, 1]$ and marginalise over the Hubble parameter and the redshift distribution as described in the text. Stated below are medians and $1\,\sigma$ errors.

	Ω_m	σ_8	$\sigma_8(\Omega_\mathrm{m} = 0.3)$	$\Omega_\mathrm{m}(\sigma_8 = 0.8)$
$\xi_\pm$	$0.44^{+0.45}_{-0.20}$	$0.88^{+0.55}_{-0.42}$	0.93 ± 0.14	0.37 ± 0.08
$\langle M_\mathrm{ap}^2 \rangle$	$0.46^{+0.30}_{-0.22}$	$0.61^{+0.32}_{-0.20}$	0.80 ± 0.10	0.31 ± 0.07

calculated for each parameter α is a reasonable control parameter for the convergence of each chain, see Tereno et al. (2005). As long as R is larger than 1.2 for each parameter α we reject all S_i with $i < n$.

To decorrelate the S_i values a thinning is applied. Only every fifth value of the chain is used as proposed by Tereno et al. (2005).

We marginalise over the Hubble parameter h and the fit parameter of the redshift distribution, z_0, α, β, γ and z_1, meaning that we project all points of the MCMC onto the $(\Omega_\mathrm{m}, \sigma_8)$, $(\Omega_\Lambda, \sigma_8)$ or $(\Omega_\mathrm{m}, \Omega_\Lambda)$-plane. Compared to the prior, the Hubble parameter and the redshift distribution parameters cannot be improved with the data at hand. To determine the $1\,\sigma, 2\,\sigma$ and $3\,\sigma$ contours, the point number density in the $(\Omega_\mathrm{m}, \sigma_8)$, $(\Omega_\Lambda, \sigma_8)$ and $(\Omega_\mathrm{m}, \Omega_\Lambda)$-plane is smoothed and the logarithm of the number density map is calculated. The maximum log-density is subtracted everywhere. In this way $-\Delta\chi^2/2 = \ln L - \ln L_\mathrm{max}$ is obtained.

6.4 Results

6.4.1 Estimated parameters

Model A

For a flat ΛCDM Universe both the aperture mass dispersion and the two-point shear correlation function is used to constrain cosmological parameters. For $\langle M_\mathrm{ap}^2 \rangle$ and $\xi_\pm$ we ran four independent MCMCs resulting in 15000 points (excluding 1500 points of the burn-in phase) and 29400 points (excluding 1000 points of the burn-in phase), respectively. As a result we obtain the joint constraints on Ω_m and σ_8, see Fig. 6.11 and Fig. 6.12. The confidence contours of σ_8 and Ω_m reveal the typical "banana"-like shape reflecting the strong degeneracy between these two parameters. Due to the degeneracy both parameters are poorly constrained without further priors, see table 6.1 and solid lines in the small panels of Fig. 6.11 and Fig. 6.12.

Assuming, as a strong prior, either $\Omega_\mathrm{m} = 0.3$ or $\sigma_8 = 0.8$, we obtain stronger constrains on σ_8 and Ω_m, respectively, see table 6.1 and dashed lines in the small panels of Fig. 6.11 and Fig. 6.12.

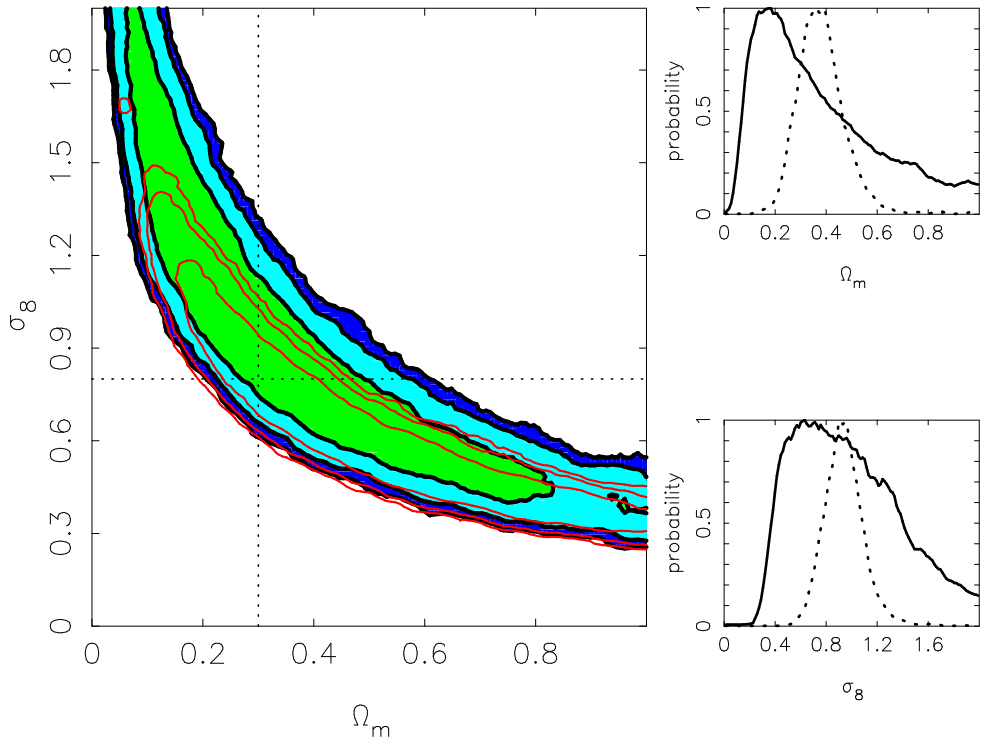

Figure 6.11: Model **A**: joint constraints on $\Omega_{\rm m}$ and σ_8 obtained from our cosmic shear analysis of the GaBoDS data set using the two-point shear-correlation function and the Peacock & Dodds model for the non-linear power spectrum. We assume $\Omega_\Lambda + \Omega_{\rm m} = 1$, $\Gamma = \Omega_{\rm m}\, h$, $n = 1$, $\Omega_{\rm m} \in [0, 1]$ and marginalise over the Hubble parameter and the redshift distribution as described in the text. *Large panel*: colour shaded confidence region: cosmic shear analysis using the two-point shear-correlation function, light red contours: aperture mass dispersion (shown are the 1σ, 2σ and 3σ contours). *Upper right panel*: solid line: PDF of $\Omega_{\rm m}$ for the marginalisation over σ_8, dashed line: PDF of $\Omega_{\rm m}$ for $\sigma_8 = 0.8$. *Lower right panel*: solid line: PDF of σ_8 for the marginalisation over $\Omega_{\rm m}$, dashed line: PDF of σ_8 for $\Omega_{\rm m} = 0.3$. Figure from Hetterscheidt et al. (2006).

Model B

For the ΛCDM model **B** only the aperture mass dispersion is utilised to constrain cosmological parameters. We ran eight independent MCMCs resulting in 39000 points (excluding 1000 points of the burn-in phase). The result is given in table 6.2 and displayed in Fig. 6.13. Again, the confidence contours of σ_8 and $\Omega_{\rm m}$ reveal the typical "banana"-like shape. The contours of model **B** are almost identical to model **A** (for the $\langle M_{\rm ap}^2 \rangle$-analysis) for $\Omega_{\rm m} > 0.3$ and differ strongly for $\Omega_{\rm m} < 0.3$ (the contours do not "close" until $\sigma_8 \approx 1.9$).

Assuming as a strong prior either $\Omega_{\rm m} = 0.3$ or $\sigma_8 = 0.8$ we obtain stronger constrains on σ_8 and $\Omega_{\rm m}$, respectively which is not the case for Ω_Λ, see table 6.1 and grey and light grey lines in the small panels of Fig. 6.13. Assuming as a strong prior $\Omega_\Lambda = 0.7$ the constraints do not improve. Hence the dependence on Ω_Λ is relatively weak, imposing only weak constraints.

However, a joint analysis of cosmic shear and supernovae measurements without as-

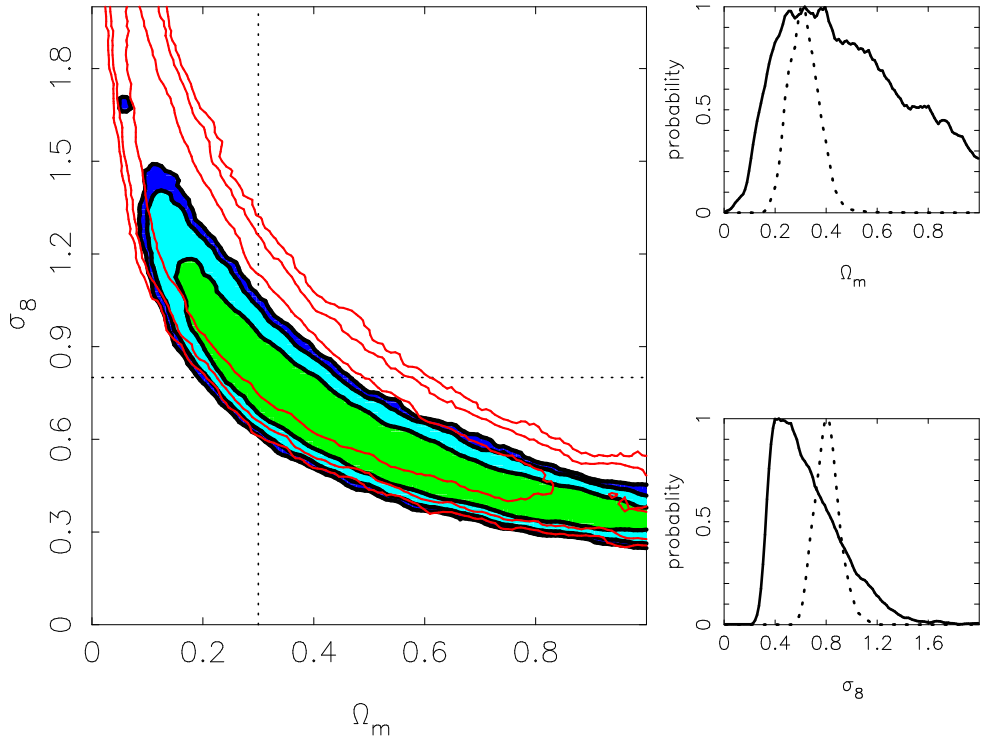

Figure 6.12: Model **A**: same as in Fig. 6.11 but now for the aperture mass dispersion (colour shaded confidence region). Light red contours: comparison to the two-point shear-correlation function. Figure from Hetterscheidt et al. (2006).

suming a flat Universe (without priors from WMAP) could provide a tight constraint on Ω_Λ. Our measurements exclude a Ω_Λ larger than unity with $3\,\sigma$ and the supernovae measurement from Knop et al. (2003) require a dark energy density ($\Omega_\Lambda > 0$) with more than $3\,\sigma$ but cannot exclude large values of Ω_Λ.

Estimating parameters with $\langle M_{\rm ap}^2 \rangle$ or $\xi_\pm$?

The difference in the constraints on $\Omega_{\rm m}$ and σ_8, stemming from the applied aperture mass dispersion $\langle M_{\rm ap}^2 \rangle$ and two-point shear correlation function $\xi_\pm$, can arise from the fact that both methods probe different parts of the mass power spectrum. Another reason for the difference arises from the fact that we fit $\langle M_{\rm ap}^2 \rangle$ in the interval $\theta_0 \in [4', 20']$ and $\xi_\pm$ in the interval $\theta_0 \in [0\farcm8, 33']$.

The aperture mass dispersion unambiguously separates E- and B-modes in the considered range, $\theta_0 \in [4', 20']$ hence this method guarantees the revelation of potential systematics in contrast to $\xi_\pm$. As our data is B-mode free for $\theta_0 > 4'$, the influence of systematics on the calculated E-mode signal is negligible within the interval $\theta_0 \in [4', 20']$. We conclude that our cosmological parameter estimate using $\langle M_{\rm ap}^2 \rangle$ is therefore preferable to $\xi_\pm$.

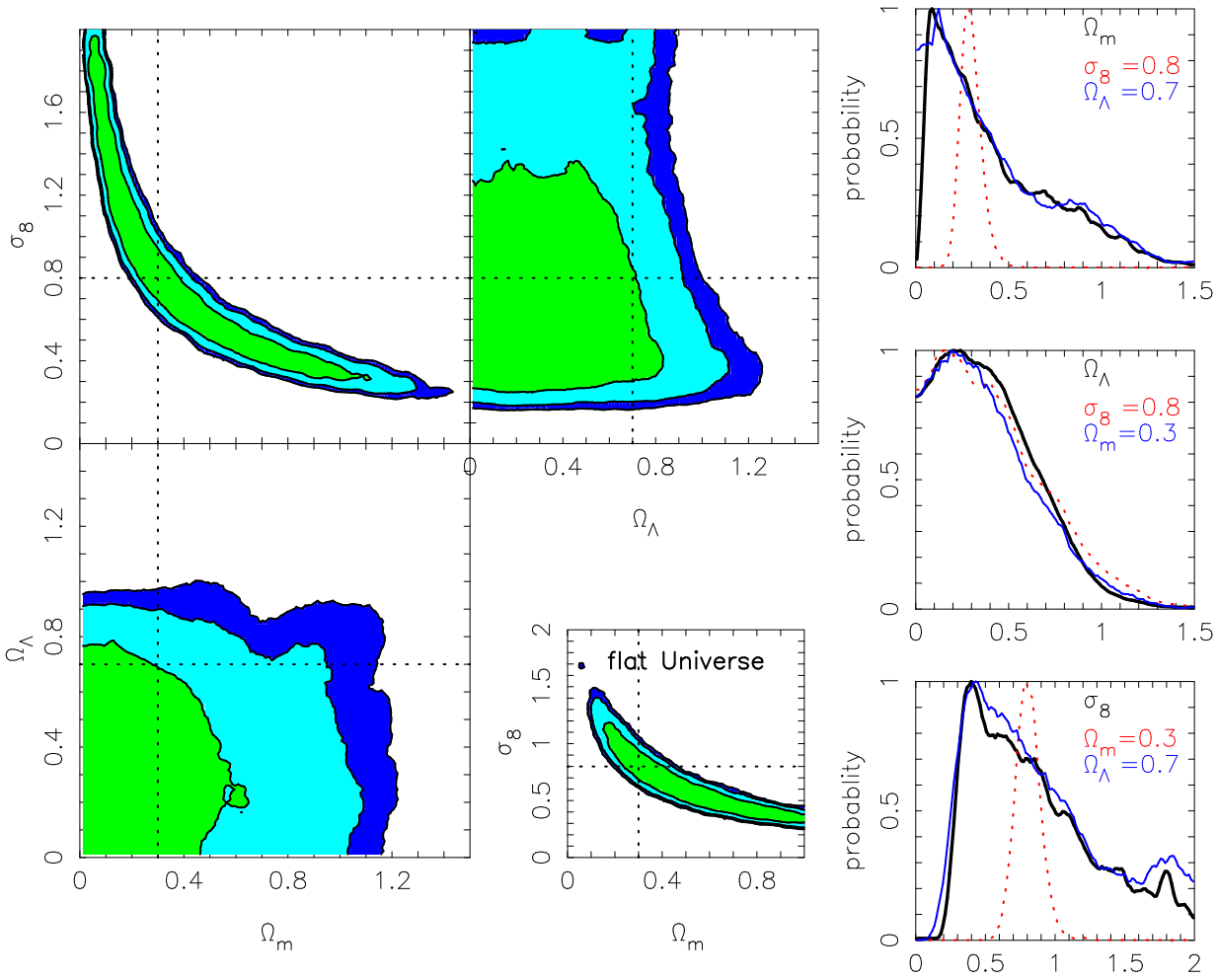

Figure 6.13: Model **B**: *bigger panels on the left*: joint constraints on Ω_m, σ_8 and Ω_Λ using the aperture mass dispersion for the Λ-Universe: Ω_Λ, $\Omega_\mathrm{m} \in [0, 1.5]$. *Upper right panel:* black line: PDF of Ω_m when marginalising over σ_8 and Ω_Λ. Blue line: PDF of Ω_m for $\Omega_\Lambda = 0.7$. Dotted red line: PDF of Ω_m for $\sigma_8 = 0.8$. *Centre right panel:* black line: PDF of Ω_Λ when marginalising over σ_8 and Ω_m. Blue line: PDF of Ω_Λ for $\Omega_\mathrm{m} = 0.3$. Dotted red line: PDF of Ω_Λ for $\sigma_8 = 0.8$. *Lower right panel:* black line: PDF of σ_8 when marginalising over Ω_m and Ω_Λ. Blue line: PDF of σ_8 for $\Omega_\Lambda = 0.7$. Dotted red line: PDF of σ_8 for $\Omega_\mathrm{m} = 0.3$. *Small panel in the lower middle*: comparison to model **A** (flat Universe): joint constraints on Ω_m, σ_8. Figure from Hetterscheidt et al. (2006).

Table 6.2: Joint constraints on Ω_m, σ_8 and Ω_Λ from our cosmic shear analysis using the aperture mass dispersion. Results for model **B** in which we assume Ω_Λ, $\Omega_\mathrm{m} \in [0, 1.5]$, $\Gamma = \Omega_\mathrm{m}\, h$, $n = 1$ and marginalise over the Hubble parameter and the redshift distribution as described in the text. Stated below are medians and $1\,\sigma$ errors.

add. prior	Ω_m	σ_8	Ω_Λ
none	$0.31^{+0.45}_{-0.21}$	$0.78^{+0.62}_{-0.36}$	$0.36^{+0.30}_{-0.23}$
$\Omega_\mathrm{m} = 0.3$	–	$0.79^{+0.09}_{-0.08}$	$0.33^{+0.33}_{-0.22}$
$\sigma_8 = 0.8$	$0.29^{+0.06}_{-0.05}$	–	$0.37^{+0.35}_{-0.26}$
$\Omega_\Lambda = 0.7$	$0.31^{+0.49}_{-0.22}$	$0.76^{+0.67}_{-0.36}$	–

6.4.2 Systematic errors

Bernardeau et al. (1997) showed that for a power-law power spectrum the cosmological parameters σ_8 and Ω_m are related to the top-hat shear variance $\langle\gamma^2\rangle$ (see Eq. 3.76) and the mean source redshift $\bar{z}_\mathrm{s}$ as:

$$\sigma_8^2\, \Omega_\mathrm{m}^{1.7} \propto \langle\gamma^2\rangle\, \bar{z}_\mathrm{s}^{-1.7}. \tag{6.22}$$

In the following we utilise this formula to obtain a rough systematic error estimate of σ_8.

Redshift distribution

The redshift of source galaxies has a large impact on the estimate of cosmological parameters, see Eq. (6.22). It is therefore crucial to know the redshift distribution accurately. See Huterer et al. (2006) and Van Waerbeke et al. (2006) for recent studies of photometric redshift errors and their influence on cosmic shear analyses.

Unlike most of the other cosmic shear surveys we estimate our redshift distribution from a sub-sample of the total lensing galaxy catalogue and not from an external redshift sample. This has two advantages. First, a redshift distribution of pure *lensing* galaxies is obtained. Second, the sample variance can be estimated from the field-to-field variance of the redshift distributions obtained from single fields and can be taken into account in the parameter fit.

The sources of error of the redshift distribution are: (A) the sample variance, as we only have redshift information available for 8% of our lensing galaxies, and (B) the uncertain redshift information especially for those galaxies with $R > 23\,\mathrm{mag}$.

To obtain a more reliable redshift distribution, about 7 % of the faint galaxies with highly uncertain redshifts are rejected using the aforementioned filter according to which the `hyper-z` 68 %-confidence interval should be smaller than $0.55\,(1 + z)$ (note that the `hyper-z`-uncertainties do not follow a Gaussian distribution). With this filter the mean redshift is 8 % lower than the mean redshift of the unfiltered redshift distribution, since most of the rejected redshifts lie in the interval $[0.8, 2.4]$, see Fig. 6.10. However, there are no spectroscopic or deep photometric redshift information obtained from bands which also

comprise the infrared available for a large part of the DPS lensing galaxies. Hence, it is impossible to judge if the rejected galaxies are really high-redshift galaxies or, for instance, dwarf galaxies at low redshift. Thus it is not possible to say whether we underestimate the mean redshift of our redshift distribution applying the aforementioned filter. Comparing our measured mean redshift with that from Brodwin et al. (2006) obtained from galaxies in the same magnitude range we are confident that at least the mean redshift of our estimated redshift distribution is not strongly biased.

To obtain a rough estimate of the systematic error in σ_8 due to the uncertain redshift distribution we simply assume the error of the mean redshift to be of the order of 8 %. This results approximately in an bias of 5 % for σ_8, see Eq. (6.22).

Non-lensing alignments

The observed ellipticity correlation, $\langle e^{\rm a}_{\rm obs} e^{\rm b}_{\rm obs}\rangle$, is given by

$$\langle e^{\rm a}_{\rm obs} e^{\rm b}_{\rm obs}\rangle = \langle e^{\rm a}_{\rm s} e^{\rm b}_{\rm s}\rangle + \langle \gamma^{\rm a} e^{\rm b}_{\rm s}\rangle + \langle \gamma^{\rm a}\gamma^{\rm b}\rangle, \tag{6.23}$$

where

- $\langle e^{\rm a}_{\rm s} e^{\rm b}_{\rm s}\rangle$ is the intrinsic correlation of galaxies (also called intrinsic alignment),
- $\langle \gamma^{\rm a} e^{\rm b}_{\rm s}\rangle$ is the correlation between the ellipticity of a galaxy at a low redshift $z_{\rm b}$ and the shear along the line-of-sight to a galaxy at a high redshift $z_{\rm a}$ (this is effect is called intrinsic shape-shear correlation), and
- $\langle \gamma^{\rm a}\gamma^{\rm b}\rangle$ is the cosmic shear signal.

The most important assumption which is made in weak lensing analyses is that correlations besides the shear-shear correlation are negligible. However, shear-shear correlation in cosmic shear analyses are typically very small and it is not obvious that the intrinsic alignment or the intrinsic shape-shear correlation will be small enough to be negligible for weak lensing studies.

Intrinsic alignment. Intrinsic alignments of spatially close galaxy pairs can arise from tidal gravitational fields of their surrounding LSS. However, the intrinsic alignment effect introduces only a small contamination of the cosmic shear signal on small angular scales ($\theta < 1.5\,$arcmin) (Heymans et al. 2006b). The contamination could be removed totally by using redshift information (King & Schneider 2003; Heymans & Heavens 2003) in the following way. Galaxy pairs with a small angular separation in the sky that are at the same redshift are simply not accounted for in the cosmic shear estimate. As we do not have multi-colour information for most of our fields we cannot correct for this effect. Furthermore, we do not test the intrinsic alignment in the DPS sample since we assume that the estimated photometric redshifts are not accurate enough. However, the intrinsic alignment contamination is probably negligible as we average over a wide range in redshift and only probe angular scales with $\theta > 4\,$arcmin (in the case of the $M_{\rm ap}$-statistics).

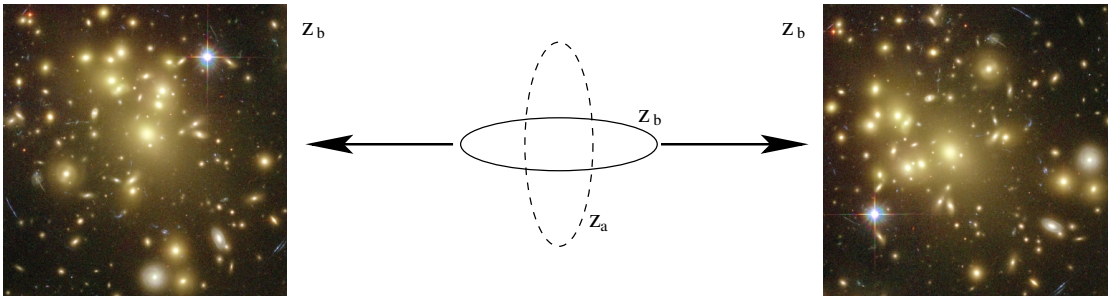

Figure 6.14: A sketch of the intrinsic shape-shear correlation: the tidal gravitational field of two galaxy clusters with redshift z_b can produce an alignment of a galaxy located at the same redshift z_b (solid ellipse) as well as a shape distortion of a more distant galaxy at redshift $z_\mathrm{a} > z_\mathrm{b}$ (dashed ellipse).

Intrinsic shape-shear correlation. A further source of bias is the intrinsic shape-shear correlation predicted by Hirata & Seljak (2004), measured by Mandelbaum et al. (2006) and analysed with numerical simulations by Heymans et al. (2006b). It can arise in the following way: a galaxy is located between two mass concentrations and is aligned according to its tidal field. A distant background galaxy is sheared according to the tidal gravitational field of the two mass concentrations, see Fig. 6.14. The resulting contribution of this intrinsic shape-shear correlation is negative, hence the measured cosmic shear signal is lowered. Heymans et al. (2006b) predicted that for a survey depth comparable to ours, this systematic effect produces a small negative B-mode and reduces the cosmic shear signal of the order of 15 % on scales below 20 arcmin resulting in an underestimate of σ_8 by about 7 %.

Model

Our estimate of cosmological parameters is based on the fitting formula proposed by Peacock & Dodds (1996). Hoekstra et al. (2005) performed a cosmic shear analysis and obtained a σ_8-value using the Smith et al. (2003) formalism of the non-linear mass power spectrum which is about 3.5 % smaller compared to the σ_8-value obtained using Peacock & Dodds. As our survey is comparable with Hoekstra et al. (2005) we assume that we overestimate σ_8 by about 4 % assuming the Smith et al. model to be closer to reality.

PSF correction

The presence of non-vanishing B-modes is a good indicator for systematics. However, Hoekstra (2004) pointed out that the influence of systematics on the cosmic shear signal (E-mode) is not necessarily the same as on the B-modes. This is probably the case in our analysis as indicated in Fig. 6.5. The PSF-anisotropy pattern of the WFI-fields have on average a larger impact on stellar E-modes than on stellar B-modes. In addition, we saw in Sect. 6.3.2 that the B-mode signal is zero and does not suffer from an imperfect anisotropy correction but the E-mode signal probably does. We concluded that the systematic error

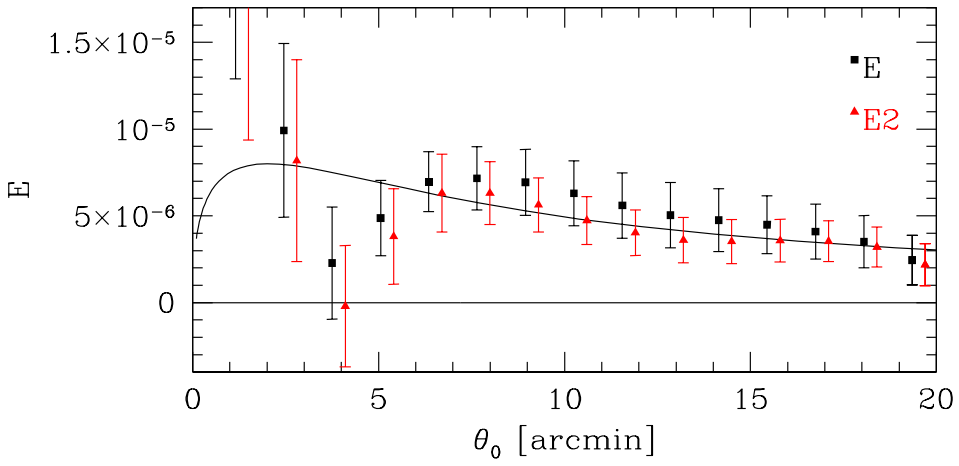

Figure 6.15: The E-mode signal of all fields (E, black points) and the E-mode signal without A901 and CL-fields (E2, red points).

of the E-mode signal for angular scales larger than four arcminutes due to an imperfect anisotropy correction is in any case significantly lower compared to the statistical errors.

The results in STEP 2 indicate that on average we overestimate the shear by 3 % resulting in an overestimation of the E-mode signal. In contrast, our cosmic shear analysis of synthetic `skymaker`-images in Sect. 6.1 suggests that we underestimate the cosmic shear signal by a few percent. Both, the probably small bias of the anisotropy correction and the bias in the shear estimate are simply accounted for by increasing the systematic error of σ_8 by $\pm 5\,\%$.

That the average B-mode signal is consistent with zero on scales larger than four arcminutes does not imply that single fields are B-mode free. It is possible that B-modes resulting from different systematic errors only average out to zero. If this is the case, the average E-mode value would be the same as without any systematic errors assuming that systematic errors bias the E-modes in the same way as B-modes. However, the full potential of the cosmic shear analysis is not achieved in this case as the errors would be larger than without any systematics. In our measurements, the error bars of the average B-mode signal for scales larger than 6 arcminutes are smaller than those of the E-mode signal. This is expected since B-modes are not affected by cosmic variance. Hence, single fields are not dominated by systematic effects and we do not include this possible increase of the systematic errors into the final error estimate.

Field selection

Our data set comprises one field with a massive cluster (A901) at low redshift ($z \approx 0.16$) and the CL-fields from the EDisCS that contain distant galaxy clusters that were known before selecting the fields (see Sect. 4.1.2). In addition, a field like A901 is unlikely to be part of a randomly chosen field sample. This can be construed as a prior knowledge which

introduces a bias on the cosmic shear signal. Replacing the E-modes of these fields by the average E-modes, the final signal decreases on average by roughly 20 % (Fig. 6.15). This results in a potential overestimation of σ_8 by approximately 10 %.

However, we found 158 shear-selected mass concentration candidates in the GaBoDS, where 72 of them are associated with concentration of bright galaxies (Schirmer et al. 2006) which is roughly in agreement with our predictions (Hetterscheidt et al. 2005). This indicates that on average at least one cluster-sized mass concentration per field could be present. Hence, it is not unlikely to randomly select fields like those from the EDisCS. We therefore assume in the following that the CL-fields do not bias our cosmic shear survey significantly towards high-density regions.

If we take into account only the A901 field as source of a field-selection bias we overestimate σ_8 by approximately 2 %.

Error summary

Taking all sources of systematic errors into account we see that we already entered a new phase of cosmic shear surveys. That is, the systematic errors are of the same order of magnitude as statistical errors. We obtain for the mass power spectrum normalisation, assuming $\Omega_\mathrm{m} = 0.3$ and including the statistical error and the rather conservative estimates of systematic errors: $\sigma_8 = 0.80(\pm 0.10 \pm 0.04 \pm 0.04 + 0.06 - 0.03 - 0.01)$ ($1\,\sigma$ statistical error, redshift bias, PSF correction bias, intrinsic shape-shear correlation bias, model bias, field selection bias). All given estimates of the systematic errors are maximum systematic errors.

Chapter 7

Summary, comparisons and outlook

7.1 Summary

We perform a cosmic shear analysis of $15\,\mathrm{deg}^2$ high-quality R-band data of the Garching-Bonn Deep Survey (GaBoDS) obtained with the Wide-Field-Imager at the ESO/MPG 2.2m telescope. The GaBoDS comprises $1.75\,\mathrm{deg}^2$ of $UBVRI$-band observations of the Deep Public Survey (DPS). We utilise this multi-colour data set to estimate a photometric redshift distribution of a sample of lensing galaxies in the magnitude interval $R \in [21.5, 24.5]$. Combining the cosmic shear signal with the photometric redshift distribution we determine constraints for the matter density Ω_m and the mass power spectrum normalisation σ_8.

Cosmic shear induces weak shape distortions of galaxy images and can only be measured statistically by averaging the distortion signal of a large number of galaxies. The GaBoDS is therefore a useful cosmic shear survey due to its field depth and seeing yielding the needed large number of background galaxies. Furthermore, the WFI has a very well-behaved point spread function over the total field-of-view permitting a robust PSF correction. With our automated data reduction pipeline developed to reduce such a large data volume in a homogeneous way and our robust PSF correction algorithm we are able to obtain a data set that is only mildly influenced by systematics yielding a cosmic shear signal that is not significantly biased on angular scales between 4 and 20 arcminutes.

Since cosmic shear analyses are independent of any assumptions on the relation between dark and luminous matter, constraints on cosmological parameters are unbiased. Hence, we employ a likelihood analysis of our data set to estimate some of these parameters, where we use the efficient Monte Carlo Markov Chain method to estimate the posterior likelihood.

As a main result we obtain for the mass power spectrum normalisation that $\sigma_8 = 0.80 \pm 0.10$ ($1\,\sigma$ statistical error) at a fixed matter density $\Omega_\mathrm{m} = 0.30$ assuming a flat Universe with negligible baryon content and marginalising over the Hubble parameter and the uncertainties in the fitted redshift distribution.

In the following we summarise is more detail the contents and main results of the individual foregoing Chapters.

Chapter 2: The standard model of cosmology

We describe the standard model of cosmology, the so-called concordance model. Combinations of CMB and other independent measurements indicate that the Universe is spatially flat. Furthermore, the dominant present-day composition of the Universe is the total matter and dark energy content, where the latter one causes the cosmic expansion to accelerate. A large part of the total matter consists of non-baryonic cold dark matter ($\sim 80\,\%$), whereas baryons only contribute with $\sim 20\,\%$.

Since we measure in our work the total matter and dark energy content, we discuss their properties and methods of constraining their values in detail. Additionally, we describe the formation of the LSS, its evolution in time and introduce the matter density power spectrum as a measure of its statistical properties. Since our final cosmic shear analysis yields a precise determination of the matter density power spectrum normalisation, σ_8, we discuss various complementary measurements of it, and give an overview of the latest cosmological parameter estimates obtained from WMAP.

Chapter 3: Weak lensing and cosmic shear

We present first the basic concepts and definitions of gravitational lensing, where we focus on weak gravitational lensing. An important connection between theory and practice is the relation between the shear and the observable ellipticity of galaxies. Here we describe this relation and introduce the aperture mass statistics. Furthermore, we present our cluster search method and findings in 50 VLT fields. Using that method we find five galaxy cluster candidates having a significant aperture mass signal ($S/N > 4$) that coincide with an overdensity in the light distribution.

Second, we discuss in detail how one can infer cosmological parameters from shear estimates. We give a derivation of a relation between the three-dimensional matter density power spectrum and the convergence power spectrum, which is linearly related to second-order shear statistics of the cosmic shear field. Finally, we present the shear estimators in practice yielding the connection to the convergence power spectrum.

Chapter 4: Data, data reduction & data quality

We present our stand-alone data reduction pipeline that the cosmology group in Bonn developed over the last six years to cope with the huge data flow from multi-chip wide field cameras used for current and future large surveys. For the subsequent cosmic shear analysis we reduce the GaBoDS data set using our pipeline. About 80 % of the data were collected from the ESO archive, the rest was obtained by own observations. The GaBoDS consists of 61 deep high-quality R-band WFI images corresponding to $15\,\mathrm{deg}^2$. The limiting magnitude ranges between 25.0 mag and 26.5 mag, and the seeing between $0\farcs75$ and $1\farcs20$. Individual fields of $30' \times 30'$ each form small patches comprising areas of $0.25\,\mathrm{deg}^2$ up to $2\,\mathrm{deg}^2$ that are randomly distributed over the sky (29 different lines-of-sight), hence single fields are nearly statistically independent. Additionally, we use the multi-colour DPS, a sub-set of GaBoDS, which was mainly carried out by the ESO Imaging Survey team. For

seven of the DPS fields *UBVRI*-band observations are available which yield photometric redshift information for 8% of the lensing galaxies considered for our complete cosmic shear analysis.

Chapter 5: From measured surface brightness to unbiased shear estimates

We describe the KSB method to correct for PSF effects and obtain a relation between shear and the observed galaxy ellipticity. Since the shear signal has to be measured from observed faint galaxy images in an accurate, unbiased way the Shear TEsting Programme, a unique collaborative programme of 16 weak lensing groups, was initiated. We present the main results. Before STEP we underestimated the shear by about 17 % using the trace of P^{g}. After reanalysing the STEP 1 data set using the full tensor calculation of P^{g} and a different weighting scheme, we obtain the average shear without any significant bias. However, using this approach the noise of the shear estimate increases strongly for real data. For our cosmic shear analysis of the GaBoDS we therefore use the trace of P^{g} and introduce a calibration factor to reduce the bias.

To obtain a catalogue of galaxy positions and shear estimates for every fully reduced GaBoDS field suitable for cosmic shear studies, we first create raw object catalogues for all fields using `SExtractor`. Second, we measure the raw ellipticities of the faint galaxies, correct them for isotropic smearing of the atmosphere and anisotropic distortions to obtain unbiased shear estimates. Third, we filter the catalogues in the magnitude-half-light radius plane to exclude noise objects and to obtain a magnitude-limited sample having a uniform depth. By this means we obtain the final shear catalogues suitable for our cosmic shear analysis and redshift estimates.

Chapter 6: Cosmic shear analysis

We perform a cosmic shear analysis of the GaBoDS. For that we use the final shear catalogues to calculate the two-point shear-shear correlation functions and subsequently the aperture mass dispersion. To reveal possible systematics in the data the aperture mass dispersion is most convenient. Our cosmic shear measurement is B-mode free within $1\,\sigma$ for angular scales larger than four arcminutes. Furthermore, the signal of the cross correlation between PSF-corrected ellipticities of galaxies and uncorrected ellipticities of stars is much smaller than the cosmic shear signal. Hence there are no significant systematic errors resulting from the data treatment (PSF correction, galaxy selection) left in the cosmic shear signal on angular scales between 4 and 20 arcminutes. This encourages us to perform a cosmological parameter estimate and to use the GaBoDS data also for further cosmological analyses, such as the galaxy bias studies carried out by Simon et al. (2006).

We estimate a redshift distribution from *lensing* galaxies of seven *UBVRI*-band images (each $0.25\,\mathrm{deg}^2$) of the DPS and do not use an external redshift sample. In this way, the total error of our redshift distribution includes cosmic variance since we estimate it from seven statistically independent WFI fields.

In contrast to many other cosmic shear analyses, we estimate the noise covariance

matrix *directly from the data without any further assumptions* and do not compute it analytically making simplified assumptions such that for evaluating the four-point function of the shear the cosmic shear field is Gaussian. This approach is possible since the GaBoDS fields are almost uncorrelated. In this way we properly account for the cosmic variance which dominates the noise of the cosmic shear measurements on angular scales beyond a few arcminutes.

For determining constraints on cosmological parameters we combine our estimated redshift distribution with the measured cosmic shear signal and employ the Monte Carlo Markov Chain method to estimate the posterior likelihood.

The size of the GaBoDS is not large enough to obtain reasonable constraints on several cosmological parameters with weak lensing alone. Our analysis is therefore basically concentrated on the mass power spectrum normalisation, σ_8, and the total matter density, Ω_m using strong priors from other experiments. Our σ_8 result for fixed Ω_m is of comparable accuracy as those obtained from measurements of the CMB and galaxy clusters. For their estimate we assume a flat ΛCDM universe ($\Omega_\mathrm{m} + \Omega_\Lambda = 1$), with negligible baryon content ($\Gamma = \Omega_\mathrm{m}\, h$), a slope of the primordial power spectrum of unity, $n_\mathrm{s} = 1$, and we use the CDM transfer function given in Bardeen et al. (1986). We derive σ_8 and Ω_m while marginalising over the uncertainties in the Hubble parameter, $h = 0.7$ using a Gaussian of width $\sigma_h = 0.1$, and the source redshift distribution, $p(z)$. As a result we obtain $\sigma_8 = 0.61^{+0.31}_{-0.20}$ and $\Omega_\mathrm{m} = 0.46^{+0.30}_{-0.22}$ from the M_ap-statistics using the Peacock & Dodds (1996) model of the non-linear mass power spectrum. For a fixed total matter density of $\Omega_\mathrm{m} = 0.3$, we obtain $\sigma_8 = 0.80 \pm 0.10$ ($1\,\sigma$ statistical error).

Finally, we discuss various systematic errors and roughly estimate their total magnitude to be of the same order as the statistical errors. With respect to the magnitude of the systematics, the most uncertain sources are the redshift distribution and the intrinsic shape-shear correlation.

7.2 Comparison with the CFHTLS

In this Section we compare our cosmic shear analysis of the GaBoDS with that of the CFHTLS performed by Hoekstra et al. (2005).

The Canada-France-Hawaii Telescope Legacy Survey (CFHTLS) aims to image 170 deg^2 in five filters using the $1 \times 1\,\mathrm{deg}^2$ *MegaCam* camera having a pixel size of $0\farcs186$. So far, Hoekstra et al. (2005), henceforth H05, analysed 22 deg^2 of i-band data. They performed a cosmic shear analysis of 1.6×10^6 galaxies in the magnitude interval $i \in [21.5, 24.5]$ resulting in effective galaxy number density of $n_\mathrm{eff} = 12\,\mathrm{arcmin}^{-2}$. Thus, the CFHTLS in the current state is of comparable size and depth as the GaBoDS.

A difference of the CFHTLS and GaBoDS is the data treatment:

- For the CFHTLS images the applied dither pattern are much smaller compared to those of our observations with WFI yielding a smaller number of objects in the overlap region. With this approach it is much more difficult to obtain a robust astrometric

solution. However, the PSF anisotropy of the stacked MegaCam images seems not to be influenced by this.

- The PSF anisotropy pattern varies smoothly over the total field-of-view. However, due to the large size of the field they correct the PSF anisotropy separately for each CCD chip of the camera with a low-order polynomial, whereas we perform this fit over the total field-of-view.

H05 obtained a cosmic shear signal that is almost B-mode free. Additionally, their cross correlation signal of uncorrected galaxies and stars is much smaller than ours. Their results seem to be free from any systematic errors resulting from insufficient PSF corrections and data treatment. Hence, the discussed points do not affect a proper cosmic shear analysis and determination of the constraints of the cosmological parameters.

For the cosmological parameter estimate H05 assumed a flat ΛCDM Universe with negligible baryon content, and used the same transfer function as we did. They determined constraints for the total matter and mass power spectrum normalisation with a top-hat prior: $\Omega_\mathrm{m} \in [0, 1]$, $\sigma_8 \in [0.5, 1.2]$. They marginalised over the uncertainties in the source redshift distribution ($z_0 \in [0.613, 0.721]$) and the Hubble parameter ($h \in [0.6, 0.8]$) also using a top-hat prior. We show in Fig. 7.1 the joint marginalised constraint on σ_8 and Ω_m obtained from their survey. For a fixed total matter density of $\Omega_\mathrm{m} = 0.3$, H05 obtained in their work $\sigma_8 = 0.88 \pm 0.06$ ($1\,\sigma$ statistical error) using the Peacock & Dodds model. The difference to our cosmic shear analysis is as follows. First, H05 used top-hat priors on the redshift distribution and the Hubble parameter, whereas we used a Gaussian prior. Second, our parameter space is eight-dimensional compared to three dimensions in their case since we used more fit parameters of the redshift distribution. Third, the Ω_m and σ_8 boundaries of the parameter space are much wider in our case. We are able to explore such a large likelihood surface since we do not calculate the likelihood function on a grid but use the more elaborate MCMC method, where the likelihood function is calculated at randomly selected positions along the Markov Chain. However, the main differences in the statistical analysis of the data in comparison to our approach are that

- they calculated the noise covariance matrix according to Schneider et al. (2002) (noise properties are assumed to be Gaussian) since their fields are not statistically independent. This results into an underestimation of the statistical errors.

- they estimated their redshift distribution from the accurate photometric redshift studies of the Hubble Deep Field North and South. Both fields are *empty* fields without prominent foreground structures, and only cover a small area in the sky ($2 \times 3' \times 3'$). Hence, their estimated redshift distribution suffers from a large cosmic variance. On the other side, our redshift estimates suffer from the limited number of filters resulting in uncertain redshift estimates especially for galaxies with $R > 23\,\mathrm{mag}$, and the limited number of photometric redshifts which can be compared with spectroscopic redshifts. The systematic errors of the final cosmological parameter constraints due to the redshift distribution are in both cases difficult to estimate.

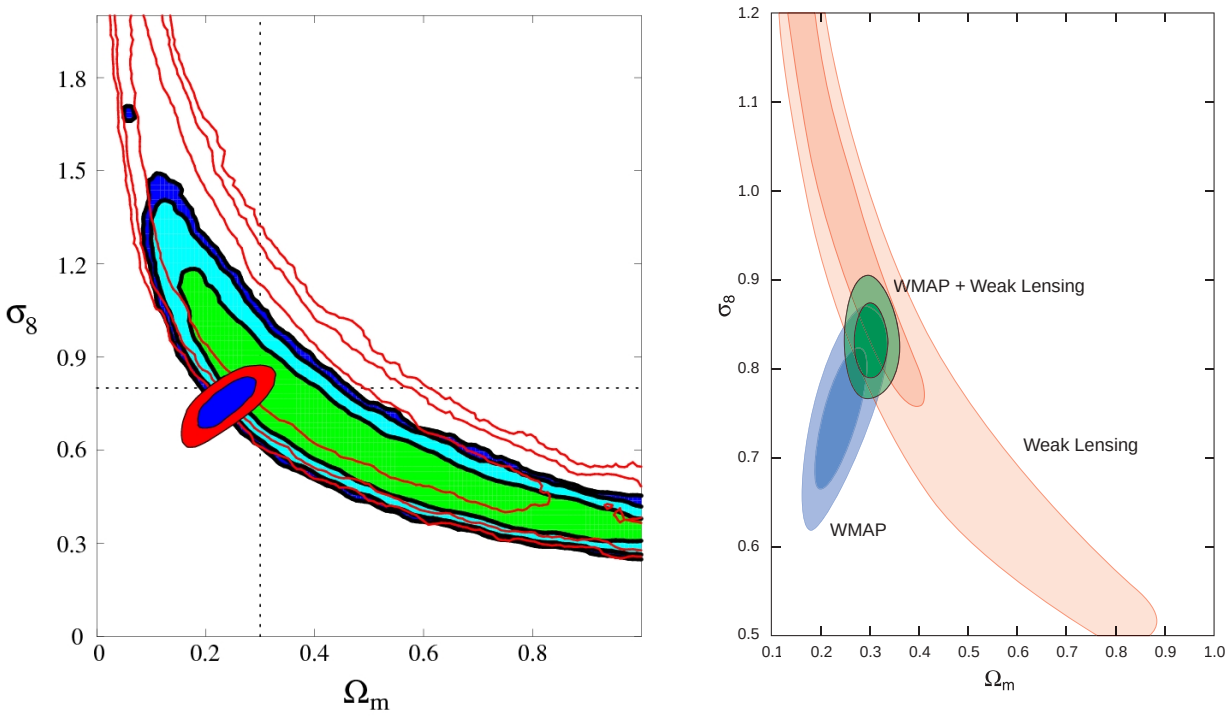

Figure 7.1: *Left panel*: Joint marginalised constraint on σ_8 and Ω_m for the GaBoDS data set (same as in Fig. 6.12). Overlaid is a sketch of the joint constraint for WMAP only ($1\,\sigma$ and $2\,\sigma$ contours in red and blue, respectively). *Right panel*: The blue, red and green ($1\,\sigma$ and 2σ) contours show the joint marginalised constraints on σ_8 and Ω_m for WMAP only, CFHTLS (weak lensing) only and WMAP + CFHTLS, respectively. For all constraints the same priors on the input parameters are assumed. In the cosmic shear analysis an additional marginalisation over the uncertainties in the source redshift distribution using a top-hat prior is performed. The right Figure is from Spergel et al. (2006).

The only conceivable bias in measuring the power spectrum normalisation is their estimated redshift distribution, most probably resulting into an overestimation of σ_8 (Yannick Mellier, private communication).

7.3 Comparison with WMAP and other experiments

We also compare recent results of determinations of the mass density power spectrum normalisation with ours, where we focus on the result of WMAP.

For the next few years CMB studies will be unsurpassed as to constraints on cosmological parameters. One exception is the matter density power spectrum normalisation, σ_8. WMAP measures the temperature power spectrum at large angular scales (significant for $\theta > 15\,\mathrm{arcmin}$) for the early Universe (about $3.8 \times 10^5\,\mathrm{yrs}$ after the Big Bang).

However, σ_8 is defined as the dispersion of the *present-day* density contrast within spheres of radius $R = 8\,h^{-1}$Mpc. Measuring σ_8 on small scales in the nearby Universe ($z < 1$) should potentially yield tighter constraints on σ_8. Furthermore, by probing the CMB σ_8 is highly degenerate with the optical depth, τ, and the slope of the initial power spectrum, n_s (Sect. 2.2.6). Only with measurements of the polarization power spectrum these degeneracies can be broken. However, it is still very difficult to obtain a clear CMB polarization power spectrum since the noise of foreground sources dominates the polarisation signal.

As already mentioned above, the WMAP and cosmic shear measurements have degeneracies in the Ω_m-σ_8 plane. But the contours of their joint marginalised constraints are almost perpendicular. Hence, combining both measurements substantially improves the estimate of σ_8 and Ω_m. In the right panel of Fig. 7.1 we display the $1\,\sigma$ and 2σ confidence regions of σ_8 and Ω_m for WMAP + CFHTLS.

In the left panel of Fig. 7.1 we display the $1\,\sigma$ and $2\,\sigma$ contours of the joint marginalised constraints on σ_8 and Ω_m for WMAP and the $1\,\sigma$, $2\,\sigma$ and $3\,\sigma$ contours obtained from our cosmic shear analysis. As in the right panel, the typical 'banana'-shaped cosmic shear contours appear, which are orientated perpendicular with respect to the WMAP contours. In contrast to the WMAP + CFHTLS results, however, the $1\,\sigma$ contour levels of WMAP and our joint constraints do overlap.

In Fig. 7.2 we display the recent determinations of σ_8 for a fixed total matter density of $\Omega_\mathrm{m} = 0.3$ obtained by cosmic shear and galaxy cluster surveys (mostly X-ray). Additionally we plot the WMAP three year result of σ_8. Within the error bars (mostly pure statistical ones) most cosmic shear results are consistent with the (unweighted) average value of $\sigma_8 \approx 0.85$ obtained from all cosmic shear surveys between 2002 and 2006. The (unweighted) average σ_8-value of galaxy clusters is $\sigma_8 \approx 0.73$ (again obtained from the given galaxy cluster surveys between 2002 and 2006). Hence, cosmic shear prefers a larger value than galaxy clusters or CMB measurements.

7.4 Outlook

The primary science goal of cosmic shear surveys in the next years is to measure the statistical properties of dark and luminous matter especially on quasi-linear and non-linear scales. Theoretical predictions of the cosmic shear signal on small angular scales are less accurate than the signal obtained from the planned large surveys.

Using additional information about the redshift distribution of galaxies, cosmic shear measurements can be used to study the structure formation model as a function of redshift. To make use of the full potential of weak gravitational lensing measurements and to reach a high accuracy in the determination of cosmological parameters it is therefore imperative to improve the shear estimates. In the framework of the STEP project we are continuously working on it. For future surveys we need sub-percent accuracy shape measurement that are unbiased and robust. Not only the average shear estimates should be unbiased but also shear estimates for different galaxy populations. Shear estimates should therefore be unbiased as a function of several parameters such as: magnitude of a galaxy, galaxy size,

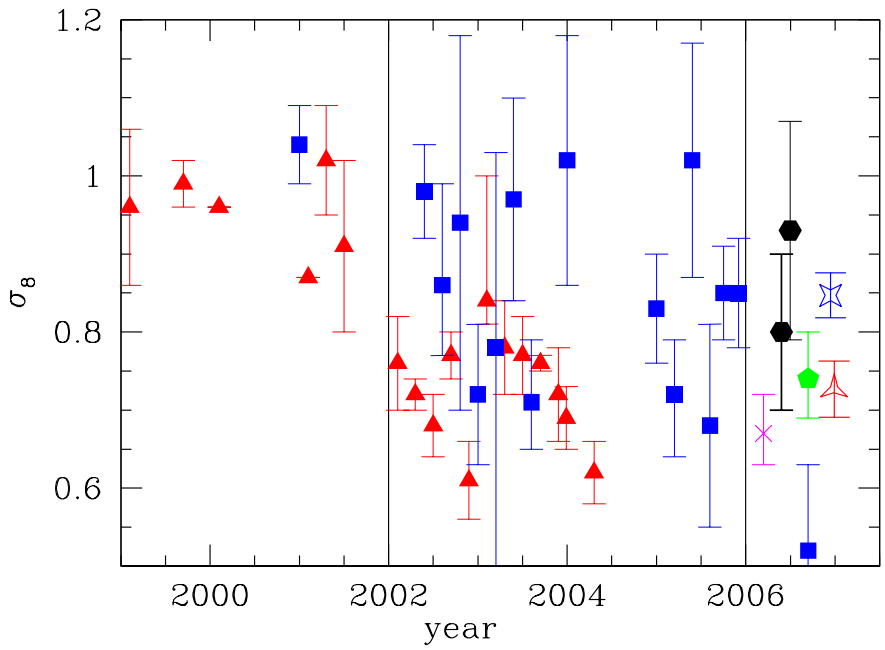

Figure 7.2: Recent determinations of $\sigma_8(\Omega_\mathrm{m} = 0.3)$ using clusters (red triangles) and cosmic shear (blue squares) in comparison to our results (M_ap: solid black hexagon with bold error bars, $\xi_\pm$: black hexagon with light error bars) and the WMAP three year result (black pentagon). The open red triangle and open blue star on the right are the average of all σ_8 determinations between 2002 and 2006 (indicated by the vertical line) using clusters and cosmic shear, respectively (error bars of single measurements are not taken into account). The WMAP result of σ_8 would be larger if Ω_m is fixed to 0.3. Within the same year the measurement points are not in chronological order. Values are taken from table 7.1. Points from right to the left in the diagram are associated with values from top down in the table. Figure from Hetterscheidt et al. (2006).

galaxy ellipticity, PSF type and PSF size. In order to optimally probe the accuracy of shape measurements as a function of these parameters it is planned to create several sets of simple ground-based simulations with these parameters kept fixed within one set. With the simple simulations at hand it should be possible to track down possible systematics in the isotropic PSF correction algorithm like the unwanted dependence of the shear estimate on magnitude and galaxy size.

Since residuals arising from an imperfect PSF anisotropy correction mimic a cosmic shear signal, we plan to implement and test the elaborate *principal component analysis* of Jarvis & Jain (2004) to reduce this effect.

Furthermore, in order not to compromise cosmological parameter estimates it is essential to have unbiased and precise redshift estimates, first to obtain unbiased redshift distributions of lensing galaxies, and secondly to eliminate possible contaminations of the intrinsic alignment and the intrinsic shape-shear correlation using shear tomography (shear

cross correlation of galaxies in different redshift bins). Although the intrinsic shape-shear correlation has been analysed with N-body simulations using simple galaxy models, the impact on deep cosmic shear measurements is still unclear. With accurate photometric redshifts at hand, measurements of cross-correlation tomography could be carried out to provide a useful diagnostic tool (Hirata & Seljak 2004).

Most cosmic shear surveys that determine constraints on cosmological parameters use the Peacock & Dodds approximation of the non-linear evolution of the matter density power spectrum. However, the approximation is not accurate enough for future large weak lensing surveys. Ray-tracing through N-body simulations are therefore planned to provide accurate theoretical predictions especially for the non-linear part of the power spectrum.

Our cosmic shear result and the ongoing improvements in redshift and shear estimates are quite encouraging for the upcoming wide-field multi-colour surveys as the future KIlo Degree Survey (KIDS), starting late in 2007. The KIDS aims to image a contiguous area of $5000\,\mathrm{deg}^2$ in five colours with the newly built OmegaCAM camera mounted at the VLT Survey Telescope (VST). In combination with UKIDS (an infrared survey with $4000\,\mathrm{deg}^2$) the data will yield photometric redshifts accurate to $\Delta z/(1+z) = 0.03$ for typical $r' = 23.5$ galaxies, rising to 10 % uncertainty at $r' = 25$. In the primary lensing colour the limiting magnitude is predicted to be $r' = 24.3$ ($10\,\sigma$ sky level measured in a circular aperture of $2''$ radius) and the median seeing is predicted to be $0\farcs6$. The depth, size and average seeing of KIDS will yield about 3×10^8 galaxies to a median redshift of $z \approx 0.8$. The KIDS will therefore be the largest cosmic shear survey for at least the next seven years.

With our new stand-alone data reduction pipeline we are well prepared to automatically process the huge amount of data. We will first focus on analysing the basic PSF properties of the OmegaCAM camera. Second, we will perform a cosmic shear analysis of the KIDS data similar to the GaBoDS data. With the KIDS data set at hand we will extract various two-point shear statistics and will be able to measure the angular matter density power spectrum on large as well as on small angular scales with high precision. Compared to current data the statistical errors of cosmological parameter estimations will be reduced at least by a factor of 20, not only because the number of background galaxies is larger but also the number of galaxy pairs will increase dramatically, in particular for large angular scales. Furthermore, with such a large multi-colour data set at hand shear tomography analyses can be performed and higher-order statistics can be applied to the data, partly breaking parameter degeneracies. With the large KIDS data set, the planned improvements in the PSF correction, redshift estimates and in the theoretical predictions using ray-tracing through N-body simulations one can start to probe the equation of state of dark energy.

Table 7.1: Recent determinations of σ_8 using clusters, cosmic shear and WMAP. The WMAP result of σ_8 would be larger if Ω_m is fixed to 0.3. The result from Chang et al. (2004) is obtained from a radio survey assuming that the median redshift is $z_\mathrm{m} = 2.2$.

Reference	σ_8 ($\Omega_\mathrm{m} = 0.3$)	Method	Sample	Area [deg^2]	n [arcmin^{-1}]
our measurements	0.80 ± 0.10	WL: $\langle M_\mathrm{ap}^2 \rangle$	GaBoDS	13	12
	0.93 ± 0.14	WL: $\xi_\pm$	GaBoDS	13	12
Schrabback et al. (2006)	$0.52^{+0.11}_{-0.15}$	WL: $\xi_\pm$	HST/ACS	0.25	96
Semboloni et al. (2006)	0.85 ± 0.06	WL: ξ^E	CFHTLS deep+shallow		
Semboloni et al. (2006)	0.94 ± 0.15	WL: ξ^E	CFHTLS deep	2.1	22
Hoekstra et al. (2005)	0.85 ± 0.05	WL: ξ^E	CFHTLS shallow	22	13
Massey et al. (2005)	1.02 ± 0.15	WL: $\xi_\pm$	WHT	4	15
Jarvis et al. (2005)	$0.72^{+0.08}_{-0.07}$	WL:	CTIO	75	7.5
Heymans et al. (2005)	0.68 ± 0.13	WL: $\xi_\pm$	HST GEMS	0.22	60
Van Waerbeke et al. (2005)	0.83 ± 0.07	WL: ξ^E	VIRMOS	8.5	12.5
Heymans et al. (2004)	0.67 ± 0.10	WL:	COMBO-17	1.25	
Rhodes et al. (2004)	1.02 ± 0.16	WL: $\langle \bar{\gamma}^2 \rangle$	HST	0.25	29
Chang et al. (2004)	1.0 ± 0.2	WL: $\langle M_\mathrm{ap}^2 \rangle$	VLA	10000	0.01
Bacon et al. (2003)	0.97 ± 0.13	WL: $\langle \bar{\gamma}^2 \rangle$	Keck &	0.6	27.5
			WHT	1.0	15
Brown et al. (2003)	0.72 ± 0.09	WL:	COMBO-17	1.25	32
Hamana et al. (2003)	$0.78^{+0.55}_{-0.25}$	WL: $\langle M_\mathrm{ap}^2 \rangle$	SUBARU	2.1	32
Jarvis et al. (2003)	$0.71^{+0.06}_{-0.08}$	WL:	CTIO	75	7.5
Hoekstra et al. (2002b)	$0.86^{+0.09}_{-0.13}$	WL: $\langle M_\mathrm{ap}^2 \rangle$	RCS	45.4	9
Hoekstra et al. (2002b)	$0.81^{+0.07}_{-0.10}$	WL: $\langle \bar{\gamma}^2 \rangle$	RCS	16.4	9
Van Waerbeke et al. (2002)	0.98 ± 0.06	WL: $\langle M_\mathrm{ap}^2 \rangle$	VIRMOS	8.5	15
Refregier et al. (2002)	0.94 ± 0.24	WL: $\langle \bar{\gamma}^2 \rangle$	HST	0.36	23
Rhodes et al. (2001)	$0.91^{+0.25}_{-0.30}$	WL: $\langle \bar{\gamma}^2 \rangle$	HST	0.05	23
Maoli et al. (2001)	1.04 ± 0.05	WL: $\langle \bar{\gamma}^2 \rangle$	VLT	0.65	21
Dahle (2006)	$0.67^{+0.05}_{-0.04}$	WL clusters			
Henry (2004)	0.62 ± 0.04	X-ray clusters	HA91+EMSS		
Allen et al. (2003)	0.70 ± 0.04	X-ray clusters	REFLEX+BCS		
Bahcall et al. (2003)	0.72 ± 0.06	X-ray clusters	SDSS		
Schuecker et al. (2003)	0.76 ± 0.01	X-ray clusters	REFLEX		
Pierpaoli et al. (2003)	0.77 ± 0.05	X-ray clusters	HIFLUGCS		
Pierpaoli et al. (2003)	0.78 ± 0.06	X-ray clusters	REFLEX		
Viana et al. (2003)	$0.84^{+0.16}_{-0.03}$	X-ray clusters			
Viana et al. (2002)	0.61 ± 0.05	X-ray clusters	REFLEX		
Reiprich & Böhringer (2002)	0.68 ± 0.04	X-ray clusters	REFLEX		
Rosati et al. (2002)	0.72 ± 0.02	X-ray clusters	RDCS		
Seljak (2002)	0.76 ± 0.06	X-ray clusters			
Wu (2001)	0.91 ± 0.11	X-ray clusters	HA91		
Pierpaoli et al. (2001)	1.02 ± 0.07	X-ray clusters			
Oukbir & Arnaud (2001)	0.91	X-ray clusters			
Blanchard et al. (2000)	0.96	X-ray clusters			
Viana & Liddle (1999)	0.99 ± 0.03	X-ray clusters			
Borgani et al. (1999)	0.96 ± 0.1	X-ray clusters			
Spergel et al. (2006)	$0.74^{+0.05}_{-0.06}$	CMB	WMAP		

Appendix A

The KSB algorithm

Kaiser, Squires & Broadhurst (hereafter KSB) developed in 1995 an algorithm to correct for PSF smearing and its anisotropy and to recover unbiased shear estimates from measured ellipticities. In this Chapter we derive the KSB algorithm, where we closely follow the derivation from the weak lensing review of Bartelmann & Schneider (2001).

The shape of an object is described by its ellipticity χ (Sect. 3.1.3),

$$\chi = \chi_1 + \mathrm{i}\chi_2 = \frac{Q_{11} - Q_{22}}{\mathrm{tr}\, Q_{ij}} + \mathrm{i}\frac{2Q_{12}}{\mathrm{tr}Q_{ij}}, \tag{A.1}$$

where Q_{ij} are the weighted quadrupole moments of the surface brightness $I(\boldsymbol{\theta})$,

$$Q_{ij} = \int \mathrm{d}^2\theta\, (\theta_i - \bar{\theta}_i)(\theta_j - \bar{\theta}_j)\, I(\boldsymbol{\theta})\, W\left(\left|\boldsymbol{\theta} - \bar{\boldsymbol{\theta}}\right|\right), \tag{A.2}$$

and $\bar{\boldsymbol{\theta}}$ is the object centre (see Sect. 5.2.1).

The observed surface brightness $I^{\mathrm{obs}}(\boldsymbol{\theta})$ of an arbitrary object is given by the convolution of the intrinsic surface brightness $I^{\mathrm{intr}}(\boldsymbol{\theta})$ and the PSF P,

$$I^{\mathrm{obs}}(\boldsymbol{\theta}) = \int \mathrm{d}^2\vartheta\, I^{\mathrm{intr}}(\boldsymbol{\vartheta}) P(\boldsymbol{\theta} - \boldsymbol{\vartheta}). \tag{A.3}$$

It is assumed that for ground-based observations P is nearly isotropic. So P can be decomposed into an isotropic part P^{iso} which is defined as the azimuthal average over P and a small anisotropic part q,

$$P(\boldsymbol{\vartheta}) = \int \mathrm{d}^2\varphi\, q(\boldsymbol{\varphi}) P^{\mathrm{iso}}(\boldsymbol{\vartheta} - \boldsymbol{\varphi}). \tag{A.4}$$

Both quantities P^{iso} and q are normalised to unity,

$$\int \mathrm{d}^2\varphi\, P^{\mathrm{iso}}(\boldsymbol{\varphi}) = 1 = \int \mathrm{d}^2\varphi\, q(\boldsymbol{\varphi}) \tag{A.5}$$

and have vanishing first moments,

$$\int \mathrm{d}^2\varphi\, \boldsymbol{\varphi}\, P^{\mathrm{iso}}(\boldsymbol{\varphi}) = 0 = \int \mathrm{d}^2\varphi\, \boldsymbol{\varphi}\, q(\boldsymbol{\varphi}) \tag{A.6}$$

In the following we define various brightness profiles which are related to the PSF, P, or its isotropic part, P^{iso}:

$$I^{\mathrm{obs}}(\boldsymbol{\theta}) = \int \mathrm{d}^2\varphi\, I^{\mathrm{l}}(\boldsymbol{\varphi}) P(\boldsymbol{\theta}-\boldsymbol{\varphi}), \tag{A.7}$$

$$I^{\mathrm{iso}}(\boldsymbol{\theta}) = \int \mathrm{d}^2\varphi\, I^{\mathrm{l}}(\boldsymbol{\varphi}) P^{\mathrm{iso}}(\boldsymbol{\theta}-\boldsymbol{\varphi}), \tag{A.8}$$

$$I^{0}(\boldsymbol{\theta}) = \int \mathrm{d}^2\varphi\, I^{\mathrm{intr}}(\boldsymbol{\varphi}) P^{\mathrm{iso}}(\boldsymbol{\theta}-\boldsymbol{\varphi}), \tag{A.9}$$

where

- I^{obs} is the observable surface brightness obtained by the lensed surface brightness, I^{l}, smeared with the PSF, P,
- I^{iso} is obtained by the lensed surface brightness, I^{l}, smeared with the isotropic part of the PSF, P^{iso}, and
- I^0 is obtained by the intrinsic surface brightness, I^{intr}, smeared with P^{iso}.

Both brightness profiles, I^{iso} and I^0, are in practice unobservable.

From each brightness profile the corresponding quadrupole tensors and ellipticities are calculated with Eqs. (A.2) and (A.1), respectively. The ellipticities χ^{iso} and χ^0 can be interpreted as the ellipticity an observer would obtain if the lensed/unlensed image would only be affected by a perfectly isotropic PSF.

The fundamental assumption for weak gravitational lensing observations was that the intrinsic ellipticities are randomly oriented, $\langle\chi^{\mathrm{intr}}\rangle = 0$ (Sect. 3.1.3). This still holds for the ellipticity χ^0, because the orientation of χ^{intr} is unaffected by the isotropic part of the PSF, P^{iso}.

A relation between χ^{iso} and χ^{obs} and the role of the smear polarisability P^{sm}

In this Section the effect of the anisotropic part of the PSF, q, on the observed ellipticity χ^{obs} is calculated. According to Eqs. (A.4), (A.7) and (A.8) we can write

$$I^{\mathrm{obs}}(\boldsymbol{\theta}) = \int \mathrm{d}^2\varphi\, q(\boldsymbol{\theta}-\boldsymbol{\varphi})\, I^{\mathrm{iso}}(\boldsymbol{\varphi})\ . \tag{A.10}$$

We now consider

$$\begin{aligned}\int \mathrm{d}^2\theta\, f(\boldsymbol{\theta})\, I^{\mathrm{obs}}(\boldsymbol{\theta}) &= \int \mathrm{d}^2\varphi\, I^{\mathrm{iso}}(\boldsymbol{\varphi}) \int \mathrm{d}^2\vartheta\, f(\boldsymbol{\varphi}+\boldsymbol{\vartheta})\, q(\boldsymbol{\vartheta}) \\ &= \int \mathrm{d}^2\varphi\, I^{\mathrm{iso}}(\boldsymbol{\varphi})\, f(\boldsymbol{\varphi}) + \frac{1}{2}\, q_{kl} \int \mathrm{d}^2\varphi\, I^{\mathrm{iso}}(\boldsymbol{\varphi}) \frac{\partial^2 f}{\partial\varphi_k \partial\varphi_l} + \mathcal{O}(q^2),\end{aligned} \tag{A.11}$$

where we assumed that $f(\boldsymbol{\theta})$ is an arbitrary function, and

$$q_{ij} = \int \mathrm{d}^2\varphi\, q(\boldsymbol{\varphi})\, \varphi_i \varphi_j. \tag{A.12}$$

We used the Taylor expansion of f given by

$$\begin{aligned} f(\boldsymbol{\varphi}+\boldsymbol{\vartheta}) &= f(\boldsymbol{\varphi}) + \vartheta_1 \frac{\partial f}{\partial \varphi_1} + \vartheta_2 \frac{\partial f}{\partial \varphi_2} + \frac{1}{2}\vartheta_1^2 \frac{\partial^2 f}{\partial \varphi_1^2} + \frac{1}{2}\vartheta_2^2 \frac{\partial^2 f}{\partial \varphi_2^2} + \vartheta_1\vartheta_2 \frac{\partial^2 f}{\partial \varphi_1 \partial \varphi_2} + R_n \\ &= f(\boldsymbol{\varphi}) + \vartheta_i \frac{\partial f}{\partial \varphi_i} + \frac{1}{2}\vartheta_i\vartheta_j \frac{\partial^2 f}{\partial \varphi_i \partial \varphi_j} + R_n, \end{aligned} \tag{A.13}$$

and the fact that q is normalised (Eq. A.5) and has zero mean (Eq. A.6). The trace of the tensor q_{ij} will change the size of the object but not the shape, so q_{ij} is trace-less: $q_{11} = -q_{22}$. In addition q_{ij} is symmetric. For convenience we define

$$q_1 \equiv q_{11} - q_{22}, \quad q_2 \equiv 2q_{12}. \tag{A.14}$$

In the following we only consider terms up to linear order in q. Hence we can replace I^{iso} by I^{obs} in the final term in Eq. (A.11) since the difference would yield a negligible term ($\propto \mathcal{O}(q^2)$). We obtain:

$$\int \mathrm{d}^2\varphi\, f(\boldsymbol{\varphi})\, I^{\mathrm{iso}}(\boldsymbol{\varphi}) \approx \int \mathrm{d}^2\theta\, f(\boldsymbol{\theta})\, I^{\mathrm{obs}}(\boldsymbol{\theta}) - \frac{1}{2}\, q_{kl} \int \mathrm{d}^2\varphi\, I^{\mathrm{obs}}(\boldsymbol{\varphi}) \frac{\partial^2 f}{\partial \varphi_k \partial \varphi_l}\,. \tag{A.15}$$

Now we choose the arbitrary function f to be:

$$f(\boldsymbol{\theta}) = \theta_i \theta_j W(|\boldsymbol{\theta}|^2/\sigma^2), \tag{A.16}$$

where the scale length of the weighting function is $\sigma \equiv \sigma_{\mathrm{iso}} = \sigma_{\mathrm{obs}}$ and the coordinate of the image centre is zero, $\boldsymbol{\theta} = \mathbf{0}$, in the definition of the quadrupole tensors Q^{iso} and Q^{obs}. This then yields

$$Q_{ij}^{\mathrm{iso}} = Q_{ij}^{\mathrm{obs}} - \frac{1}{2} Z_{ijkl} q_{kl}\,, \tag{A.17}$$

where we used the Einstein summation convention, and

$$Z_{ijkl} = \int \mathrm{d}^2\varphi\, I^{\mathrm{obs}}(\boldsymbol{\varphi}) z_{ijkl}, \tag{A.18}$$

with

$$z_{ijkl}(\boldsymbol{\varphi}) = \frac{\partial^2}{\partial \varphi_k \partial \varphi_j} \left[\varphi_i \varphi_j W\left(\frac{|\boldsymbol{\varphi}|^2}{\sigma^2} \right) \right]. \tag{A.19}$$

The single entries are

$$z_{1111} = 2W + \frac{10}{\sigma^2}\varphi_1^2 W' + \frac{4}{\sigma^4}\varphi_1^4 W'', \tag{A.20}$$

$$z_{1112} = z_{1121} = \frac{4}{\sigma^2}\varphi_1\varphi_2 W' + \frac{4}{\sigma^4}\varphi_1^3\varphi_2 W'', \tag{A.21}$$

$$z_{1122} = \frac{2}{\sigma^2}\varphi_1^2 W' + \frac{4}{\sigma^4}\varphi_1^2\varphi_2^2 W'', \tag{A.22}$$

$$z_{1211} = \frac{6}{\sigma^2}\varphi_1\varphi_2 W' + \frac{4}{\sigma^4}\varphi_1^3\varphi_2 W'', \tag{A.23}$$

$$z_{2211} = \frac{2}{\sigma^2}\varphi_2^2 W' + \frac{4}{\sigma^4}\varphi_2^2\varphi_2^2 W'', \tag{A.24}$$

$$z_{2212} = z_{2221} = \frac{4}{\sigma^2}\varphi_1\varphi_2 W' + \frac{4}{\sigma^4}\varphi_1\varphi_2^3 W'', \tag{A.25}$$

$$z_{2222} = 2W + \frac{10}{\sigma^2}\varphi_2^2 W' + \frac{4}{\sigma^4}\varphi_2^4 W''. \tag{A.26}$$

With this and the definitions given in Eq. (A.14) we calculate the trace of $z_{ijkl}q_{kl}$:

$$\mathrm{tr}(z_{ijkl}q_{kl}) = \frac{1}{2}(z_{1111} - z_{1122} + z_{2211} - z_{2222})q_1 + \frac{1}{2}(z_{1112} + z_{1121} + z_{2212} + z_{2221})q_2 \tag{A.27}$$

$$= 2\left[(\varphi_1^2 - \varphi_2^2)\frac{2W'}{\sigma^2} + (\varphi_1^4 - \varphi_2^4)\frac{W''}{\sigma^4}\right] q_1 + 4\left[\varphi_1\varphi_2(2\frac{W'}{\sigma^2} + (\varphi_1^2 + \varphi_2^2)W'')\right] q_2, \tag{A.28}$$

where we used $q_{11} = -q_{22}$ and $q_{12} = q_{21}$. With the definitions

$$\eta_1(\boldsymbol{\varphi}) = \varphi_1^2 - \varphi_2^2; \quad \eta_2(\boldsymbol{\varphi}) = 2\varphi_1\varphi_2 \tag{A.29}$$

it follows

$$\mathrm{tr}(z_{ijkl}q_{kl}) = 2\left(\frac{2W'}{\sigma^2} + |\boldsymbol{\varphi}|^2\frac{W''}{\sigma^4}\right)(\eta_1(\boldsymbol{\varphi})q_1 + \eta_2(\boldsymbol{\varphi})q_2), \tag{A.30}$$

yielding the trace of Q^{iso}:

$$\mathrm{tr}(Q^{\mathrm{iso}}) = \mathrm{tr}(Q^{\mathrm{obs}}) + \frac{1}{2}\mathrm{tr}(Z_{ijkl}q_{kl}) = \mathrm{tr}(Q^{\mathrm{obs}}) + x_\alpha q_\alpha, \tag{A.31}$$

with

$$x_\alpha = \int \mathrm{d}^2\varphi\, I^{\mathrm{obs}}(\boldsymbol{\varphi})\left(\frac{2W'}{\sigma^2} + |\boldsymbol{\varphi}|^2\frac{W''}{\sigma^4}\right)\eta_\alpha(\boldsymbol{\varphi}), \tag{A.32}$$

where the sums run over $\alpha = 1, 2$[1].

The same we calculate for $z_{11kl}q_{kl} - z_{22kl}q_{kl}$:

$$z_{11kl}q_{kl} - z_{22kl}q_{kl} = \frac{1}{2}(z_{1111} - z_{1122} - z_{2211} + z_{2222})q_1 + \frac{1}{2}(z_{1112} + z_{1121} - z_{2212} - z_{2221})q_2 \tag{A.33}$$

$$= 2\left(W + 2|\boldsymbol{\varphi}|^2\frac{W'}{\sigma^2} + \eta_1^2(\boldsymbol{\varphi})\frac{W''}{\sigma^4}\right) q_1 + 2\eta_1(\boldsymbol{\varphi})\eta_2(\boldsymbol{\varphi})\frac{W''}{\sigma^4}q_2. \tag{A.34}$$

[1]The Greek indices $\alpha, \beta = 1, 2$ are not tensor indices, in contrast to the used Latin indices.

With this we obtain $(Q_{11}^{\rm iso} - Q_{22}^{\rm iso})$

$$(Q_{11}^{\rm iso} - Q_{22}^{\rm iso}) = (Q_{11}^{\rm obs} - Q_{22}^{\rm obs}) - \frac{1}{2}(Z_{11kl}q_{kl} - Z_{22kl}q_{kl}) = (Q_{11}^{\rm obs} - Q_{22}^{\rm obs}) - X_{1\alpha}q_\alpha \quad \text{(A.35)}$$

and correspondingly $Q_{12}^{\rm iso}$:

$$Q_{12}^{\rm iso} = Q_{12}^{\rm obs} - \frac{1}{2}Z_{12kl}q_{kl} = Q_{12}^{\rm obs} - X_{2\alpha}q_\alpha, \quad \text{(A.36)}$$

where

$$X_\alpha q_\alpha = \int {\rm d}^2\varphi\, I^{\rm obs}(\boldsymbol{\varphi}) \left[\left(W + 2|\boldsymbol{\varphi}|^2\frac{W'}{\sigma^2}\right)\delta_{\alpha\beta} + \eta_\alpha(\boldsymbol{\varphi})\eta_\beta(\boldsymbol{\varphi})\frac{W''}{\sigma^4}\right]. \quad \text{(A.37)}$$

With these preparatory calculations we are now able to calculate a relation between $\chi^{\rm iso}$ and $\chi^{\rm obs}$. To this end we define the following.

$$\begin{array}{lllllll} T^{\rm iso} & \equiv & {\rm tr}(Q^{\rm iso}) & = & T^{\rm obs} + \delta T^{\rm obs} & = & {\rm tr}(Q^{\rm obs}) - x_\alpha q_\alpha, \\ Q_1^{\rm iso} & \equiv & (Q_{11}^{\rm iso} - Q_{22}^{\rm iso}) & = & Q_1^{\rm obs} + \delta Q_1^{\rm obs} & = & (Q_{11}^{\rm obs} - Q_{22}^{\rm obs}) - X_{1\alpha}q_\alpha, \\ Q_2^{\rm iso} & \equiv & 2Q_{12}^{\rm iso} & = & Q_2^{\rm obs} + \delta Q_2^{\rm obs} & = & 2Q_{12}^{\rm obs} - X_{2\alpha}q_\alpha, \end{array} \quad \text{(A.38)}$$

with $T^{\rm obs} = {\rm tr}(Q^{\rm obs})$, $Q_1^{\rm obs} = Q_{11}^{\rm obs} - Q_{22}^{\rm obs}$ and $Q_2^{\rm obs} = 2Q_{12}^{\rm obs}$. Note that the quantities δT and δQ_α are small compared to T and Q_α. A relation between $\chi^{\rm iso}$ and $\chi^{\rm obs}$ is obtained by inserting Eqs. (A.38) into the definition of the ellipticity (5.2),

$$\chi_\alpha^{\rm iso} = \frac{Q_\alpha^{\rm iso}}{T^{\rm iso}} = \frac{Q_\alpha^{\rm obs} + \delta Q_\alpha^{\rm obs}}{T^{\rm obs} + \delta T^{\rm obs}}. \quad \text{(A.39)}$$

By multiplying with $(T^{\rm obs} - \delta T^{\rm obs})/(T^{\rm obs} - \delta T^{\rm obs})$ and neglecting the higher-order terms $\delta^2 T^{\rm obs}$ and $\delta T^{\rm obs}\delta Q_\alpha^{\rm obs}$, we obtain up to linear order in q_α,

$$\chi_\alpha^{\rm iso} = \frac{Q_\alpha^{\rm obs}}{T^{\rm obs}} + \frac{\delta Q_\alpha^{\rm obs}}{T^{\rm obs}} - \frac{Q_\alpha^{\rm obs}}{T^{\rm obs}}\frac{\delta T^{\rm obs}}{T^{\rm obs}}, \quad \text{(A.40)}$$

or

$$\chi_\alpha^{\rm iso} = \chi_\alpha^{\rm obs} - P_{\alpha\beta}^{\rm sm}\, q_\beta, \quad \text{(A.41)}$$

where

$$P_{\alpha\beta}^{\rm sm} = X_{\alpha\beta}^{\rm sm} - \chi_\alpha^{\rm obs}\chi_\beta^{\rm sm}, \quad \text{(A.42)}$$

with the definitions

$$X_{\alpha\beta}^{\rm sm} \equiv \frac{1}{{\rm tr}Q^{\rm obs}}X_{\alpha\beta}, \text{ and } \quad \chi_\alpha^{\rm sm} \equiv \frac{1}{{\rm tr}Q^{\rm obs}}x_\alpha. \quad \text{(A.43)}$$

The quantity $P_{\alpha\beta}^{\rm sm}$ is called *smear polarisability* (Kaiser et al. 1995). The relation (A.41) corrects the ellipticity $\chi^{\rm obs}$ of an observed image for the anisotropic part of the PSF to obtain the hypothetical ellipticity $\chi^{\rm iso}$. Note that $P_{\alpha\beta}^{\rm sm}$ depends on the weighting function and the observed shape and size of the galaxy. In particular, its size decreases for larger images, as $P_{\alpha\beta}^{\rm sm}$ is proportional to $1/{\rm tr}Q^{\rm obs}$. This is expected because the ellipticities of larger images are less affected by a PSF anisotropy than those of smaller images. We use a Gaussian weighting function. Its scale length, the half-light radius, depends on the size and shape of the object.

The determination of the anisotropy part of the PSF, q_α

In order to apply relation (A.41), the anisotropy term q_α has to be known. It can be determined from the shape of stellar images. Since stars are point-like and unaffected by lensing, their isotropically smeared images have zero ellipticity, $\chi^{\rm iso*} = 0$. Hence, from (A.41),

$$q^*_\alpha = (P^{\rm sm*})^{-1}_{\alpha\beta}\,\chi^{\rm obs*}_\beta\ . \tag{A.44}$$

In general, the PSF is a function of image position, but can only be measured at the star position. However, the PSF correction has to be applied to galaxies. Assuming that the PSF varies smoothly over the total field-of-view, q can be determined for a set of stars, and approximated by a low-order two-dimensional polynomial across the data field. With this polynomial fit it is then possible to estimate the anisotropy kernel q by the value of the polynomial function, $q^{\rm poly}$, at the position of galaxies.

A relation between $\chi^{\rm iso}$ and χ^0 and the role of the shear polarisability $P^{\rm sh}$

In this Section we relate $\chi^{\rm iso}$ to the ellipticity χ^0 of a hypothetical image obtained from isotropic smearing of the unlensed source. We use Eq. (A.9) and the locally linearised lens mapping (3.13) in the form $I^{\rm l}(\boldsymbol{\theta}) = I^{\rm intr}(\mathcal{A}\boldsymbol{\theta})$. The relation between the lensed and isotropically smeared image and the source $I^{\rm s}$ is given by,

$$\begin{aligned} I^{\rm iso}(\boldsymbol{\theta}) &= \int {\rm d}^2\varphi\, I^{\rm intr}(\mathcal{A}\boldsymbol{\varphi})\, P^{\rm iso}(\boldsymbol{\theta}-\boldsymbol{\varphi}) \\ &= \frac{1}{\det\mathcal{A}} \int {\rm d}^2\zeta\, I^{\rm intr}(\boldsymbol{\zeta})\, P^{\rm iso}(\boldsymbol{\theta}-\mathcal{A}^{-1}\boldsymbol{\zeta}) \equiv \hat{I}(\mathcal{A}\boldsymbol{\theta}). \end{aligned} \tag{A.45}$$

In the second step we transform the integration variable, and in the last step we define the brightness moment,

$$\hat{I}(\boldsymbol{\theta}) = \int {\rm d}^2\varphi\, I^{\rm intr}(\boldsymbol{\varphi})\, \hat{P}(\boldsymbol{\theta}-\boldsymbol{\varphi}) \quad \text{with} \quad \hat{P}(\boldsymbol{\theta}) \equiv \frac{1}{\det\mathcal{A}} P^{\rm iso}(\mathcal{A}^{-1}\boldsymbol{\theta}). \tag{A.46}$$

The function $\hat{P}$ is normalised and has a vanishing first moment. We now calculate the $\hat{Q}_{ij}$ from $\hat{I}$:

$$\begin{aligned} \hat{Q}_{ij} &= \int {\rm d}^2\beta\, \beta_i\beta_j\, \hat{I}(\boldsymbol{\beta})\, W\left(\frac{|\boldsymbol{\beta}|^2}{\hat{\sigma}^2}\right) \\ &= \det\mathcal{A}\, \mathcal{A}_{ik}\mathcal{A}_{jl} \int {\rm d}^2\theta\, \theta_k\theta_l\, I^{\rm iso}(\boldsymbol{\theta})\, W\left(\frac{|\boldsymbol{\theta}|^2 - \delta_\alpha\,\eta_\alpha(\boldsymbol{\theta})}{\sigma^2}\right), \end{aligned} \tag{A.47}$$

where

$$|\boldsymbol{\beta}|^2 = |\mathcal{A}\,\boldsymbol{\theta}|^2 = (1-\kappa)^2(1+|g|^2)\,\left(|\boldsymbol{\theta}|^2 - \delta_\alpha\,\eta_\alpha(\boldsymbol{\theta})\right), \tag{A.48}$$

with the distortion $\delta = 2g/(1+|g|^2)$. The relation between the two filter scales is then given by $\hat{\sigma}^2 = (1-\kappa)^2(1+|g|^2)\sigma^2$. In the weak lensing approximation δ is small and we

can perform a Taylor expansion of the weight function, W, to first order (as in the last Section $I^{\rm iso}$ is in the following replaced by $I^{\rm obs}$). This results in a relation between $\hat{\chi}$ and $\chi^{\rm iso}$

$$\chi^{\rm iso}_\alpha - \hat{\chi}_\alpha = P^{\rm sh}_{\alpha\beta} g_\beta, \tag{A.49}$$

where we used the following definitions,

$$\begin{aligned} P^{\rm sh}_{\alpha\beta} &= 2\delta_{\alpha\beta} - 2\chi^{\rm iso}_\alpha \chi^{\rm iso}_\beta + \frac{2}{{\rm tr}(Q^{\rm iso})}\,\chi^{\rm iso}_\alpha\, L_\beta - \frac{2}{{\rm tr}(Q^{\rm iso})}\,B_{\alpha\beta}, \\ B_{\alpha\beta} &= -\int {\rm d}^2\theta\, I^{\rm obs}(\boldsymbol{\theta})\, W'\left(\frac{|\boldsymbol{\theta}|^2}{\sigma^2}\right)\frac{1}{\sigma^2}\,\eta_\alpha(\boldsymbol{\theta})\,\eta_\beta(\boldsymbol{\theta}), \\ L_\alpha &= -\int {\rm d}^2\theta\, |\boldsymbol{\theta}|^2\, I^{\rm obs}(\boldsymbol{\theta})\, W'\left(\frac{|\boldsymbol{\theta}|^2}{\sigma^2}\right)\frac{1}{\sigma^2}\,\eta_\alpha(\boldsymbol{\theta}). \end{aligned} \tag{A.50}$$

The quantity $P^{\rm sh}$ is called *shear polarisability* (Kaiser et al. 1995). Note that $P^{\rm sh}$ is defined in terms of $I^{\rm iso}$. However, since we assumed that q and g are small, the difference of $P^{\rm sh}$ calculated with $I^{\rm iso}$ and $I^{\rm obs}$ would only cause a second-order change in Eq. (A.49). Hence, we calculate the shear polarisability $P^{\rm sh}$ directly from the observed brightness profile, $I^{\rm obs}$, as in the case of smear polarisability, $P^{\rm sm}$.

In analogy to the PSF anisotropy correction (Eq. A.4), we decompose $\hat{P}$ into an isotropic and an anisotropic part (the shear),

$$\hat{P}(\boldsymbol{\theta}) = \int {\rm d}^2\varphi\, \hat{P}^{\rm iso}(\boldsymbol{\varphi})\, \hat{q}(\boldsymbol{\theta} - \boldsymbol{\varphi}). \tag{A.51}$$

We define the brightness profile I^0 which would be obtained from smearing the unlensed surface brightness of the source, $I^{\rm intr}$, with the isotropic PSF $\hat{P}^{\rm iso}$ as

$$\hat{I}^0(\boldsymbol{\theta}) = \int {\rm d}^2\varphi\, I^{\rm intr}(\boldsymbol{\varphi})\, \hat{P}^{\rm iso}(\boldsymbol{\theta} - \boldsymbol{\varphi}), \tag{A.52}$$

and obtain

$$\hat{I}(\boldsymbol{\theta}) = \int {\rm d}^2\varphi\, \hat{I}^0(\boldsymbol{\varphi})\, \hat{q}(\boldsymbol{\theta} - \boldsymbol{\varphi}). \tag{A.53}$$

The relation between $\hat{I}$ and $\hat{I}^0$ is the same as that between $I^{\rm obs}$ and $I^{\rm iso}$, and the ellipticities are

$$\hat{\chi}^0_\alpha = \hat{\chi}_\alpha - P^{\rm sm}_{\alpha\beta}\,\hat{q}_\beta. \tag{A.54}$$

Again, due to the assumed smallness of g and q, the differences between $I^{\rm obs}$, $I^{\rm iso}$, and $\hat{I}$ are also small. Hence, we calculate $P^{\rm sm}$ using the observable surface brightness, $I^{\rm obs}$, instead of $\hat{I}$.

Estimating the reduced shear g from observed ellipticities $\chi^{\rm obs}$

We eliminate $\hat{\chi}$ from Eqs. (A.49) and (A.54), and obtain

$$\chi^{\rm iso}_\alpha = \hat{\chi}^0_\alpha + P^{\rm sh}_{\alpha\beta} g_\beta + P^{\rm sm}_{\alpha\beta}\hat{q}_\beta. \tag{A.55}$$

For point-like objects, like stars, both $\hat{\chi}^0$ and $\chi^{\rm iso}$ vanish. Hence, a we obtain a relation between $\hat{q}$ and g,

$$\hat{q}_\alpha = -(P^{\rm sm*})^{-1}_{\alpha\beta} P^{\rm sh*}_{\beta\gamma} g_\gamma, \tag{A.56}$$

where the asterisk * indicates that $P^{\rm sm}$ and $P^{\rm sh}$ are to be calculated from stellar images.

The correction factors $P^{\rm sm*}$ and $P^{\rm sh*}$ should in principle not depend on the choice of the scale length, σ, in the weight function. However, in practice it does, as pointed out by Hoekstra et al. (1998). They concluded that $P^{\rm sm*}$ and $P^{\rm sh*}$ should be calculated with the same scale length as is used for an individual galaxy. We now define

$$P^g_{\alpha\beta} = P^{\rm sh}_{\alpha\beta} - P^{\rm sm}_{\alpha\gamma}(P^{\rm sm*})^{-1}_{\gamma\delta} P^{\rm sh*}_{\delta\beta}, \tag{A.57}$$

and combine Eqs. (A.41) and (A.55). We finally obtain

$$\hat{\chi}^0_\alpha = \chi^{\rm obs}_\alpha - P^{\rm sm}_{\alpha\beta} q_\beta - P^g_{\alpha\beta} g_\beta. \tag{A.58}$$

This equation relates the observed ellipticity, $\chi^{\rm obs}$, to that of the source smeared by an isotropic PSF. The two tensors $P^{\rm sm}$ and P^g can be calculated from the observed surface brightness of the considered galaxy and star images. The derivation of Eq. (A.58) was restricted to first order in the PSF anisotropy and the shear. However, Kaiser et al. (1995), Hoekstra et al. (1998), and also Heymans et al. (2006a) showed in their simulations that the KSB algorithm can be applied even for large shear ($\gamma \approx 0.1$). Since the expectation value of $\hat{\chi}^0$ is zero, Eq. (A.58) yields an unbiased estimate of of the reduced shear g,

$$\langle g \rangle = \langle (P^{\rm g})^{-1} (\chi^{\rm obs} - P^{\rm sm} q) \rangle. \tag{A.59}$$

Modifications of the algorithm presented have been suggested by Rhodes et al. (2000) and Kaiser (2000), but will not be discussed here.

Appendix B

Single fields

In this appendix we display the field position in the sky of those fields of the GaBoDS that form patches of a least four contiguous fields. Additionally, the relevant $M_{\rm ap}$-statistics of all GaBoDS fields are plotted.

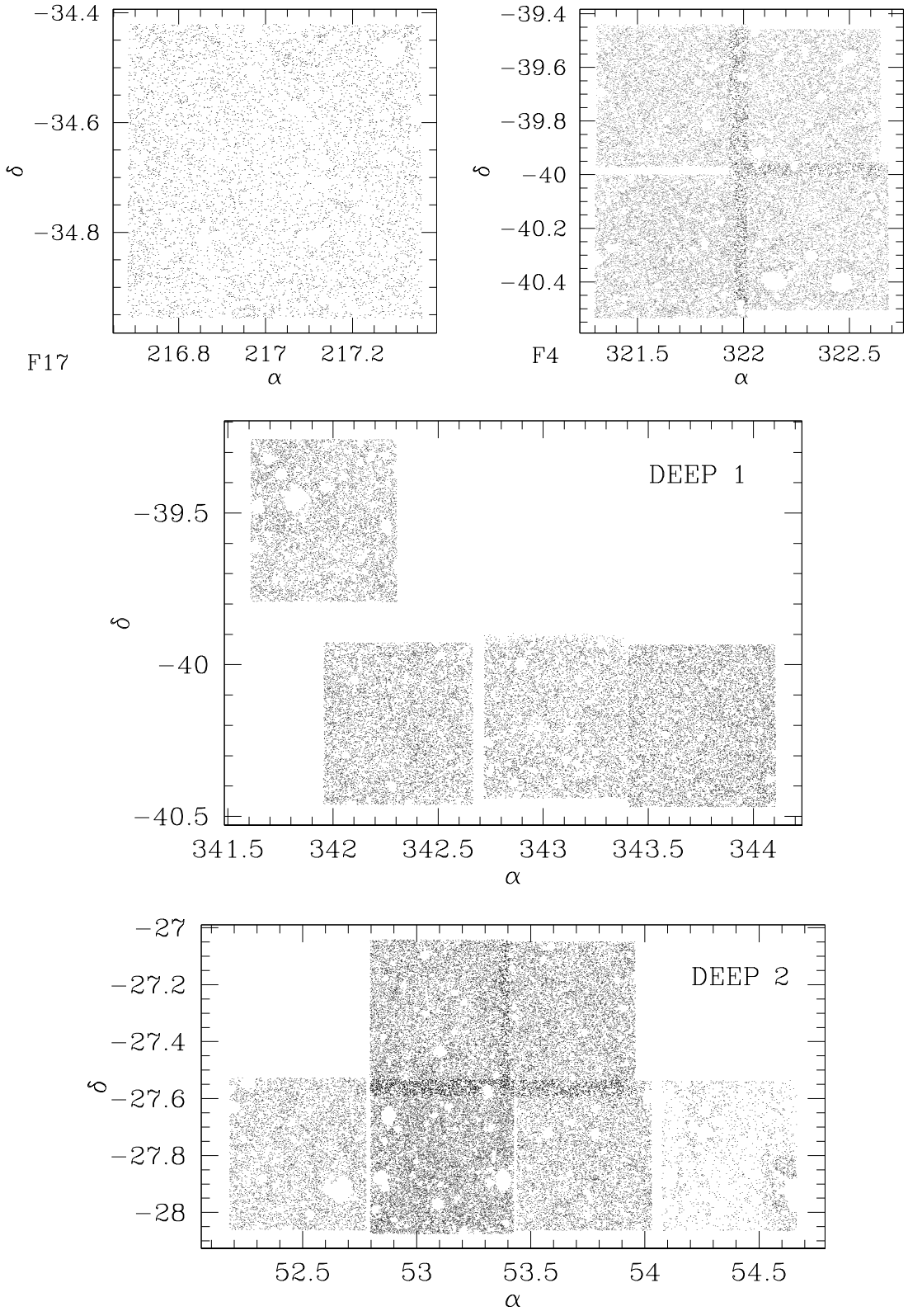

Figure B.1: Field position in the sky. The density of points represent the number density of galaxies in the corresponding field.

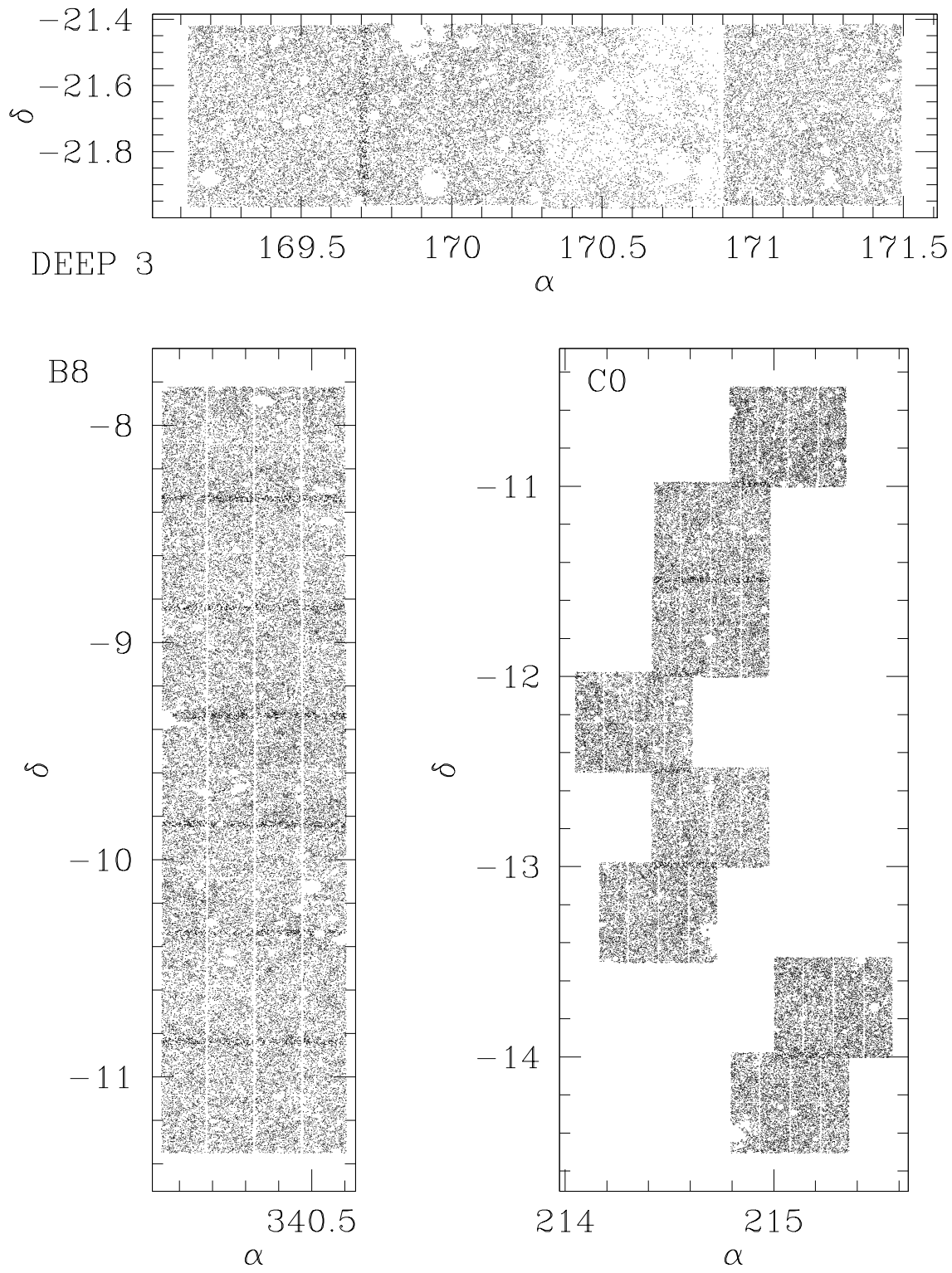

Figure B.2: Same as in Fig. B.1.

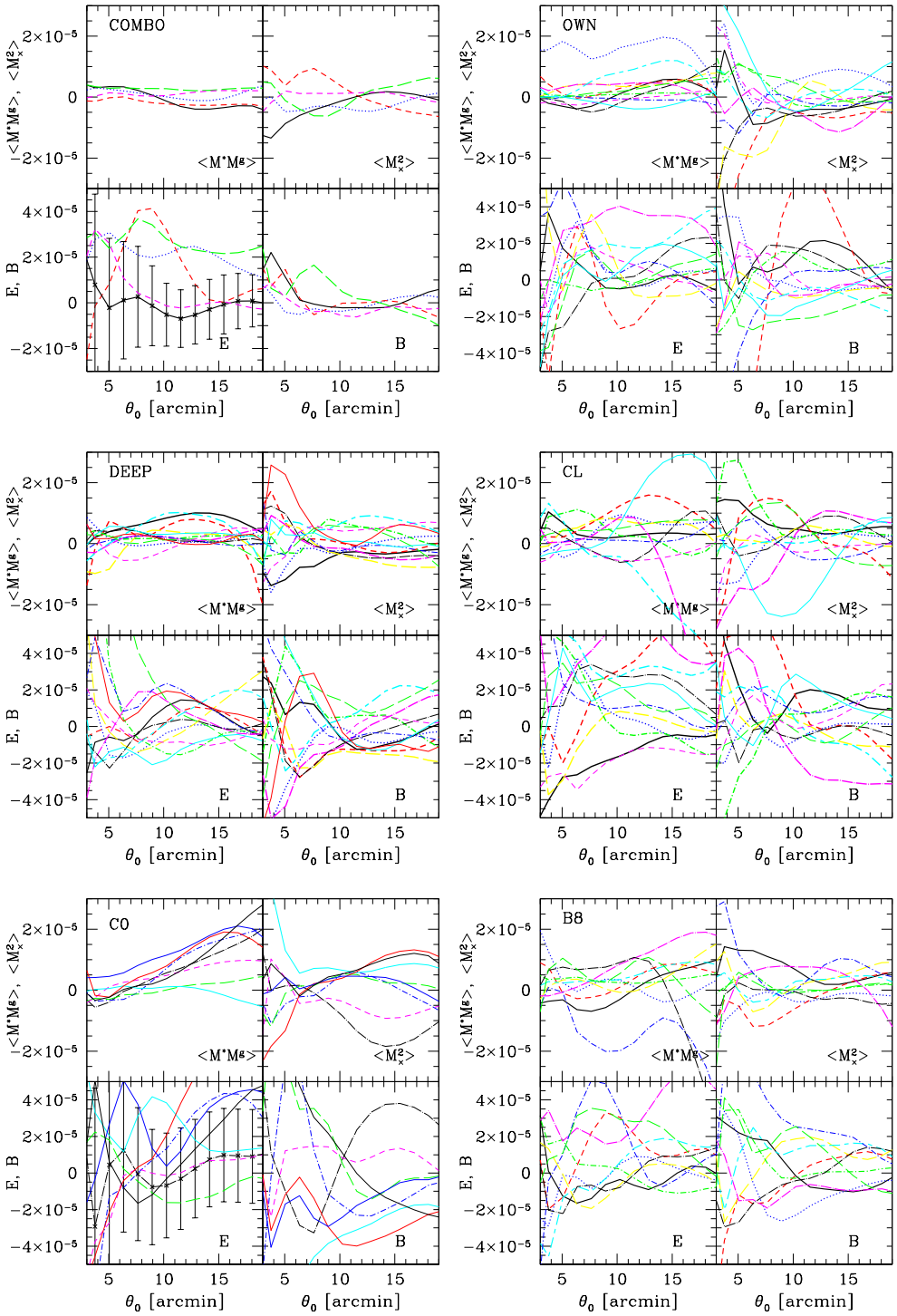

Figure B.3: In each diagram various $M_{\rm ap}$ statistics are displayed for each field: cross-correlation between uncorrected stars and anisotropy corrected galaxies, $\langle M^* M^{\rm g} \rangle$, cross-correlation between the tangential component and the cross component of the shear, $M_\times$, and the E- and B-modes. The name codes are given in table 4.2. For two fields we plotted the statistical errors: FDF (upper left panel) and C04p3 (lower left panel). The type of each line is the same as in Fig. 6.6. Figure from Hetterscheidt et al. (2006).

Bibliography

Adams, W. S. 1941, ApJ, 93, 11 17

Afonso, C., Albert, J. N., Alard, C., et al. 2003, ApJ, 404, 145 22

Allen, S. W., Schmidt, R. W. amd Fabian, A. C., & Ebeling, H. 2003, MNRAS, 342, 287 148

Angloher, G., Bucci, C., Christ, P., et al. 2005, Astroparticle Physics, 23, 325 21

Arnouts, S., Vandame, B., Benoist, C., et al. 2001, A&A, 379, 740 80

Baade, D. 2002, Wide Field Imager User Manual, ESO 62

Bacon, D., Massey, R. J., Refregier, A., & Ellis, R. 2003, MNRAS, 344, 673 111, 115, 117, 118, 148

Bacon, D., Refregier, A., & Ellis, R. 2000, MNRAS, 318, 625 9, 97, 111

Bahcall, N., Dong, F., Bode, P., Kim, R., et al. 2003, ApJ, 585, 182 29, 148

Bardeen, J. M., Bond, J. R., Kaiser, N., & Szalay, A. S. 1986, ApJ, 304, 15 27, 128, 142

Bartelmann, M. & Schneider, P. 1999, A&A, 345, 17 55

—. 2001, Phys. Rep., 340, 291 11, 36, 50, 51, 149

Bernardeau, F., van Waerbeke, L., & Mellier, Y. 1997, A&A, 322, 1 134

Bernstein, G. M. & Jarvis, M. 2002, AJ, 123, 583B 85, 97

Bertin, E. 2001, Eye v1.1 User's guide 71

—. 2002, Swarp v1.34 User's guide 76

Bertin, E. & Arnouts, S. 1996, A&AS, 117, 393 90

Bertin, E., Mellier, Y., Radovich, M., et al. 2002, in ASP Conf. Ser. 281: Astronomical Data Analysis Software and Systems XI, p. 228 76

Blanchard, A., Sadat, R., Bartlett, J. G., & Le Dour, M. 2000, A&A, 362, 809 148

Blandford, R. D., Saust, A. B., Brainerd, T. G., & Villumsen, J. V. 1991, MNRAS, 251, 600 42, 54

Bolzonella, M., Miralles, J. M., & Pelló, R. 2000, A&A, 363, 476 124

Borgani, S., Plionis, M., & Kolokotronis, V. 1999, MNRAS, 305, 866 148

Bradac, M., Clowe, D., Gonzalez, A. H., et al. 2006, ArXiv Astrophysics e-prints 20

Bridle, S. L., Gull, S., Bardeau, S., & Kneib, J. P. 2001, Scientific N. W., ed., Proceedings of the Yale Cosmology Workshop The Shapes of Galaxies and their Dark Halos 85, 97

Brodwin, M., Lilly, S. J., Porciani, et al. 2006, ApJS, 162, 20 125, 135

Brown, M. L., Taylor, A. N., Bacon, D. J., Gray, M. E., et al. 2003, MNRAS, 341, 100 111, 117, 148

Bruzual, A. G. & Charlot, S. 1993, AJ, 402, 538 124

Chang, T.-C., Refregier, A., & Helfand, D. J. 2004, ApJ, 617, 794 148

Clowe, D., Bradac, M., Gonzalez, A. H., et al. 2006a, ArXiv Astrophysics e-prints 20, 21

Clowe, D., Gonzalez, A., & Markevitch, M. 2004, ApJ, 604, 596 20

Clowe, D., Schneider, P., Aragón-Salamanca, A., et al. 2006b, A&A, 451, 395 64

Coleman, G. D., Wu, C.-C., & Weedman, D. W. 1980, ApJS, 239, 898 124

Colless, M., Dalton, G., Maddox, S., et al. 2001, MNRAS, 328, 1039 22

Crittenden, R. G., Natarajan, P., Pen, U.-L., & Theuns, T. 2001, ApJ, 559, 552 121

—. 2002, ApJ, 568, 20 58

Dahle, H. 2006, ArXiv Astrophysics e-prints 148

Davis, M. & Peebles, P. J. E. 1983, ApJ, 267, 465 81

Dicke, R. H., Peebles, P. J. E., Roll, P. G., & Wilkinson, D. T. 1965, ApJ, 142, 414 17

Dietrich, J. P. 2006, Combined Weak Lensing and X-ray Search for Galaxy Clusters and the Filaments Connecting Them (PhD thesis, Universität Bonn) 76

Dodelson, S. & Efstathiou, G. 2004, Physics Today, 57, 60 31

Eddington, A. S. 1919, The Observatory, 42, 119 36

—. 1920, Space, time and gravitation. an outline of the general relativity theory (Cambridge Science Classics, Cambridge: University Press, 1920) 36

Einstein, A. 1916, Annalen der Physik, 49, 769 12

Erben, T., Schirmer, M., Dietrich, J. P., et al. 2005, AN, 326, 432 10, 61, 62, 68, 74, 75, 76, 78, 79, 80, 82, 83, 92

Erben, T., van Waerbeke, L., Bertin, E., Mellier, Y., & Schneider, P. 2001, A&A, 366, 717 92, 93, 94, 96, 97, 107, 113

Fließbach, T. 1998, Allgemeine Relativitätstheorie (Spektrum Akademischer Verlag) 11

Freedman, W. L., Madore, B. F., Gibson, B. K., et al. 2001, ApJ, 553, 47 14

Friedmann, A. 1922, Z. Phys., 10, 377 13

—. 1924, Z. Phys., 21, 326 13

Fruchter, A. S. & Hook, R. N. 2002, PASP, 114, 144 76

Gelman, A. & Rubin, D. B. 1992, Statistical Science, 7, 457 129

Giavalisco, M., Ferguson, H. C., Koekemoer, A. M., et al. 2004, ApJL, 600, L93 80

Gnedin, N. Y. & Hamilton, A. J. S. 2002, MNRAS, 334, 107 28

Gonzalez, A. H., Zaritsky, D., Dalcanton, J. J., & Nelson, A. 2001, ApJS, 137, 117 64

Grazian, A., Fontana, A., de Santis, C., et al. 2006, A&A, 449, 951 124

Groth, E. J. & Peebles, P. J. E. 1977, ApJ, 217, 385 82

Hamana, T., Miyazaki, S., Shimasaku, K., et al. 2003, ApJ, 597, 98 111, 148

Hamana, T., Takada, M., & Yoshida, N. 2004, MNRAS, 350, 893 112

Hartlap, J., Simon, P., & Schneider, P. 2006, ArXiv Astrophysics e-prints 127

Hastings, W. K. 1970, Biometrika, 57, 97 129

Heavens, A., Refregier, A., & Heymans, C. 2000, MNRAS, 319, 649 121

Henry, J. P. 2004, ApJ, 609, 603 29, 148

Hetterscheidt, M., Erben, T., Schneider, P., et al. 2005, A&A, 442, 43 10, 35, 45, 47, 48, 113, 138

Hetterscheidt, M., Simon, P., Schirmer, M., et al. 2006, ArXiv Astrophysics e-prints 10, 61, 85, 95, 112, 114, 115, 116, 117, 118, 120, 122, 123, 126, 131, 132, 133, 146, 160

Heymans, C., Brown, M., Heavens, A., et al. 2004, MNRAS, 347, 895 148

Heymans, C., Brown, M. L., Barden, M., et al. 2005, MNRAS, 361, 160 111, 148

Heymans, C. & Heavens, A. 2003, MNRAS, 339, 711 121, 135

Heymans, C., Van Waerbeke, L., Bacon, D., et al. 2006a, MNRAS, 368, 1323 10, 85, 86, 95, 96, 97, 98, 99, 108, 111, 113, 156

Heymans, C., White, M., Heavens, A., & Van Waerbeke, L. 2006b, preprint astro-ph/0604001 111, 121, 135, 136

Hildebrandt, H., Erben, T., Dietrich, J. P., et al. 2006, A&A, 452, 1121 10, 64

Hinshaw, G., Nolta, M. R., Bennett, C. L., et al. 2006, ArXiv Astrophysics e-prints 30, 33

Hinshaw, G., Spergel, D. N., Verde, L., et al. 2003, ApJS, 148, 135 28

Hirata, C. M. & Seljak, U. 2002, MNRAS, 343, 459 97

—. 2004, Phys.Rev.D, 063526 111, 136, 147

Hoekstra, H. 2004, MNRAS, 347, 1337 111, 136

Hoekstra, H., Franx, M., & Kuijken, K. 2000, ApJ, 532, 88 100, 101

Hoekstra, H., Franx, M., Kuijken, K., & Squires, G. 1998, ApJ, 504, 636 85, 92, 93, 97, 156

Hoekstra, H., Mellier, Y., Van Waerbeke, L., Semboloni, E., et al. 2005, astro-ph/0511089 32, 94, 136, 142, 148

Hoekstra, H., Van Waerbeke, L., & Gladders, D. 2002a, ApJ, 577, 604 83, 84

Hoekstra, H., Yee, H. K. C., & Gladders, M. D. 2002b, ApJ, 577, 595 111, 148

Hoekstra, H., Yee, H. K. C., Gladders, M. D., et al. 2002b, ApJ, 572, 55 28, 148

Howell, S. B. 2000, Handbook of CCD astronomy (Cambridge university press) 69

Hubble, E. 1929, Proceedings of the National Academy of Science, 15, 168 12

Huterer, D., Takada, M., Bernstein, G., & Jain, B. 2006, MNRAS, 366, 101 134

Jarosik, N., Barnes, C., Greason, M. R., et al. 2006, ArXiv Astrophysics e-prints 30

Jarvis, M., Bernstein, G. M., Fischer, P., et al. 2003, AJ, 125, 1014 111, 148

Jarvis, M. & Jain, B. 2004, astro-ph/0412234 92, 146

Jarvis, M., Jain, B., Bernstein, G., & Dolney, D. 2005, ApJ in press, astro-ph/0502243 111, 148

Kaiser, N. 1992, ApJ, 388, 272 52, 54

Kaiser, N. 1998, ApJ, 498, 26 52, 53

—. 2000, ApJ, 537, 555 97, 99, 156

Kaiser, N., Squires, G., & Broadhurst, T. 1995, ApJ, 449, 460 153, 155, 156

Kaiser, N., Wilson, G., & Luppino, G. 2000, ApJL, submitted, preprint astro-ph/0003338 9, 111

Kilbinger, M., Schneider, P., & Eifler, T. 2006, astro-ph/0604520 113, 121

King, L. J. & Schneider, P. 2003, A&A, 398, 23 121, 135

Knop, R. A., Aldering, G., Amanullah, R., et al. 2003, ApJ, 598, 102 132

Kochanek, C. S. & Schechter, P. L. 2004, in Measuring and Modeling the Universe, ed. W. L. Freedman, 117–+ 14

Koranyi, D. M., Kleyna, J., & Grogin, N. A. 1998, PASP, 110, 1464 75

Kuijken, K. 2006, A&A, 456, 827 97

Landolt, A. U. 1992, AJ, 104, 372 74

Landy, S. D. & Szalay, A. S. 1993, ApJ, 412, 64 81

Le Fevre, O., Vettolani, G., Paltani, S., et al. 2004, A&A, 228, 1043 124

Limber, D. N. 1953, ApJ, 117, 134 52

Luppino, G. A. & Kaiser, N. 1997, ApJ, 475, 20 85, 87, 97

Ma, Z., Hu, W., & Huterer, D. 2006, ApJ, 636, 21 111

Mandelbaum, R., Hirata, C. M., Ishak, M., Seljak, U., & Brinkmann, J. 2006, MNRAS, 367, 611 136

Maoli, R., van Waerbeke, L., Mellier, Y., et al. 2001, A&A, 368, 766 111, 148

Massey, R., Heymans, C., Berge, J., et al. 2006, ArXiv Astrophysics e-prints 10, 85, 86, 92, 104, 105, 106, 107, 108, 113

Massey, R. & Refregier, A. 2005, MNRAS, 363, 197 97

Massey, R., Refregier, A., Bacon, D., Ellis, R., & Brown, M. L. 2005, MNRAS, 359, 1277 111, 148

Massey, R., Refregier, A., Conselice, C. J., David, J., & Bacon, J. 2004, MNRAS, 348, 214 104

Mather, J. C., Cheng, E. S., Eplee, Jr., R. E., et al. 1990, ApJL, 354, L37 17

McCracken, H., Radovich, M., Bertin, E., et al. 2003, A&A, 410, 17 80, 81

McKellar, A. 1940, PASP, 52, 187 17

Mellier, Y. 1999, ARA&A, 37, 127 39

Meszaros, P. 1974, ApJ, 37, 225 27

Metropolis, N., Rosenbluth, A. W., Rosenbluth, M. N., Teller, A., & Teller, E. 1953, Journal of Chemical Physics, 21, 1087 129

Meylan, G., Jetzer, P., North, P., et al., eds. 2006, Gravitational Lensing: Strong, Weak and Micro 11, 28, 36

Moffat, J. W. 2006, ArXiv Astrophysics e-prints 20

Monet, D. B. A., Canzian, B., Dahn, C., et al. 1998, VizieR Online Data Catalog, 1252, 0 74

Nonino, M., Bertin, E., da Costa, L., et al. 1999, A&AS, 137, 51 71

Norberg, P., Baugh, C., Hawkins, E., et al. 2001, MNRAS, 328, 64 81

Oukbir, J. & Arnaud, M. 2001, MNRAS, 326, 453 148

Page, L., Hinshaw, G., Komatsu, E., et al. 2006, ArXiv Astrophysics e-prints 30, 33

Peacock, J. A. 1999, Cosmological physics (Cambridge University Press) 11, 81

Peacock, J. A. & Dodds, S. J. 1996, MNRAS, 280, 19 28, 53, 113, 128, 136, 142

Peebles, P. J. E. 1980, The large-scale structure of the universe (Research supported by the National Science Foundation. Princeton, N.J., Princeton University Press, 1980. 435 p.) 23

Penzias, A. A. & Wilson, R. W. 1965, ApJ, 142, 419 17

Perlmutter, S., Aldering, G., Goldhaber, G., et al. 1999, ApJ, 517, 565 22

Pierfederici, F. 2001, in Proc. SPIE Vol. 4477, p. 246-253, Astronomical Data Analysis, Jean-Luc Starck; Fionn D. Murtagh; Eds., ed. J.-L. Starck & F. D. Murtagh, 246–253 63

Pierpaoli, E., Borgani, S., Scott, D., & White, M. 2003, MNRAS, 342, 163 148

Pierpaoli, E., Scott, D., & White, M. 2001, MNRAS, 325, 77 148

Refregier, A. 2003, MNRAS, 338, 35 85

Refregier, A. & Bacon, D. 2003, MNRAS, 338, 48 85

Refregier, A., Rhodes, J., & Groth, E. J. 2002, ApJ, 572, L131 111, 148

Reiprich, T. H. & Böhringer, H. 2002, ApJ, 567, 716 29, 148

Rhodes, J., Refregier, A., Collins, N. R., et al. 2004, ApJ, 605, 29 111, 148

Rhodes, J., Refregier, A., & Groth, E. 2000, ApJ, 536, 79 156

—. 2001, ApJ, 552, L85 111, 148

Riess, A. G., Filippenko, A. V., Challis, P., et al. 1998, AJ, 116, 1009 22

Riess, A. G., Li, W., Stetson, P. B., et al. 2005, ApJ, 627, 579 14

Riess, A. G., Strolger, L.-G., Tonry, J., et al. 2004, ApJ, 607, 665 22

Robertson, H. P. 1935, ApJ, 82, 284 12

Roche, N., Shanks, T., Metcalfe, N., & Fong, R. 1993, MNRAS, 263, 360 82

Rosati, P., Borgani, S., & Norman, C. 2002, ARA&A, 40, 539 148

Sachs, R. K. & Wolfe, A. M. 1967, ApJ, 147, 73 18

Saha, P., Coles, J., Maccio', A. V., & Williams, L. L. R. 2006, ArXiv Astrophysics e-prints 14

Schirmer, M. 2004, PhD thesis, Universität Bonn, uRN: urn:nbn:de:hbz:5n-03263; URL: http://hss.ulb.uni-bonn.de/diss_online/math_nat_fak/2004/schirmer_mischa 47, 76, 92

Schirmer, M., Erben, T., Hetterscheidt, M., & Schneider, P. 2006, ArXiv Astrophysics e-prints 10, 35, 45, 48, 92, 138

Schirmer, M., Erben, T., Schneider, P., et al. 2003, A&A, 407, 869 63, 92

Schneider, P. 1996, MNRAS, 283, 837 45, 47

Schneider, P. 2006, Einführung in die extragalaktische Astronomie und Kosmologie (Einführung in die extragalaktische Astronomie und Kosmologie / Peter Schneider. Berlin: Springer, ISBN 3-540-25832-9, ISBN 978-3-540-25832-2, 2006, XV+452 pp.) 11

Schneider, P., Ehlers, J., & Falco, E. E. 1992, Gravitational Lenses (Springer Verlag, Heidelberg) 35

Schneider, P. & Kilbinger, M. 2006, astro-ph/0605084 121

Schneider, P. & Seitz, C. 1995, A&A, 294, 411 44

Schneider, P., Van Waerbeke, L., Jain, B., & Kruse, G. 1998, MNRAS, 296, 873 45, 53, 54, 56

Schneider, P., van Waerbeke, L., Kilbinger, M., & Mellier, Y. 2002, A&A, 396, 1 127, 143

Schneider, P., Van Waerbeke, L., & Mellier, Y. 2002, A&A, 389, 729 56, 57, 58, 121

Schrabback, T., Erben, T., Simon, P., et al. 2006, ArXiv Astrophysics e-prints 107, 148

Schramm, T. & Kayser, R. 1995, A&A, 299 44

Schuecker, P., Böhringer, H., Collins, C. A., & Guzzo, L. 2003, A&A, 398, 867 148

Seitz, C. & Schneider, P. 1997, A&A, 318, 687 44

Seljak, U. 2002, MNRAS, 337, 774 148

Seljak, U., Makarov, A., McDonald, P., et al. 2005, The American Physical Society, 71 22

Semboloni, E., Mellier, Y., van Waerbeke, L., et al. 2006, A&A, 452, 51 32, 119, 126, 148

Shapley, H. 1924a, Harvard College Observatory Circular, 255, 1

—. 1924b, Harvard College Observatory Circular, 268, 1

Silk, J. 1968, ApJ, 151, 459 26

Simon, P. 2005, PhD thesis, Rheinischen Friedrich-Wilhelms-Universität Bonn 84

Simon, P., Hetterscheidt, M., Schirmer, M., et al. 2006, ArXiv Astrophysics e-prints 29, 141

Slipher, V. M. 1917, Proceedings of the American Philosophical Society, 56, 403 12

Smith, R. E., Peacock, J. A., Jenkins, A., et al. 2003, MNRAS, 341, 1311 136

Smoot, G. F., Bennett, C. L., Kogut, A., et al. 1992, ApJ, 396, L1 17

Spergel, D. N., Bean, R., Dore', O., et al. 2006, preprint astro-ph/0603449 22, 29, 30, 32, 144, 148

Spergel, D. N., Verde, L., Peiris, H. V., et al. 2003, ApJS, 148, 175 31

Springel, V., White, S. D. M., Jenkins, A., et al. 2005, Nature, 435, 629 30

Stetson, P. B. 2000, PASP, 112, 925 74

Tammann, G. A., Sandage, A., & Reindl, B. 2003, A&A, 404, 423 14

Tegmark, M., Blanton, M. R., Strauss, M. A., et al. 2004, ApJ, 606, 702 28, 29

Tereno, I., Dore, O., Van Waerbeke, L., & Mellier, Y. 2005, A&A, 429, 383 129, 130

Van Waerbeke, L. & Mellier, Y. 2003, ArXiv Astrophysics e-prints 36, 57

Van Waerbeke, L., Mellier, Y., Erben, T., et al. 2000, A&A, 358, 30 9, 111

Van Waerbeke, L., Mellier, Y., & Hoekstra, H. 2005, A&A, 429, 75 111, 148

Van Waerbeke, L., Mellier, Y., Pello, R., et al. 2002, A&A, 393, 369 111, 148

Van Waerbeke, L., Mellier, Y., Radowich, M., et al. 2001, A&A, 374, 757 111

Van Waerbeke, L., White, M., Hoekstra, H., & Heymans, C. 2006, astro-ph/0603696 111, 134

Viana, P. T. P., Kay, S. T., Liddle, A. R., Muanwong, O., & Thomas, P. A. 2003, MNRAS, 346, 319 148

Viana, P. T. P. & Liddle, A. R. 1999, MNRAS, 303, 535 148

Viana, P. T. P., Nichol, R. C., & Liddle, A. R. 2002, MNRAS, 336, 541 148

Viel, M. & Haehnelt, M. G. 2006, MNRAS, 365, 231 29

Viel, M., Haehnelt, M. G., & Lewis, A. 2006, MNRAS, 370, L51 29

Walker, A. G. 1936, Proc. Lond. Math. Soc. (2), 42, 90 12

Wang, X., Tegmark, M., Jain, B., & Zaldarriaga, M. 2003, PhRvD, 68, 123001 28

White, S. D. M., Clowe, D. I., Simard, L., et al. 2005, A&A, 444, 365 64

Wittman, D., Tyson, J. A., Margoniner, V. E., et al. 2001, ApJ, 557, 89 97

Wittman, D. M., Tyson, J. A., Kirkman, D., et al. 2000, Nature, 405, 143 9, 111

Wu, J.-H. P. 2001, MNRAS, 327, 629 148

Zehavi, I., Blanton, M. R., Frieman, J. A., et al. 2002, ApJ, 571, 172 81

Zehavi, I., Weinberg, D. H., Zheng, Z., et al. 2004, ApJ, 607, 655 81

Zhang, L. L. & Pen, U. 2004, preprint astro-ph/0305447 81

Zwicky, F. 1933, Helv. Phys. Acta, 6, 110 20

Zwicky, F. 1937, ApJ, 86, 217 20

Remark: The small numbers after the references indicate the page numbers where the citations occur.

Acknowledgements

I would like to thank

- Peter Schneider for his supervision,
- Klaas S. de Boer for being the co-corrector of my thesis,
- Thomas Erben who was always patient to answer any kind of technical questions,
- Patrick Simon who shared with me his knowledge about statistics,
- Ole Marggraf and Oliver Cordes for solving any arising computer problems,
- the participants of the exam panel for their time.

Furthermore, I would like to thank my collaborators Thomas Erben, Patrick Simon, Peter Schneider, Mischa Schirmer, Hendrik Hildebrandt, Tim Schrabback, R. Maoli, L. Van Waerbeke, Y. Mellier who made substantial contributions to my first author publications, and Thomas Erben, Daniel Hudson, Martin Kilbinger, Ole Marggraf, Thomas Reiprich, Phillip Richter, Jens Rödinger, Patrick Simon, Tim Schrabback and Peter Watts for their careful reading of chapters of my thesis.

Not to forget the other, former and current, members of the AIfA Lensing Group: Anja von der Linden, Daniela Wuttke, Donate Weghorn, Er Xinzhong, Holger Israel, Ismael Tereno, Jan Hartlap, Jasmin Pielorz, Jörg Dietrich, Leonardo Castaneda, Marusa Bradac, Oliver Czoske, Oxana Nenestyan, Patrick Hudelot, Patricia Becker, Peter Erni, Philippe Heraudeau, Tim Eifler, Douglas Clowe, Lindsay King, Marco Lombardi. No substantial work can be done without a positive distraction to gain new mental power. Hence, I would like to thank Ole, Manuel, Jan, Patrick, Phillip, Olli, Martin, Peter W., Peter E., Hartmut, Wolfgang, Alessio, Ulf, Jasmin, Er, and Ingo.

This work was supported by the German Ministry for Science and Education (BMBF) through DESY under the project 05AE2PDA/8, and Transregio 33: The Dark Universe.

List of publications

- Probing the Universe using a mostly virtual survey: The Garching-Bonn Deep Survey
  M. Hetterscheidt, P. Simon, T. Erben, P. Schneider, M. Schirmer, J. P. Dietrich, H. Hildebrandt, O. Cordes, T. Schrabback, L. Haberzettl, O. Schmithuesen, C. Trachternach, C. Wolf, K. Meisenheimer, A. Micol, and F. Pierfederici
  to appear in **The Messenger**, No. 126 - December 2006

- The Shear TEsting Programme 2: Factors affecting high precision weak lensing analyses
  R. Massey, C. Heymans, J. Berge, G. Bernstein, S. Bridle, D. Clowe, H. Dahle, R. Ellis, T. Erben, **M. Hetterscheidt**, F. W. High, C. Hirata, H. Hoekstra, P. Hudelot, M. Jarvis, D. Johnston, K. Kuijken, V. Margoniner, R. Mandelbaum, Y. Mellier, R. Nakajima, S. Paulin-Henriksson, M. Peeples, C. Roat, A. Refregier, J. Rhodes, T. Schrabback, M. Schirmer, U. Seljak, E. Semboloni, and L. Van Waerbeke
  astro-ph/0608643, accepted for publication in MNRAS

- Cosmic shear analysis of archival HST/ACS data: I. Comparison of early ACS pure parallel data to the HST/GEMS Survey
  T. Schrabback, T. Erben, P. Simon, J.-M. Miralles, P. Schneider, C. Heymans, T. Eifler, **M. Hetterscheidt**, R.A.E. Fosbury, W. Freudling, H. Hildebrandt, and N. Pirzkal
  astro-ph/0606611, submitted to A&A

- GaBoDS: The Garching-Bonn Deep Survey; VIII. Probing galaxy bias using weak gravitational lensing
  P. Simon, **M. Hetterscheidt**, M. Schirmer, T. Erben, P. Schneider, C. Wolf, and K. Meisenheimer
  astro-ph/0606622, accepted for publication in A&A

- GaBoDS: The Garching-Bonn Deep Survey; VII. Cosmic shear analysis
  M. Hetterscheidt, P. Simon, M. Schirmer, H. Hildebrandt, T. Schrabback, T. Erben, and P. Schneider
  astro-ph/0606622, submitted to A&A

- GaBoDS: The Garching-Bonn Deep Survey; VI. A sample of 158 shear-selected mass

concentration candidates
M. Schirmer, T. Erben, **M. Hetterscheidt**, and P. Schneider
astro-ph/0607022, submitted to A&A

- GaBoDS: The Garching-Bonn Deep Survey; V. Data release of the ESO Deep-Public-Survey
H. Hildebrandt, T. Erben, J. P. Dietrich, O. Cordes, L. Haberzettl, **M. Hetterscheidt**, M. Schirmer, O. Schmithuesen, P. Schneider, P. Simon, and C. Trachternach
A&A 2006, volume 452, page 1121

- The Shear TEsting Programme 1: Weak lensing analysis of simulated ground-based observations
C. Heymans, L. Van Waerbeke, D. Bacon, J. Berge, G. Bernstein, E. Bertin, S. Bridle, M. L. Brown, D. Clowe, H. Dahle, T. Erben, M. Gray, **M. Hetterscheidt**, H. Hoekstra, P. Hudelot, M. Jarvis, K. Kuijken, V. Margoniner, R. Massey, Y. Mellier, R. Nakajima, A. Refregier, J. Rhodes, T. Schrabback, and D. Wittman
MNRAS 2006, volume 368, page 1323

- Searching for galaxy clusters using the aperture mass statistics in 50 VLT fields
M. Hetterscheidt, T. Erben, P. Schneider, R. Maoli, L. Van Waerbeke, and Y. Mellier
A&A 2005, volume 442, page 43

- GaBoDS: The Garching-Bonn Deep Survey; IV. Methods for the image reduction of multi-chip cameras demonstrated on data from the ESO Wide-Field Imager
T. Erben, M. Schirmer, J. P. Dietrich, O. Cordes, L. Haberzettl, **M. Hetterscheidt**, H. Hildebrandt, O. Schmithuesen, P. Schneider, P. Simon, J. C. Cuillandre, E. Deul, R. N. Hook, N. Kaiser, M. Radovich, C. Benoist, M. Nonino, L. F. Olsen, I. Prandoni, R. Wichmann, S. Zaggia, D. Bomans, R. J. Dettmar, and J. M. Miralles
AN 2005, volume 326, page 432

- GaBoDS: The Garching-Bonn Deep Survey - III. Lyman-Break Galaxies in the Chandra Deep Field South
H. Hildebrandt, D. J. Bomans, T. Erben, P. Schneider, M. Schirmer, O. Czoske, J. P. Dietrich, T. Schrabback, P. Simon, R. J. Dettmar, L. Haberzettl, and O. Cordes, **M. Hetterscheidt**
A&A 2005, volume 441, page 905

- Searching for clusters using weak lensing
M. Hetterscheidt, T. Erben, and P. Schneider Proceedings of "Baryons in Dark Matter Halos". Novigrad, Croatia, 5-9 Oct 2004. Editors: R. Dettmar, U. Klein, P. Salucci.
Published by SISSA, Proceedings of Science, http://pos.sissa.it, p.79.1